Hadronic Processes of Energetic Particles in Star-Forming Galaxies and High-Redshift Protogalactic Environments

Ellis Richard Owen

Thesis submitted for the degree of

Doctor of Philosophy

of

University College London

Mullard Space Science Laboratory

Department of Space and Climate Physics

University College London

2019

I, Ellis Richard Owen confirm that the work presented in this thesis is my own. Where information has been derived from other sources, I confirm that this has been indicated in the thesis. This thesis is based on my research in collaboration with Prof. Kinwah Wu, Dr Idunn B. Jacobsen, Ms Pooja Surajbali, Ms Xiangyu Jin, Ms Suetyi Chan and Ms Noriko Kataoka.

_____

_____

Abstract

In this thesis, the heating and feedback effect of energetic cosmic rays (CRs) in star-forming galaxies and protogalaxies is investigated. Galaxies undergoing violent starburst episodes are expected to be rich in CRs. This is due to an abundance of stellar end-products (which are able to accelerate CRs up to PeV energies), coupled with the rapid development of a μG interstellar magnetic field soon after the onset of star-formation, which is able to contain CRs inside the host galaxy. Hadronic CR particles can undergo interactions with photons and baryons. In star-forming galaxies, target photons are supplied by stellar radiation and the cosmological microwave background, while target baryons comprise the interstellar and circumgalactic medium. CR interactions enable their deposition of energy, causing the surrounding medium to be heated. This occurs either by the Coulomb thermalisation, or by the inverse Compton X-ray emission, of CR secondary particles (which are injected by the hadronic CR interactions). CR heating processes are found to attain a power of 10^{-25} erg cm^{-3} s^{-1} in an idealised galaxy with 1 core collapse SN event per decade. This falls to 10^{-28} erg cm^{-3} s^{-1} if concentrated starburst activity in the system leads to the development of a galactic-scale outflow. It is argued that CR-driven heating processes can lead to quenching and/or stunning of subsequent star-formation activity in the host. The level of CR feedback in 16 observed starburst/post-starburst high-redshift galaxies is estimated, based on the star-formation rates they could have sustained during their starburst episodes. It is found that CR feedback cannot be neglected in these systems: it has the strength to suppress star-formation, and can even maintain a post-starburst period of quiescence which is consistent with their inferred star-formation histories.

Impact Statement

The impact of this research falls into three themes:

1. Impact on the understanding of galaxy formation and evolution

This research establishes energetic particles as a critical component in the regulation of star-formation in galaxies of the early Universe. It outlines how they can influence the thermal evolution of these systems, and lays the theoretical foundations for new research directions which bridge the gap between microscopic particle physics and the macroscopic astrophysics of galactic evolution. This changes the current research paradigm in the field which, until now, has focussed on photonic processes. To date, there are substantial gaps in our understanding of high-redshift star-forming galaxies, ranging from the main fuelling mechanism of their burst-like star-formation, to the regulation and feedback processes operating therein. This work begins to address these gaps by fundamentally changing the view of galaxy formation and evolution, in particular by taking account of particles as an agent by which feedback can be delivered. This research has been reported in specialised scientific journals, and has also been presented and discussed at national and international scientific conferences.

2. Impact on the methodology in astrophysical research

A century ago, astronomy was based only on optical light. Since then, this has sub-divided across the electromagnetic spectrum, with both theoretical and observational research being conducted in optical, infrared, radio, X-ray and even γ-ray wavebands. In recent years, this has advanced even further beyond purely photonic information to also embrace multi-messenger astronomy: cosmic ray astrophysics/astro-particle physics has gained momentum, while gravitational wave astronomy has also started to offer a new perspec-

tive. This work reflects this broader progress, and adopts a holistic approach towards modelling feedback in actively star-forming galaxies, bringing multi-messenger astrophysics to the field of galactic evolution for the first time. It introduces new mechanisms by which energy can pass into the media and surroundings of star-forming galaxies from energetic particles, and the crucial role played by large-scale magnetic fields in the containment of energetic charged particles to focus their feedback effect is shown.

3. Impact on public engagement and education

This work draws from exciting fields in astrophysics and physics which, individually, are often used for public engagement. It therefore lends itself easily for use in outreach activities, and has already been employed in such a capacity with aspects having been used in STEM talks[1] for secondary school audiences, and discussion with prospective Physics/Astronomy students at the annual *World Class Study in London* Exhibition in Hong Kong (organised by a consortium of London Universities, including UCL). Moreover, aspects of this work have also provided the basis for secondary school and undergraduate summer research projects. It has also provided a scientific basis for outreach talks that I presented, and has helped to inform internet blog posts. Some of these posts have been widely read, discussed and shared by the public. Scientific articles published during the completion of this thesis have also gained attention on social media beyond the academic sphere.

---

[1]Presented by Prof. Kinwah Wu.

Acknowledgements

First and foremost, I would like to extend my gratitude to Prof. Kinwah Wu, my supervisor. His lecture course was my first introduction to cosmic rays and high-energy astrophysics, and I consider myself very fortunate to have had the privilege to explore these areas further under his excellent supervision. He has been a generous and inspirational teacher, and has provided unwavering support, thoughtful advice and seemingly limitless patience throughout my time at MSSL for which I will always be grateful.

I also extend my thanks to Dr. David Sobral (Lancaster), and Dr. Ignacio Ferreras (IAC) for taking the time to assess this thesis, and for assuming their roles as my examiners.

I thank Dr. Christoph Deil and Prof. Dr. Werner Hofmann of the Max-Planck-Institut für Kernphysik, who supervised and supported my first steps into the world of academic research and astroparticle physics. I am grateful for their support and guidance during my time in Heidelberg. I also thanks to Drs. Alison Mitchell and Axel Donath, and to Ms. Pooja Surajbali for discussions and collaborations.

I thank Dr. Jason McEwen for assuming the role of my second supervisor, Dr. Ignacio Ferreras for always making the time to answer my questions in an interesting and inspiring way, and Prof. Daisuke Kawata, Prof. Mark Cropper and Dr. Ziri Younsi for their kind advice, direction and discussion over the years. I am grateful to Prof. Shih-Ping Lai and Prof. Albert Kong for supporting my visits to NTHU, and to their students for their scientific and technical research help, and for kindly welcoming me to Hsinchu. I thank Prof. Masami Ouchi and Dr. Khee-Gan Lee for teaching me about high-redshift galaxies and for hosting me at ICRR and IPMU respectively, Prof.

Contents

List of Figures

List of Tables

Chapter 1

Introduction

Energetic hadronic cosmic ray (CR) particles and their influence on astrophysical systems have been studied extensively since the discovery of CRs over 100 years ago, particularly in the context of the solar-terrestrial setting and the wider Milky Way. Their interactions in astrophysical environments has been discussed extensively in the literature in a range of contexts (e.g. Greisen 1966; Zatsepin and Kuz'min 1966; McCray and Buff 1972; Nath and Biermann 1993; Valdés et al. 2010), however their role in distant galaxies and larger structures is arguably less well understood. This is particularly the case in star-forming galaxies, where energetic CR particles are expected to be much more abundant than in our own cosmic neighbourhood (see e.g. Karlsson 2008; Lacki et al. 2011; Wang and Fields 2014; Brunetti and Jones 2014). This would imply that their processes and effects are even more important in star-forming galaxies than they are in the Milky Way.

Conditions in the early Universe, when galaxies were forming their first generations of stars and when luminous quasars first emerged, are ideal for the acceleration of hadronic CRs. This is because CRs are products of violent astrophysical events, for example supernova (SN) explosions, large-scale shocks (e.g. in colliding galaxies and galaxy clusters) and the extreme environments arising in compact objects, e.g. those which develop from stellar end-products (see Berezinskii et al. 2006; Dar and de Rújula 2008; Kotera and Olinto 2011). High rates of star-formation activity boosts SN activity. This is because star-formation produces stars of a wide range of masses. Those of

large mass move through their evolutionary paths very rapidly, within just a few million years. They will therefore quickly yield SN events only a short time after the onset of star-formation activities (on astrophysical timescales). In environments where star-formation is relatively quiescent, only lower-mass components of the population typically persist in any substantial number (except in unusual cases where massive stars may form late due to, e.g. the merger of lower-mass stars, as per the formation of blue stragglers in globular clusters from binary progenitors). It follows that the SN rate in these passive systems would therefore be similarly reduced.

In rapidly star-forming (starburst) galaxies, the stellar end-products (particularly SN remnants) contribute seed particles, while the associated shocks from the SN explosions and other violent astrophysical events introduce the necessary conditions required to accelerate these seed particles up to PeV energies (Bell 1978; Kotera and Olinto 2011; Schure and Bell 2013; Bell 2013) through diffusive shock acceleration processes - e.g. second-order Fermi acceleration (Fermi 1949). Higher energy particles, above a PeV, are likely to have extragalactic sources, where larger acceleration regions and/or stronger magnetic fields can operate to push them to these extreme energies (Hillas 1984; Becker 2008; Kotera and Olinto 2011; Blasi 2014).

Ionisation and excitation of atomic matter, such as that found in interstellar (ISM) and intergalactic media (IGM), can be caused by keV CR protons. Such ionisation, collisions and Coulomb interactions (e.g. Rutherford scattering) between a CR and its environment can heat the interstellar and intergalactic medium along the propagation path of the particle (see e.g. Nath and Biermann 1993; Sazonov and Sunyaev 2015). However, the Galactic CR spectrum would indicate that a much greater proportion of energy density lies in the higher-energy population of protons, above around 1 GeV – perhaps accounting for as much as 99% of the energy density in the Galactic CR population (see, e.g. Benhabiles-Mezhoud et al. 2013). These high-energy CRs are much less engaged with atomic and Coulomb interaction processes – such actions could only account for a maximum of 2.5% of the energy loss experienced by a GeV CR-proton during a Hubble timescale, even if the density

of the medium through which such a CR propagated were held as that of the IGM of $z = 20$ (see Sazonov and Sunyaev 2015). Instead, energetic CRs interact predominantly through hadronic processes. In the case of intergalactic propagation, the Gresisen-Zatsepin-Kuzmin (GZK) cutoff (Greisen 1966; Zatsepin and Kuz'min 1966) is an example of such an effect, where the high-energy GeV CRs are suppressed by their hadronic interactions with cosmic microwave background (CMB) photons. Similar effects arise with sufficiently dense matter fields, if the CR energy is above a threshold of 0.28 GeV (see, e.g. Kafexhiu et al. 2014). These processes allow energetic CRs to deposit their energy far more efficiently than their lower-energy keV counterparts.

While the effects of CRs in the high-redshift Universe have started to attract the attention of researchers in recent years (see Giammanco and Beckman 2005; Stecker et al. 2006; Valdés et al. 2010; Bartos and Marka 2015; Sazonov and Sunyaev 2015; Leite et al. 2017), detailed studies and modelling of CR production, propagation and interactions within young galaxy environments are still in their infancy. This is despite the important action that energetic CRs may have in regulating star-formation activity during the cosmic dawn (see Pfrommer et al. 2007; Chen et al. 2016), as well as their potential role in driving large-scale galactic outflows (see Socrates et al. 2008; Weiner et al. 2009; Samui et al. 2010). Such outflows can enable CRs to transport energy from their host galaxy to the surrounding circumgalactic medium (CGM) and IGM. This means that their impact on the dynamical and thermal properties of systems may not just be limited to their galaxy of origin – their effects may actually be felt further afield, in the CGM and beyond (e.g. Leite et al. 2017). This opens up new questions about the influence CRs can have on large-scale structures, and even on wider astrophysical and cosmological processes – e.g. their ability to contribute to the heating and pressure support of intra-cluster gas in galaxy clusters and proto-clusters (e.g. Pfrommer et al. 2007; Enßlin et al. 2007; Guo and Oh 2008; Pinzke and Pfrommer 2010; Hennebelle 2012; Ruszkowski et al. 2017), their role in the amplification of intra-cluster and/or intergalactic magnetic fields (Miniati and Bell 2011; Beck et al. 2013; Lacki 2015), and their potential ability as a contributing agent towards the

pre-heating of intergalactic gases in advance of cosmic reionisation (Nath and Biermann 1993; Samui et al. 2005; Tueros et al. 2014; Sazonov and Sunyaev 2015; Leite et al. 2017).

This work is the first to consider the thermodynamical impacts of hadronic CR heating in the context of protogalactic and starburst environments, and the direct and indirect feedback processes CRs may contribute to therein. The first results of this work appear in:

(i) *"Interactions between ultra-high-energy particles and protogalactic environments"*, Owen E. R., Jacobsen, I. B., Wu, K., Surajbali, P., 2018, MNRAS, 481, 666;

(ii) *"Hadronic interactions of energetic charged particles in protogalactic outflow environments and implications for the early evolution of galaxies"*, Owen E. R., Jin. X., Wu, K., Chan, S., 2019, MNRAS, 484, 1645;

(iii) *"Starburst and post-starburst high-redshift protogalaxies: the feedback impact of high-energy cosmic rays"*, Owen E. R., Wu, K. Jin, X. Surajbali, P. Kataoka, N., 2019, A&A, 626, A85.

Much of the analysis and many of the results presented in this thesis are drawn from these papers (including the remainder of this introduction). The models presented here constitute the first approach in quantifying the hadronic feedback impact of CRs on star-forming and high-redshift protogalactic environments in a manner which connects the macroscopic astrophysics and microscopic astroparticle physics to the astrophysical dynamics and evolution of these systems.

1.1 Protogalaxies in an Astrophysical Context

The formation of structure in the Universe was hierarchical, with the large gravitationally-bound objects observed in the current epoch developing from a history of mergers and coalescence of smaller, older structures (e.g. Press and Schechter 1974; Lacey and Cole 1993; Peacock 1999): over cosmological time, clusters formed by accumulating groups of galaxies, while the galaxies themselves emerged from accretion flows of baryonic gas (e.g. Dayal and Ferrara 2018), and mergers of their smaller progenitors – hereafter referred to as proto-

galaxies. Such structure formation can be illustrated by a merger tree as that shown in Fig. 1.1 (see also Lacey and Cole 1993). It follows that high-redshift protogalaxies have smaller characteristic sizes, of only around a few kpc (see Bouwens et al. 2004; Ferguson et al. 2004; Bradley et al. 2008; González et al. 2010; Zheng et al. 2012; Watson et al. 2015; Knudsen et al. 2016; Hashimoto et al. 2018; Dayal and Ferrara 2018, for examples of high-redshift star-forming galaxy observations) and lower masses of around $10^9 - 10^{10}$ M$_\odot$ (Bouwens and Illingworth 2006; González et al. 2010; Watson et al. 2015; Hashimoto et al. 2018) compared to the larger, evolved galaxies that can be observed in the current Universe.
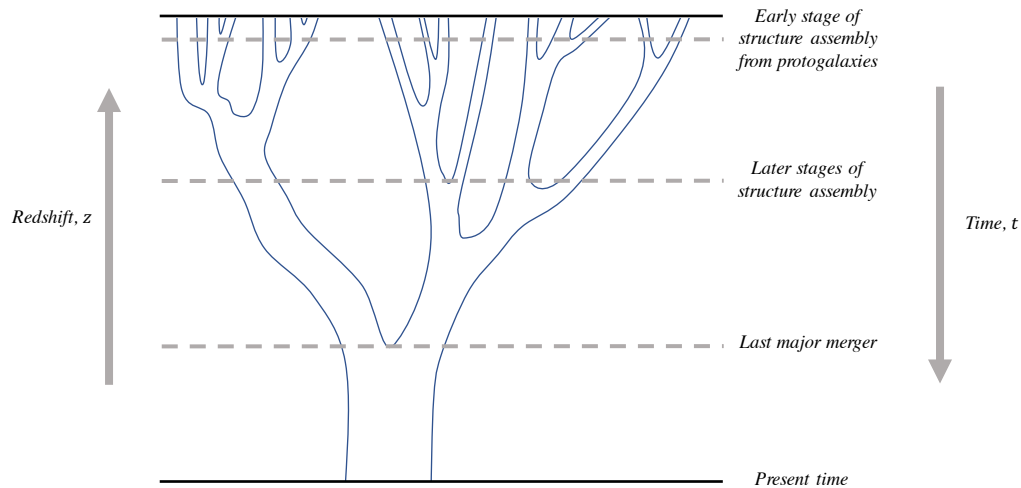
Fig. 1.1: Merger tree schematic to illustrate the formation of galaxies in the Universe via mergers and accretion under hierarchical structure formation, based on Fig. 3 of (Lacey and Cole 1993). Each 'branch' represents the mass of a galaxy halo or progenitor, with convergence of branches indicating a merger event. Broadening of the branches without a merger represents accretion.

Merger events of protogalaxies are violent and catastrophic. They can inject substantial instabilities into the interstellar gas of the resulting system, and it has been argued that this can trigger star-formation (e.g. Larson and Tinsley 1978; Joseph and Wright 1985; Moster et al. 2011; Ostriker and Shetty 2011; Hirschmann et al. 2012).[1] As galaxies coalesce into large structures such

---

[1] Note that, by contrast, it has also been argued that the turbulence also injected during merger events can lead to the regulation and even quenching of subsequent star-formation activity (Ostriker and Shetty 2011).

as groups and proto-clusters, they will occupy smaller regions of space with their physical separations becoming closer under the pull of gravity. This increases the frequency of tidal interactions between galaxies and, even if these nearby interactions do not cause them to merge, they may still be sufficient to drive the instabilities necessary to instigate a burst of star-formation (Larson and Tinsley 1978; Lambas et al. 2003; Alonso et al. 2004; Nikolic et al. 2004). However, more recently it has been argued that mergers and tidal interactions are not actually the most important causes of star-formation at high-redshift. Indeed, some simulation studies have suggested that tidal interactions and major merger events are not actually particularly effective at high-redshift in enhancing star-formation at all, unlike such actions in lower-redshift systems (Wang et al. 2011; Combes 2013; Sánchez Almeida et al. 2014; Fensch et al. 2017). Moreover, Fensch et al. (2017) find this to remain the case even in the absence of stellar feedback. Instead, cold accretion via filamentary inflows has been proposed as the principal mechanism by which star-formation in a high-redshift protogalaxy is driven (e.g Kereš et al. 2005; Fumagalli et al. 2011; Sánchez Almeida et al. 2014; Dayal and Ferrara 2018). These flows would be able to supply gas via e.g. cold mode accretion (Birnboim and Dekel 2003; Kereš et al. 2005) to a galaxy from the chemically pristine cosmic web, enabling it to sustain a period of rapid star-formation (Dekel et al. 2009b; Khochfar and Silk 2009; Ceverino et al. 2010; Genel et al. 2012).

Cold inflows seem to operate most effectively at high-redshifts, with as much as 90% of baryons arriving into protogalaxies by this channel (Benson and Bower 2011). These flows are thought to be critical in supplying the fuel to drive bursts of star-formation in the early stages of galaxy evolution (Kereš et al. 2005; Dekel et al. 2009a; Stewart et al. 2013; Goerdt and Ceverino 2015; Goerdt et al. 2015). Their activity peaks at redshifts of around $z \approx 2 - 4$ (Woods et al. 2014; Goerdt and Ceverino 2015), but falls away exponentially after $z \approx 2$ (Woods et al. 2014). While there is not a clear reason as to why this change in behaviour should arise specifically at $z \approx 2$, some researchers have proposed that it may be due to a reduction in the availability of cold gas as the Universe develops. This would presumably correspond to the

build-up of the warm–hot IGM (Mo et al. 2005; Woods et al. 2014; Sánchez Almeida et al. 2014), possibly caused by feedback processes.

Filamentary cold inflows have not yet been unambiguously detected, but a mounting bank of circumstantial evidence provides increasing support for their existence (Mandelker et al. 2018). For example, the emission structure of Lyman-α blobs (LABs) is consistent with the morphology and luminosity expected from cold inflow streams above $z = 2$ (Steidel et al. 2000; Matsuda et al. 2006; Goerdt et al. 2010; Matsuda et al. 2011; Rauch et al. 2011; van de Voort et al. 2012), while absorption features along Quasar lines of sight as a means of probing the CGM of host systems are also consistent with a chemically pristine composition of accreting material (Bouché et al. 2013, 2016). Furthermore, the constant flow velocity predicted by simulations of cold inflow streams (e.g. Goerdt and Ceverino 2015, see also Dekel et al. 2009a; Goerdt et al. 2012) may be observed in Lyman-α emission (Dijkstra and Loeb 2009; Faucher-Giguère et al. 2010; Goerdt et al. 2010) – although the detection of (blue-shifted) Lyman-α emission in high-redshift systems well into the Epoch of Reionisation (EoR) and the interpretation of such emission as being associated with inflows does impart certain challenges: modelling of the EoR predicts only negligible transmission of Lyman-α bluewards of the systematic redshift of a system (e.g. Weinberger et al. 2018), with radiative transfer calculations indicating a transmission fraction of below 0.1% above $z = 5$ (Laursen et al. 2011). Nevertheless, a strong blue peak in the Lyman-α profile is still detected in some galaxies well into EoR redshifts, e.g. COLA1 at $z = 6.59$ (Matthee et al. 2018) and MACS1149-JD1 at $z = 9.11$ (Hashimoto et al. 2018). One explanation is the presence of a large ionised bubble around the emitting galaxy, presumably ionised by starlight. This may be sufficient to allow Lyman-α emission to be redshifted out of resonance. At $z = 6.59$, this would require an ionised region of around 0.3 Mpc, or 0.2 Mpc at $z = 9.11$ (Matthee et al. 2018). Alternative possibilities include a large semi-ionised circumgalactic region which would greatly improve the Lyman-α transmission to large distances (also facilitating its redshift out of resonance), or the presence of an intervening absorber with a large velocity offset (Matthee et al. 2018).

Possible evidence for cold inflows also arguably lies in the inference of star-formation activity and its history in high-redshift systems: for example, a star-formation rate of $4.2^{+0.8}_{-1.1}$ M$_\odot$ yr^{-1} was determined for the high-redshift starburst MACS1149-JD1, which was spectroscopically confirmed at $z = 9.11$ using the doubly-ionised Oxygen [O III] line at 88μm (Hashimoto et al. 2018). This redshift corresponds to a time only 550 Myr after the Big Bang (Wright 2006; Hashimoto et al. 2018). Given that the system is around 3.7 ± 1.1 kpc by 1.4 ± 0.9 kpc in size (Hashimoto et al. 2018), the resulting star-formation rate surface density Σ^*_{obs} is around 250 times that of the Milky Way, which has a characteristic size of 30 kpc (Xu et al. 2015) and star-formation rate of around $0.68 - 1.45$ M$_\odot$ yr^{-1} (Robitaille and Whitney 2010). While there is some possibility that MACS1149-JD1 is actually two interacting sources, the preferred interpretation of Hashimoto et al. (2018) is that it is a single galaxy. This scenario would largely rule-out tidal interactions as a cause of the inferred star-formation which leaves filamentary inflows as a plausible explanation.

Alongside the ongoing observed star-formation activity, the wider spectrum and position of the Balmer break detected for MACS1149-JD1 indicates the possibility of a second, much older population of stars is present in this system. Some caution is advised with this interpretation as it relies on photometric points beyond the Balmer break which come from *Spitzer* IRAC photometry and this has poor spatial resolution (and so may be associated with different sources). Moreover, Hashimoto et al. (2018) indicate that there is a possibility that MACS1149-JD1 is comprised of two galaxies with a kinematic separation of 450 km s^{-1} (corresponding to the measured blueshift in the Lyman-α line compared to the [O III] 88-μm rest-frame), with the IRAC excess associated with only one of these. However, if the interpretation that the IRAC excess and Balmer break arise due to a two-age stellar population is assumed to be correct, the existence of the older stars can be understood to arise from a burst of star-forming activity at a much earlier epoch: from the estimated stellar population age, this would have arisen at least 100 Myr before the observational epoch at $z = 9.11$, which implies that this system was already well established when the Universe was still in its infancy. To

have formed a stellar mass of $1.1^{+0.5}_{-0.2} \times 10^9$ M$_\odot$ by $z = 9.11$, either the star-formation rate must have been extremely high, around 16 M$_\odot$ yr^{-1} (starting around $z = 15.4$), or it must have begun extremely early in cosmic time, at around $z = 17.0$ (if adopting a star-formation rate of 8 M$_\odot$ yr^{-1}).

While very early star-forming activity at $z = 17.0$ cannot be categorically ruled out for this galaxy, it seems pragmatic to adopt the intermediate star-formation history model proposed by Hashimoto et al. (2018), which estimates the start of star-formation at $z = 15.4$. This continues for 200 Myr at a rate of 8 M$_\odot$ yr^{-1}, and implies that star-formation activity was initiated at only around 250 Myr after the Big Bang. A period of 100 Myr during which star-formation was relatively suppressed would then account for the two distinct stellar population ages inferred from the spectrum. While this early onset of star-formation alone is a remarkable finding, its implications are even more consequential for this work: such behaviour and evolution of MACS1149-JD1 provides the first indication that cold filamentary inflows may indeed be operating in this system and are responsible for its early, high-rate star-formation burst. This can be understood by consideration of the quiescence period of the system: if star-formation was driven by a cold gas supply by filamentary inflows, a period of quiescence would indicate that this supply must somehow have been cut-off. This could have been caused by feedback from star-formation, as argued by Hashimoto et al. (2018), whereby the large amount of ultraviolet (UV) radiation from the young stars and/or X-rays (from ISM gases and stellar remnants) carve out a hot, ionised bubble within the surrounding IGM. Hashimoto et al. (2018) considered a uniform IGM of number density 10^{-2} cm^{-3} and UV escape fraction of 20%, which would produce a Strömgren (1939) sphere of radius 0.4 Mpc around MACS1149-JD1. This hot, ionised region bathed in abundant UV and X-ray radiation would presumably halt and evaporate filamentary inflows. Thus to rejuvenate star-formation, filamentary inflows would need to be re-established in order to supply the required cool gases. This could occur either by CGM gases cooling and condensing to re-form clumps and filaments from the hot ambient medium of the Strömgren (1939) bubble, or by the return of cold gaseous inflows from beyond

the ionised bubble.

In the first scenario, the cooling timescale can be estimated by considering that due to thermal free-free cooling for a hot ionised gas:

$$\tau_{\text{cool}} \approx \frac{n_{\text{e}} k_{\text{B}} T_{\text{e}}}{\Lambda_{\text{cool}}(n_{\text{e}}, T_{\text{e}}, |q|)} \ . \tag{1.1}$$

Here, Λ_{cool} is the cooling rate, n_{e} is the electron number density, T_{e} is the electron (gas) temperature, $|q|$ is the charge number of ions, and k_{B} is the Boltzmann constant. Eq. 1.1 may be more conveniently expressed as

$$\tau_{\text{cool}} \approx 100 \left(\frac{n_{\text{e}}}{10^{-2}\,\text{cm}^{-3}} \right)^{-1} \left(\frac{T_{\text{e}}}{10^7\,\text{K}} \right)^{1/2} \text{Myr} \ . \tag{1.2}$$

The electron number density can be estimated as $n_{\text{e}} = \langle n_{\text{H}} \rangle \approx 10^{-2}$ cm^{-3} (where n_{H} is the number density of the medium) following from the Strömgren (1939) sphere calculation in Hashimoto et al. (2018). An electron temperature of $T_{\text{e}} = 10^7$ K gives a cooling time equal to the duration of the 100 Myr quiescent period established for this system. While these conditions represent the 'perfect' requirement to match the inferred quiescence period for MACS1149-JD1, they are not actually implausible: the temperature T_{e} could indeed reach 10^7 K (e.g. Bykov et al. 2008) in a gas photo-ionised by UV radiation and/or keV X-rays, with an example of such being the Warm-Hot IGM, WHIM (Draine 2011). Electron number densities within ionised regions could be much lower than the value used above – for example, WHIM number densities are typically of the order $n_{\text{e}} \approx 10^{-5}$ to 10^{-6} cm^{-3} (e.g. Nicastro et al. 2008, 2018). This could substantially increase the cooling timescale compared to the above prescription. On the other hand, if CGM and ISM gases are multi-phase and/or only partially ionised with various temperatures in the range $10^4\,\text{K} < T < 10^7\text{K}$, then cooling may instead be much faster than equation 1.2 suggests. This is because, in a semi-ionised state, much more efficient recombination and collisional excitation processes can operate in addition to thermal free-free cooling processes, with such bound-free and bound-bound cooling being strongly dependent on the metallicity and composition of the gas itself (see Sutherland and Dopita 1993).

In the scenario where the re-establishment of star-formation is driven by the re-emergence of filamentary inflows from beyond the Strömgren sphere, a free-fall velocity of around $4,000$ km s^{-1} (i.e. about 1% of the speed of light) would be required for gases beyond 0.4 Mpc to be able to reach the galaxy in the time required (100 Myr). Such an inflow velocity is clearly excessive, especially given that the measured blueshift in the Lyman-α line compared to the [O III] 88-μm rest-frame was found to be an order of magnitude lower for this galaxy (see also Dijkstra et al. 2006; Verhamme et al. 2015, for further details and applications of this technique to detect inflows). Instead, a more consistent argument indicates that both cooling and inflows are jointly responsible for the observed behaviour of MACS1149-JD1, and that its CGM is a highly non-uniform multiphase medium. The Strömgren sphere prescription would plausibly hold in the low-density regions between filaments, where H II regions may extend out to hundreds of kpc (i.e. a large fraction of the 0.4 Mpc Strömgren radius, allowing for the redshift of Lyman-α out of resonance and its subsequent escape from the system). However, the existence of clumps and remnant filaments would mean that some level of shielding against the heating and ionising radiation from the galaxy (as well as enhanced cooling in over-densities) prevents the full Strömgren extent of the H II region from developing isotropically. For instance, in the direction of lines of sight traversing over-densities and inflow remnants, the extent of the H II region would be substantially diminished compared to the idealised case above. For an ionisation distance in the direction of the filaments of around 10% of the Strömgren radius of MACS1149-JD1, it follows that a much lower inflow velocity, around 400 km s^{-1}, would be sufficient to account for the rejuvenation of star-forming activity within 100 Myr. Indeed, such a velocity corresponds well with that inferred from the offset of the Lyman-α line (Hashimoto et al. 2018).

1.2 The Circumgalactic Environment

The CGM connects the interstellar (internal) environment of a galaxy with its intergalactic/intra-cluster (external) setting. The structure of the CGM and the processes at work therein are crucial in determining how a galaxy
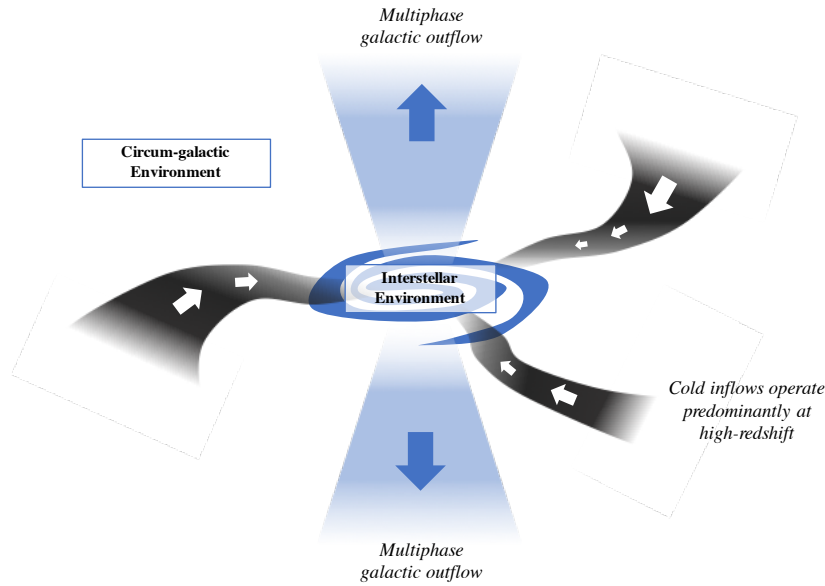
Fig. 1.2: Schematic showing the main features in the CGM around a high-redshift protogalaxy. The circumgalactic environment and interstellar environment are indicated, together with cold inflowing filaments (in black) providing cool gas from the cosmic web to fuel star-formation and hot multiphase outflows (in blue) driven by star-formation activity. These outflows can deliver energy, metals, hot gases, magnetic fields and CRs into the circumgalactic environment and beyond. Based on the schematic in Tumlinson et al. (2017).

and its environment interact. The discussion up to this point has shown that the features of the CGM are dependent on the system in question: at high-redshift, when galaxies were forming their first generations of stars, a substantial flow of baryons would be supplied via cold inflows passing through the CGM. Such flows do not operate at low-redshift. These inflows of gas can fuel intense starburst periods which, in turn, may drive galactic scale outflows (see section 1.2.2 for further details). These multi-phase outflows have the capacity to transport energy, hot gases, magnetic fields and CRs (all products of star-formation) from the internal galaxy environment into the CGM and beyond, impacting on the chemical, thermal and magnetic evolution of the circumgalactic environment (Kronberg et al. 1999; Völk and Atoyan 2000; Bertone et al. 2006; Durrer and Neronov 2013). Inflows and outflows around a protogalaxy are illustrated in Fig. 1.2, and are discussed in the following subsections.

1.2.1 Filamentary Inflows

Although the exact properties of cold filamentary inflows remain uncertain, indications are (primarily from simulations) that they have a multi-phase configuration, comprised of a hot tenuous ionised component beaded with dense, cool less-ionised clumps (see Fumagalli et al. 2011; Faucher-Giguère and Kereš 2011; Cornuault et al. 2018). They extend to distances of up to $R = 50$ kpc, beyond which they are not clearly resolved in simulations (e.g. Dekel et al. 2009a; Stewart et al. 2013; Goerdt and Ceverino 2015). At larger distances, they presumably connect to the cosmic web from which they have been demonstrated to draw their gas supply (Steidel et al. 2002; Kacprzak et al. 2010; Goerdt and Ceverino 2015; Danovich et al. 2015; Libeskind et al. 2018). Such a source of gas would indicate that these flows are relatively chemically pristine (Kacprzak et al. 2012; Bouché et al. 2013; Crighton et al. 2013), with the chemical enrichment of the galaxies they feed seemingly being governed solely by their internal star-formation rate, with no external sources of metallicity (Kacprzak et al. 2016) – see also, e.g. Mannucci et al. (2010); Bothwell et al. (2013); Forbes et al. (2014); Maier et al. (2015) for observational studies which also support this.

The exact ionisation fraction of the inflowing gas is unclear, however simulation work suggests a fiducial value of $x_i = 0.9$ is appropriate and consistent with the expectation that cold inflows would be predominantly ionised (Fumagalli et al. 2011; Faucher-Giguère and Kereš 2011). Simulation work also indicates that the temperature of the gases in these inflows is typically $10^4 - 10^5$ K (Dekel and Birnboim 2006; Dekel et al. 2009a; Goerdt and Ceverino 2015), being sufficiently cool to unlock efficient bound-free and even bound-bound cooling regimes in their densest regions (Dayal and Ferrara 2018). The precise flow density and substructure is also unknown, but a characteristic value for the flow density may be estimated if assuming them to be the principal means by which star-formation in a protogalaxy is fuelled (e.g Kereš et al. 2005; Fumagalli et al. 2011; Sánchez Almeida et al. 2014). Under such circumstances, the star-forming efficiency is typically quoted to

be of tens of percent[2], and a fiducial value of 30% (i.e. $\eta^{\star}_{\mathrm{inflow}} = 0.3$) is adopted here. The characteristic inflow velocity of gas through these cold filaments is typically a few hundred km s^{-1} (e.g. van de Voort et al. 2012; Goerdt and Ceverino 2015). For the present purposes, its value in MACS1149-JD1 may be reasonably estimated from the Lyman-α velocity offset, around $v_{\mathrm{Ly}\alpha} \approx 400$ km s^{-1} (Hashimoto et al. 2018). An inflow covering fraction would typically be between 5% and 40% – see e.g. Dekel et al. 2009a; Ribaudo et al. 2011; Fumagalli et al. 2011; Faucher-Giguère and Kereš 2011 (note also that some redshift evolution is discussed in the literature, with smaller covering fractions arising at later times – see, e.g. Fumagalli et al. 2011), thus a conservative estimate appropriate for high-redshift systems of 10% is used. This gives a corresponding effective flow radius to be around 30% of that of the galaxy which it feeds. An estimate for the number density of the inflowing filament follows as

$$n_{\mathrm{H}} \approx \frac{\mathcal{R}_{\mathrm{SF}}}{\eta^{\star}_{\mathrm{inflow}}\, v_{\mathrm{Ly}\alpha}\, \sigma_{\mathrm{f}}\, m_{\mathrm{p}}} \ , \tag{1.3}$$

in which $\sigma_{\mathrm{f}} = \pi r_{\mathrm{f}}^2$ is the approximate cross sectional area of the flow and m_{p} is the proton rest mass (being comparable to the total mass of a hydrogen atom). For the flow parameter values specified above, this treatment gives filament number densities of around $n_{\mathrm{H}} \approx 20$ cm^{-3} for a system with $\mathcal{R}_{\mathrm{SF}} = 16$ M$_{\odot}$ yr^{-1}. Such a value would appear to fall within a sensible range of values supported by literature studies, which propose anything in the range $n_{\mathrm{H}} \approx 10^{-1} - 10^{1}$ cm^{-3} (Kereš et al. 2009; Ceverino et al. 2010; Goerdt et al. 2012; Goerdt and Ceverino 2015; Falgarone et al. 2017).

1.2.2 Protogalactic Outflows

Large, galactic-scale outflows are ubiquitous among starburst galaxies in the local Universe, with well-studied examples including Arp 220 (e.g. Lockhart et al. 2015; Barcos-Muñoz et al. 2018), M82 (e.g. Heckman et al. 1990; Seaquist and Clark 2001; Walter et al. 2002) and NGC 253 (e.g. Strickland

---

[2]See, for instance Sun and Furlanetto 2016, which finds efficiencies of this order, around 30%, for halo masses above 10^{11} M$_{\odot}$ (i.e. corresponding to stellar masses of around 10^{9} M$_{\odot}$, not unlike MACS1149-JD1). Moreover, Meier et al. 2002; Behroozi and Silk 2015 and Turner et al. 2015 quote similar efficiencies in the local star-forming galaxy NGC 5253 which, despite being driven by different processes, may at least be indicative of the levels to be expected in these types of systems.

et al. 2000; Bolatto et al. 2013). This is also the case in the more distant Universe, where outflows frequently develop around star-forming hosts and protogalaxies (Frye et al. 2002; Ajiki et al. 2002; Benítez et al. 2002; Rupke et al. 2005a,b; Bordoloi et al. 2011; Arribas, S. et al. 2014). Work by Samui et al. 2008 argues that galactic outflows at high-redshift have a strong impact on the thermodynamics and subsequent evolution of the IGM, with smaller galaxies of characteristic masses around 10^9 $M_\odot$ (see also Bertone et al. 2005; Salvadori et al. 2014; Mac Low and Ferrara 1999; Madau et al. 2001; Samui et al. 2009; Booth et al. 2012) making the largest contributions. Their dominance is due to their weaker gravitational potentials, which facilitates the launch of an outflow wind. As such, much of the following analysis regards outflows arising in model galaxies with this characteristic mass.

Outflows are complex, multi-phase structures comprised of warm partly-ionised gases, hot ionised bubbles and cold, dense, minimally ionised clumps and clouds. They may also harbour complex, turbulent magnetic fields and could provide the means by which weak seed magnetic fields can be transported from within the galaxy to the surrounding environment (Aguirre et al. 2001b,a; Martin et al. 2002; Rupke et al. 2003; Adelberger et al. 2003; Aguirre et al. 2005; Bertone et al. 2005) where they may be amplified by large-scale shear motions, or by turbulence, to the μG levels seen in observations (De Young 1992; Goldshmidt and Rephaeli 1993; Dolag et al. 1999; Dolag, K. et al. 2002; Bertone et al. 2006; Vazza et al. 2018). Similarly, these systems play an important role in efficiently injecting mechanical energy, metals and other matter including low and high-energy particles (e.g. CRs and their secondaries) into circumgalactic and intergalactic space to distances of tens of kpc (see Aguirre et al. 2001a; Scannapieco et al. 2002; Pettini et al. 2003; Heesen et al. 2016), with their total mechanical power estimated to be as high as 10^{43} erg s^{-1} in some cases (see Cecil et al. 2002b).

There is substantial observational evidence that metal[3] enrichment of the intergalactic medium arose alongside the evolution of galaxies over a large range of redshifts (Aguirre and Schaye 2007). Indeed, metal absorption lines in

---

[3]Here 'metal' refers to any substance that is not Hydrogen or Helium.

quasar spectra (e.g. C III, C IV, Si IV, O VI) have revealed the IGM is enriched to up to around 0.1-1% of solar metallicity ($Z_\odot$) by $z \approx 3$ in low-density regions (Zhang et al. 1998; Davé et al. 1998; Aguirre et al. 2001a), while there is also evidence of chemical enrichment arising as early as $z = 5$ (Pettini et al. 2003; Simcoe 2006), but with the history of this process being uneven throughout cosmic time (e.g. there is surprisingly little evidence of substantial metal enrichment occurring between $z = 2$ and 4 – see Schaye et al. 2003). This enrichment is also apparently very widespread, with metal absorption lines even being detected well outside of regions known to contain galaxies, deep within the IGM (Songaila and Cowie 1996; Davé et al. 1998; Ellison et al. 2000; Schaye et al. 2003; Aguirre et al. 2004; Shen et al. 2010). The original source of these metals is presumably the stellar populations that formed in galaxies, with metals being injected into the interior media of these galaxies by terminal SN explosions and then later being released into the IGM by outflows. This is because the original matter from which the (pristine) IGM is comprised consists only of hydrogen, helium, small amounts of lithium and traces of heavier elements, being those which could form in Big Bang Nucleosynthesis, BBN (e.g. Ferrara et al. 2000; Kusakabe et al. 2014; Coc 2016) – so this alone can not account for the metallicities inferred from observations.

In general, simulation work has indicated that there are three principal mechanisms by which galactic outflows may be driven in order to deliver metals into the IGM. These are discriminated by the mass of the host galaxy: low-mass systems are typically mechanically driven (by SN events), intermediate mass systems (below around 10^{11} $M_\odot$) are usually momentum-driven by outward radiative and/or CR pressure, while high mass systems tend to rely on the action of an active galactic nucleus (AGN) to support a jet-driven outflow to eject metals to the IGM (Côté et al. 2015). The action of chemical enrichment via outflows leads to a symbiotic relationship between the evolution of a galaxy and the evolution of its environment: as the metallicity of the intergalactic gas becomes increasingly enriched, it continues to supply a substantial fraction of the fuel required to drive star-formation (via inflows). The entrenchment of metals in inflowing gases enhances the avenues by which

it may cool and, as such, increases its tendency to fragment and collapse under gravity. This can boost star-formation activity overall (see, e.g. Dib et al. 2011; Yates et al. 2012, for recent studies into this effect), but can also modify the mass distribution of these forming stars: it may be argued that higher metallicity media tend to promote a so-called 'bottom-heavy' initial mass function (IMF) with an enhanced number of lower-mass stars in the forming stellar population's mass distribution – although this remains an ongoing discussion in the community – see, e.g Bastian et al. (2010); Cen (2010) for reviews and discussion of the state of the field, and section 1.3.1.

Chemical enrichment can also reduce the timescale over which hot gas, expelled into the CGM by outflows, can cool and fall back into the host system to be re-used in star-formation. In shortening this timescale, a subsequent increase in the infall and recycling rate of CGM gases (as well as the collapse of any baryonic reservoir in a galaxy) arises. This could account for the shift in the gas supply mechanism to galaxies over cosmic time, wherein the cold inflows of relatively pristine gas (important at high-redshift) are largely replaced by the cooling flows of recycled streams of ISM/IGM gas at low-redshift (e.g., see Ford et al. 2014).

The bulk transport of energy in these systems is illustrated by the schematic diagram in Fig. 1.3. The source of energy in a star-forming galaxy is typically the SN events (following from star-formation). This energy can be transported by the hot gases in an outflow wind fluid into the CGM and IGM[4]. Typically, cooling of CGM gases allows them to re-enter the interstellar environment. This means that energy transport would predominantly follow the 'outflow' paths in the figure, with a much smaller amount of energy returning to the host galaxy within cooler inflows.

The energy injected by star-formation activity (via SN events) is not just a pool to be re-distributed by inflows and outflows. It can also provide the kinetic energy of the outflows themselves (Veilleux et al. 2005). Indeed, earlier models considered the thermal pressure (resulting from stellar heating, or by

---

[4]In a sufficiently far-reaching outflow, such transport of energy may actually contribute to the heating and ionisation of the IGM (Oppenheimer and Davé 2008) – this may particularly be the case if ionising energetic CRs are also advected along with the outflow wind.
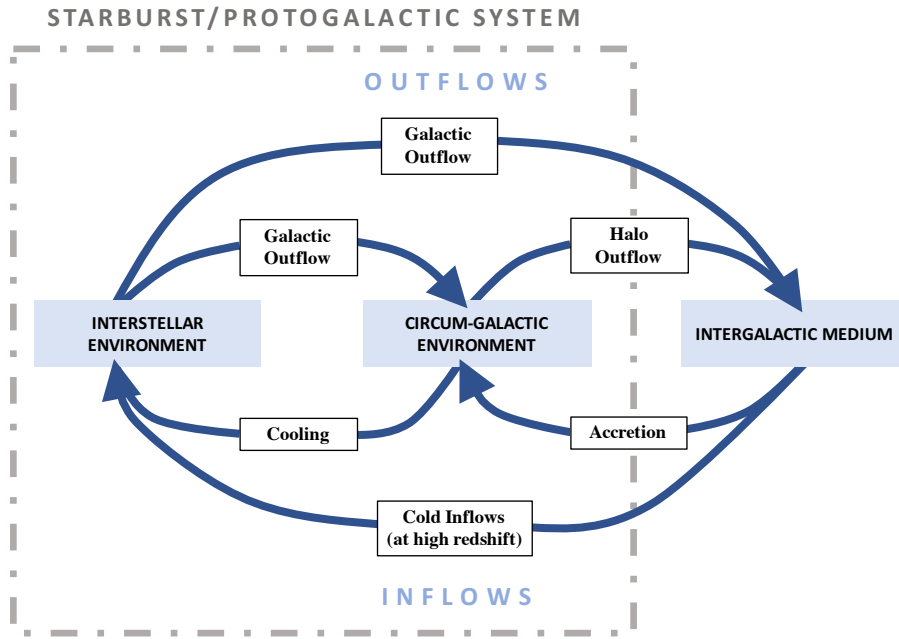
Fig. 1.3: Diagram illustrating the transport of matter (and energy) in and around the CGM of star-forming galaxies – at both high and low-redshift. At high-redshift, cold inflows preferentially supply gas to the interstellar environment directly which yields high rates of star-formation. This star-formation can then drive outflows into the CGM and/or the IGM, transporting matter and energy to both of these environments. Outflows with wide opening angles may also entrain gas from the CGM and transport it out to greater, intergalactic distances. At lower redshifts, cold inflows seem to be superseded by hot accretion – the so-called 'baryon recycling' process (e.g., see Ford et al. 2014). Hot gas from outflows or from the intergalactic environment can cool, and slowly fall back into the ISM to contribute to subsequent star-formation – however the metallicity of this recycled gas would be substantially higher than that supplied by the earlier cold inflows. Based on Fig. 1 of Côté et al. 2015.

the direct thermal injection from SN events) and the mechanical pressure arising from the confluence of mechanical forces associated with SN explosion (when concentrated in a starburst core region of a galaxy) as an outflow driving mechanism in its own right (Larson 1974; Chevalier and Clegg 1985; Dekel and Silk 1986; Nath and Trentham 1997; Efstathiou 2000; Madau et al. 2001; Furlanetto and Loeb 2003; Scannapieco 2005; Samui et al. 2008). Radiation-driven systems have been considered in more recent works, which invoke more advanced models (see Dijkstra and Loeb 2008; Nath and Silk 2009; Thompson et al. 2015). Despite this, after much discussion within the community, the prevailing view is that CRs are the most likely means by which large-scale galactic outflows are driven – and this is particularly thought to be the case at high-redshifts (Samui et al. 2010; Uhlig et al. 2012).

Even in the CR-driven case, the outflow energy source is still ultimately

the injection of energy by SN explosions – though the exact mechanism by which energy and momentum is passed from these SN events to the outflow wind differs between various model prescriptions. The SN events themselves would follow the underlying spatial distribution of star-formation. This is typically concentrated in the innermost few hundred pc in a typical starburst, and the resulting proximity between SN events would enable the outflows driven by individual (frequent) SN explosions to readily coalesce into a larger-scale wind. If the host galaxy is a disc, the galactic outflow wind will develop according to a bi-conical structure along the minor axis (Veilleux et al. 2005). This is because the direction of emergence of a galactic outflow is governed by the 'path of least resistance' (and so would vary between system geometries). The original outflow wind itself is spherical. However, if emerging from a central star-forming region, its progress would be hampered considerably by dense planar material. Instead, the wind would be able to pass through the smaller amount of material above and below the host galactic plane more easily along the minor axis, leading to the emergence of a bi-conical structure. If there is no clear path of least resistance (e.g. in a spherical galaxy morphology), a more isotropic flow may develop. This is because the wind would interact with the edge of the galaxy at a similar time in each direction from the centre, while inflowing pressures working against the flow would not have a preferred orientation.

For a typical bi-conical outflow structure, observations in the local Universe indicate they would generally have a very broad opening angle, sometimes as large as $100°$ (Heckman et al. 1990; Veilleux et al. 2005) in extreme cases (although this value would differ between galaxies and is typically somewhat less than this). Opening angles of outflow cones of tens of degrees would usually be expected in systems. For example, in the star-forming galaxy NGC 253, an outflow cone opening angle in the range $26°-60°$ is found (Strickland et al. 2000; Bolatto et al. 2013), or $60°$ in M82 (Heckman et al. 1990; Walter et al. 2002). The extent of a galactic outflow can also vary considerably, and seems to be strongly dependent on the underlying driving mechanism(s) of the flow as well as environmental factors. Observations have shown hot dif-

fuse X-ray emitting gas from an outflow wind fluid reaching up to a few kpc above and below the plane of the host galaxy (Strickland et al. 2000; Cecil et al. 2002a; Cecil et al. 2002b), with indications that the full structure of the flow could even be an order of magnitude larger than this (see Veilleux et al. 2005; Bland-Hawthorn et al. 2007; Bordoloi et al. 2011; Martin et al. 2013; Rubin et al. 2014; Bordoloi et al. 2016). Outflow velocities are even more diverse, but again seem to depend on the local conditions as well as the mechanism predominately operating to drive the flow (e.g. see Samui et al. 2010, which considers outflows that are both thermally and CR-driven compared to purely CR driven, and finds substantially different flow terminal velocities in each case). They can reach hundreds or even thousands of km s^{-1} in some cases (Cecil et al. 2002b; Rupke et al. 2005b; Rubin et al. 2014). In most studies, the profile of the outflow velocity along the cone is found to increase rapidly at low altitudes (where most of the energy and momentum transfer to the wind fluid arises), but reaches a roughly constant terminal (asymptotic) velocity at heights of several kpc to tens of kpc (e.g. Chevalier and Clegg 1985; Samui et al. 2010).

1.3 The Interstellar Environment

While many basic features of the interstellar environment of star-forming galaxies would be similar to the Milky Way, other aspects can vary drastically. Within our own Galaxy, the local ISM is a multi-phase system comprised of a hot, ionised low-density plasma component (temperature, $T \approx 10^4$ K, density $n_{\rm H} \approx 10^{-4}$ cm^{-3}) filling around 70% of the volume, interspersed with cold dense clouds of neutral and molecular gas (temperature, $T \approx 10 - 100$ K, density $n_{\rm H} \approx 10^2 - 10^5$ cm^{-3} or greater) in pressure equilibrium with the hot phase (see, e.g. Ferriere 2001; Draine 2011). A further component of interstellar dust forms around 1% of the mass of the ISM of our Galaxy (e.g. Compiégne 2010) which has an important role in re-processing radiation (Draine 2011) and altering ISM conditions by heating the gas through the photo-electric effect (Draine 1978). While the proportion of cold dense clouds (molecular clouds, MCs) to the hot ionised medium (HIM) in star-forming galaxies (including both local

starbursts as well as high-redshift protogalaxies) would differ to that in the Milky Way, the fundamental picture of a multi-phase medium in pressure equilibrium would still hold, with evidence of such having been detected in local starburst galaxies, including M82 (although the high-energy environment of this system does yield some differences: see Strickland and Heckman 2007; Fuente et al. 2008; Strickland and Heckman 2009 for details on the molecular cloud structure and fragmentation, and the high pressure environment powered by frequent SN events, or Westmoquette et al. 2009 for a review) and NGC 253 (e.g. Mohan et al. 2005).

A notable feature of starburst galaxies in the local Universe is that they are rich in interstellar dust, even more so than the local conditions in the Milky Way – for example, based on reddening, M82 has a dust fraction almost 10 times that of our own Galaxy (see Gao et al. 2015; Hutton et al. 2015, among others). This dust was presumably formed in sources such as Asymptotic Giant Branch (AGB) and evolved stars (see e.g. Ferrara et al. 2016, among others), and would therefore accumulate over a timescale comparable to the evolutionary timescales of the host starburst galaxy – in some cases, this is similar to the Hubble time. The strong scattering and radiative reprocessing effects of this dust on stellar emission has a critical role in facilitating feedback in these systems, and acts as an important catalyst in recapturing the energy emitted from stars. This principally imparts a heating effect on the interstellar gases.

Protogalaxies would differ in this respect. The formation of dust in the early Universe is more likely to result from core collapse SN events on short timescales (see, e.g. Gall et al. 2011; Bocchio et al. 2016). This is because AGB stars and other sources of dust pass through their evolutionary cycles more slowly. Core collapse SNe are not actually expected to be particularly efficient in producing dust. This is because their powerful (in particular, reverse) shocks would be able to penetrate deep into the SN ejecta to destroy forming dust grains (Bianchi and Schneider 2007; Nozawa et al. 2007; Nath et al. 2008; Silvia et al. 2010) and substantially diminish the resulting dust yield (see, e.g. Yamasawa et al. 2011). Indeed, this is supported by observations, as less

dust is seen in high-redshift star-forming galaxies, particularly above $z \approx 5$, than in their lower redshift counterparts (Walter et al. 2012; Ouchi et al. 2013; González-López et al. 2014; Ota et al. 2014; Riechers et al. 2014; Capak et al. 2015; Maiolino et al. 2015; Bouwens et al. 2016). Recent work has also established that there is some evolution of the dust content of galaxies as they develop and evolve (Ginolfi et al. 2018), with protogalaxies at $z \sim 7$ plausibly harbouring around 1% of the dust that would be expected in an otherwise similar galaxy at $z = 0$. As such, the important dust scattering and radiative absorption/re-emission processes at work in local starburst galaxies would be unlikely to play a significant role in their dust-poor protogalactic counterparts in the early Universe.

The following sub-sections introduce a model for a high-redshift protogalactic environment, which establishes the relevant features of such a system on a galactic scale. This model forms the basic framework in which CR interactions will be assessed and is sufficiently specified using the internal star-formation activity (which sets the energy budget for the system), together with three fields: an interstellar density field, a magnetic field and a radiation field (comprised of stellar contributions as well as a cosmological component). Complexities such as the multi-phase structure of the interstellar medium and the local anisotropies in the radiation and magnetic fields, while important, are finer details which are left to follow-up studies.

1.3.1 Star-Formation in Starbursts and Protogalaxies

The star-formation rate of a galaxy essentially governs its energy budget. The accumulation of the stellar population (in proportion to the star-formation rate) specifies the rate at which stellar radiation is supplied to the system, while the (related) SN event rate determines the energy passed to turbulence, magnetic field amplification and CR injection within a galaxy. The star-formation rate and SN event rate of a galaxy are therefore crucial model parameters and it is important to define an appropriate, consistent relation between these related quantities in order to bridge between observationally-

derived (star-formation rates) and theoretical (SN event rate) values.[5] This can be accomplished by using the underlying stellar mass-function for forming stars – the so-called Initial Mass Function (IMF) – to quantify the number of SN events produced per unit mass of stars formed for a stellar population. The IMF models the relative proportion of stars forming in a system as a function of the mass of those stars. This is physically useful as the evolutionary track that a star will follow is specified by its mass: stellar mass predominantly determines how long a star will live for, its spectral type and, if a star is sufficiently massive to yield a SN event, then it will strongly influence the characteristics of that SN event.

Star-Formation Characteristics

There is a growing amount of observational evidence to suggest that the IMF is non-Universal, with theoretical arguments to support this. For example, low metallicity systems cool less effectively than high metallicity ones, and this increases the mass required for an over-dense region to collapse and form stars. Presumably this would yield a top-heavy initial stellar mass distribution (e.g. Abel et al. 2002; Bromm et al. 2002; Bastian et al. 2010; Gargiulo et al. 2015), with the resulting stellar population becoming skewed to include more metal-poor, massive, luminous short-lived O- and B-type stars. Such a distribution would tend to favour core collapse SN channels at the end of stellar evolutionary paths, compared to a stellar population distribution observing a more 'standard' Salpeter IMF. Arguably this could also lead to a different star-formation history in a galaxy over cosmic time, with a top-heavy IMF driving a tendency towards prompt 'burst'-like star-formation, rather than the more gradual process seen in the current epoch in the local Universe (see, e.g. Lacey et al. 2008). A top-heavy IMF has been proposed for some nearby star-forming galaxies (Weidner et al. 2011; Bekki and Meurer 2013; Chabrier et al. 2014), e.g. in M82 (Rieke et al. 1993; McCrady et al. 2003) and NGC

---

[5]Models for the injection rate of energy and CRs used throughout this research are more directly related to the SN event rate, $\mathcal{R}_{SN}$, than to the star-formation rate, $\mathcal{R}_{SF}$. However, as it can be difficult to infer the IMF of stars from observations directly, thus complicating reasonable SN event rate estimates for systems (especially at high-redshift), it is useful to model the relation between the two quantities. Doing so also allows comparisons to be more readily made between results in the literature (which are more often defined in terms of $\mathcal{R}_{SF}$) and those presented here.

3603 (Harayama et al. 2008), but variations in the IMF have also been suggested for individual clusters near the centre of our own Galaxy (Stolte et al. 2005; Maness et al. 2007), where the standard Salpeter IMF significantly underestimates the production of high-mass stars and SN events. In line with this, there is also some observational evidence for a redshift-dependence in the IMF of galaxies (Lacey et al. 2008; Davé 2008; van Dokkum 2008; Hayward et al. 2013), as would be expected given the lower metallicities associated with primordial environments. Moreover, work has also proposed that the IMF can be influenced by the CMB temperature, particularly at high-redshifts, whereby molecular cloud collapse is affected so as to distort the thermal and dynamical equilibrium balance of a collapsing system. The increase in the resulting Jeans' mass for any collapsing instability would thus be passed on to a top-heavy IMF (Jermyn et al. 2018).

Of particular relevance to this work, the impact of a top-heavy IMF would be an increased rate of core collapse Type II P SN and hypernovae. These have progenitor masses of $M_{\mathrm{SN}} = 8.5$ M$_\odot$ or higher, as indicated by a best-fit value of approximately 8 ± 1 M$_\odot$ – see Smartt et al. (2009), also Smartt (2009), and provide an effective means of injecting energy into their environment, with $E_{\mathrm{SN}} \approx 10^{53}$ erg per event (Smartt 2009). However, in the absence of a clear alternative IMF model suitable for starburst and high-redshift protogalaxies, the standard Salpeter function is adopted hereafter, with index $\Upsilon = 2.35$. This is sufficient for the first calculations presented in this thesis, but the exact form of this function and its potential redshift and environmental dependence is worthy of follow-up study.

The Star-Formation to Supernova Relation

The fraction of stars of mass sufficiently large to yield a Type II SN can be estimated for a given IMF to give a conversion parameter $\alpha^\star$, where $\mathcal{R}_{\mathrm{SN}} = \alpha^\star \mathcal{R}_{\mathrm{SF}}$. Invariance between systems – particularly at high-redshift – is not guaranteed. However, the following approach is sufficient for a first estimate until a better understanding of the nature of star-formation in broadly different

environments and redshifts has been established. It is calculated by

$$\alpha^\star \approx \frac{\int_{M_{\rm SN}}^{M_{\rm max}} \mathrm{d}M\, M^{-\Upsilon}}{\int_{M_{\rm cut}}^{M_{\rm max}} \mathrm{d}M\, M^{-\Upsilon}} \ , \tag{1.4}$$

where $M_{\rm SN} = 8.5$ $\rm M_\odot$ is the lower progenitor mass for a core collapse SN event, and $M_{\rm max} = 50$ $\rm M_\odot$ is its upper limit. The value of the parameter $M_{\rm max}$ is greatly is uncertain, and subject to ongoing debate in the literature. Values as low as 16.5 $\rm M_\odot$ are proposed in some cases (e.g. Smartt et al. 2009), but progenitor red super-giant stars are observed to exist up to masses of at least 25 $\rm M_\odot$ (see Smith et al. 2011). Moreover, core collapse Type-IIn SN events are thought to have progenitor stars with masses of above 40 $\rm M_\odot$ (e.g. Muno et al. 2006; Tominaga et al. 2008), which pushes the possible limit for this parameter even higher (see also Smith et al. 2004, 2009). Observational studies of the nearby galaxies M31 and M33 agree with this high cut-off mass, indicating values of around $35-45$ $\rm M_\odot$ (e.g. Jennings et al. 2014; Díaz-Rodríguez et al. 2018). The suggested theoretical maximum limit for a progenitor able to yield a core collapse SN event is adopted here, and is sufficient for the present purposes, given that the $\alpha^\star$ parameter is not sensitive to the exact choice of value adopted. This value is 50 $\rm M_\odot$, above which direct collapse into a black hole is favoured over the production of a SN explosion (see Fryer 1999; Heger et al. 2003). $\alpha^\star$ represents a fraction of a stellar population, and thus must be normalised by the total number of stars in that population. For this, cut-off parameters of $M_{\rm cut} = 1$ $\rm M_\odot$ to the same $M_{\rm max} = 50$ $\rm M_\odot$ are used, which assumes a negligible population fraction of stars with $M > 50$ $\rm M_\odot$, and $M < 1$ $\rm M_\odot$. These choices give $\alpha^\star \approx 0.05$, and thus a conversion of $\mathcal{R}_{\rm SF} \approx 160$ $\rm M_\odot yr^{-1}(\mathcal{R}_{\rm SN}/yr^{-1})$, which are both used throughout the rest of this thesis.

1.3.2 Interstellar Density Field

The density profile of a galaxy can be described parametrically in terms of a core and halo model. While originally adopted for dark matter distributions, such a model as the Dehnen (1993) profile (see also Tremaine et al. 1994) is a reasonable approximation to the gas profile of a protogalaxy. The interstellar

density field is modelled as an over-density on the background CGM according to this profile, which is an analytically tractable but reasonable description of a galactic gas profile in an elliptical galaxy for which the mass $M(<r)$ does not diverge with increasing radius, r, i.e.

$$n_{\text{H}}(r) = \frac{n_{\text{H},0}}{(1 + \xi_{\text{c}})(1 + \xi_{\text{h}})} \qquad (1.5)$$

(Dehnen 1993), where $\xi_{\text{c}} = (r/r_{\text{c}})^2$ and $\xi_{\text{h}} = (r/r_{\text{h}})^2$ for $r_{\text{c}} = 1$ kpc and $r_{\text{h}} = 2$ kpc as the galaxy profile core and halo radius respectively. The profile is normalised to a central density of $n_{\text{H},0} = 10 \, \text{cm}^{-3}$, considered an approximate average over the dense clouds and HIM. This is superposed onto a background density of $n_{\text{H}} = 10^{-3} \, \text{cm}^{-3}$ (which yields CGM densities of order $n_{\text{H}} = 10^{-2}$ cm^{-3} in the vicinity of the galaxy). This background value is taken to represent one possible environment, although a range of both higher and lower values would also be reasonable (variation of this value is not particularly consequential for the work presented here).

1.3.3 Magnetic Field

In the context of protogalaxies, a number of mechanisms have been proposed to explain what drives galactic magnetic field growth. The most notable of these mechanisms invoke turbulence driven by accretion and SN events, thus harnessing the power of the frequent explosions to rapidly strengthen the magnetic field (see e.g. Beck et al. 2012; Latif et al. 2013). Observations and simulations indicate that young protogalaxies develop magnetic fields very rapidly after the onset of star-formation, reaching μG strengths comparable to magnetic fields of galaxies in the current Universe within just a few Myr of their appearance (Bernet et al. 2008; Beck et al. 2012; Hammond et al. 2012; Rieder and Teyssier 2016; Sur et al. 2017). This requires the presence of ample mechanisms during the protogalactic stages of galaxy evolution in which amplification processes transform weak seed intergalactic fields, of around 10^{-20} G (see e.g. Sigl et al. 1997; Howard and Kulsrud 1997) which initially permeate galaxies, to the saturation fields of a few μG observed in galaxies today (Beck, R. et al. 2005; Fletcher et al. 2011; Adebahr, B. et al.

2013; Beck and Wielebinski 2013).

Schober et al. (2013) introduced an appropriate turbulent dynamo model which suitably demonstrates the rapid growth of a galactic magnetic field following the onset of turbulence resulting from a high SN rate (Rees 1987; Balsara et al. 2004). The time-evolution of the field is described on two scales: a local-scale viscous field $B_\mathrm{v}(t)$ and a large-scale ordered field $B_\mathrm{L}(t)$. While the large-scale field is of interest to modelling in later parts of this thesis, its evolution is predominantly governed by the viscous field which provides the link between the injected magnetic turbulence at the SN level and the magnetic energy density on galactic scales.

For the small-scale viscous field $B_\mathrm{v}(t)$, the growth $\mathcal{W}(t)$ is modelled by an exponential strengthening of a seed field B_0 to saturation levels $B_\mathrm{v,sat} = \mathcal{S}(\ell_\mathrm{v}/L_\mathrm{f})^{\theta_\mathrm{Turb}} f_\mathrm{turb}$ at a rate Γ_w (see Braginskii 1965; Kazantsev 1968) in a time t_v, i.e. $\mathcal{W}(t) = B_0 \exp(\Gamma_\mathrm{w} t)$, beyond which non-linear evolution begins to dominate. θ_Turb is introduced here as the slope of the turbulent velocity spectrum, which takes a value of around $1/2$. By comparison, for fully incompressible Kolmogorov turbulence, the value is around $1/3$ (see section 4.1 for further details, where the influence of turbulence models on cosmic ray diffusion is discussed), and increases with compressibility (see, e.g. Burgers 1948). ℓ_v is the viscous scale of the field and $\mathcal{S}$ essentially follows from equipartition with the kinetic energy of the turbulent velocity v_f of the interstellar gas, i.e $\mathcal{S} = \sqrt{4\pi\rho}\, v_\mathrm{f}$. $\rho = \rho(r) = n_\mathrm{H}\, m_\mathrm{p}$ is the local protogalaxy matter density which, given the assumption that the magnetic field is predominantly driven by SNe, follows the distribution of the underlying gas profile which dictates where star-formation (and subsequently, SN events) will arise. $f_\mathrm{turb} = 0.1$ is the fraction of the turbulent kinetic energy transferred to magnetic energy, estimated from simulations (see Federrath et al. 2011). The viscous evolution of the magnetic field is scaled by a factor of $(\ell_\mathrm{v}/L_\mathrm{f})^{5/4}$ to describe the large-scale field evolution up to a saturation time t_v. Beyond this time, large scale
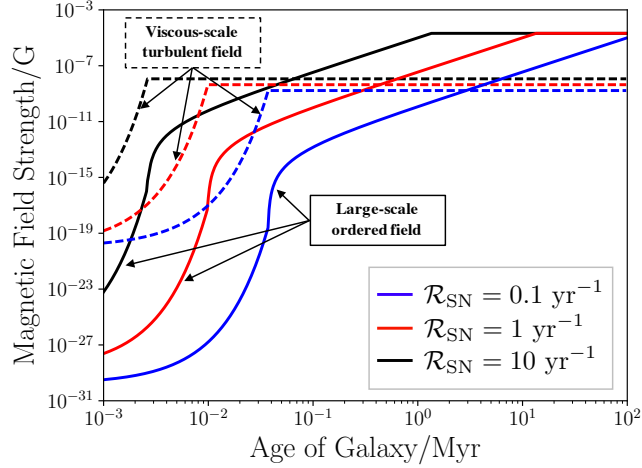
Fig. 1.4: Plot to illustrate the magnetic field growth and subsequent saturation for protogalaxies with SN event rates of 0.1, 1 and 10 yr^{-1} (respectively the blue, red and black lines) according to the adopted model, with parameter choices of $\alpha^\star = 0.05$, and $\beta = 0.05$ (informed by simulation work – see, e.g. Latif et al. 2013). The solid lines represent the large-scale evolution of the ordered magnetic field, whereas the dashed lines represent the growth of the viscous scale, turbulent magnetic field.

turbulent growth dominates the evolution. Overall, this gives:

$$
B_{\mathrm{L}}(r,t) = \begin{cases} \mathcal{W}(r,t) \cdot \left(\frac{\ell_{\mathrm{v}}}{L_{\mathrm{f}}}\right)^{5/4} & [t < t_{\mathrm{v}}] \\[2ex] \mathcal{S}(r) \cdot f_{\mathrm{turb}} \cdot \left(\frac{\ell_{\mathrm{p}}(t)}{L_{\mathrm{f}}}\right)^{\theta_{\mathrm{Turb}}+5/4} & [t_{\mathrm{v}} \le t < t_{\mathrm{sat}}] \\[2ex] B_{\mathrm{L,sat}}(r) & [t > t_{\mathrm{sat}}] \end{cases} \quad (1.6)
$$

Here, $\ell_{\mathrm{p}} = \ell_{\mathrm{v}} + [v_{\mathrm{f}}(t - t_{\mathrm{v}})/L_{\mathrm{f}}^{\theta_{\mathrm{Turb}}}]^{1/(1-\theta_{\mathrm{Turb}})}$ is the scale of peak energy of the magnetic field (Schober et al. 2013), and the saturation strength is $B_{\mathrm{L,sat}}(r) = \mathcal{S}(r)\, f_{\mathrm{turb}}$, corresponding to a scaled energy equipartition. This formulation can be used to model the magnetic field growth in a starburst protogalaxy based on the star-formation rate (and hence the SN rate) for a spherical system. In this case, one can estimate the velocity $v_{\mathrm{f}} \approx r_{\mathrm{gal}}(2\pi\rho G/3)^{1/2}$ from a pressure/gravity hydrostatic equilibrium approximation, and the forcing (driving) scale of the turbulence, $L_{\mathrm{f}} \approx \rho v_{\mathrm{f}}^3/(\mathcal{R}_{\mathrm{SN}}\beta E_{\mathrm{SN}})$ by comparing the energy dissipation rate with the input rate due to SNe, through the SN rate $\mathcal{R}_{\mathrm{SN}}$ (Schober et al. 2013). Here, β is an efficiency parameter, specifying the fraction of SN energy transferred into ISM turbulence.

Models describing the magnetic field development in the ISM of a protogalaxy can be specified in terms of SN rate by setting values for the efficiency

parameters $\alpha^\star = 0.05$ (see equation 1.4) and $\beta = 0.05$ (Latif et al. 2013), and by adopting the approximate expressions for v_f and L_f above. Plots to demonstrate this evolution are shown in Fig. 1.4, in which a plausible range of values for SN event rates, between $0.1 \, \mathrm{yr}^{-1}$ (fairly quiescent) to $10 \, \mathrm{yr}^{-1}$ (an extremely violent star-forming environment, perhaps possible in a system undergoing a major merger[6] or subject to cold inflows if a high-redshift protogalaxy) have been considered.

1.3.4   Radiation Field

The radiation field in a star-forming protogalaxy is comprised of two principal components: the contribution from stars and stellar end products (astrophysical), and the contribution from the CMB (cosmological). The cosmological contribution is isotropic and easily modelled as a simple blackbody. It can be conveniently written in terms of $\epsilon = \mathrm{h}\nu/m_\mathrm{e}\mathrm{c}^2$, being the energy of a photon of frequency ν normalised to the electron mass (such a formulation is helpful in subsequent calculations for interactions involving blackbody radiation fields – see section 3.1), with the spectral number density given by

$$n_\gamma^{\mathrm{CMB}}(\epsilon) = \frac{8\pi}{\lambda_\mathrm{C}^3} \frac{\epsilon^2}{\exp\left(\epsilon \, m_\mathrm{e}\mathrm{c}^2/\mathrm{k_B}T\right) - 1} \; . \tag{1.7}$$

Here, $\lambda_\mathrm{C} = \mathrm{h}/m_\mathrm{e}\mathrm{c}$ is the electron Compton wavelength, and T is the effective temperature of the radiation field. In the case of CMB radiation, $T(z) = T_0(1+z)$, with $T_0 = 2.73 \, \mathrm{K}$ being the CMB temperature in the current epoch (Planck Collaboration et al. 2018). The associated energy density in the CMB radiation field follows from equation 1.7 as

$$\begin{aligned} U_{\mathrm{CMB}} &= \int_0^\infty \mathrm{d}\epsilon \, m_\mathrm{e}\mathrm{c}^2 \epsilon \, n_\gamma^{\mathrm{CMB}}(\epsilon) \\ &= \frac{8\pi^5}{15} \frac{\mathrm{k_B^4} \, T^4}{\mathrm{h}^3\mathrm{c}^3} = \frac{4\sigma_\mathrm{B}}{\mathrm{c}^3} T^4 \; , \end{aligned} \tag{1.8}$$

---

[6]Some studies have suggested that Arp 220 could have a similar SN event rate of 2-4 yr^{-1} (Lonsdale et al. 2006; Varenius et al. 2017). Moreover, in Lonsdale et al. (2006), 4 new radio sources were seen in 12 months, and the authors argue that this is consistent with 4 new SN events and a corresponding SN rate, but statistics in this study are limited – the more recent study by Varenius et al. (2017) suggests a similar rate of $4 \pm 2 \, \mathrm{yr}^{-1}$ on the basis of the number of events observed, but assumes that only a small fraction of SN events are actually detected; the true level is likely to be lower than their estimated value (Page 2018). Thus the SN rate mentioned here of $10 \, \mathrm{yr}^{-1}$ should be regarded as an extreme case, included for completeness.

([Dermer and Menon 2009](#)) where σ_B is the Stefan-Boltzmann constant.

The astrophysical contribution is expected to be dominated by the abundant population of massive O- and B-type stars. This is because other contributions, e.g. stellar end products, would not yet have formed in large numbers in these young systems. Unlike the CMB, the radiation field due to discrete stellar sources is not isotropic or homogeneous. Instead, its spatial profile is governed by two factors: (1) the way in which stars are distributed within the system, and (2) the geometric spreading of photons radiating from these stars. The first of these is essentially determined by the underlying density profile of the system, while the second requires careful consideration of the radiative intensity resulting from a distributed ensemble of sources.

A model stellar distribution in a protogalaxy may be set to follow its underlying density profile (from which stars would form), up to a cutoff of $R_{cut} = 10$ kpc. The large choice of R_{cut} compared to the scale of the model galaxy itself avoids any unphysical 'edges' to the distribution. Under such a prescription, the vast majority of the stars are positioned within the central 1 kpc core (see e.g. [Whalen et al. 2013](#); [Ono et al. 2013](#)). If each individual star is type O or B, then each source may be modelled as a blackbody (see equation [1.7](#)) of characteristic temperature of around $T_* = 30,000$ K. The radiation field intensity around a single star, if well-modelled by a blackbody, can then be calculated using the Stefan-Boltzmann relation, which gives the corresponding luminosity as

$$L_* = 4\pi R_*^2 \sigma T_*^4 \ . \tag{1.9}$$

Here, R_* is the stellar radius, and the radiation energy density is $U^\star = L_*/4\pi r^2 c$. The photon number density of the field is found by dividing the energy density by the modal photon energy, i.e. around $E_\gamma \approx 2.82\, k_B T_*$, to correspond with the peak of the Planck spectrum (the detailed spectral distribution of stellar photons is not typically required in this work). It then follows that $n_\gamma^\star \approx U^\star/2.82\, k_B T_*$. The generalisation from this single point source to a distribution can now be considered, in which an ensemble of N individual

point sources is distributed in the manner described above. It is encoded by a distribution function $f(r)$, which may be written as

$$f(r) = \frac{3}{4\pi} N \left(r_{\text{gal}}^3 - \tilde{r}^3 \right)^{-1} \omega(r) .$$ (1.10)

Here, a weighting $\omega(r) \propto n_{\text{H}}(r)$ has been applied to the uniform distribution function $f_{\text{u}}(r)$. In the uniform case, $f_{\text{u}}(r)$, the effective distance between a nearest source and some observer position located within the spherical distribution is denoted as $\tilde{r}$, while the maximum possible distance between a source and an observer position is the radius of the extended distribution itself, i.e. r_{sph}. The average energy density due to the radiation from the full distribution of sources in the ensemble then follows as

$$\begin{aligned} U &= \frac{L}{4\pi\text{c}} \int_{\tilde{r}}^{r_{\text{sph}}} \text{d}r \, 4\pi r^2 \frac{f_{\text{u}}(r)}{r^2} \\ &= \frac{L}{\text{c}} \int_{\tilde{r}}^{r_{\text{sph}}} \text{d}r \, f_{\text{u}}(r) , \end{aligned}$$ (1.11)

For the case of a uniform spherical distribution of sources, this yields

$$\begin{aligned} U &= \frac{3}{4\pi} \frac{L}{\text{c}} N \left(\frac{r_{\text{sph}} - \tilde{r}}{r_{\text{sph}}^3 - \tilde{r}^3} \right) \\ &= \frac{3}{4\pi} \frac{L}{\text{c}} N r_{\text{sph}}^2 \left[1 + \left(\frac{\tilde{r}}{r_{\text{sph}}} \right) + \left(\frac{\tilde{r}}{r_{\text{sph}}} \right)^2 \right]^{-1} , \end{aligned}$$ (1.12)

where the number of sources within the ensemble can be calculated by the ratio of volume taken up by the source (based on the characteristic nearest distance from the observer) compared to the size of the extended distribution, r_{sph}. This gives

$$N = \frac{4\pi r_{\text{sph}}^3}{4\pi \tilde{r}^3} = \left(\frac{r_{\text{sph}}}{\tilde{r}} \right)^3 ,$$ (1.13)

which implies that

$$\frac{\tilde{r}}{r_{\text{sph}}} = \left(\frac{1}{N} \right)^{1/3} .$$ (1.14)

Substitution of 1.14 into equation 1.12 then gives

$$U = \frac{3}{4\pi} \frac{L}{c} \frac{N}{r_{\mathrm{sph}}^2} \left[1 + \left(\frac{1}{N} \right)^{1/3} + \left(\frac{1}{N} \right)^{2/3} \right]^{-1} . \qquad (1.15)$$

In the limit of $N \to 1$, the usual inverse-square law result for radiation is recovered, i.e. $U = L/4\pi c\, r_{\mathrm{sph}}^2$ while, for large N, the result becomes[7]

$$U \to \frac{LN}{4\pi c} \left(\frac{3}{r_{\mathrm{sph}}^2} \right) . \qquad (1.16)$$

The photon number density can be found by dividing 1.15 by the typical photon energy of $2.82\,k_{\mathrm{B}}T_*$, to give

$$\begin{aligned}
n_\gamma^\star(r) &= \frac{3\omega(r)}{12\pi k_{\mathrm{B}}T_*} \frac{L}{c} \frac{N}{r_{\mathrm{gal}}^2} \left[1 + \left(\frac{1}{N} \right)^{1/3} + \left(\frac{1}{N} \right)^{2/3} \right]^{-1} \\
&= \frac{L \cdot N \cdot \omega(r)}{4\pi c\, k_{\mathrm{B}}T_* D_{\mathrm{N}}},
\end{aligned} \qquad (1.17)$$

where $D_{\mathrm{N}} = 1 + N^{-1/3} + N^{-2/3}$, and where $\omega(r)$ re-introduces the weighting required to transform the result from that due to a uniform source distribution to that following the underlying density profile. In the case of the protogalaxy model, a value of $N = 10^6$ was adopted. The form of $\omega(r)$ is simply a normalised profile $n_{\mathrm{H}}(r)$.

A scaling between equation 1.17 and the photon number density arising for an undiluted blackbody $n_\gamma^\star/n_\gamma^{\mathrm{BB}}$ can be defined by integrating the blackbody spectrum, giving $n_\gamma^{\mathrm{BB}} = 8\pi\Theta^3\Gamma(3)\zeta(3)/\lambda_{\mathrm{C}}^3$. Here, n_γ^{BB} may be thought of as the photon number density at the 'surface' of a radiation source, and $\Theta = k_{\mathrm{B}}T/m_{\mathrm{e}}c^2$ is defined its dimensionless temperature. This scaling allows the geometrical spreading effect of a radiation field due to the spatial distribution of an ensemble of sources to be properly taken into account (and is employed in later calculations throughout this thesis).

---

[7]This analytical result was confirmed by a numerical Monte-Carlo approach for the case of a uniform distribution.

Chapter 2

Cosmic Rays in Star-Forming Galaxies

This chapter is based on research, with part of the results published in the following research papers:

(i) *"Interactions between ultra-high-energy particles and protogalactic environments"*, Owen, E. R., Jacobsen, I. B., Wu, K., Surajbali, P., 2018, MNRAS, 481, 666

(ii) *"Hadronic interactions of energetic charged particles in protogalactic outflow environments and implications for the early evolution of galaxies"*, Owen, E. R., Jin. X., Wu, K., Chan, S., 2019, MNRAS, 484, 1645.

The sources of CRs in protogalaxies and starbursts are predominantly stellar end-products, e.g. SN events and their remnants, accreting black holes and neutron stars. In these environments, seed particles can be efficiently accelerated by shocks up to PeV energies, via diffusive shock acceleration (DSA) processes. The favoured mechanism is first order Fermi acceleration (Fermi 1949; Bell 1978). In this process energetic particles gain energy, in magnetised shocks and irregularities, through elastic scattering. This yields a resulting power-law energy spectrum of particles with an index consistent with that of the observed Galactic CR spectrum above a GeV (Bell 1978).

In the context of DSA, the acceleration of a particle can only persist while it continues to engage with an astrophysical accelerator (see appendix A for details). This is governed by the gyro-radius, or Larmour radius, of that particle in the accelerator's magnetic fields compared to the characteristic scale-size of the accelerator itself. The gyro-radius is the curvature of the path described by an energetic particle of energy E GeV in a uniform magnetic field of B μG. If it is possible to characterise the strength of the magnetic field(s)

driving a particle's acceleration in terms of a mean value over a length-scale similar to the gyro-radius, then the resulting effect on the charged particle may be safely approximated by that due to a uniform field of the same strength. The gyro-radius, r_{L}, is defined as

$$r_{\mathrm{L}} = \frac{3.3 \times 10^{12}}{|q|} \left(\frac{E}{10^9\,\mathrm{eV}} \right) \left(\frac{\mu\mathrm{G}}{\langle |B| \rangle} \right) \; \mathrm{cm} \; , \tag{2.1}$$

where $|q| = 1$ is the magnitude of the charge of the particle being accelerated (in units of the electron charge), and E is its energy at a given point in its acceleration cycle. $\langle |B| \rangle$ is the characteristic (mean) magnetic field strength over the gyro length-scale. This gives a characteristic length-scale over which the energetic charged particle engages with the accelerator. If it is smaller than the size of the system, r_{sys}, the particle is likely to remain contained in the accelerator, and it is possible for it to continue to undergo acceleration cycles. However, $r_{\mathrm{L}} \propto E$, so it follows that the probability of particle containment (and subsequent additional acceleration events) reduces with each scattering and energy boost experienced by a particle. Eventually, after many scattering events, a particle may achieve an energy at which $r_{\mathrm{L}} > r_{\mathrm{sys}}$. At this point, the particle can no longer effectively be contained by the magnetic field of the accelerating system – and is therefore unable to continue to engage with further acceleration cycles. Therefore, E_{max} is the maximum energy to which charged particles may be accelerated for a given accelerator. Placing this requirement on equation 2.1 allows this maximum energy to be specified as

$$E_{\mathrm{max}} = |q| \; \langle |B| \rangle \; r_{\mathrm{sys}} \; , \tag{2.2}$$

which is known as the Hillas criterion (Hillas 1984). It sets the theoretical maximum energy a particle can be accelerated to in a given astrophysical system, with knowledge of only the system's size and characteristic magnetic field strength. Candidate sources of energetic particles can thus be identified to account for the acceleration of charged CR particles to their observed high-energies. These range from sub-galactic objects (e.g. SN remnants, white

dwarfs, pulsar wind nebulae[1], micro-quasars and X-ray binaries) to galactic and extragalactic systems, e.g. AGN and their jets, intergalactic shocks, and shocks in galaxy clusters (see, e.g Hillas 1984; Gaisser et al. 1995; Beall and Bednarek 2002; Alvarez-Muniz et al. 2002; Zhang et al. 2003; Nagataki 2004; Christiansen et al. 2006; Becker 2008; Kotera and Olinto 2011; Aharonian et al. 2013; Jacobsen et al. 2015), as are indicated on the Hillas plot in Fig. 2.1 (adapted from Hillas 1984; Kotera and Olinto 2011; Jacobsen et al. 2015). In Fig. 2.1, interstellar environments are highlighted in orange – they are internal to galaxies and typically offer the capacity to accelerate CRs up to a theoretical limit of around a PeV. Since these interstellar accelerators are mainly formed from stellar end-products (namely neutron stars, white dwarfs and SN remnants) and are ubiquitous to star-forming galaxies, they are of foremost interest in this work.
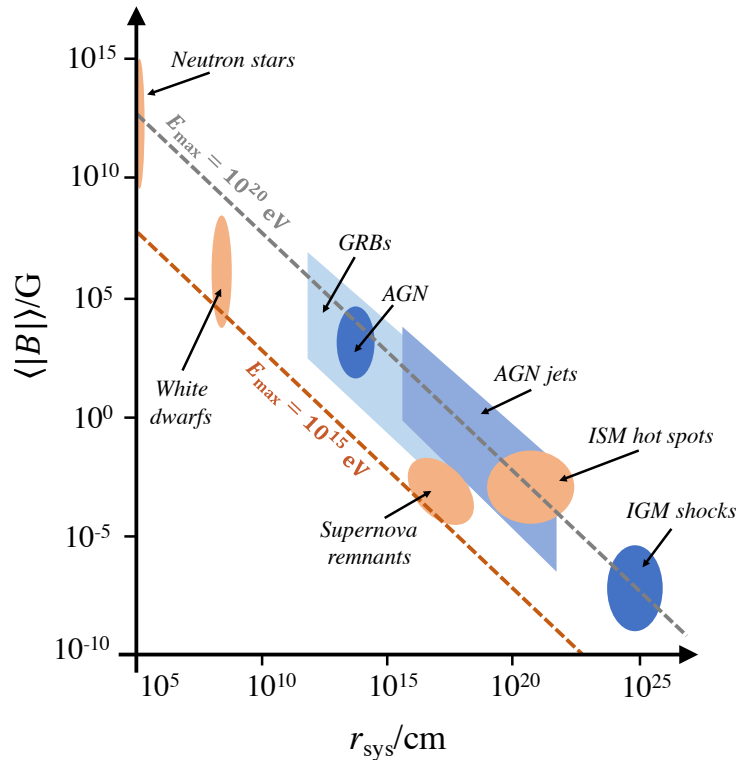
Fig. 2.1: The Hillas plot, which indicates the maximum energy that protons can be accelerated to in the indicated astrophysical environments, adapted from Kotera and Olinto (2011), see also Hillas (1984); Jacobsen et al. (2015). Uncertainties in the parameters for each of the candidate accelerators is taken into account, and the dashed lines indicate the maximum possible proton energy possible for a given source size and magnetic field strength, according to the Hillas criterion (equation 2.2).

---

[1]These are young pulsars contained within a SN remnant shell.

In most galaxies at low-redshift, all the stellar end-product environments shown in Fig. 2.1 would presumably operate to accelerate CRs to some degree. An extragalactic CR (EGCR) component would also permeate interstellar environments, being supplied by accelerators operating over larger scales (to attain higher energies, $\gtrsim 1$ PeV). Of the stellar end-products, white dwarfs (WDs), microquasars and pulsar wind nebulae (which are classified as SN remnants for the current purposes) are presumably key CR sources. In the local Galactic environment, WD stars contribute the most. This is because they typically develop from established and ageing stellar populations. It follows, therefore, that they are not unusual in the local Galactic neighbourhood of the Milky Way, with 8 WDs present in the hundred nearest stars to the Sun (Fontaine et al. 2001). WDs are the end product of stars with insufficient mass to yield a SN explosion (and subsequent neutron star/black hole), i.e. less than around 8 $M_\odot$ (e.g. Fontaine et al. 2001; Heger et al. 2003). They have an evolutionary timescale of 1-10 Gyr (Fontaine et al. 2001) so would be unlikely to have had sufficient time to form in ample numbers in galaxies at high-redshift, or in starbursts during their ongoing star-forming phase. It thus follows that WDs would not be expected in protogalaxies at all, and would not be present in substantial numbers in starburst galaxies in the current epoch either. Thus, they would not contribute greatly to CR acceleration in these systems. Instead CR production at high-redshift and in local starbursts would be dominated by SN remnant environments, and possibly neutron stars (if sufficient time had passed to enable a neutron star population to accumulate since the onset of star-formation).

CR acceleration processes can account for the distinctive power-law spectrum detected on Earth and in the local solar neighbourhood. Fig. 2.2 shows the observed CR spectrum, taken from Gaisser (2007), which indicates the contributions from individual particles (protons and leptons) as well as the all-particle spectrum (which also includes heavier nuclei). From GeV energies, the observed spectrum exhibits a distinctive power-law, $E^{-\Gamma}$, measured up to 10^{20} eV and, with the exceptions of a 'knee' at around a PeV, a less distinctive second 'knee' at around 300 PeV, and an 'ankle' at around 10 EeV, it is

remarkably featureless.
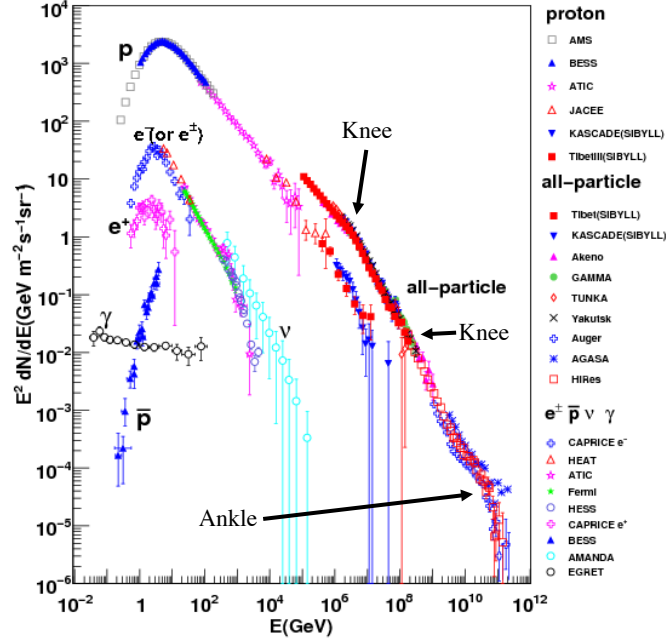
Fig. 2.2: The observed spectrum of UHECRs over 14 orders of magnitude, adapted from the plot compiled by Gaisser (2007), using data from *AMS*, *BESS*, *ATIC*, *JACEE*, *KASCADE*, *Tibet*, *Akeno*, *GAMMA*, *TUNKA*, *Yakutsk*, *PAO*, *AGASA*, *HIRes*, *CAPRICE*, *HEAT*, *Fermi-LAT*, *HESS*, *AMANDA* and *EGRET* experiments, for purely protonic contributions. The all particle spectrum and the lepton and γ-ray spectra shown separately. While the distinctive power-law is apparent above a GeV, remarkable detail is also evident with the 10^6 GeV 'knee' arising due to the transition from galactic to extragalactic sources, and the 10^{10} GeV 'ankle' feature likely due to GZK attenuation effects as CRs propagate through intergalactic radiation fields.

Below the main knee feature (at around 1 PeV), the power-law spectral index Γ takes a value of around 2.7. This main knee in the spectrum is broadly attributed to the transition from GCRs to extragalactic CRs (EGCRs), which is expected to arise between 10^6 and 10^9 GeV (Nagano et al. 1992; Wibig and Wolfendale 2004; Allard et al. 2005; Kotera and Olinto 2011; Aloisio et al. 2012), as determined by the maximum feasible limits to which galactic sources (i.e. SN remnants, merging neutron stars and pulsars) could plausibly accelerate CRs to according to the Hillas criterion. A second knee is also observed at around 300 PeV, with a steeper slope between the two knees of around $\Gamma \approx 3$. This power-law index steepens between the higher-energy spectral knee and the ankle (between 300 PeV and 10 EeV), tending towards around $\Gamma \approx 3.3$. This ankle is observed at around 10 EeV and likely results from

GZK attenuation (Greisen 1966; Zatsepin and Kuz'min 1966) effects arising as CRs propagate through intergalactic radiation fields, predominantly comprised of cosmological microwave background radiation (Abbasi et al. 2004, 2008b,a; Abraham et al. 2010) and the extragalactic background light, EBL (being a diffuse photon background comprised of radiation contributed by e.g. star-forming galaxies and AGN emission). The spectral index above the ankle is around $\Gamma \approx 2.6$, and the spectrum becomes heavily suppressed by the GZK effect above around 3×10^{10} GeV (Abbasi et al. 2008b; Abraham et al. 2010). Despite the GZK effect, CRs are still observed up to energies of around 10^{11} GeV (Linsley 1963; Pierre Auger Collaboration 2007; Kotera and Olinto 2011) with the highest energy CR detected at 3×10^{11} GeV (Bird et al. 1993).

In the remainder of this thesis the term 'CR' is used to refer to energetic protons, unless specified otherwise. CR protons and CR electrons may be explicitly referenced in order to differentiate between the two where necessary. While CR electron secondary particles are discussed in this thesis, electron primary particles are not. This is because they exhibit much higher cooling rates than CR protons, and so their energy is deposited in the immediate vicinity of their source environment (compared to galactic scales) meaning that their larger-scale astrophysical implications are less important.

2.1 Cosmic Ray Injection Models

From a theoretical perspective, CR injection in starburst galaxies and protogalaxies occurs in a point-like fashion due to the discrete ensemble of SN-remnant sources which dominate their acceleration. This may be modelled by some source function, Q, which would depend on the CR energy, E, to encode the distinctive power-law spectrum, the position within the protogalaxy, and the total CR emission power (luminosity) of a source. The resulting distribution of CRs throughout the host galaxy environment would then depend on how they propagate away from their injection location. This propagation is intrinsically linked to the nature of the interstellar environment itself and, in particular, the large scale flows arising therein. In a medium in which bulk motion is random and limited to local scales, the propagation of CRs would

arise effectively by diffusion due to their random scatterings as they become entangled within an interstellar magnetic field (Berezinskii et al. 1990; Aharonian et al. 2012; Gaggero 2012). However, in a system where large scale bulk motions transport the magnetic field and CRs in a flow, e.g. as would arise in a galactic-scale outflow or jet, CRs propagate away from their source environment by advection at a speed far higher than could be achieved by diffusion alone (Berezinskii et al. 1990; Schlickeiser 2002; Aharonian et al. 2012; Heesen et al. 2016). Such action yields a substantially lower local CR energy density compared to a pure-diffusion scenario, and motivates the case for different environments to be considered. As star-forming galaxies are often able to host an outflow (cf. section 1.2.2), it is necessary to consider both a 'One-Zone' model for CR injection into an interstellar medium in which no large-scale ISM flows/galactic outflows are present, and a 'Two-Zone' model in which a galactic outflow operates and affects the distribution of CRs. In both cases, the total power in the injected CR protons, $L_{\mathrm{CR,eff}}$, may be written as

$$L_{\mathrm{CR,eff}} = \varepsilon \xi E_{\mathrm{SN}} \mathcal{R}_{\mathrm{SN}} = \alpha^{\star} \left[\frac{\varepsilon \xi E_{\mathrm{SN}} \mathcal{R}_{\mathrm{SF}}}{M_{\mathrm{SN}}} \right] \ , \tag{2.3}$$

which sets the total CR energy budget for the system. $E_{\mathrm{SN}} \approx 10^{53}$ erg is introduced as the total energy output of a single core collapse Type II P SN or hypernova event, and M_{SN} is the typical mass of its progenitor star. To ensure that the subsequent calculations are conservative, the maximum possible value for M_{SN} is adopted, being 50 $\mathrm{M}_{\odot}$ (cf. section 1.3.1). The parameter $\varepsilon \sim 0.1$ is the fraction of SN power converted into to CR power (see Fields et al. 2001; Lemoine-Goumard et al. 2012; Caprioli 2012; Morlino and Caprioli 2012; Dermer and Powale 2013; Wang and Fields 2018), while $\xi = 0.01$ is the fraction of SN energy available after accounting for neutrino losses. The quantity $1 - \xi$ is thus the SN energy fraction lost to neutrinos, being the largest portion of the power emitted by the explosion at around 99%.[2]

---

[2]There are large uncertainties in the values adopted for these particular parameters, especially ξ, which depends on the types of SNe expected and the local interstellar environment (see e.g. Iwamoto and Kunugise 2006). Neutrino losses are expected to be around 99% ($\xi = 0.01$), however some have argued that actually neutrino losses are even more severe, at around 99.9% or $\xi = 0.001$ (see, e.g. Smartt 2009; Janka 2012, for reviews and discussion of neutrino losses in various environments and systems). By comparison, Type 1a/b SN explosions, which would be less common

It is also necessary to consider the level of mass injection arising per SN event, as this will later govern the mass-loading experienced by an outflow. This varies with SN type, with Type II SNe yielding a characteristic mass contribution to their environment of around $M_{\rm inj} = 10\,{\rm M}_\odot$ per explosion. This compares with just a few ${\rm M}_\odot$ for a Type Ib/c SN event (see, e.g. Branch 2010; Perets et al. 2010).

2.1.1 One-Zone Model

When modelling a galaxy as a single propagation environment, hereafter referred to as the *One-Zone model*, the CR source function $\mathcal{I}_{\rm p}$ is simply defined as a product of two separable components, the energy-dependent CR spectrum $\mathcal{L}_{\rm CR}(E)$ and the spatial distribution,

$$\mathcal{I}_{\rm p}(E, r) = \left\{ \mathcal{L}_{\rm CR}(E)\, Q_{\rm p}(r) \right\} , \tag{2.4}$$

where $Q_{\rm p}(r)$ is the total rate of CR (proton) injection per unit volume at some position r. This is weighted according to the protogalaxy model density profile (see section 1.3.2), which follows from the expectation that CRs are injected by stellar end-products and these, in turn, are distributed according to the underlying stellar distribution that forms from the gas and density profile of the host galaxy.

The energy spectrum, $\mathcal{L}_{\rm CR}(E)$, of the freshly accelerated CR hadronic particles is well-described by a power-law (see appendix A),

$$\mathcal{L}_{\rm CR}(E) = \mathcal{L}_0 \left(\frac{E}{E_0} \right)^{-\Gamma} , \tag{2.5}$$

in which the index $\Gamma = 2.1$ is adopted, as following from observations of the galactic differential CR flux power spectrum (see Allard et al. 2007; Kotera et al. 2010; Kotera and Olinto 2011 – although steeper indices of 2.3–2.4 have

---

in protogalaxies and result from longer-lived lower-mass stars, typically lose a far smaller fraction of their energy to neutrinos, perhaps a maximum of around 10%, with ξ being between 0.9 and 1 (Smartt 2009). For ε, the fraction of SN power converted to CR power, recent observational and theoretical studies that suggest a range of 7% (Lemoine-Goumard et al. 2012) to 30% (Caprioli 2012) would be appropriate, with 10% (i.e. $\varepsilon \sim 0.1$) usually being adopted as a characteristic value (see e.g. Fields et al. 2001; Morlino and Caprioli 2012; Dermer and Powale 2013; Wang and Fields 2018, among others). In line with this, $\varepsilon \sim 0.1$ is used here as a conservative estimate within a physically realistic range.

been suggested more recently in the case of pure proton spectra, e.g. Adrián-Martínez et al. 2016; H.E.S.S. Collaboration 2018).

This is slightly less steep than the spectral index of Galactic CRs below the spectral knee (see Fig. 2.2), but this is because the CR spectrum detected on Earth is comprised of particles which have had sufficient time during their propagations to be affected by cooling processes (these would more severely affect the particles at higher energies than lower energies). For electrons, the effective injection spectral index would be steeper than for protons. This is because they suffer much more severe radiative losses in and around their source environments compared to protons (see e.g. Amenomori et al. 2008). In the above (equation 2.5), a reference energy of $E_0 = 10^9$ eV (i.e. 1 GeV) is adopted, while a maximum energy of $E_{\mathrm{max}} = 10^{15}$ eV (i.e. 1 PeV) is used for the remainder of the work presented in this thesis (unless specified otherwise), being the theoretical maximum energy expected from CRs accelerated within a galactic or protogalactic environment (Bell 1978; Kotera and Olinto 2011; Schure and Bell 2013; Bell et al. 2013). The normalisation term $\mathcal{L}_0$ in equation 2.5 is defined by

$$\mathcal{L}_0 = \frac{L_{\mathrm{CR,eff}}(1 - \Gamma)E_0^{-\Gamma}}{E_{\mathrm{max}}^{1-\Gamma} - E_0^{1-\Gamma}} \, , \tag{2.6}$$

in which $L_{\mathrm{CR,eff}}$ is the effective CR power term (equation 2.3).

2.1.2 Two-Zone Model

In the presence of a large-scale galactic outflow, a One-Zone model configuration is clearly no longer appropriate. Instead, a *Two-Zone model* is adopted in which separate dynamical ISM zones are introduced, hereafter denoted Zones A and B. As shown in Fig. 2.3, Zone A is a conical region under the direct dynamical influence of a galactic outflow, while Zone B instead reflects the conditions of the One-Zone model, i.e. the static ISM outside of the outflow cone (see also outflow wind morphology in e.g. Strickland et al. 2000; Ohyama et al. 2002; Veilleux et al. 2005; Cooper et al. 2008).

In Zone A, the outflow wind velocity is altitude-dependent. Typically, flow velocities near the base of the outflow cone are low, while much higher
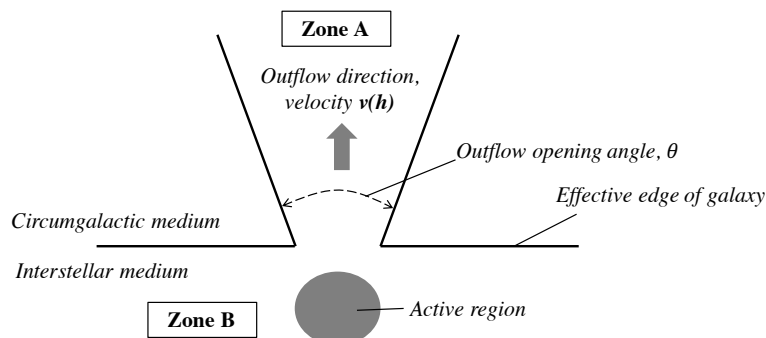
Fig. 2.3: Schematic figure for the geometric structure of the 'Two-Zone' galaxy model. The two zones, labelled A and B, represent the regions in which CR transport is governed by: (A) the bulk movement of gases, or (B) by diffusion. This structure is based on the outflow wind morphology outlined in, e.g. Strickland et al. (2000); Ohyama et al. (2002); Veilleux et al. (2005); Cooper et al. (2008).

(terminal) velocities are achieved further away from the actively star-forming region at the base of the cone (Chevalier and Clegg 1985; Samui et al. 2010). These winds are bulk flows of the medium in which CRs are entrained and, when their flow velocity is sufficiently fast, they can efficiently redistribute CRs at a rate that easily dominates over their diffusive propagation. Such bulk flows thus reduce the effective local energy density of CRs in the lower regions of an outflow cone compared to a pure diffusion scenario.

The provision of CR injection into each of the two zones A and B determines their non-thermal energy budgets. This is because the transfer of CRs between the two zones is effectively negligible. The internal magnetic structure of the outflow cone would be expected to preclude substantial CR propagation over the A/B zone interface, given that its predominant orientation within the outflow (i.e. Zone A) would be perpendicular to the galactic plane of the host.[3] CR penetration of the Zone A/B interface would rely on diffusion across the brane surface. With the flow-aligned magnetic field struc-

---

[3]This is consistent with the inferred structure of the magnetic field in the nearby starburst M82, where a poloidal field extends to kpc distances above and below the galactic plane (in particular, see the recent recent analysis by *HAWC+* in Rodriguez 2018). Radio observations of the synchrotron emission above and below the planes of other local starburst galaxies known to host outflows also reveal a polarisation direction aligned with the orientation of the hot, outflowing gases detected in other wavebands (see, e.g. Hummel et al. 1988; Sukumar and Allen 1990, 1991; Hummel et al. 1991; Brandenburg et al. 1993; Chyży et al. 2006; Soida et al. 2011; Mora and Krause 2013). Simulation studies, e.g. Kulpa-Dybeł et al. (2011), also argue in support of co-aligned magnetic fields and outflows. Theoretically, these large-scale ordered aligned fields are expected to develop by advection of interstellar magnetic fields by the fast outflowing gases (Bertone et al. 2005), while additional amplification along the cone may also arise by the action of the CR streaming instability if the CR energy density is substantial (Uhlig et al. 2012).

ture, CRs diffusing from Zone B into Zone A would encounter a perpendicular magnetic field. Their subsequent propagation would therefore be substantially more likely to occur back into Zone B, where the magnetic structure is more favourable to receive them. This is because CR diffusion is guided by the field lines and arises one or two orders of magnitude faster when aligned with the magnetic field (as compared to when in a perpendicular orientation).[4] A similar argument prevents substantial CR transfer from Zone A into Zone B, although in regions when the flow velocity is sufficiently fast, CR propagation would be governed by advection and, generally, they would not have sufficient time to fully pass across the interface with Zone B (unless they were injected very close to it, and the flow velocity was slow). The two zones may therefore safely be regarded as independent from the energetic perspective of CR injection.

The CR injection budget for a given zone is determined by the fraction of the galaxy core (from which the CRs are entrained) subtended. This is given by the solid angle fraction of the respective zone, $f_A = \Omega_A/4\pi$ for Zone A, while $f_B = \Omega_B/4\pi$ for Zone B, where

$$\Omega_A = 2\pi \left[1 - \cos(\theta/2)\right] \ , \tag{2.7}$$

and Ω_B follows as $4\pi - \Omega_A$. The corresponding CR luminosity injected into each zone is then simply $L_{\mathrm{CR,eff},i} = L_{\mathrm{CR,eff}} \, f_i$ where $i = \{A, B\}$. The angle θ (also indicated in Fig. 2.3) represents the full opening angle of the outflow cone. In-line with the previous discussion (see section 1.2.2), this research considers a range of opening angles θ, between $45°$ and $65°$, with a baseline of $55°$ adopted. The models explored here are intended to be a parametric simplification of a true outflow. They do not reflect all of the detail that a more sophisticated simulation could achieve, but are sufficient as a framework in which the relevant physics may be discussed and explored. For instance, hydrodynamical simulations suggest that a diverging cone with opening angles

---

[4]Theoretically, such behaviour is encoded in a diffusion coefficient (see Chapter 3 for further details and discussion), which can adopt a directional dependence (e.g. Shalchi et al. 2004, 2006; Hussein and Shalchi 2014).

that start at a low value of $10°-45°$ near their base and then increase to $45°-100°$ at high altitudes would be more appropriate than retaining a uniform opening angle through the extent of the outflow (Mac Low and Ferrara 1999; Martel and Shapiro 2001; Pieri et al. 2007; Bordoloi et al. 2016). This finer detail in the flow substructure is not accounted for in the simple parametric outflow model adopted here. Instead, an estimated range of opening angles is used to reflect the morphology of the wider part of the main flow, as this is most important for the relevant astrophysics.

The magnetic field strength along an outflow may be modelled as

$$B(h, \mathcal{R}_{SN}) = B_{ISM} \left(\frac{\mathcal{R}_{SN}}{\mathcal{R}_{SN,0}} \right)^{1/2} \left(1 + \left[\frac{h}{h_B} \right]^2 \right)^{-1} , \qquad (2.8)$$

where B_{ISM} is its mean field strength at the base of the outflow zone (i.e. well within the ISM of the host galaxy). $\mathcal{R}_{SN,0} = 0.1 \text{ yr}^{-1}$ is the SN event rate of the host system, which governs the saturation strength of the final field (see Beck and Wielebinski 2013 for a turbulent dynamo magnetic amplification model which yields such a dependency on SN event rate). A representative value of $B_0 = 5\mu G$ is adopted, being appropriate for the adopted value of $\mathcal{R}_{SN,0}$ (see Schober et al. 2013). h_B is introduced as a characteristic length-scale over which the magnetic field retains an approximately uniform strength within the interstellar environment of the host system. This ensures that variations with h of the magnetic field only become relevant in regions of the model which are well-within the outflow cone, i.e. where such variation would be necessary to conserve magnetic flux $(B(h) h^2 \approx \text{const})$. A parameter choice of $h_B = 1.5$ kpc yields a suitable structure, with a relatively uniform strength within 0.5 kpc of the central star-forming core of the host galaxy, and falling by only around 10% of its peak value in the ISM region (within 1 kpc).

While this treatment is appropriate for some star-forming systems that exhibit μG-strength magnetic fields for comparable SN event rates (e.g. NGC 253 – see Thompson et al. 2006 for magnetic fields in a range of other galaxies), some studies argue that further magnetic amplification processes may also operate in starburst systems. For instance, Miranda et al. (1998) assert

that amplification could arise via a Biermann battery effect (Biermann 1950; Khanna 1998) operating in the shocks of SN explosions. They demonstrate that this would lead to non-parallel temperature, magnetic and density gradients which would enhance the seed ISM magnetic fields upon which a turbulent dynamo mechanism may operate. Indeed, evidence of such further amplification may take the form of the nearby starburst galaxy, M82. With a SN event rate of around $\mathcal{R}_{\mathrm{SN},0} = 0.1$ yr^{-1} (Lenc and Tingay 2006; Fenech et al. 2010), its interstellar magnetic field is disproportionately stronger by more than an order of magnitude compared to the prescription instigated here (e.g. Thompson et al. 2006; Adebahr, B. et al. 2013). This may indicate that mechanisms beyond a simple turbulent dynamo could be at work to boost the field strength in certain intensely star-forming galaxies. However, such complications fall beyond the scope of this thesis, and their impact on the present results is not substantial (less than an order of magnitude).

2.2 Dynamical Implications of Cosmic Ray Injection

CRs propagating through a magnetic field will gyrate and scatter along the field lines. If they are initially streaming at speeds faster than the Alfvén velocity $v_{\mathrm{A}} = B(h)/\sqrt{4\pi\rho}$ of an ambient plasma (of density ρ and local magnetic field strength $B(h)$), they will rapidly amplify Alfvén waves of wavelengths comparable to the gyro-radii of the streaming CRs, in a process known as the streaming instability (Wentzel 1968; Kulsrud and Pearce 1969; Kulsrud and Cesarsky 1971). The amplified Alfvén waves can resonantly scatter the CRs. This slows CR propagation and operates to transfer their energy and momentum to the ambient medium as waves are damped. The rate at which this energy transfer arises is specified locally by $|v_{\mathrm{A}} \cdot \nabla P_{\mathrm{C}}|_h$ (e.g. Wentzel 1971; Ipavich 1975; Breitschwerdt et al. 1991; Uhlig et al. 2012), where $\nabla P_{\mathrm{C}}|_h$ is the CR pressure gradient at some location h. If CRs harbour a substantial energy density within their host system (as would be the case in a starburst galaxy), and if their pressure gradient is non-negligible, their transfer of momentum and energy by the CR streaming instability can provide an important contribution to the driving process of a large-scale galactic outflow. In extreme cases, when

thermal and mechanical SN feedback are not effective, a 'cold' CR-driven outflow could even develop in which a wind would be entirely driven by the CR pressure gradient. While SN-driven systems are driven by the thermal and mechanical energy deposition at their base (Chevalier and Clegg 1985), CRs can accelerate the outflow gas along the full length of the outflow cone. A consequence of this is that outflows with a substantial CR driving component tend to extend to higher altitudes compared to those driven purely by SN events, potentially reaching tens of kpc (Naab and Ostriker 2017; Jacob et al. 2018; Girichidis et al. 2018).

2.2.1 Cosmic Ray Driven Outflows

Energetics

The energy budget of CRs in an outflow is specified by their injection rate due to SN events. The treatment in the Two-Zone model (section 2.1.2) dictates the fraction of CR energy injected into an outflow, being proportional to the cone's solid angle. It follows that the total CR power provided to the outflow zone, A, would be $L_{\mathrm{CR,eff,A}} = L_{\mathrm{CR,eff}} \left[1 - \cos\left(\theta/2\right)\right]/2$. A large fraction of this supplied energy is actually lost to driving the outflow wind, as accounted for by the parameter ν_{d} for which a value of 0.1 is adopted (Murray et al. 2005; Samui et al. 2010). Note that this factor applies equally to the CRs injected as an energy scaling, but the true number of CRs themselves stays the same. ν_{d} is different to the CR acceleration efficiency parameter ε introduced earlier in equation 2.3, which instead specifies the total SN power converted to CR power. Thus, the total (remaining) energy injection rate into an outflow zone by the CRs is given by

$$\dot{\epsilon}_{\mathrm{CR}}^{\mathrm{outflow}} = \nu_{\mathrm{d}} L_{\mathrm{CR,eff,A}} \ . \tag{2.9}$$

However, the total energy budget of an outflow wind is not solely comprised of the CR component. Instead, consider the direct energy input by SN events (i.e. SN mechanical power and/or thermal power due to SN shock and radiative heating). The volumetric rate of thermal/SN energy directly injected

at the base of the outflow cone is given by

$$\dot{\epsilon}_{\text{th}}^{\text{outflow}} = \mathcal{Q} \left[\nu_{\text{d}} \xi \mathcal{R}_{\text{SN}} E_{\text{SN}} \right] \ , \tag{2.10}$$

which introduces a new term, $\mathcal{Q}$, being the thermalisation efficiency. This parameter accounts for energy absorption processes within the outflow wind, including the combined impacts of radiative cooling and the energy lost in heating, ionising and evaporating clumps which become entrained within the outflow (such clumps are known to be present in outflow winds due to the detection of charge-exchange line emission from nearby star-forming galaxies hosting outflows; it arises at phase boundaries where dense clumps interface with a hot wind fluid – see, e.g. Liu et al. 2012; Wang and Liu 2012; Wu et al. 2019).

Strong constraints on the value of $\mathcal{Q}$ have yet to be determined by theory or simulation, however observations of nearby starburst galaxies, e.g. M82, suggest that $\mathcal{Q}$ takes a value in the range $0.01 - 1$ (Watson et al. 1984; Chevalier and Clegg 1985; Seaquist et al. 1985; Heckman and Thompson 2017). It should be noted that the value of this parameter is poorly constrained in most systems, to the level that conflicting values can even be assigned to the same system by different studies (cf. Bradamante et al. 1998; Strickland et al. 2000; Veilleux 2008; Zhang et al. 2014). For the present application, it is sufficient to adopt a conservative benchmark value of $\mathcal{Q} = 0.01$.

Equation 2.9 and 2.10 may be combined to give the total SN injection power (accounting for direct injection and that via CRs) in terms of SN event rate $\mathcal{R}_{\text{SN}}$, or star-formation rate $\mathcal{R}_{\text{SF}}$, as

$$\dot{\epsilon} = \eta_{\text{SNe}} \left[\nu_{\text{d}} \xi \mathcal{R}_{\text{SN}} E_{\text{SN}} \right] = \eta_{\text{SNe}} \left[\frac{\nu_{\text{d}} \xi \alpha^{\star} \mathcal{R}_{\text{SF}} E_{\text{SN}}}{M_{\text{SN}}} \right] \ , \tag{2.11}$$

where the combined SN energy injection efficiency term η_{SNe} is defined as

$$\eta_{\text{SNe}} = \left(\mathcal{Q} + \varepsilon \frac{\Omega_{\text{A}}}{4\pi} \right) \ . \tag{2.12}$$

In outflows where CRs make a non-negligible contribution to the driving force

of the flow, a fraction f_g of their energy is lost in doing work against the gravitational potential of the system. Note that this is yet a further efficiency loss, separate (and operating in addition to) the factors ν_d and ε introduced previously. The final volumetric energy injection term into the outflow wind by SNe (including the contribution via CRs) is

$$f_\mathrm{g}\dot{\epsilon} = f_\mathrm{g}\eta_\mathrm{SNe}\left[\frac{\nu_\mathrm{d}\xi\,\alpha^\star\mathcal{R}_\mathrm{SF}E_\mathrm{SN}}{M_\mathrm{SN}}\right] \ , \tag{2.13}$$

where f_g depends on the gravitational potential of the system. One may adopt an NFW (Navarro–Frenk–White, Navarro et al. 1996) gravitational potential of the form

$$\Phi(h) = -\frac{3\mathrm{G}M_\mathrm{tot}}{h}\ln\left\{1 + \frac{h}{R_\ell}\right\} \ , \tag{2.14}$$

where R_ℓ is set as a scale length for the system (defined as the ratio of the virial radius of a galaxy to its concentration parameter, i.e. $R_\mathrm{vir}/c_\mathrm{g}$) and M_tot is the total galaxy (dynamical) mass. Such a gravitational potential would be appropriate for the starburst and high-redshift star-forming protogalaxies considered in this work, given that simulations show it to be a good approximation for virialised dark matter haloes over a broad range of galaxy masses and redshifts (e.g. Navarro et al. 1996; Jing 2000). Under such a gravitational potential, Samui et al. (2010) show that f_g would typically take values of a few percent (5-10%); they also provide an analytical expression for f_g in terms of the specifying parameters of the host galaxy. Hereafter, a value of $f_\mathrm{g} = 0.1$ is adopted.

Mass Loading

Mass may be injected into an outflow wind by the SN events themselves or by interstellar clumps, clouds and gases becoming entrained and/or evaporated in the flow. While detailed theoretical models regarding the mass-loading of outflows have not yet been fully established, the mass injection rate can instead be simply parametrised as

$$q_\mathrm{inj} = \mathcal{P}\left[\mathcal{R}_\mathrm{SN}M_\mathrm{inj}\right] = \mathcal{P}\left[\frac{\alpha^\star\mathcal{R}_\mathrm{SF}M_\mathrm{inj}}{M_\mathrm{SN}}\right] \ , \tag{2.15}$$

where the mass-loading factor is introduced as $\mathcal{P}$ and other terms retain their earlier definitions (M_{SN} being characteristic SN progenitor mass, and M_{inj} being the mass of the ejecta contributed by a single SN explosion). $\mathcal{P}$ is a scaling parameter used to specify the amount of mass loaded into a wind fluid for a given mass ejected from the progenitor star. This parameter could, in principle, have a value of above 1 (for example see Martin et al. 2002, which finds mass loading 'fractions' of 10 and above in NGC 1569) where additional mass becomes entrained or condenses into the SN ejecta. However, in the absence of detailed theoretical models able to offer constraints on appropriate values of $\mathcal{P}$, a conservative value $\mathcal{P} = 0.1$ is adopted hereafter (unless specified otherwise).

Hydrodynamical Model

A hydrodynamical model for a CR-powered outflow wind emanating from a galaxy was first considered by Ipavich (1975), which invoked a 1-dimensional spherically symmetric prescription for the flow emerging from a star-forming region around a galactic core. A point-like mass was used to represent the gravitational influence of the host galaxy on the ensuing wind dynamics. This treatment led to a natural parameterisation by energy and mass injection, both being scaled by the star-formation rate (and hence the SN event rate). Ipavich (1975) solved the associated system of magnetohydrodynamic fluid equations numerically, and found multiple solutions. These could be specified according to the adopted boundary conditions imposed at a so-called 'critical point' where the flow solution transitioned between supersonic and subsonic regimes. Of particular interest was an outflow wind solution, which exhibited a supersonic asymptotic velocity at high altitudes and a rapid flow velocity increase through the critical point from the origin. This approach formed the basis of the model and solution framework employed in several subsequent studies which investigated galactic outflows with a driving contribution from CRs, including Breitschwerdt et al. (1987, 1991, 1993); Everett et al. (2008); Bustard et al. (2016); Recchia et al. (2016), and the aforementioned Samui et al. (2010). These studies, particularly Samui et al. (2010) form the basis of

the following discussion where a spherically-symmetric approach is adopted, and a galactic outflow is modelled as two separate (but interacting) components: the hot thermal wind fluid, and the CRs as a relativistic fluid with non-negligible energy density but negligible mass density. In the following, h is used to denote the coordinate variable along a flow streamline (i.e. the radial distance from the galactic core). As well as transferring energy and momentum to the wind fluid by the CR streaming instability (see the introductory discussion at the start of section 2.2.1), the CR component of the outflow also experiences losses to the wind fluid from the work done by the CR pressure gradient in a bulk wind of velocity v, which arises at a rate of $|v \cdot \nabla P_{\mathrm{C}}|$ (Samui et al. 2010). Together, these two contributions allow the total energy exchange I between the baryonic wind fluid and the CR component to be defined as

$$I = -(v + v_{\mathrm{A}})\frac{\mathrm{d}P_{\mathrm{C}}}{\mathrm{d}h} \ , \tag{2.16}$$

(Samui et al. 2010) which is negative to denote that the energy exchange processes result in a net loss from the CR component, and a net gain by the wind fluid.

Under this prescription, the steady-state spherically symmetric form of associated CR and fluid equations are written as

$$\frac{1}{h^2}\frac{\mathrm{d}}{\mathrm{d}h}\left(\rho v h^2\right) = 0 \tag{2.17}$$

$$v\rho\frac{\mathrm{d}v}{\mathrm{d}h} = -\frac{\mathrm{d}P}{\mathrm{d}h} - \frac{\mathrm{d}P_{\mathrm{C}}}{\mathrm{d}h} - \rho\frac{\mathrm{d}\Phi}{\mathrm{d}h} \tag{2.18}$$

$$\frac{1}{h^2}\frac{\mathrm{d}}{\mathrm{d}h}\left[\rho v h^2\left(\frac{1}{2}v^2 + \frac{\gamma_{\mathrm{g}}}{\gamma_{\mathrm{g}}-1}\frac{P}{\rho}\right)\right] = -\rho v\frac{\mathrm{d}\Phi}{\mathrm{d}h} + I \tag{2.19}$$

$$\frac{1}{h^2}\frac{\mathrm{d}}{\mathrm{d}h}\left[\frac{\gamma_{\mathrm{C}}}{\gamma_{\mathrm{C}}-1}P_{\mathrm{C}}h^2(v+v_{\mathrm{A}})\right] = -I \ , \tag{2.20}$$

(Ipavich 1975; Breitschwerdt et al. 1991; Samui et al. 2010) in which 2.17 is the mass continuity equation, 2.18 is the momentum equation, 2.19 is the energy equation for the wind fluid, 2.20 is the evolution equation for the CR fluid component of the wind, ρ is the density of the wind fluid, v is the wind velocity, P is the pressure of the wind fluid (gas), P_{C} is the CR pressure, Φ is the

gravitational potential, $\gamma_{\mathrm{g}} = 5/3$ is the adiabatic index for the gas component, and $\gamma_{\mathrm{C}} = 4/3$ is the adiabatic index for the relativistic CR component. The inner term $\rho v h^2 = q_{\mathrm{inj}}$, from equation 2.17, is specified by q_{inj} as the volumetric mass injection rate at the base of the outflow due to SN mass-loading of the wind, as specified by equation 2.15.

Following Samui et al. (2010), the system of equations 2.17 to 2.20 can be manipulated as follows: First, combining equations 2.16 and 2.19 gives

$$\rho v \left[v \frac{\mathrm{d}v}{\mathrm{d}h} + \frac{\gamma_{\mathrm{g}}}{\gamma_{\mathrm{g}} - 1} \frac{\mathrm{d}}{\mathrm{d}h} \left(\frac{P}{\rho} \right) \right] = -\rho v \frac{\mathrm{d}\Phi}{\mathrm{d}h} - (v_{\mathrm{A}} + v) \frac{\mathrm{d}P_{\mathrm{C}}}{\mathrm{d}h} , \qquad (2.21)$$

(for $h > h_{\mathrm{inj}}$, i.e. above the maximum injection altitude of CRs). Next, multiplying equation 2.18 by v and subtracting from the new equation 2.21 gives

$$\frac{\mathrm{d}P}{\mathrm{d}h} = \gamma_{\mathrm{g}} \frac{P}{\rho} \frac{\mathrm{d}\rho}{\mathrm{d}h} - (\gamma_{\mathrm{g}} - 1) \left(\frac{v_{\mathrm{A}}}{v} \right) \frac{\mathrm{d}P_{\mathrm{C}}}{\mathrm{d}h} . \qquad (2.22)$$

The Alfvén velocity is given by $v_{\mathrm{A}} = B(h)/\sqrt{4\pi\rho}$ with $B(h)\,h^2$ being conserved throughout the most part of the outflow cone (scaled to give B_{ISM} as the interstellar magnetic field at the base of the outflow). Thus, v_{A} may be differentiated to give

$$\frac{1}{v_{\mathrm{A}}} \frac{\mathrm{d}v_{\mathrm{A}}}{\mathrm{d}h} = -\frac{2h}{h_{\mathrm{B}}^2 + h^2} - \frac{1}{2\rho} \frac{\mathrm{d}\rho}{\mathrm{d}h} , \qquad (2.23)$$

which, when $h_{\mathrm{B}} < h$, simplifies to

$$\frac{1}{v_{\mathrm{A}}} \frac{\mathrm{d}v_{\mathrm{A}}}{\mathrm{d}h} \approx -\frac{2}{h} - \frac{1}{2\rho} \frac{\mathrm{d}\rho}{\mathrm{d}h} , \qquad (2.24)$$

which holds for all h where the second term dominates (and this is an appropriate approximation here without losing generality). Now, differentiating equation 2.17 gives

$$\frac{1}{\rho} \frac{\mathrm{d}\rho}{\mathrm{d}h} + \frac{1}{v} \frac{\mathrm{d}v}{\mathrm{d}h} + \frac{2}{h} = 0 . \qquad (2.25)$$

Equations 2.20 and 2.16 can next be combined with these two results (equa-

tions 2.24 and 2.25) to yield

$$\frac{\mathrm{d}P_{\mathrm{C}}}{\mathrm{d}h} = \frac{\gamma_{\mathrm{C}} P_{\mathrm{C}}}{\rho} \left(\frac{v + v_{\mathrm{A}}/2}{v + v_{\mathrm{A}}} \right) \frac{\mathrm{d}\rho}{\mathrm{d}h} \ , \tag{2.26}$$

while P, the thermal gas pressure, may be found from this together with equation 2.27 (and integrating the result), i.e.

$$\frac{\mathrm{d}P}{\mathrm{d}h} = \left\{ \gamma_{\mathrm{g}} P - \gamma_{\mathrm{C}}(\gamma_{\mathrm{g}} - 1) P_{\mathrm{C}} \left[\frac{v + v_{\mathrm{A}}/2}{v + v_{\mathrm{A}}} \right] \left(\frac{v_{\mathrm{A}}}{v} \right) \right\} \frac{1}{\rho} \frac{\mathrm{d}\rho}{\mathrm{d}h} \ . \tag{2.27}$$

Together with equation 2.26, equation 2.27 is substituted into 2.18 to yield

$$\rho v \frac{\mathrm{d}v}{\mathrm{d}h} + c_*^2 \frac{\mathrm{d}\rho}{\mathrm{d}h} = -\rho \frac{\mathrm{d}\Phi}{\mathrm{d}h} \ . \tag{2.28}$$

This introduces the notation c_* for the effective sound speed, which is defined as

$$c_*^2 = \frac{\gamma_{\mathrm{g}} P}{\rho} - \frac{\gamma_{\mathrm{C}} P_{\mathrm{C}}}{\rho} \left\{ \left(\frac{v + v_{\mathrm{A}}/2}{v + v_{\mathrm{A}}} \right) \left(\gamma_{\mathrm{C}} - \gamma_{\mathrm{C}}(\gamma_{\mathrm{g}} - 1) \left[\frac{v_{\mathrm{A}}}{v} \right] \right) \right\} \ . \tag{2.29}$$

Equation 2.25 can now be used to substitute for the density gradient in 2.28, which leads to the velocity gradient in the form

$$\frac{\mathrm{d}v}{\mathrm{d}h} = \frac{2v}{h} \frac{\left(c_*^2 - \frac{h}{2} \frac{\mathrm{d}\Phi}{\mathrm{d}h} \right)}{v^2 - c_*^2} \ , \tag{2.30}$$

where it should be noted that the outflow velocity v transitions from subsonic to supersonic at some critical point, h_*, in an outflow wind solution. It thus follows that, at the critical point itself, the flow velocity must be equal to the effective sound speed, (i.e. $v = c_*$) and so the denominator will vanish. For a physical (non-vanishing) smooth solution through the critical point, the numerator must also vanish, and must do so more quickly than the denominator. It thus follows that

$$c_*^2 - \frac{h}{2} \frac{\mathrm{d}\Phi}{\mathrm{d}h} = 0 \ . \tag{2.31}$$

The requirement 2.31 allows for an alternative estimate at the critical point h_* to be made for the value of the effective sound speed c_* (and hence

v). At this location, the gravitational potential gradient may be expressed in terms of the circular velocity $V_{c,*}^2 = \mathrm{G}M(h_*)/h_*$, i.e.

$$
\begin{aligned}
c_*^2 &= \frac{h}{2}\frac{\mathrm{d}\Phi}{\mathrm{d}h}\bigg|_{h_*} \\
&= \frac{\mathrm{G}M(h_*)}{2h_*} = \frac{F^2 V_{c,\mathrm{vir}}^2}{2} \ ,
\end{aligned}
\tag{2.32}
$$

in which $M(h_*)$ is introduced to denote the enclosed mass of the distribution of the galaxy integrated to the critical point. Here, F is introduced as a correction factor. This is required because galaxy rotation curves are typically observed to be roughly flat at large radii, even in systems at high-redshifts – see Sofue and Rubin (2001) for a review. Thus, the circular velocity far out at the virial radius would be expected to be comparable to that at the critical point for most galaxies hosting an outflow. This means that the full dynamical mass of the system may be used in place of $M(h_*)$ in the above formulation, which enables easier parametrisation. More importantly, it means that the circular velocity of the galaxy at its virial radius may be used to approximate the circular velocity at the critical point, i.e. $V_{c,\mathrm{vir}} \approx V_{c,*}$, with the use of the corrective factor $F/\sqrt{2}$ to account for minor differences between the two velocities. This factor is typically of order 1 for any reasonable choices of model parameters (see also Samui et al. 2010).

Equation 2.30 may be solved numerically to yield a velocity profile for a reference model. For a galaxy with mass 10^9 M$_\odot$ and SN rate of $\mathcal{R}_{\mathrm{SN}} = 0.1$ yr^{-1}, a solution with a mass outflow rate of $q_{\mathrm{inj}} = 0.01$ M$_\odot$ yr^{-1}, energy flux of $\dot{\epsilon} = 3.0 \times 10^{38}$ erg s^{-1} per outflow cone, and a critical radius of $h_* = 0.32$ kpc results, with a corrective factor of $F = 1.05$. This gives sufficient information to specify the flow velocity at the critical point, and this can be used as a boundary condition from which equation 2.30 can be integrated. This must be done in two steps: firstly inwards towards the base of the outflow cone, and then separately (but using the same boundary condition) outwards to large h. The two solutions conjoin continuously across the boundary. A fourth-order Runge-Kutta method (Press et al. 2007) was employed to integrate in both directions, although a linear gradient across the critical point was locally
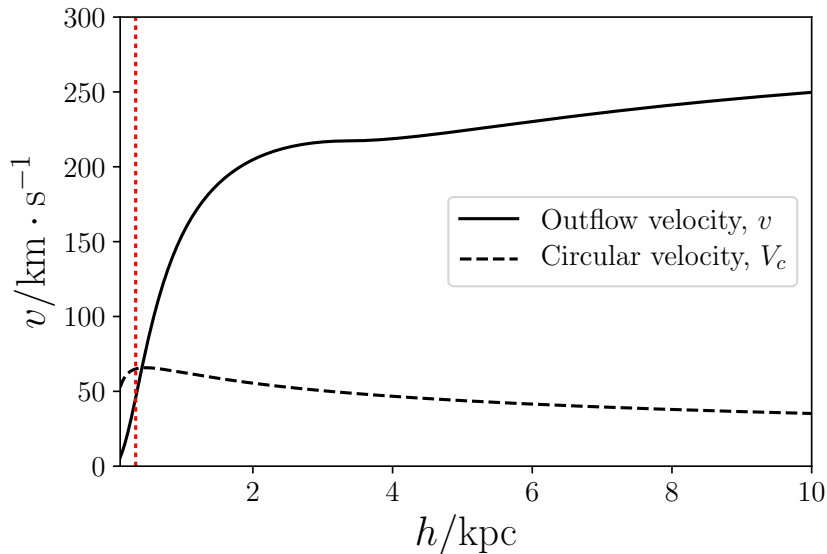
Fig. 2.4: Velocity profile for the CR-driven outflow model (solid black line), as described in the text for the reference protogalaxy model of mass 10^9 M$_\odot$ and SN event rate 0.1 yr^{-1}. At large h values of around 50 kpc, the flow reaches a terminal flow velocity of around $v_\infty \approx 290$ km s^{-1}, which yields a mass outflow rate of $q_{\rm inj} = 0.01$ M$_\odot$ yr^{-1}, energy flux of $\dot{\epsilon} = 3.0 \times 10^{38}$ erg s^{-1} per outflow cone and critical point location at $h_* = 0.32$ kpc (this position is indicated by the red vertical dashed line). For comparison, the dashed black line shows the circular velocity profile due to the underlying NFW gravitational potential. This is comparable to the outflow velocity at the critical point (differing only by the correction factor $F/\sqrt{2}$).

enforced to ensure a smooth, physical solution is found – this adjustment is discussed in Ipavich (1975). The resulting velocity profile for the outflow solution for this system is shown in Fig. 2.4, which demonstrates that the solution converges towards a terminal flow velocity of around $v_\infty \approx 290$ km s^{-1} at high altitudes. The critical point is indicated by the vertical dashed red line. For comparison, the circular velocity is also shown (dashed black line), which demonstrates the roughly flat rotation curve that results from the NFW profile, and further supports the approximation invoked in the calculation, i.e. that $V_{\rm c,vir} \approx V_{\rm c,*}$.

The density profile which corresponds to this outflow solution (as shown in Fig. 2.5) is instrumental to the subsequent work because the local density determines the ambient conditions with which CRs can interact[5], and so sets the resulting hadronic CR heating rate (this will be discussed in chapter 3). The solution yields an ISM density (within the host galaxy) of around 10 cm^{-3},

---

[5]CR and gas pressure profiles can also be calculated, and similar results are shown in Samui et al. (2010). These are not shown for the present discussion as they are not relevant to the subsequent analysis.
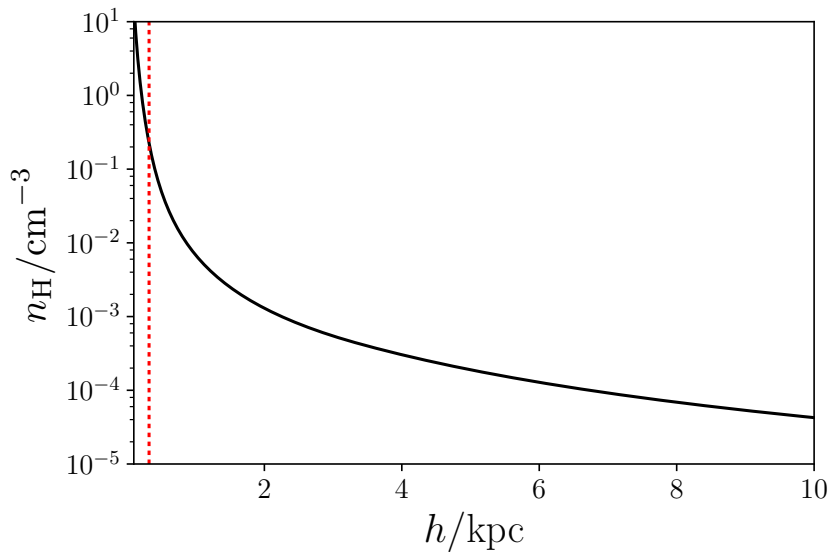
Fig. 2.5: Corresponding density profile for the outflow model described in the text (black line). This adopts the same parameters as used in Fig. 2.4. The critical point location, at $h_* = 0.32$ kpc, is again marked by the red vertical dashed line. At the base of the outflow cone (at $h \approx 0$), this gives an interstellar medium density of around 10 cm^{-3} (consistent with the earlier One-Zone model), and a critical-point temperature of approximately 10^5 K.

and a baryonic gas temperature of around 10^5 K in the vicinity of the critical point.

Chapter 2 summary: *This chapter outlines the likely sources of CRs in star-forming galaxies, and introduces a simple injection model to specify the CR energy budget in these systems. Supernova remnants are identified as the likely dominant CR accelerator in high-redshift star-forming protogalaxies, indicating a strong link between their CR energy densities and star-formation (and hence supernova) rates. Models are introduced to detail the injection rate of CRs into a so-called 'One-Zone' model galaxy environment where an effectively stationary ISM is assumed (in which there are no large-scale bulk flows of gas), and a 'Two-Zone' model where a bi-conical galactic outflow zone is also introduced. In this outflow zone, the hydrodynamical wind is driven by the thermalisation of energy provided by supernova events and by the coupling of the non-thermal CR component to the magnetic field in the wind. These models set the stage for later chapters, in which the propagation and interaction of CRs are considered in these One-Zone and Two-Zone environments.*

Chapter 3

Hadronic and Leptonic Interactions in Protogalactic Environments

This chapter is based on research, with part of the results presented in the following research papers:

(i) *"Interactions between ultra-high-energy particles and protogalactic environments"*, Owen, E. R., Jacobsen, I. B., Wu, K., Surajbali, P., 2018, MNRAS, 481, 666

(ii) *"Hadronic interactions of energetic charged particles in protogalactic outflow environments and implications for the early evolution of galaxies"*, Owen, E. R., Jin. X., Wu, K., Chan, S., 2019, MNRAS, 484, 1645

(iii) *"Starburst and post-starburst high-redshift protogalaxies: the feedback impact of high-energy cosmic rays"*, Owen, E. R., Wu, K., Jin, X., Surajbali, P., Kataoka, N., 2019, A&A, 626, A85.

Atomic media can be excited and ionised by keV CR protons and electrons, causing them to lose their energy along their propagation paths (see e.g. Nath and Biermann 1993; Sazonov and Sunyaev 2015). Higher-energy CRs (i.e. those with energy $\gtrsim 1\,\mathrm{GeV}$) do not shed their energy particularly efficiently via atomic interactions: indeed, if ionisation and atomic excitation were the only means by which they could exchange energy with their environment, energetic protons initially at 0.5 GeV would only lose around 2.5% of their energy over a Hubble timescale as they propagated through a cosmological medium – even if the density of that medium were maintained as that at $z = 20$ (see Sazonov and Sunyaev 2015). Above a threshold of of 0.28 GeV (Kafexhiu et al. 2014), the energy losses of CR protons are actually dominated by other processes. Chief among these are pion-producing hadronic interactions. The Gresisen-Zatsepin-Kuzmin (GZK) cutoff (Greisen 1966; Zatsepin and Kuz'min

1966) is an example of this, whereby energetic CRs are absorbed along their propagation paths due to the hadronic pion-producing and pair-production interactions they undergo with CMB radiation photons. Other, similar hadronic interactions with the baryonic ISM of a galaxy can also arise to enable effective transfer/deposition of CR energy. While hadronic processes only affect energetic CRs of around a GeV and above, in the Milky Way a large fraction (more than 99%) of the total CR energy density is actually harboured in hadronic particles above this threshold (see, e.g. Benhabiles-Mezhoud et al. 2013) and, presumably, this would also be the case in star-forming galaxies and protogalaxies. The energy transfer/deposition by these particles via hadronic processes could therefore be substantial in star-forming environments and, as such, is discussed in this chapter together with the associated energy transfer rates to their media, and calculations regarding the length-scales over which beams of CR particles subjected to these processes would typically survive.

3.1 Energetic Hadronic Interactions

In the following, the energy of incident CR protons is described by $E_{\rm p} = \gamma_{\rm p} m_{\rm p} {\rm c}^2$, where $\gamma_{\rm p}$ is the Lorentz factor. The energy of CR electrons is similarly described by $E_{\rm e} = \gamma_{\rm e} m_{\rm e} {\rm c}^2$. As with the CMB radiation field spectral number density (equation 1.7, where photon energies where given in terms of $\epsilon = {\rm h}\nu/m_{\rm e}{\rm c}^2$), it is convenient to normalise these particle energies to the electron rest mass, i.e. $\epsilon_{\rm p} = \gamma_{\rm p}(m_{\rm p}/m_{\rm e})$ and $\epsilon_{\rm e} = \gamma_{\rm e}$ for protons and electrons respectively. In interactions involving target baryons in the ISM, those ISM baryons may be assumed to be at rest without losing generality, with normalised energy $\epsilon = m_{\rm p}/m_{\rm e}$. This is because their energy is negligible compared to that of an incident CR proton in a given interaction event. In photo-pion production calculations, it is useful to define an invariant normalised energy, $\epsilon_{\rm r} = \gamma_{\rm p}(1 - \beta_{\rm p}\mu)\epsilon$, in which the cosine of the angle between the momentum vectors of the incident proton and photon is given by μ, and where $\beta_{\rm p}$ is the velocity of the incident CR proton normalised to the speed of light, c.

3.1.1 Absorption Processes

Photo-pion production and pp pion production are inelastic hadronic interaction processes which lead to the effective absorption and (near) complete energy release of an energetic CR proton within one or very few interaction events. The first of these processes accounts for interactions of an energetic proton with a radiation field, while the second is due to interactions with a baryonic interstellar density field.

Photo-Pion Production

The dominant interactions in this process are single-pion production via resonant production and direct production, or multiple-pion production (Mücke et al. 1999) with other processes being less significant (e.g. diffractive scattering). Multi-pion production branches dominate at $\epsilon_r \gtrsim 3500$, while single-pion production is more important at lower energies (see Mücke et al. 1999). For the case of single-pion production, resonant production occurs through the formation of the Δ^+ resonance. This can decay through two major channels in which charged and neutral pions are produced,

$$\mathrm{p} + \gamma \rightarrow \Delta^+ \rightarrow \begin{cases} \mathrm{p} + \pi^0 \rightarrow \mathrm{p} + 2\gamma \\ \mathrm{n} + \pi^+ \rightarrow \mathrm{n} + \mu^+ + \nu_\mu \end{cases} \tag{3.1}$$

where the muon μ^+ undergoes the further decay process

$$\mu^+ \rightarrow \mathrm{e}^+ + \nu_e + \bar{\nu}_\mu \tag{3.2}$$

(see Berezinskii and Gazizov 1993). The branching ratios for the $\Delta^+ \rightarrow \pi^0$ and $\Delta^+ \rightarrow \pi^+$ channels are 2/3 and 1/3, respectively. Direct pion production occurs at around 1/3 of the rate of resonant production for $\epsilon_r \approx 500$. These ratios would seem to suggest that there should be more neutral pions than charged pions in single-pion production mechanisms. However, additional charged pions may form in residual interactions. When taking these into account (including, e.g. $\mathrm{p} + \gamma \rightarrow \Delta^{++} + \pi^-$ and $\mathrm{p} + \gamma \rightarrow \Delta^0 + \pi^+$), each type of pion is found to be produced in similar numbers (see Dermer and

Menon 2009).

Based on experimental data (Baldini et al. 1987), the total cross-section of the photo-pion interaction may be split into three energy regions for which an average cross-section may be expressed. This allows the following step-function approximation to be invoked:

$$\sigma_{\gamma\pi}(\epsilon_{\rm r}) \approx \begin{cases} 340 \ \mu{\rm b} & [\epsilon_{\rm th} \leq \epsilon_{\rm r} < 980] \\ 240 \ \mu{\rm b} & [980 \leq \epsilon_{\rm r} < 3500] \\ 120 \ \mu{\rm b} & [3500 \leq \epsilon_{\rm r}] \end{cases} \tag{3.3}$$

(cf. the approximated two-step function used in Dermer and Menon 2009), and here $\epsilon_{\rm th}(\approx 390)$ is the threshold energy for the pion production process. The incident protons lose approximately 20% of their energy at low-energies in the resonant production process, with similar rates of production for each type of pion. The incident protons at higher-energies will lose a much more substantial fraction of their energy, around 60%, due to the multi-pion production process (Dermer and Menon 2009). This leads to the effective inelastic cross-section, which may be written as: $\hat{\sigma}_{\gamma\pi} \equiv \sigma_{\gamma\pi}(\epsilon_{\rm r})K_{\gamma\pi}(\epsilon_{\rm r})$, for which the inelasticity coefficient has been introduced as

$$K_{\gamma\pi}(\epsilon_{\rm r}) \approx \begin{cases} 0.2 & [\epsilon_{\rm th} \leq \epsilon_{\rm r} < 3500] \\ 0.6 & [3500 \leq \epsilon_{\rm r}] \end{cases}, \tag{3.4}$$

which yields

$$\hat{\sigma}_{\gamma\pi} \approx \begin{cases} 68 \ \mu{\rm b} & [\epsilon_{\rm th} \leq \epsilon_{\rm r} < 980] \\ 48 \ \mu{\rm b} & [980 \leq \epsilon_{\rm r} < 3500] \\ 72 \ \mu{\rm b} & [3500 \leq \epsilon_{\rm r}] \end{cases} . \tag{3.5}$$

For the current purposes, detailed variations of the inelastic cross-section over energy may be neglected such that it may be simply expressed as $\hat{\sigma}_{\gamma\pi} \approx \hat{\sigma}_{\gamma\pi}^* \ \mathcal{H}(\epsilon_{\rm r} - \epsilon_{\rm th})$, where $\mathcal{H}(...)$ is the Heaviside step function. In light of this,

$\hat{\sigma}^*_{\gamma\pi} = 70$ μb is adopted, and $\epsilon_{\text{th}} = 390$. These are the same as the values suggested by Dermer and Menon (2009) (see also Atoyan and Dermer 2003).

The CR proton collision rate is defined in terms of the collisional timescale through the relation $\tau_{\gamma\pi,\text{coll}}(\gamma_{\text{p}}) = \dot{N}(\gamma_{\text{p}})^{-1}_{\gamma\pi,\text{coll}}$ for a CR proton with Lorentz factor γ_{p}. Some fraction of these collisions can be attributed to elastic interactions, while others may be attributed to the pion-producing inelastic pathway. The total collision rate accounts for both of these but, for the current calculation, only the CR proton absorption rate is required - i.e. the fraction of collisions that successfully yield pion-production (and subsequent CR absorption). This may be defined as

$$\dot{N}_{\gamma\pi,\text{abs}}(\gamma_{\text{p}}) = [\tau_{\gamma\pi,\text{abs}}(\gamma_{\text{p}})]^{-1}$$
$$= \frac{c}{2\gamma_{\text{p}}} \int_0^\infty d\epsilon \frac{n_\gamma(\epsilon)}{\epsilon} \hat{\sigma}_{\gamma\pi}(\gamma_{\text{p}}) , \quad (3.6)$$

where $n_\gamma(\epsilon)$ is the number density of the (assumed isotropic) radiation field and, rather than using the total cross-section $\sigma_{\gamma\pi}$ for the interaction (as with the collision rate), the inelastic interaction cross-section $\hat{\sigma}_{\gamma\pi} = K(\gamma_p)\sigma_{\gamma\pi}$ is applied, being some corresponding fraction of the total cross-section defined by $K(\gamma_p)$, which accounts solely for the inelastic contribution.

As most radiation fields of interest (either the CMB or the stellar radiation) will be thermal blackbodies[1], substituting such a radiation field for $n_\gamma(\epsilon)$ (from equation 1.7) then gives

$$\dot{N}_{\gamma\pi,\text{abs}}(\gamma_{\text{p}}) = \frac{c}{2\gamma_{\text{p}}} \int_0^\infty d\epsilon \frac{8\pi}{\lambda_{\text{C}}^3} \frac{\epsilon}{\exp\left[\frac{\epsilon}{\Theta}\right] - 1} \hat{\sigma}_{\gamma\pi}(\gamma_{\text{p}})$$
$$= \frac{4\pi\hat{\sigma}_{\gamma\pi}(\gamma_{\text{p}})\Theta^2}{\gamma_{\text{p}}\lambda_{\text{C}}^3} \int_0^\infty \frac{x\,dx}{\exp(x) - 1} , \quad (3.7)$$

where the substitution $x = \epsilon/\Theta$ has been applied (in which Θ retains its meaning from section 1.3.4 as the dimensionless temperature of the radiation field). The integral has a standard result of $\pi^2/6$, thus giving the final absorption

---

[1]Note that, in the case of a diluted radiation field a scaling factor (as that described by $n_\gamma^\star/n_\gamma^{\text{BB}}$ in section 1.3.4) is required to decrease the interaction rate, as appropriate.

rate as

$$\dot{N}_{\gamma\pi,\text{abs}}(\gamma_{\text{p}}) = \frac{2\pi^3 \hat{\sigma}_{\gamma\pi}(\gamma_{\text{p}})\Theta^2}{3\gamma_{\text{p}}\lambda_{\text{C}}^3} \ . \tag{3.8}$$

pp-**Pion Production**

This mechanism is the analogous case for pion-production in which the target is a baryon field instead of a radiation field. The process proceeds in a similar way, and also produces charged and neutral pions through the dominant channels

$$p + p \to \begin{cases} p + \Delta^+ \to \begin{cases} p + p + \pi^0 + \xi_0(\pi^0) + \xi_\pm(\pi^+, \pi^-) \\ p + p + \pi^+ + \pi^- \xi_0(\pi^0) + \xi_\pm(\pi^+, \pi^-) \\ p + n + \pi^+ + \xi_0(\pi^0) + \xi_\pm(\pi^+, \pi^-) \end{cases} \\ n + \Delta^{++} \to \begin{cases} n + p + \pi^+ + \xi_0(\pi^0) + \xi_\pm(\pi^+, \pi^-) \\ n + n + 2\pi^+ + \xi_0(\pi^0) + \xi_\pm(\pi^+, \pi^-) \end{cases} \end{cases} . \tag{3.9}$$

Here, ξ_0 and $\xi_\pm$ are the multiplicities for neutral and charged pions respectively, and the Δ^+ and Δ^{++} baryons are the resonances (see Almeida et al. 1968; Skorodko et al. 2008). The total inelastic cross-section for this process is well-described by the Kafexhiu et al. (2014) analytic parameterisation,

$$\hat{\sigma}_{\text{p}\pi} = \left(30.7 - 0.96\ln(\chi) + 0.18(\ln\chi)^2\right)\left(1 - \chi^{-1.9}\right)^3 \text{ mb} , \tag{3.10}$$

in which $\chi = E_{\text{p}}/E_{\text{p}}^{\text{th}}$, and the threshold energy is $E_{\text{p}}^{\text{th}} = (2m_{\pi^0} + m_{\pi^0}^2/2m_{\text{p}})c^2 \approx 0.28$ GeV, i.e. the energy required for the formation of the lowest energy product of the interaction: a neutral pion, π^0. It follows that the rate of CR absorption rate due to pp-pion production is thus given by

$$\dot{N}_{\text{p}\pi,\text{abs}}(\gamma_{\text{p}}) = c\ n_{\text{CR}}(\gamma_{\text{p}})\ \hat{\sigma}_{\text{p}\pi}(\gamma_{\text{p}})\ n_{\text{H}} , \tag{3.11}$$

which holds for interactions of high-energy CR protons when engaging with the baryons of the CGM or ISM of number density n_{H}.

3.1.2 Cooling Processes

This section considers the photo-pair interaction process which cannot be well-described as an absorption process. This is because it causes continuous rather than stochastic energy loss of the initiating proton which can be regarded to survive the interaction as it proceeds.

Photo-pair Production

The photo-pair Bethe-Heitler process (Bethe and Heitler 1934) which produces leptons via

$$A + \gamma \rightarrow A' + l^+ + l^- \ , \tag{3.12}$$

where A and A$'$ are nucleons, and l^+ and l^- are positively and negatively charged leptons, respectively. These leptons are predominantly found to be electron/positron pairs at the energies of interest in this study (Blumenthal 1970; Klein 2006).

Stepney and Guilbert (1983) considered an analytic fit to the cross-section for the photo-electron pair production ($p + \gamma \rightarrow p + e^+ + e^-$) process and found

$$\hat{\sigma}_{\gamma e}(\epsilon_r) \approx \left\{ \frac{7}{6\pi} \alpha_f \left(\psi - \frac{109}{42} \right) + \left[473.65 + 241.26\psi \right. \right.$$
$$\left. \left. + 81.151\psi^2 + 5.3814\psi^3 \right] \left(\frac{10^{-5}}{\epsilon_r} \right) \right\} \sigma_T \tag{3.13}$$

(see also Jost et al. 1950; Bethe and Maximon 1954; Blumenthal 1970) to be a reasonable approximation, where α_f is the fine structure constant, σ_T is the Thomson cross-section, and $\psi = \ln 2\epsilon_r$. Presently, only CR protons yielding $\epsilon_r \gtrsim 60$ are considered. In this regime, the cross-section expression above may be approximated as

$$\hat{\sigma}_{\gamma e}(\epsilon_r) \approx \left\{ \frac{7}{6\pi} \alpha_f \ln \left[\frac{\epsilon_r}{k_{\gamma e}} \right] \right\} \sigma_T \ , \tag{3.14}$$

where the parameter $k_{\gamma e} = 6.7$, which was found to be appropriate for this energy range. The same expression for the cross-section (equation 3.14) was used in Dermer and Menon (2009), however they adopted a lower value of

$k_{\gamma e} = 2$ instead, following from their use of a different energy bound, $\epsilon_r \gtrsim 40$.

Assuming that the electron-positron pairs are formed in the zero-momentum frame of the interaction (Dermer and Schlickeiser 1991), and that the invariant energy of the interaction is dominated by the contribution from the CR energy, the timescale for interactions of CR protons interacting with a blackbody radiation field[2] by this process is given by

$$t_{\gamma e} \approx \frac{m_p}{m_e} \frac{\gamma_p^2}{c} \left\{ \int_{\gamma_p^{-1}}^{\infty} d\epsilon \, \frac{n_\gamma^{BB}(\epsilon)}{\epsilon^2} \int_2^{2\gamma_p\epsilon} d\epsilon_r \, \frac{\epsilon_r \hat{\sigma}_{\gamma e}(\epsilon_r)}{\sqrt{1 + 2\epsilon_r}} \right\}^{-1} \qquad (3.15)$$

(see Protheroe and Johnson 1996; Dermer and Menon 2009). This implies an energy loss rate of

$$b_{\gamma e}(\gamma_p) \approx \frac{112}{9} \frac{c^2 m_e \alpha_f \sigma_T \mathcal{F}_{\gamma e}}{\lambda_C^3 \gamma_p^2 u^{5/3}} \, , \qquad (3.16)$$

as $b_{\gamma e}(\gamma_p) = m_p c^2 \gamma_p t_{\gamma e}^{-1}$. Here, $u = m_e c^2 / \gamma_p k_B T$ and

$$\mathcal{F}_{\gamma e} = \mathcal{C}(u) + \mathcal{D}(u) \ln \left[\frac{1}{0.974 u k_{\gamma e}} \right] + (0.382 u k_{\gamma e})^{3/2} \mathcal{E}(u) \, . \qquad (3.17)$$

The functions $\mathcal{C}(u)$, $\mathcal{D}(u)$ and $\mathcal{E}(u)$ result from standard integrals, with $\mathcal{C}(u) = 0.74$ and $\mathcal{D}(u) = \Gamma(5/2)\zeta(5/2)$ when $b \ll 1$, $\mathcal{C}(u) = u^{3/2} \ln(u) e^{-u}$ and $\mathcal{D}(u) = u^{3/2} e^{-u}$ when $u \gg 1$, and $\mathcal{E}(u) = -\ln[1 - e^{-u}]$ for all values of u (Dermer and Menon 2009).

3.1.3 Hadronic Path Lengths

An energetic particle subjected to interactions will lose its energy over a characteristic length-scale. For a proton of initial energy E_p (which is taken to be larger than the hadronic interaction threshold energy of 0.28 GeV), the characteristic path length over which it would lose its energy is defined by

$$r_{int} = \left\{ \frac{d \ln E_p}{ds} \right\}^{-1} = \left\{ \frac{d \ln \epsilon_p}{ds} \right\}^{-1} \, , \qquad (3.18)$$

where ds is the differential path length element (see Blumenthal 1970). A corresponding interaction timescale may also be defined t_{int}, being the time taken

---

[2]Again, a scaling factor, e.g. $n_\gamma^\star / n_\gamma^{BB}$, cf. section 1.3.4, may be required in a diluted radiation field.

for the characteristic energy-loss path length to be traversed by a (relativistic) CR, i.e.

$$r_{\text{int}} \approx c\beta_{\text{p}} t_{\text{int}} . \tag{3.19}$$

These definitions can be used together with the interaction timescales in sections 3.1.1 and 3.1.2 for the CR protons to allow their effective path lengths to be calculated in specified galactic environments.

In a protogalaxy, the internal radiation fields, which can act as a target for photo-pion and photo-pair production, are supplied by stellar emission and the permeating CMB radiation field. Both of these radiation fields are well modelled by a locally isotropic blackbody, and their photon number density is given by a Planck function (see equation 1.7). This is specified by the effective temperature of the radiation field, T,[3] and would be scaled in the case of a diluted (e.g. stellar) radiation field. The timescale over which the photo-pion interaction arises in a blackbody radiation field is given by

$$t_{\gamma\pi}(\gamma_{\text{p}}) = \frac{2\gamma_{\text{p}}^2 \lambda_{\text{C}}^3}{8\pi c} \left\{ \int_0^\infty \frac{\mathrm{d}\epsilon}{e^{\epsilon m_{\text{e}} c^2 / k_{\text{B}} T} - 1} \int_0^{2\gamma_{\text{p}}\epsilon} \mathrm{d}\epsilon_{\text{r}} \, \epsilon_{\text{r}} \hat{\sigma}_{\gamma\pi} \right\}^{-1} \tag{3.20}$$

in the high-energy limit, i.e. when $\beta_{\text{p}} \to 1$ (Dermer and Menon 2009). The corresponding path length over which the energy of the CR proton is deposited due to this process (in an undiluted radiation field) follows as $r_{\gamma\pi} = c\beta_{\text{p}} t_{\gamma\pi}(\gamma_{\text{p}})$. For energetic protons, $\beta_{\text{p}} \approx 1$. Also the cross-section may be approximated as $\hat{\sigma}_{\gamma\pi} \approx \hat{\sigma}_{\gamma\pi}^* \mathcal{H}(\epsilon_{\text{r}} - \epsilon_{\text{th}})$, which allows the latter integral in equation 3.20 to be evaluated. By also imposing the requirement that $2\gamma_{\text{p}}\epsilon \geq \epsilon_{\text{th}}$, it follows that

$$r_{\gamma\pi} \approx \frac{\lambda_{\text{C}}^3}{8\pi \, \hat{\sigma}_{\gamma\pi}^*} \left(\frac{m_{\text{e}} c^2}{k_{\text{B}} T} \right)^3 \mathcal{J}^{-1} , \tag{3.21}$$

where

$$\mathcal{J} = \int_\eta^\infty \mathrm{d}\zeta \, \frac{\zeta^2 - \eta^2}{e^\zeta - 1} = 2 \sum_{k=1}^\infty \left(\frac{\eta}{k^2} + \frac{1}{k^3} \right) e^{-k\eta} \tag{3.22}$$

and $\eta = \epsilon_{\text{th}} m_{\text{e}} c^2 / 2\gamma_{\text{p}} k_{\text{B}} T$.

---

[3]In the case of the source being the stellar population of a galaxy, this would be at least around $T_* = 30{,}000$ K, as it would be dominated by contributions from massive O- and B- type stars. This compares to $T(z) = T_0(1 + z)$, in the case of the CMB with $T_0 = 2.73$ K as temperature in the current epoch (Planck Collaboration et al. 2018), as outlined in section 1.3.4.

The timescale for the photo-pair production process in a blackbody radiation field was given in equation 3.15. It can be shown that this interaction gives a path length of

$$r_{\gamma\mathrm{e}}(\gamma_\mathrm{p}) \approx \frac{9}{112} \frac{m_\mathrm{p} \lambda_\mathrm{C}^3 \gamma_\mathrm{p}^3 b^{5/3}}{m_\mathrm{e} \alpha_\mathrm{f} \sigma_\mathrm{T} \mathcal{F}_{\gamma\mathrm{e}}} \quad \mathrm{Gpc} \ , \tag{3.23}$$

where symbols retain their earlier definitions.

The corresponding path length due to the pp interaction is more straightforward to calculate, because the target field is now comprised of low-energy (i.e. non-relativistic) baryons. These do not significantly contribute energy to the ensuing interaction, so the path length effectively reverts to its classical form, i.e.

$$r_{\mathrm{p}\pi} = \frac{1}{\hat{\sigma}_{\mathrm{p}\pi} n_\mathrm{H}} \ , \tag{3.24}$$

where n_H is the baryon number density in the target field.

Those protons which are able to escape from their host galaxy to propagate in intergalactic space will freely-stream over cosmological distances. In doing so, they will be affected by the expansion of the Universe itself, thus undergoing adiabatic losses. This would arise over a length-scale of

$$r_{\exp} = \mathrm{c} \left| \frac{1}{E} \left(\frac{\mathrm{d}E}{\mathrm{d}t} \right)_{\exp} \right|^{-1} = \frac{\mathrm{c}}{\mathrm{H}_0 \sqrt{\Omega_\mathrm{m}(1+z)^3 + \Omega_\Lambda}} \ , \tag{3.25}$$

(see Gould 1975; Berezinskii and Grigor'eva 1988; Berezinskii et al. 2006) in which the general energy term E is used (instead of E_p), as this process is not a specific interaction for CR protons but would apply to any particle propagating over cosmological distances. Here, $\mathrm{H}_0 = (67.8 \pm 0.9)$ km s^{-1} Mpc^{-1} is the present value of the Hubble parameter in the current epoch, $\Omega_\mathrm{m} = 0.308 \pm 0.012$ is the matter density of the Universe and $\Omega_\Lambda = 0.691 \pm 0.0062$ is the dark energy density of the Universe (see also appendix B for further information about these parameters). Contributions due to curvature and radiation energy density are negligible (Planck Collaboration 2016). In most cases, these adiabatic cosmological expansion losses would not be relevant for a GeV CR particle within an interstellar setting – however it is still useful to
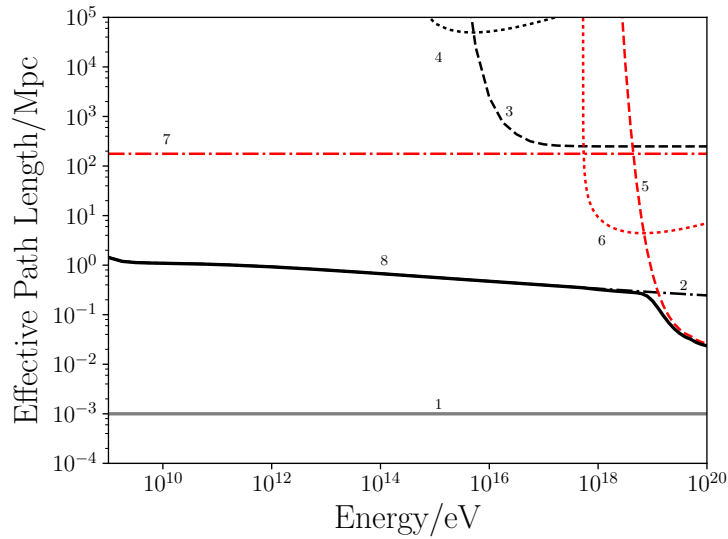
Fig. 3.1: Effective interaction (energy-loss) path lengths of energetic CR protons in a typical model interstellar environment of gas density $n_H = 10 \ \text{cm}^{-3}$, and a stellar population of $N_* = 10^6$ type O/B massive stars. The impact of the magnetic field on CR propagation is omitted from this plot. Path lengths are calculated assuming an underlying CMB radiation field at redshift $z = 7$. The path lengths due to CMB-interaction losses are plotted in red, while path lengths due to CRs interacting with elements of the foreground galaxy model are plotted in black. The combined effect of all loss processes is represented by the thick black line. The lines, as labelled, are (1) Host galaxy radius of 1 kpc (for comparison - although note that losses are calculated assuming uniform conditions along particle propagation paths); (2) pp Pion-production loss path lengths (pp, $p\pi^{\pm}\pi^0$); (3) Galactic Radiation Photo-pion loss path lengths ($p\gamma, \pi^{\pm}\pi^0$); (4) Galactic Radiation Photo-pair loss path lengths ($p\gamma, e^{\pm}$); (5) CMB Photo-pion loss path lengths ($p\gamma, \pi^{\pm}\pi^0$); (6) CMB Photo-pair loss path lengths ($p\gamma, e^{\pm}$); (7) Adiabatic particle cooling due to cosmological expansion; (8) Total.

provide context, and to specify an upper physical limit to the distance over which a CR must deposit most of its energy.

Each of these energy loss path lengths is plotted against CR proton energy in Fig. 3.1. This uses the protogalaxy model as defined by the density and radiation fields described in chapter 1, and demonstrates that the relative importance of stellar photons in governing the energy deposition processes of the energetic protons is negligible, with the effects of the CMB radiation field (at $z = 7$) driving far more significant hadronic CR losses. This is reflected by the path lengths corresponding to losses in the stellar radiation fields (lines 3 and 4 respectively) being substantially longer than those attributed to CMB induced losses (red lines 5, 6 and 7). Overall, Fig. 3.1 demonstrates that interaction losses are entirely dominated by those due to pp interactions with the interstellar baryons of the galaxy (dashed black line 2), with the only exception arising at the very highest of energies, above 10^{19} eV, when CMB

photo-pion losses take-over (although, at such energies, the power-law nature of the CR spectrum means that the energetic particle flux would be very low). The thick black line in Fig 3.1 indicates the resultant losses calculated as the reciprocal sum of all contributions, which is almost entirely governed by the path length resulting from the pp interactions alone. In general, both of the pγ interactions (photo-pair and photo-pion) bear little importance, demonstrating that CR absorption is predominantly influenced by the density field of the host environment. For comparison, the grey line (1) indicates the characteristic size of the model protogalaxy, i.e. 1 kpc. While this plot would indicate CRs can generally escape from their source galaxy and deposit energy elsewhere, it should be noted that these calculations do not account for the hampering effect of galactic magnetic fields on the propagation of the CRs. These will be considered in chapter 4.

3.2 Products of Cosmic Ray Interactions

All three of the previously discussed hadronic interaction processes can produce charged and neutral pions (see Pollack and Fazio 1963; Gould and Burbidge 1965; Stecker et al. 1968; Mücke et al. 1999; Berezinskii et al. 2006; Dermer and Menon 2009). These pions undergo certain decay processes over very short timescales, meaning that their fleeting existence is of interest only due to the result of their decay process, rather than due to any astrophysical importance of the pions themselves.

Neutral pions predominantly decay into two photons through an electromagnetic process,

$$\pi^0 \to 2\gamma \ , \tag{3.26}$$

which arises with a branching ratio of 98.8% (Patrignani et al. 2016), over a very short timescale of 8.5×10^{-17} s. Charged pions instead produce leptons (and neutrinos). This proceeds via two main mechanisms. The first option is by their decay into muons and muon neutrinos with a branching ratio of 99.99% (e.g. Patrignani et al. 2016) over a timescale of 2.6×10^{-8} s. This

proceeds as

$$\pi^+ \rightarrow \mu^+ + \nu_\mu$$
$$\pi^- \rightarrow \mu^- + \bar{\nu}_\mu \tag{3.27}$$

with the muons decaying further into electrons and positrons as per process 3.2 (and the equivalent for negative muons, $\mu^- \rightarrow e^- + \bar{\nu}_e + \nu_\mu$). Alternatively, the pions can decay directly to electrons and positrons with a branching ratio of 0.012% (e.g. Fazzini et al. 1958; Patrignani et al. 2016), proceeding as

$$\pi^+ \rightarrow e^+ + \nu_e$$
$$\pi^- \rightarrow e^- + \bar{\nu}_e \; . \tag{3.28}$$

The remaining decays (e.g. via neutral pion production or inverse beta-decay) have negligible branching ratios of less than 10^{-8} (e.g. Patrignani et al. 2016).

The γ-rays produced by the neutral pion decays interact only minimally with their source environment, but this makes them very useful for tracing the location of CR interactions and provides an observational signature. By contrast, the leptons produced in the decay of the charged pions are much more instrumental in influencing their surrounding environment. This makes them the predominant channel by which CRs can transfer their energy to their astrophysical environment.

3.2.1 γ-ray Emission as an Observational Signature

In π^0 decay, all of the pion energy is transferred to γ-rays. Thus, the relation between the CR spectral energy density and that of γ-rays is governed entirely by the inelastic cross-section for the production of π^0 secondaries compared to the total inelastic cross-section for the hadronic process that causes the pion production in the first place – in an interstellar environment, Fig. 3.1 shows this to predominantly be the pp interaction. This is because the energy transferred to the secondary pions is proportional to their production cross-sections.

A parameterisation of the pion-production cross-sections is introduced by

Blattnig et al. (2000) and, when considering all pion-production branches, is found to give a reasonable fit to empirical measurements of the cross-section at different energies, with only a minor discrepancy below 50-GeV (Jacobsen 2015). The pion-production cross-sections for the formation of $\{\pi^+, \pi^-, \pi^0\}$ as a fraction of the total pp inelastic cross-section are respectively $\{0.6, 0.1, 0.3\}$ at 1-GeV, which tends towards around $\{0.3, 0.4, 0.3\}$ at higher energies. The cross-section ratio (and hence energy transfer fraction) for the formation π^0 secondaries is therefore only weakly dependent on the energy of the CR primary, being roughly 0.3 across all energies of interest (between 1 GeV and 1 PeV) – see Kelner et al. (2006); Kafexhiu et al. (2014). This gives a relation between the CR flux of energetic protons, and the γ-ray energy flux resulting from their interactions, which can be expressed as

$$E_\gamma \frac{\mathrm{d}\Phi(E_\gamma)}{\mathrm{d}E_\gamma} \approx \left(\frac{\sigma_{\pi^0}}{\hat{\sigma}_{\mathrm{p}\pi}} \right)\Bigg|_{E_0} E \, \frac{\mathrm{d}\Phi(E)}{\mathrm{d}E} \ , \tag{3.29}$$

where E_γ is the γ-ray photon energy. This relation relies on two assumptions: (1) that the vast majority of CRs are attenuated by pp interactions within their host galaxy; and (2) that the CR flux is isotropically experienced by any point within the target medium of the host galaxy. While these are reasonable for a first calculation, future work should assess the validity of these assumptions more carefully. Equation 3.29 can be related to the CR energy density by

$$\frac{\mathrm{d}\Phi(E)}{\mathrm{d}E \, \mathrm{d}\Omega} = \frac{(1 - \Gamma)E_0^{-\Gamma}}{E_{\mathrm{max}}^{1-\Gamma} - E_0^{1-\Gamma}} \, \frac{v_{\mathrm{CR}} \, \epsilon_{\mathrm{CR}}}{E_0} \left(\frac{E}{E_0} \right)^{-\Gamma} \ , \tag{3.30}$$

where the differential solid angle $\mathrm{d}\Omega$ is introduced to account for the incident angles of approaching CR particles. ϵ_{CR} is the general CR energy density, and v_{CR} is the effective CR velocity, being governed by the dominant propagation mechanism of the CRs in their environment. In a fully advective system, v_{CR} would simply be the advective speed; for a diffusion-dominated scenario, this would be the diffusive speed (this can be defined by dimensional analysis as $D(E)/\ell_{\mathrm{diff}}$, where ℓ_{diff} is the characteristic length-scale of the system, and $D(E)$ is introduced as the energy-dependent diffusion coefficient). If free-

streaming, CRs would simply have an effective velocity of around c, the speed of light.

It is worth considering $\epsilon_{\rm CR}$ in the diffusion-dominated case more carefully at this point. This is because it can be used to offer a useful observational connection that validates the approach adopted thus far. The diffusion-dominated CR propagation scenario would be applicable to e.g. a galaxy where no outflow operates (as per the set-up described by the One-Zone model), in which CR energy density is roughly given by

$$\epsilon_{\rm CR,diff} = \frac{L_{\rm CR,eff}}{4\pi \ell_{\rm diff} \; D(E)} \; . \tag{3.31}$$

This may be used with equation 3.30 to provide a bridge between the (observable) γ-ray emission for a system and its CR energy density. While γ-ray detections of young protogalaxies in the distant Universe are not possible, there is sufficient data to assess the energy density model in the context of the Milky Way (which may be scaled from the model protogalactic case) using γ-ray measurements of the Galactic ridge region (GRR) between $l < |0.8°|$ in Galactic longitude, and $b < |0.3°|$ in Galactic latitude above 1-GeV. The GRR is a region of abundant gas clouds and star-formation, and is presumably useful to trace ongoing CR interactions (via the resulting γ-ray emission) and their underlying spectrum. This is because the dense clouds would act as a 'sponge' for CR absorption, and can be used to crudely estimate the level of CR energy density in the GRR region of the Milky Way if it is assumed that a substantial fraction of CRs injected by this this region, or passing through it, are absorbed (with ensuing γ-ray emission).[4]

In equation 3.31, the diffusion coefficient characterises the ability of a CR to propagate through a magnetic field, accounting for the scattering, ambient magnetic field strength and turbulence. It is therefore position, energy, and scale-dependent. The scale-dependence can be assessed by considering the CR energy and magnetic field using the gyro-radius (also called the Larmour

---

[4]In reality this may be a bold assumption. CRs may not be fully absorbed by the dense clouds in the GRR, which means that the bounds placed on the energy density by this method should be regarded as conservative.

radius, see equation 2.1) which specifies a characteristic scattering scale (the gyro-radius) for a charged particle in a magnetic field. A parametric form for the coefficient can be adopted in terms of the Larmor radius,

$$D(E, \mathbf{x}) = D_0 \left[\frac{r_L(E, \langle |B_{\mathrm{ISM}}| \rangle)|_{\mathbf{x}}}{r_{\mathrm{L},0}} \right]^{\theta_{\mathrm{Turb}}} , \qquad (3.32)$$

in which $\langle |B_{\mathrm{ISM}}| \rangle = B(\mathbf{x})$ denotes the characteristic mean value of the magnetic field at a location x. The normalisation $D_0 = 3.0 \times 10^{28}$ cm^2 s^{-1} is comparable to observations in the Milky Way ISM (see, e.g. Berezinskii et al. 1990; Aharonian et al. 2012; Gaggero 2012) and corresponds to the value of the diffusion coefficient for a 1 GeV CR proton in a $B_{\mathrm{ISM}} = 5\mu$G magnetic field (where $r_{\mathrm{L},0}$ is the proton gyro radius under such circumstances). The index θ_{Turb} is governed by the energy spectrum of the turbulence in the system, which is often modelled as a power law, i.e.

$$E(k) = E_0 \left(\frac{k}{k_0} \right)^{-q_{\mathrm{t}}} . \qquad (3.33)$$

Here, $E(k)$ is the energy of turbulence waves of wavenumber k, for normalisation E_0 at k_0, and the power-law index q_{t} relates to the index of the diffusion coefficient, $\theta_{\mathrm{Turb}} = 2 - q_{\mathrm{t}}$ (see chapter 2 of Gaggero 2012, for details). In the case of purely self-similar Kolmogorov-like turbulence, q_{t} takes a value of 5/3 (for further details on Kolmogorov turbulence and the derivation of this value, see Kolmogorov 1941a,b, 1962) so it follows that $\theta_{\mathrm{Turb}} = 1/3$. By comparison, smaller values would arise for these indices ($q_{\mathrm{t}} \approx 3/2$ and $\theta_{\mathrm{Turb}} \approx 1/2$) in the case of more compressible Kraichnan turbulence (for details, see Kraichnan 1959, 1965, 1971; Gaggero 2012). A value of $\theta_{\mathrm{Turb}} = 1/2$ is adopted hereafter for the following calculations (noting that it bears only a very weak dependency on the models and calculations presented in this thesis).

The underlying CR spectral energy densities in five different model specifications are shown in Fig. 3.2, including four protogalaxy models and a further model intended to represent the Milky Way (shown in grey). The four protogalaxy models adopt different SN event rates (corresponding to different levels of star-formation which would scale in proportion to SN activity)
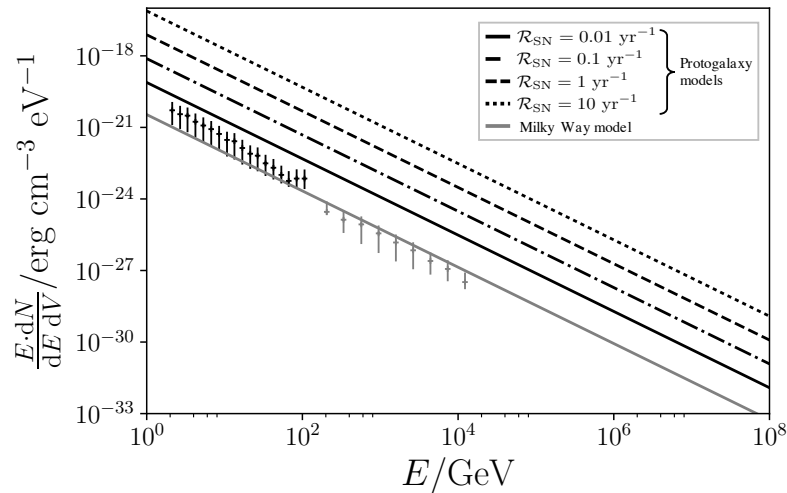
Fig. 3.2: CR spectral energy densities in protogalaxy systems with SN event rates of $\mathcal{R}_{SN} = 0.01, 0.1, 1.0$ and 10.0 yr^{-1} (the four black lines, solid, dashed-dotted, dashed and dotted respectively) compared to the estimated case for the Milky Way CRs (solid grey line). Inferred data points derived from γ-ray observations of the Galactic Ridge region (GRR), between $l < |0.8°|$ in (Galactic) longitude, and $b < |0.3°|$ in latitude above a GeV with *Fermi*-LAT and H.E.S.S. are plotted in black and grey respectively, and are consistent with the Milky Way model line. The data points are derived from γ-ray data provided in Aharonian et al. (2006) and Gaggero et al. (2017).

with $\mathcal{R}_{SN} = 0.01, 0.1, 1.0$ and 10.0 yr^{-1} represented respectively by the solid, dashed-dotted, dashed and dotted black lines. For reference, the adopted SN event rate for the Milky Way is taken to be 0.015 yr^{-1} (e.g. Dragicevich et al. 1999; Diehl et al. 2006; Hakobyan et al. 2011; Adams et al. 2013). Moreover, in calculating the line for the Milky Way, the SN characteristic energy is set to be lower than in the protogalaxies. Here, $E_{SN} \approx 10^{51}$ erg for the Milky Way, resulting from the Type 1a SN events that are more prevalent for the lower mass progenitor stars with longer lifetimes that drive SN activity in our own Galaxy. This compares with $E_{SN} = 10^{53}$ erg for the core collapse SNe relevant to starburst systems. In line with this, the characteristic energy loss fraction in these SN events to neutrinos, ξ, is taken to be 0.9 for the Milky Way model (as suggested by, e.g. Wright et al. 2017, which indicate neutrino losses are of a few percent in Type 1a SN energy), rather than the value of 0.01, as suited for protogalaxies and their core collapse events (e.g. Iwamoto and Kunugise 2006; Smartt 2009; Janka 2012). The size of the systems is also taken to be different in the calculations, with a diffusion length of $\ell_{diff} \approx 30$ kpc appropriate for the Milky Way, being comparable to its physical size (see, e.g. Xu et al. 2015),

and $\ell_{\mathrm{diff}} = 1$ kpc instead being adopted for the protogalaxy models.

The Milky Way model line in Fig. 3.2 is compared with GRR data derived from γ-ray observations with *Fermi*-LAT (the black points in Fig. 3.2, see Gaggero et al. 2017)[5] and H.E.S.S. (the higher energy grey points, from Aharonian et al. 2006, also shown in Gaggero et al. 2017), which demonstrate good consistency and validate the approach adopted (although uncertainties in the parameters used would presumably result in the uncertainty bound for the model lines in being substantially larger than the error bars of the plotted data points, so some care should be taken when comparing the two).[6]

3.2.2 Secondary Leptonic Cosmic Ray Injection

It was shown in process 3.2 that the charged pions resulting from CR interactions (e.g. via the pp and photo-pion processes) can decay to eventually yield energetic electrons. These electrons are generally considered CRs in their own right but, having been formed from the prior interaction of the CR proton, they are regarded as 'secondary' CRs. Electrons and positrons would be produced by hadronic interactions in roughly comparable proportion. However, for the most part, there would be little difference in their subsequent astrophysical impacts. Thus, both are referred to hereafter as electrons, without loss of generality.

These secondary CR electrons are expected to comprise around 60-80% of the CR electron and positron population of starburst galaxies above a GeV, being more important than the direct acceleration of these particles (see, e.g. Loeb and Waxman 2006; Lacki et al. 2011; Lacki and Beck 2013; Schober et al. 2015). This interpretation is consistent with more detailed studies of such star-

---

[5]This directly re-uses the results of the *Fermi* analysis undertaken in Gaggero et al. (2017), which uses the Fermi Science tools V10R0P4 with 422 weeks of PASS 8 data, and event class CLEAN.

[6]It may be argued that these data points could support a slightly steeper spectral index than the adopted index of -2.1 for the models: the separate analyses for the H.E.S.S. and the combined H.E.S.S./*Fermi*-LAT data in Gaggero et al. (2017) suggest best-fit power-law indices of -2.29 ± 0.27 and $-2.49^{+0.09}_{-0.08}$ respectively. However, this may be attributed to systematics, or arguments could be made about the GRR region exhibiting certain spectral differences to the CRs found in high-redshift protogalaxies, or that certain details are omitted in the crude conversion between γ-ray flux and CR spectral energy density used to produce the model lines in Fig. 3.2. The adopted model value is sufficient for its purposes in this work, and the exact choice of the index does not strongly impact any of the results presented in this thesis. Moreover, the tension between the data value and model spectral index is not sufficient to robustly justify a steeper spectral index which may not be any more or less physical for a high-redshift system.

forming regions in the nearby Universe (e.g. Paglione et al. 1996; Torres 2004; Domingo-Santamaría and Torres 2005; Persic et al. 2008; de Cea del Pozo et al. 2009; Rephaeli et al. 2010), where conditions would be favourable to encourage the hadronic CR interactions required to produce an abundance of CR electron secondaries. The injection spectrum of such secondaries can be determined from the exclusive inelastic cross-section of the predominant CR interaction(s), the interaction pathways and multiplicities, together with the energy spectrum of the primary CR particles, as presented in Kelner et al. (2006); Kamae et al. (2006). The dominating processes are photo-pion production in radiation-dominated systems (i.e. where $n_\gamma \gg n_\mathrm{H}$), or pp-pion production in matter-dominated systems ($n_\mathrm{H} \gg n_\gamma$). In general, the effective absorption experienced by a beam of particles is the sum of the contributions from all interaction channels of all target particle species. This may be expressed as the absorption coefficient. Without losing generality, it may be written as:

$$\alpha(E, r) = \sum_\mathrm{x} n_\mathrm{x}(r)\, \sigma_\mathrm{x}(E) \ , \tag{3.34}$$

where $n_\mathrm{x}(r)$ is the number density of target particles of species x, and $\sigma_\mathrm{x}(E)$ is their corresponding interaction cross-section evaluated at some energy E. In the case of CR proton absorption, this becomes

$$\alpha(E_\mathrm{p}, r) = \left(n_\mathrm{H}\hat{\sigma}_{\mathrm{p}\pi} + n_\gamma \hat{\sigma}_{\mathrm{p}\gamma} \right) |_{E_\mathrm{p}, r} \ , \tag{3.35}$$

in which the positional dependence (in the case of inhomogeneous radiation or density fields) is encoded in r, while the spectral energy dependence of the pp cross-section (although weak) is specified with the CR primary proton energy, E_p. Without losing generality, equation 3.34, when used with the (energy dependent) multiplicity of the immediate secondary interaction products and the CR primary energy spectrum, provides the foundation from which the CR secondary electron spectral injection rate can be determined, as

$$Q_\mathrm{e}(E_\mathrm{e}, r) = \mathrm{c} \int_{E_\mathrm{e}}^\infty \alpha(E_\mathrm{p}, r)\, F_\mathrm{e}\left(\frac{E_\mathrm{e}}{E_\mathrm{p}}, E_\mathrm{p} \right) \frac{\Phi_\mathrm{p}(E_\mathrm{p}, r)}{E_\mathrm{p}}\, \mathrm{d}E_\mathrm{p} \tag{3.36}$$

(Kelner et al. 2006; Kamae et al. 2006). This is the injection rate of electrons per unit volume per energy interval (between E_e and $E_e + dE_e$), which introduces the differential CR proton energy density as

$$\Phi_p(E_p, r) = \left. \frac{E_p \, dN_p}{dV \, dE_p} \right|_{E_p, r} .\qquad(3.37)$$

This is related to the differential number density of protons (number density per energy interval) by the relation $\Phi_p = E_p \cdot n_p$. In equation 3.36, the function F_e was introduced. This is defined as the number of electrons released per interaction per energy interval (i.e. the differential multiplicity of electron production). If $E_p > 100$ GeV, the study by Kelner et al. (2006) shows that this function may be parameterised as

$$F_e\left(x, \frac{E_e}{x}\right) = -\frac{\mathcal{B}_e \left[1 + \mathcal{K}_e \left(\ln x\right)^2\right]^3 \, \ln^5(x)}{x \left[1 + 0.3 x^{-\varkappa_e}\right]} ,\qquad(3.38)$$

where the substitution $x = E_e/E_p$ has been used for clarity. In this,

$$\mathcal{B}_e = \left[68.5 - 2.26 \ln \chi + 0.3 \left(\ln \chi\right)^2\right]^{-1} ,\qquad(3.39)$$

with $\chi = E_p/E_p^{th}$ retaining its earlier definition as the CR proton energy normalised to the pp interaction threshold energy,

$$\mathcal{K}_e = \frac{0.0172 \left(\ln \chi\right)^2 - 0.141 \ln \chi - 1.02}{0.3 + \left(\ln \chi - 5.88\right)^2} ,\qquad(3.40)$$

and

$$\varkappa_e = \left[0.00042 \left(\ln \chi\right)^2 + 0.063 \ln \chi - 0.28\right]^{-1/4} .\qquad(3.41)$$

Below 100 GeV, Kelner et al. (2006) show that this parametrisation of F_e is no longer suitable. Instead, they suggest the use of a delta-function (also see Aharonian and Atoyan 2000), in which the interaction process is broken-down into its underlying component mechanisms (i.e. the process of charged pion production, followed by the subsequent process of their decay). The pion production number for CR primaries in the range 1-100 GeV per interaction per energy interval (this time between $E_{\pi^\pm}$ and $E_{\pi^\pm} + dE_{\pi^\pm}$) may now be

modelled as

$$F_{\pi^\pm}\left(\frac{E_{\pi^\pm}}{E_{\rm p}}, E_{\rm p}\right) \approx \delta\left(E_{\pi^\pm} - K_{\pi^\pm}(E_{\rm kin})\right) \ , \tag{3.42}$$

which introduces a total kinetic energy term in a notation contraction, $E_{\rm kin} = E_{\rm p} - m_{\rm p}{\rm c}^2$. $K_{\pi^\pm}$ here is an efficiency term, which encodes the energy fraction passed from the CR proton to the resulting pions. Each type of pion $(\pi^\pm, \pi^0)$ forms in approximately equal numbers, with the branching ratios being approximately 1/3 for each in both the pp- and photo-production channels. These branching ratios are also not strongly dependent on energy (Aharonian and Atoyan 2000; Blattnig et al. 2000).

Some fraction of the energy of the CR primaries is passed on to neutrinos, which effectively stream away from the vicinity of the interaction and carry their energy away with them without any further astrophysical implications of consequence to this work. The energy retained by the pions is a fraction of around 0.6-0.7 of the CR primary (see Dermer and Menon 2009), although the subsequent calculations adopt a value of $K_{\pi^\pm} = 0.6$, i.e. at the conservative end of this range. Applying the delta-function approximated functional form (equation 3.42) to 3.36 yields the injection rate of charged pions per unit volume per energy interval as:

$$Q_{\pi^\pm}(E_{\pi^\pm}, r) = {\rm c} \int_{E_{\pi^\pm}}^{\infty} \alpha \ \delta\left(E_{\pi^\pm} - K_{\pi^\pm} E_{\rm kin}\right) \Phi_{\rm p} \ E_{\rm p}^{-1} \ {\rm d}E_{\rm p} \tag{3.43}$$

which makes use of the notation contractions $\alpha = \alpha(E_{\rm p}, r)$ and $\Phi_{\rm p} = \Phi_{\rm p}(E_{\rm p}, r)$, and other symbols retain their earlier definitions. The evaluated integral then follows simply as

$$Q_{\pi^\pm}(E_{\pi^\pm}, r) = \frac{\rm c}{K_{\pi^\pm}} \ \alpha\left(L, r\right) \ \Phi_{\rm p}\left(L, r\right) \tag{3.44}$$

(Aharonian and Atoyan 2000), where the energy term $L = m_{\rm p}{\rm c}^2 + \frac{E_{\pi^\pm}}{K_{\pi^\pm}}$ has been used.

The produced charged pions may decay to electrons (both e^+ and e^-). Since each of the charged pions, and the neutral pions are produced in equal proportions, the fraction of CR energy directed into lepton-producing channels

is around 2/3 (if assuming the primary CR energy is split uniformly between them). Of this, 73.5% ($\approx 3/4$) of the primary energy is transferred to neutrinos (e.g. Lipari 2003; Lacki and Beck 2013), with the remainder being passed to the produced electrons. This energy is presumably split roughly equally between the produced electrons, with their number being governed by the multiplicity, $\mathcal{M}$ – itself being energy-dependent.

Formalising this, the energy injection rate by pions of a specified energy may be written as $E_{\pi^\pm}^2 Q_{\pi^\pm}(E_{\pi^\pm})$. Conservation of energy means that this is equal to the energy provided by the corresponding decays of electrons such that $\mathcal{M}|_{E_\mathrm{p}} E_\mathrm{e}^2 Q_\mathrm{e}(E_\mathrm{e}) \approx K_\mathrm{e} E_{\pi^\pm}^2 Q_{\pi^\pm}(E_{\pi^\pm})$, where $K_\mathrm{e} = 0.265$ is the efficiency of energy transfer from pions to electrons. The multiplicity is usually determined empirically for a process, and in this case is parameterised using a fitting function of the form $c_1 + c_2 s^{c_3}$ as specified in Fiete Grosse-Oetringhaus and Reygers (2010) and Albini et al. (1976) with $c_1 = 0.0$, $c_2 = 3.102$ and $c_3 = 0.178$ (s is the GeV centre-of-mass interaction energy). These fitting parameters are based on experimental pion-production data from Slattery (1972); Whitmore (1974); Thome et al. (1977); Arnison et al. (1983); Breakstone et al. (1984); Alner et al. (1984, 1985); Ansorge et al. (1989); Albajar et al. (1990); Abe et al. (1990); Wang (1991); Rimondi (1993); Alexopoulos et al. (1998). This demonstrates that, at 1-GeV, the electron production multiplicity is 4, with the centre-of-mass energy being governed by E_p. When also accounting for the neutrino losses discussed in the paragraph above, this means that each secondary electron inherits around 3-5% of the energy of the CR proton primary initiating the interaction. The volumetric rate of injection of secondary electrons may thus be expressed as

$$
\begin{aligned}
Q_\mathrm{e}(E_\mathrm{e}, r) &= \frac{K_\mathrm{e}}{\mathcal{M}|_{E_\mathrm{p}}} \frac{E_{\pi^\pm}^2}{E_\mathrm{e}^2} \, Q_{\pi^\pm}(E_{\pi^\pm}, r) \\
&= \frac{K_\mathrm{e}}{\mathcal{M}|_{E_\mathrm{p}}} \frac{E_{\pi^\pm}^2}{E_\mathrm{e}^2} \, \frac{\mathrm{c}}{K_{\pi^\pm}} \, \alpha\left(L, r\right) \, \Phi_\mathrm{p}\left(L, r\right) \; .
\end{aligned}
\tag{3.45}
$$

Now, the pion energy is equal to the fraction of energy passed from the primary CR, being regulated by $K_{\pi^\pm}$ as the efficiency parameter. Thus, $E_{\pi^\pm} = K_{\pi^\pm} E_\mathrm{p}$,

which leads to the following expression

$$Q_{\mathrm{e}}(E_{\mathrm{e}}, r) = \frac{\bar{K}}{\mathcal{M}|_{E_{\mathrm{p}}}} \frac{E_{\mathrm{p}}^2}{E_{\mathrm{e}}^2} \, \mathrm{c} \, \alpha \, (L, r) \; \Phi_{\mathrm{p}} \, (L, r) \;\;, \qquad (3.46)$$

where $\bar{K} = K_{\mathrm{e}} K_{\pi^{\pm}}$ is the effective overall energy efficiency parameter for the production of electrons from CR protons, accounting for both the efficiencies in the pion production and in the pion decay steps. For consistency with earlier notation, i.e. in terms of the electron and proton Lorentz factors, equation 3.46 may also be written as

$$Q_{\mathrm{e}}(\gamma_{\mathrm{e}}, r) = \frac{\bar{K}}{\mathcal{M}|_{\gamma_{\mathrm{p}}}} \left(\frac{\gamma_{\mathrm{p}}}{\gamma_{\mathrm{e}}} \right)^2 \left(\frac{m_{\mathrm{p}}}{m_{\mathrm{e}}} \right)^2 \, \mathrm{c} \, \alpha \, (L, r) \; \Phi_{\mathrm{p}} \, (L, r) \;\;. \qquad (3.47)$$

3.3   Secondary Cosmic Ray Interactions

While CR proton primaries are predominantly absorbed, energetic electrons are instead far more susceptible to continuous cooling processes. These include contributions from radiative emission (e.g. inverse Compton, synchrotron), pair production processes, or by free-free and Coulomb interactions (among other processes). As with protons, electrons generally are confined, or they lose their energy too quickly for adiabatic cosmological losses to be relevant. However, electrons also cool substantially faster than protons in most astrophysical environments – particularly when governed by a radiative process (e.g. inverse Compton or synchrotron emission). This causes most CR electrons to lose their energy in the vicinity of their injection location, rather than over long distances throughout the extent of their host galaxy.

3.3.1   Energy Loss Processes

The free-free cooling rate was previously introduced in chapter 1 (see equation 1.2), but its action is of little importance at the (MeV and above) energies of interest here. In general, collisional excitation/de-excitation and electromagnetic scattering effects are less important at these higher energies than they are at lower, keV energies.

Inverse-Compton and Synchrotron

Charged particles may cool radiatively by inverse Compton scattering and synchrotron emission. The cooling rate $\dot{E}_e = -dE_e/dt$ due to inverse Compton and synchrotron processes may be expressed in a similar form, i.e.

$$b_{\mathrm{IC,synch}}(\gamma_e) = \dot{E}_e^{\mathrm{rad,B}} = -\frac{4}{3}\sigma_{\mathrm{T}}c\gamma_e^2 U_{\mathrm{rad,B}} \tag{3.48}$$

where $U_{\mathrm{rad,B}} = \{U_{\mathrm{rad}}, U_{\mathrm{B}}\}$ is either the energy density in the radiation field, U_{rad} (relevant to inverse Compton scattering) or in the magnetic field U_{B} (relevant to synchrotron cooling).

It should be noted that radiative processes are relevant to any charged particle, including CR protons as well as secondary electrons. However, the effective cross-section for this process, the Thomson cross-section (which governs the rate at which it occurs for a given particle), is actually inversely dependent on the square of the particle mass[7]

$$\sigma_{\mathrm{T}} = \frac{8\pi}{3}\left(\frac{|q|^4}{m^2 c^4}\right) , \tag{3.49}$$

where q is the particle charge in units of electron charge. Moreover, equation 3.48 shows a further inverse-square dependency on mass via $\gamma^2 = E^2/m^2 c^4$. This means that CR protons lose their energy much less rapidly by these mechanisms compared to electron, by a factor of $(m_e/m_p)^4$ (i.e. around 12 orders of magnitude).

The appropriate cross-section for inverse Compton scattering at relativistic energies (yielding a noticeable deviation in cooling lengths above around 1 TeV – see Fig 3.3) is described by the Klein-Nishina (KN) formula (Klein and Nishina 1929). For the purposes of the present analysis, however, impacts from those CR electrons in the Thomson limit tend to dominate, and the KN regime effects can be safely neglected in electron cooling calculations.

---

[7]The value usually quoted for σ_{T} is that for electron scattering.

Triplet Pair-Production

At energies above a TeV, triplet pair-production (TPP) can provide some contribution to the cooling of electrons. This process is practically identical to the Bethe-Heitler pair-production interaction experienced by energetic protons (see section 3.1.2), and proceeds as

$$\mathrm{e} + \gamma \rightarrow \mathrm{e}' + l^+ + l^- \ , \tag{3.50}$$

(e.g. Schlickeiser 2002) with e and e$'$ being the CR electrons before and after the interaction, while l^+ and l^- are positively and negatively charged leptons produced in the process, respectively. These produced leptons would predominantly be electrons.

For $\epsilon_\mathrm{r} \geq 30$, an approximation for the cross-section (correct to within 0.1%) can be found in a similar manner to the photo-pair interaction cross-section considered previously (equation 3.13). This gives

$$\hat{\sigma}_{\mathrm{TPP}}(\epsilon_\mathrm{r}) \approx \left\{ \frac{7}{6\pi} \alpha_\mathrm{f} \left(\psi - \frac{109}{42} \right) + \left[24.3 - 9.57\psi \right. \right. \\ \left. \left. + 3.36\psi^2 - 1.16\psi^3 \right] \left(\frac{10^{-3}}{\epsilon_\mathrm{r}} \right) \right\} \sigma_\mathrm{T} \tag{3.51}$$

(Borsellino 1947; Joseph and Rohrlich 1958; Haug 1981), where $\psi = \ln(2\epsilon_\mathrm{r})$. Over the energies of interest (i.e. imposing $\epsilon_\mathrm{r} \geq 60$), the approximation adopted for the photo-pair interaction may also be applied here, i.e.

$$\hat{\sigma}_{\mathrm{TPP}}(\epsilon_\mathrm{r}) \approx \hat{\sigma}_{\gamma\mathrm{e}}(\epsilon_\mathrm{r}) \approx \left\{ \frac{7}{6\pi} \alpha_\mathrm{f} \ln \left[\frac{\epsilon_\mathrm{r}}{k_{\gamma\mathrm{e}}} \right] \right\} \sigma_\mathrm{T} \tag{3.52}$$

with $k_{\gamma\mathrm{e}} = 6.7$ again giving a suitable fit. The cooling rate then follows as

$$b_{\mathrm{TPP}}(\gamma_\mathrm{e}) \approx \frac{112}{9} \frac{c^2 m_\mathrm{e}^2 \alpha_\mathrm{f} \sigma_\mathrm{T} \mathcal{F}_{\gamma\mathrm{e}}}{m_\mathrm{p} \lambda_\mathrm{C}^3 \gamma_\mathrm{e}^2 u^{5/3}} \ , \tag{3.53}$$

(from $b_{\mathrm{TPP}}(\gamma_\mathrm{e}) \approx m_\mathrm{e} c^2 \gamma_\mathrm{e} t_{\gamma\mathrm{e}}^{-1}$), where the same function $\mathcal{F}_{\gamma\mathrm{e}}$ from eq. 3.17 is adopted due to the equivalences of the cross-sections, and $u = m_\mathrm{e} c^2 / \gamma_\mathrm{e} k_\mathrm{B} T$.

Adiabatic Losses

While not strictly a microphysical process, the adiabatic losses experienced by both CR primaries and secondaries should be noted. It was mentioned earlier (in section 3.1.3) that adiabatic losses due to free-streaming protons escaping into the cosmic flow would give an upper limit to their propagation distance. More locally, in expanding flows (e.g. for outflows or jets with substantial opening angles and high flow velocities), adiabatic losses may become severe. In such cases, they would be quantified by

$$b_{ad} = \frac{2}{3} \frac{1}{h^2} \frac{\partial}{\partial h} \left[h^2 v(h) \right] E_e \ , \tag{3.54}$$

(Longair 2011), which applies equally to CR protons as it does electrons.

3.3.2 Path Lengths

The energy loss path length for a CR electron of energy γ_e when cooling at a rate b follows from equation 3.19, being given by

$$r_{int} \equiv c \, \beta \, t_{int} \approx \frac{\gamma_e}{b(\gamma_e)} \, c \ , \tag{3.55}$$

for which the earlier definitions are retained, i.e. β is the velocity of the particle normalised to the speed of light (at high energies $\beta \approx 1$) and t_{int} is the timescale of an interaction. The path lengths associated with the cooling processes experienced by CR (secondary) electrons as detailed above when propagating within an interstellar protogalactic environment (with density and radiation fields as specified in chapter 1, at $z = 7$, and with an ambient magnetic field strength of 5 μG[8]), are plotted in Fig. 3.3. Here, a lower energy range, starting at 10^7 eV, is considered than was adopted for CR protons. This is to account for the lower energy at which the secondary electrons may be injected into their environment. For the secondary CR electrons, losses are evidently dominated by Coulomb losses and inverse Compton losses with the CMB (additionally stellar photons may contribute to inverse Compton effect

---

[8]The magnetic field itself is not assumed to perturb or influence the propagation of the CR particles (an idealistic scenario such that the synchrotron cooling rate can be reasonably compared to other processes).
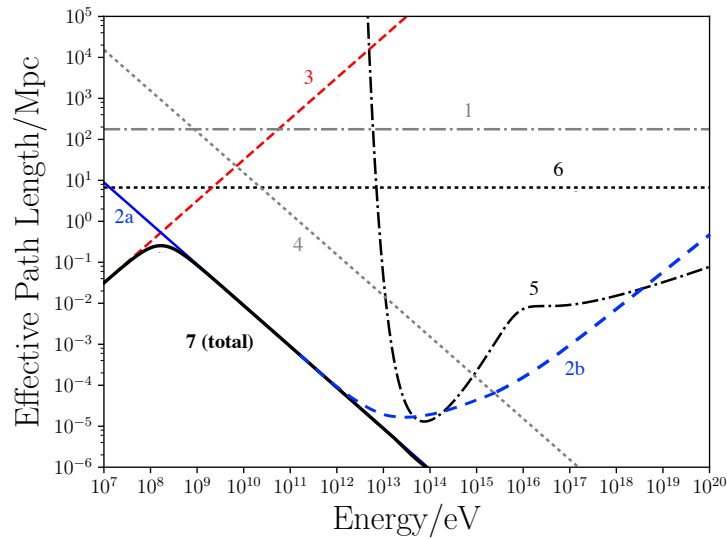
Fig. 3.3: Secondary CR electron energy loss (cooling) path lengths in the same environment as used to calculated the lines in Fig. 3.1. As labelled, the lines represent path lengths for (1) adiabatic particle losses due to cosmic expansion; (2) inverse Compton (radiative) cooling due to the CMB for which (2a) is the estimated path length in the Thomson limit, and (2b) is the estimated path length if accounting for the relativistic transition to Klein-Nishina behaviour at high energies; (3) Coulomb losses; (4) Synchrotron (radiative) cooling, under the assumption of a uniform 5 μG magnetic field; (5) triplet Pair-Production (eγ, e$^{\pm}$); (6) Free-free (Bremsstrahlung) losses; (7) Total, accounting for all processes together.

in extremely active star-forming systems – see chapters 4 and 5 for details), with other cooling mechanisms having a comparatively negligible effect.

3.3.3 Cosmological Evolution

There is some dependency of the relative cooling/interaction rates on the underlying cosmological evolution. Fig. 3.4 shows the total CR electron losses in the same model protogalaxy environment as used previously (in Fig. 3.1 and Fig. 3.3) at redshifts of $z = 0, 2, 4, 6, 8$ and 10 (as indicated by the legend). This dependency on cosmological redshift stems from the electron cooling losses in being strongly influenced by inverse Compton cooling off CMB photons at high-redshift. This dominates over Coulomb cooling at lower energies as redshift increases, with the turn-over (the peak in the cooling curve) occurring above 10 GeV at $z = 0$, falling to 0.1 GeV by $z = 10$. Such behaviour is consistent with the increasing photon number density of the CMB at higher redshifts, and indicates a fundamental shift in the balance of energy transfer processes in such environments over redshift. This behaviour is different to that experienced by the primary CR protons. Proton losses are instead
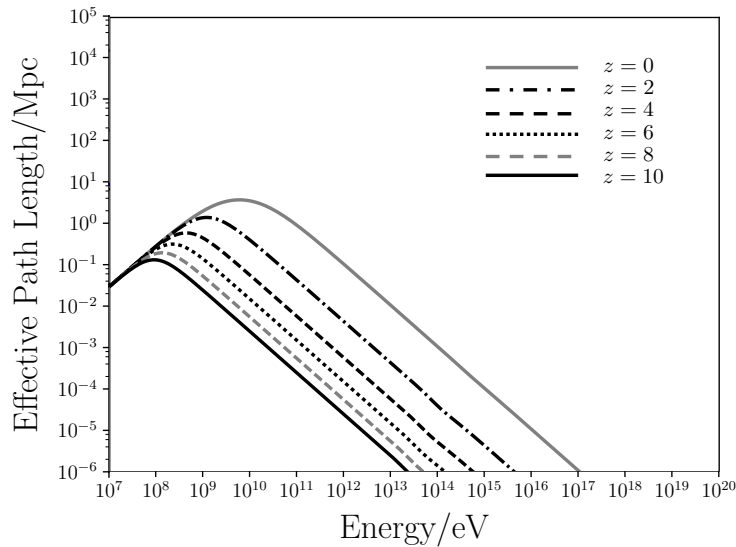
Fig. 3.4: Combined energy-loss path lengths for interacting CR electrons accounting for all processes plotted in Fig. 3.3, as determined at redshifts from $z = 0$ to 10.

strongly dominated by the pp-pion production channel, so their interactions and cooling effectively become decoupled from the evolution of the CMB.

3.4 Cosmic Ray Thermalisation and Heating

CR proton thermalisation does not arise instantaneously after a hadronic interaction. Instead, it operates through the channels afforded by the secondary particles (the electrons). These determine the fraction of energy which thermalises, and the mechanism by which it may do so. Indeed, it has already been shown that a large fraction of the initial CR proton energy does not actually thermalise at all – instead, it is lost to neutrinos and γ-rays which may freely stream away from the point of initial interaction without substantial energy release to the medium. The remaining energy fraction that is passed to the electron secondaries thermalises predominantly via two processes: (1) by Coulomb scattering with an ionised or semi-ionised medium, hereafter referred to as *Direct Coulomb heating* (DC heating); or (2) by the inverse Compton X-rays emitted by the energetic electrons which can then go on to scatter and heat an ionised or semi-ionised medium, hereafter referred to as *Indirect Inverse Compton X-ray heating* (IX heating). Clearly the microphysics of these two processes are very different and, astrophysically, their effects also manifest themselves in different ways. While DC thermalisation occurs rela-

tively locally (with charged energetic electrons being effectively contained by their ambient magnetic fields, and their propagation being governed by diffusion), IX thermalisation deposits energy over much larger scales, operating over broad regions and extending far away from the actual location of the X-ray emission.

3.4.1 Direct Coulomb Heating

After undergoing a pion-producing interaction, a 1-GeV CR primary proton typically yields electron secondaries of energies around 3-5% of its own (see section 3.2.2), corresponding to a characteristic secondary energy of around $E_e \approx 40$ MeV. In a 10 cm^{-3} ionised ISM (being the conditions adopted for the baseline protogalaxy model), these electrons thermalise by Coulomb scattering, on a timescale of

$$\tau_{\text{th}} \approx 0.39 \left(\frac{E_e}{40 \text{ MeV}} \right) \left(\frac{n_{\text{H}}}{10 \text{ cm}^{-3}} \right)^{-1} \text{ Myr }. \tag{3.56}$$

In a free-streaming scenario, in which CRs are able to propagate at close to the speed of light, this thermalisation timescale would correspond to a distance of hundreds of kpc, being considerably larger than a protogalactic host (of size order 1 kpc). However, the propagation of the charged CR protons and electrons in a magnetised protogalactic ISM is actually governed by diffusion (cf. section 3.2.1, and also later in chapter 4). For electrons, the associated diffusion coefficient would take the same form as that for protons (equation 3.32). This is because the propagation of the charged particles by magnetic scattering/diffusion is determined by only their energy and the magnitude of their effective charge.[9] The thermalisation length, ℓ_{th} should therefore be considered in terms of the diffusion length which can be achieved by a 40-MeV CR secondary electron over its thermalisation timescale τ_{th}, i.e.

$$\ell_{\text{th}} \approx \sqrt{4 \, D \, \tau_{\text{th}}}$$

$$\approx 0.17 \left(\frac{E_e}{40 \text{ MeV}} \right)^{3/4} \left(\frac{n_{\text{H}}}{10 \text{ cm}^{-3}} \right)^{-1/2} \text{ kpc }, \tag{3.57}$$

---

[9]At lower energies, a mass dependence would also emerge. But when at tens of MeV, the diffusion coefficient (via the gyro-radius of the electrons) remains mass-independent – see e.g. Kulsrud (2005).
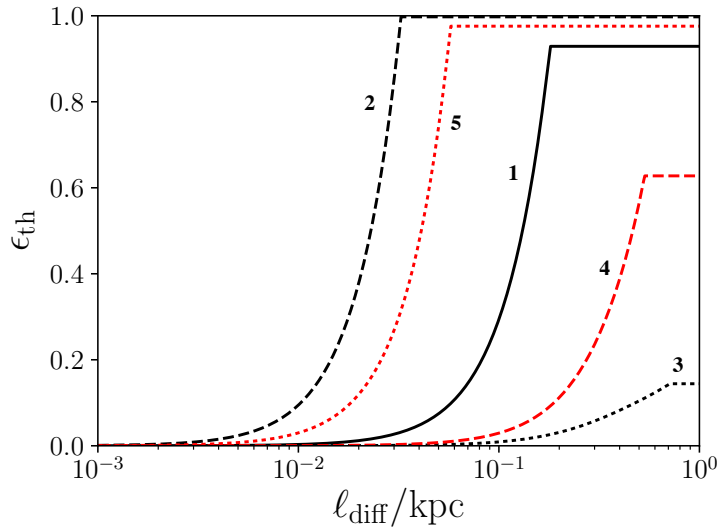
Fig. 3.5: The fraction of a CR secondary electron beam thermalised over distance from its source, under diffusive propagation. A reference calculation for $E_e = 40$ MeV electrons traversing an ionised medium of density $n_H = 10.0$ cm^{-3} is shown by the solid black line (1). The case for $E_e = 4$ MeV (line 2) and 400 MeV (line 3) in the same medium are shown by the dashed and dotted black lines respectively, while red lines show the case for 40 MeV electrons with different media densities, of $n_H = 1.0$ cm^{-3} (dashed - line 4) and 100.0 cm^{-3} (dotted - line 5). Line plateaus indicate incomplete beam thermalisation, with some energy losses instead being due to free-free and radiative processes (i.e. processes which do not directly lead to thermalisation by the channel considered by ϵ_{th} here). Where relevant, electron cooling rates have been calculated according to a stellar radiation energy density corresponding to the presence of a stellar population with $\mathcal{R}_{SN} = 0.1$ yr^{-1} (this bears some influence on radiative losses, and hence ϵ_{th} efficiency).

which is around an order of magnitude smaller than the characteristic size of the host protogalaxy, and even allows (relatively) local CR thermalisation to be argued.

The thermalisation fraction of a beam of secondary CR electrons ϵ_{th} is plotted in Fig. 3.5 over their diffusion propagation distance, ℓ_{diff}. The figure explores the impact that the energy of the electrons and the density of an ambient (ionised) medium have on Coulomb thermalisation, where ϵ_{th} is calculated by comparing the rate of energy transfer by Coulomb scattering compared to the total electron loss rate by all processes. The reference case is shown by the solid black line. This represents the thermalisation efficiency for CR secondary electrons of energy $E_e = 40$ MeV propagating in a protogalaxy model with an ISM density $n_H = 10$ cm^{-3}. Variations of the energy parameter are shown by the dashed and dotted black lines, for electron energies of $E_e = 4$ MeV and 400 MeV respectively, while variations of the ambient density are shown by the dashed and dotted red lines, respectively for $n_H = 1.0$ cm^{-3} and 100.0 cm^{-3}.

This shows that higher energy CRs typically thermalise less efficiently than their lower-energy counterparts (with ϵ_{th} reaching less than 20% for $E_{\mathrm{e}} = 400$ MeV) and that they do so over longer distances. Conversely, it is evident that CRs propagating though higher density environments thermalise more efficiently and more quickly – as indicated by the red dotted line, where a 40 MeV electron in a medium just 10 times more dense than the reference case is able to thermalise within just a few tens of pc. It is of interest to note that incomplete thermalisation of the beam (as shown by a plateau in the plotted lines) results from some of the electron energy being lost to free-free and radiative processes, and these do not directly contribute to the DC thermalisation process. Some of such radiative losses actually power the IX process, but this is not accounted for by ϵ_{th}.

3.4.2 Inverse-Compton X-ray Heating

Energetic MeV electrons can up-scatter lower-energy ambient photons (e.g. those contributed by the CMB, or by stellar radiation) to keV energies, creating a diffuse, non-thermal X-ray glow (Lacki and Beck 2013; Schober et al. 2015). This X-ray emission can then proceed to heat the environment and its surroundings by scattering off ambient free electrons. At high-redshift, this process is particularly effective due to the increased number density of CMB photons. This may also be the case in and around intensely star-forming high-redshift environments, particularly when starburst activity is concentrated into clumps. This could produce an energy density in stellar radiation fields that is sufficiently high to be comparable, or even exceed, the contribution from the CMB.

The total power available in X-rays to participate in the IX heating process may be estimated by use of energy conservation, as follows. The inverse Compton loss rate of a single electron with energy $E_{\mathrm{e}} = \gamma_{\mathrm{e}}\, m_{\mathrm{e}} c^2$ in a radiation field of energy density U_{rad} is given by equation 3.48, which may also be written as

$$\frac{\mathrm{d}E_{\mathrm{e}}}{\mathrm{d}t} = -\frac{4}{3}\sigma_{\mathrm{T}} c \left(\frac{E_{\mathrm{e}}}{m_{\mathrm{e}} c^2}\right)^2 U_{\mathrm{rad}} \;, \tag{3.58}$$

(Rybicki and Lightman 1979) where symbols retain their earlier definitions.

This corresponds to the energy transfer rate from a single CR electron, of energy E_e, to ambient (lower-energy) photons. It thus sets the inverse Compton power due to a single electron as

$$P_{IC} = -\frac{dE_e}{dt} \ . \tag{3.59}$$

The characteristic energy E_γ to which low-energy photons in the radiation field can be up-scattered by the high-energy electrons (of characteristic energy $\langle E_e \rangle$) is given by

$$E_\gamma \approx 2.82 \, \frac{\Theta}{m_e \, c^2} \, \langle E_e \rangle^2 \ , \tag{3.60}$$

where $\langle E_e \rangle$ may be estimated from the peak of the local electron spectrum, and Θ retains its earlier definition from section 1.3.4 as the dimensionless temperature of the radiation field. This would suggest a characteristic emitted up-scattered photon energy of around 10 to 100 keV, i.e. in the X-ray band, for a 40-MeV CR secondary electron. While this falls just into the relativistic regime, these keV energies do not actually cause a substantial deviation from the Thomson scattering cross-section when applied to the Klein-Nishina formula, and σ_T may simply be adopted to approximate the scattering cross-section to within 10%, i.e. $|\sigma_{KN} - \sigma_T|/\sigma_{KN} < 0.1$. The resulting heating power of these inverse Compton X-rays is effectively governed solely by their absorption rate in their ambient medium, i.e. following $\mathcal{I}_{IX} \, n_e \, \sigma_T$, for $\mathcal{I}_{IX}$ as the intensity of an irradiating X-ray beam emitted by the inverse Compton process.[10] Further details and application of this IX heating process together with the DC mechanism is provided in chapter 5.

---

[10]While there would also be an attenuation term here, the attenuation factor through a typical ISM setting is small. Over larger distances, this attenuation is taken into account.

Chapter 3 summary: *The essential particle interactions are discussed in this chapter, outlining the mechanisms by which energetic CRs can interact and deposit their energy in astrophysical interstellar environments. Primary CRs, predominantly comprised of protons, engage with $p\gamma$ (including photo-pion production and photo-pair production) and pp pion-production interactions above a threshold energy of 0.28 GeV, but the pp channel is shown to dominate in a typical protogalactic environment over most energies of interest. These hadronic interactions release electrons and pions into their environment, with the pions rapidly decaying into leptons to provide a secondary CR component. The secondaries can interact with their environment via radiative losses, triplet pair-production, Coulomb interactions and free-free losses and are able the mediate the thermalisation rate and efficiency of the CRs into their ambient astrophysical media through the Coulomb and radiative loss channels. Coulomb (Rutherford) scattering enables a direct thermalisation of CR secondary electrons, and is effective at depositing energy into denser, ionised plasmas (a process introduced as 'Direct Coulomb', or DC heating). By contrast, at higher energies, radiative inverse-Compton losses dominate electron cooling, creating an X-ray glow when the host galaxy is located at high-redshift. These X-rays can then deposit energy over larger scales (an indirect process referred to as 'Inverse-Compton X-ray', or IX heating) and can act to facilitate feedback beyond the confines of the host ISM.*

Chapter 4

Propagation of Energetic Charged Particles in Starburst and High-Redshift Protogalaxies

Propagation of relativistic charged CR particles may be free-streaming, diffusive or advective. The latter two of these are typical in magnetised interstellar environments. In all cases, the true speed of the particles is close to the speed of light, c. However, when scattered and entangled in ambient turbulent magnetic fields, propagating CRs are continually deflected. This reduces their apparent macroscopic propagation speed. Variation of the particle orientations arise due to their gyro-motion in magnetic field domains (these domains are of small length-scales compared to the size of the host system, so many such scatterings would occur as a CR propagates). An individual CR 'sees' these gyro-perturbations in the same way that it would experience discrete classical stochastic scattering events. This leads to the randomisation of its propagation direction (and sometimes also its energy/momentum) which, macroscopically, leads to a diffusive behaviour. If the magnetised medium through which CRs

propagate moves with a bulk flow that is faster than the effective CR diffusive speed, it follows that the overall particle propagation would be dominated by advection in this flow.

Momentum (energy) diffusion of CRs is usually driven by radiative and/or scattering processes, as was outlined in chapter 3. While this is technically true for both the primary CR hadronic particles as well as their leptonic secondaries, it was also shown that hadrons are very inefficient emitters, thus their energy loss/diffusion timescales (and hence their diffusion through momentum space) are substantially longer compared to those of other relevant processes (physical diffusion, advection or absorption) in typical interstellar conditions (Ko 2017). As such, the energy loss of a CR proton population in a galaxy is presumably dominated by particle attenuation rather than by momentum-space diffusion, while the opposite is true for electrons. CR propagation in momentum and physical space can be modelled using the transport equation, and this can be applied to protogalactic environments (including the One-Zone and Two-Zone models introduced in chapter 2).

4.1 The Transport Equation

In general, the evolution of an ensemble of particles in physical and momentum space can be modelled using the transport equation, which is written as

$$\frac{\partial n_{\mathrm{CR}}}{\partial t} = \nabla \cdot [D(E, \mathbf{x})\nabla n] - \nabla \cdot [\mathbf{v} n_{\mathrm{CR}}] + \frac{\partial}{\partial E} [b(E, \mathbf{x}) n_{\mathrm{CR}}] + Q(E, \mathbf{x}) - S(E, \mathbf{x}) \, ,$$

(4.1)

where $n_{\mathrm{CR}} = n_{\mathrm{CR}}(E, \mathbf{x})$ is the local (differential) number density of CRs per energy interval between E and $E + \mathrm{d}E$, defined as

$$n_{\mathrm{CR}}(E, \mathbf{x}) = \frac{\mathrm{d}N_{\mathrm{CR}}}{\mathrm{d}V \, \mathrm{d}E}\bigg|_{E, \mathbf{x}}$$

(4.2)

in which N_{CR} as the number of CR particles in some volume V, as positioned at some location $\mathbf{x}$. The first term, $\nabla \cdot [D(E, \mathbf{x})\nabla n_{\mathrm{CR}}]$, accounts for the spatial diffusion of particles as quantified by the diffusion coefficient, $D(E, \mathbf{x})$. The second term, $\nabla \cdot [\mathbf{v} n_{\mathrm{CR}}]$, represents the impact of particle advection, where $\mathbf{v}$ is

the velocity of any bulk flow which locally influences the transport of CRs. Q represents the local (volumetric) CR injection rate, i.e. the CR 'source' term, while S is their absorption (the CR 'sink' term). Q and S are both dependent on the CR energy and position, and the particle species. Moreover, $b(E, \mathbf{x})$ is dependent on particle species together with its energy and location, and retains its earlier definition as the (total) cooling function,

$$b(E, \mathbf{x}) = -\frac{\mathrm{d}E}{\mathrm{d}t}\bigg|_{\mathbf{x}} , \tag{4.3}$$

which represents continuous energy loss processes for the CR particle (as appropriate for the species in question). Given that, for CR protons, cooling processes are effectively negligible while, for CR electrons, absorption processes are negligible, the transport equation reduces to different forms in each case. For example, in the simple One-Zone model (in which the effects of advection may be ignored), spherical symmetry may be adopted in which r denotes a radial geometry from the centre of a CR distribution, and equation 4.1 may be rewritten for protons in the form

$$\frac{\partial n_{\mathrm{CR,p}}}{\partial t} = \frac{1}{r^2}\frac{\partial}{\partial r}\left[D(E_{\mathrm{p}}, r)\, r^2\frac{\partial n_{\mathrm{CR,p}}}{\partial r}\right] + Q_{\mathrm{CR,p}}(E_{\mathrm{p}}, r, t) - S_{\mathrm{CR,p}}(E_{\mathrm{p}}, r, t) , \tag{4.4}$$

where $Q_{\mathrm{CR,p}}$ is the proton source (injection) term and $S_{\mathrm{CR,p}}$ is the proton sink (absorption) term. $D(E_{\mathrm{p}}, r)$ is the associated proton diffusion coefficient, which is modelled based on the magnetic field strength and structure (see equation 3.32). For electrons, equation 4.1 instead reduces to the form

$$\frac{\partial n_{\mathrm{CR,e}}}{\partial t} = \frac{1}{r^2}\frac{\partial}{\partial r}\left[D(E_{\mathrm{e}}, r)\, r^2\frac{\partial n_{\mathrm{CR,e}}}{\partial r}\right] + \frac{\partial}{\partial E_{\mathrm{e}}}\left[b(E, r)n_{\mathrm{CR,e}}\right] + Q_{\mathrm{CR,e}}(E_{\mathrm{e}}, r, t) , \tag{4.5}$$

where the source term is again present, together with the further inclusion of the cooling term $b(E_{\mathrm{e}}, r)$, but the sink term is no longer required. The solutions of these two equations are explored in sections 4.2 and 4.3 respectively.

4.2 Propagation of Energetic Protons

CR propagation can be considered in the context of the previously introduced One-Zone model (section 2.1.1) or Two-Zone model (section 2.1.2). In the former case, CRs propagate within a spherically-symmetric interstellar medium in a manner best described by diffusion; in the latter case, a bi-conical galactic outflow operates such that both diffusive and advective propagation of CRs must be considered – in the outflow cones (Zone A), the bulk flow facilitates predominantly advective CR propagation, while the remainder of the host system (Zone B) is dominated by diffusion.

4.2.1 One-Zone Propagation

The sink term in equation 4.4 is dominated by absorptions due to pp-pion production over the energies of interest, as was shown in chapter 3. The CR proton absorption rate due to this process is given by the product of the effective irradiating CR power and the interaction surface area of the target field. The irradiating CR power may be regarded as the equivalent beam intensity, if the CRs were freely streaming in a uniform direction. This is given by c $n_{\mathrm{CR,p}}$, being the product of their effective number density at a point, and their true microscopic propagation speed, c. The inverse interaction path length is defined as the number density of interstellar protons multiplied by the total exclusive pp interaction cross-section, i.e $\hat{\sigma}_{\mathrm{p}\pi} \, n_{\mathrm{H}}$, and it follows that the volumetric CR absorption rate is then given as c $n_{\mathrm{CR,p}}(E_{\mathrm{p}}, r) \, \hat{\sigma}_{\mathrm{p}\pi}(E_{\mathrm{p}}) \, n_{\mathrm{H}}(r)$.

The source term $Q_{\mathrm{CR,p}}$ in equation 4.4 is the local volumetric injection rate of protons. The term $\mathcal{I}_{\mathrm{p}}$ was first introduced in equation 2.4. However, this gives the volumetric energy injection rate of CR protons at a specific proton energy E_{p}. In general, this is related to the (differential) injected rate of CRs per energy interval between E_{p} and $E_{\mathrm{p}} + \mathrm{d}E_{\mathrm{p}}$ by

$$Q_{\mathrm{CR,p}}(E_{\mathrm{p}}, r) = \left. \frac{\partial \mathcal{I}_{\mathrm{p}}}{\partial E_{\mathrm{p}}} \right|_{E_{\mathrm{p}}, r} , \tag{4.6}$$

however it is convenient to consider the injection at a specific energy E_{p}, and

restate equation 4.4 in such terms, as

$$\frac{\partial n_{\mathrm{CR,p}}}{\partial t} = \frac{1}{r^2} \frac{\partial}{\partial r} \left[r^2\, D(E_{\mathrm{p}}, r) \frac{\partial n_{\mathrm{CR,p}}}{\partial r} \right] + \mathcal{I}_{\mathrm{p}}(E_{\mathrm{p}}, r) - \mathrm{c}\, n_{\mathrm{CR,p}}\, \hat{\sigma}_{\mathrm{p\pi}}\, n_{\mathrm{H}} \ . \quad (4.7)$$

Now, consider a reformulation of equation 4.7 to an initial value problem (IVP), describing a single proton injection event in a discrete source region,

$$\frac{\partial n_{\mathrm{CR,p}}}{\partial t} = \frac{1}{r'^2} \frac{\partial}{\partial r'} \left[r'^2\, D(E_{\mathrm{p}}, r') \frac{\partial n_{\mathrm{CR,p}}}{\partial r'} \right] - \mathrm{c}\, n_{\mathrm{CR,p}}\, \hat{\sigma}_{\mathrm{p\pi}}\, n_{\mathrm{H}} \ , \quad (4.8)$$

where the new coordinate variable r' has been introduced as a radial distance between an injection point at position $\mathbf{r}_i$ and some general position $\mathbf{r}$ such that $r' = |\mathbf{r} - \mathbf{r}_i|$. Equation 4.8 is an inhomogeneous partial differential equation (PDE), but it can be readily converted to a homogeneous form by use of the substitution

$$\mathcal{Y} = n_{\mathrm{CR,p}} \exp \left\{ \int_0^t \mathrm{c}\, \mathrm{d}t'\, \hat{\sigma}_{\mathrm{p\pi}}\, n_{\mathrm{H}} \right\} \ . \quad (4.9)$$

Here, it should be noted that the integration element $\mathrm{c}\, \mathrm{d}t' = \mathrm{d}s'$ represents a displacement along the true path *actually traversed* by a CR proton, being that along which a proton beam would be attenuated. Equation 4.9 assumes a locally uniform medium density, n_{H}. Such an assumption is justified because CR proton propagation is most important to the present calculations in the inner regions of the host galaxy's ISM, where there would only be small variations in the radial density profile. CR propagation in the peripheral regions of a galaxy is instead governed by the complicated structures arising in the magnetic field as it connects to those in the CGM and beyond. Research into these interfacing magnetic fields is very uncertain, and the development of a robust CR propagation model in this region lies beyond the scope of the present work, instead being worthy of a future dedicated investigation.

The relation between the proton path coordinate s' and the spatial coordinate r' varies with position and CR energy, but may be locally defined without losing generality as $\mathrm{d}s' = \varsigma(E_{\mathrm{p}}, r')\, \mathrm{d}r'$, where $\varsigma(E_{\mathrm{p}}, r')$ can be expressed as the

ratio of the free-streaming to diffusive path lengths of CR protons,

$$\varsigma(E_{\rm p}, r') = \frac{r_{\rm p\pi}}{\ell_{\rm diff}} = \sqrt{\frac{c}{4 \, D(E_{\rm p}, r') \, n_{\rm H} \, \hat{\sigma}_{\rm p\pi}(E_{\rm p})}} \; . \tag{4.10}$$

This may be written more generally in terms of the absorption coefficient (defined in equation 3.34), where here the pp-pion production process dominates CR absorption, thus $c \, {\rm d}t' \, \hat{\sigma}_{\rm p\pi} \, n_{\rm H} = \varsigma(E_{\rm p}, r') \, {\rm d}r' \, \alpha(E_{\rm p}, r')$. This allows a CR attenuation factor to be introduced, defined as

$$\mathcal{A}(E_{\rm p}, \mathbf{r}; \mathbf{r}_i) = \exp \left\{ -\int_{\mathbf{r}_i}^{\mathbf{r}} \varsigma(E_{\rm p}, \mathbf{r}') \, \alpha(E_{\rm p}, \mathbf{r}') \, {\rm d}r' \right\} \; , \tag{4.11}$$

which quantifies the total level of attenuation experienced by a beam of hadronic CRs as they propagate between a source position $\mathbf{r}_i$ and a location $\mathbf{r}$.

Rewriting equation 4.8 in homogeneous form using the substitution 4.9 yields

$$\frac{\partial \mathcal{Y}}{\partial t} = \frac{1}{r'^2} \frac{\partial}{\partial r'} \left[r'^2 \, D(E_{\rm p}, r') \frac{\partial \mathcal{Y}}{\partial r'} \right] \; . \tag{4.12}$$

If an initial injection episode at $\mathbf{r} = \mathbf{r}_i$ is taken as a boundary condition, which provides a normalisation constant $\mathcal{Y}_0$, then the solution is well understood. It can be found, for example by method of Green's functions, which gives

$$\mathcal{Y} = \frac{\mathcal{Y}_0}{[4\pi D(E_{\rm p}, r') \, t']^{m/2}} \exp \left\{ -\frac{r'^2}{4D(E_{\rm p}, r') \, t'} \right\} \; , \tag{4.13}$$

which can be shown to converge uniformly to $\mathcal{Y}_0$ when $r' \to 0$ and $t' \to 0$, as required. This introduces m as a geometrical parameter for an m-dimensional system, and in the case of a 3-dimensional spherical system such as required here, it takes the value $m = 3$. t' denotes the time elapsed since the CR injection episode took place. The normalisation quantity $\mathcal{Y}_0$ following from the boundary condition is effectively the number of CRs injected, as determined by the strength of the CR injection episode. It is specified as the product of the volumetric injection rate $Q_{\rm CR,p}(E_{\rm p})$, the characteristic assigned source

size, $\mathcal{V}_\mathrm{S}$ and the time Δt over which the injection episode was active i.e. $\mathcal{Y}_0 = Q_\mathrm{CR,p}(E_\mathrm{p}, \mathbf{r}_i)\,\mathcal{V}_\mathrm{S}\,\Delta t$. This may be substituted into the solution 4.13 to give

$$n_\mathrm{CR,p} = \frac{Q_\mathrm{CR,p}(E_\mathrm{p}, \mathbf{r}_i)\,\mathcal{V}_\mathrm{S}\,\Delta t\,\mathcal{A}(E_\mathrm{p}, \mathbf{r}; \mathbf{r}_i)}{\left[4\pi D(E_\mathrm{p}, r')\,t'\right]^{3/2}}\,\exp\left\{-\frac{r'^2}{4D(E_\mathrm{p}, r')\,t'}\right\}\,. \qquad (4.14)$$

This result conveniently allows for the diffusive evolution term and the attenuation term to be treated separately. They may be calculated independently and later be re-combined, which has certain computational advantages. But the focus now is to seek a general solution to the full problem at hand: the case of multiple CR sources continually injecting protons. It is easier to consider this in two steps: first the generalisation to a continuous injection of CRs by a single source. Then, secondly, an extension to a full ensemble of discrete, spatially distributed injection sources. The first of these steps may be done analytically as it effectively follows from the convolution of solutions from successive, individual injection events. In the continuous limit, this reverts to a time-integral, where the general solution is

$$n_\mathrm{CR,p} = \frac{Q_\mathrm{CR,p}(E_\mathrm{p}, \mathbf{r}_i)\,\mathcal{V}_\mathrm{S}\,\mathcal{A}(E_\mathrm{p}, \mathbf{r}; \mathbf{r}_i)}{4\pi^{3/2}\,r'D(E_\mathrm{p}, r')}\,\Gamma\left(\frac{1}{2}, x\right)\,, \qquad (4.15)$$

and is applicable to each source location $\mathbf{r}_i$. The parameter x is defined here as

$$x = \frac{r'^2}{4\,D(E_\mathrm{p}, r')\,t}\,. \qquad (4.16)$$

The result 4.15 tends towards a steady-state (i.e. $\mathrm{d}n_\mathrm{CR,p}/\mathrm{d}t = 0$) to become

$$n_\mathrm{CR,p} = \frac{Q_\mathrm{CR,p}(E_\mathrm{p}, \mathbf{r}_i)\,\mathcal{V}_\mathrm{S}\,\mathcal{A}(E_\mathrm{p}, \mathbf{r}; \mathbf{r}_i)}{4\pi r'D(E_\mathrm{p}, r')}\,, \qquad (4.17)$$

in the limit where $t \to \infty$. The upper incomplete Gamma function was evaluated here as

$$\Gamma\left(\frac{1}{2}, x\right) = \sqrt{\pi}\left[1 - \mathrm{erf}(\sqrt{x})\right]\,, \qquad (4.18)$$

however it can be seen that $x \to 0$ as $t \to \infty$, thus

$$\Gamma\left(\frac{1}{2}, x\right) \to \pi^{1/2} \qquad (4.19)$$

as $t \to \infty$. This indicates that the CR distribution rapidly reaches a steady-state condition (compared to the dynamical timescales associated with hosting galaxies) and thus presents an effective equilibrium state while CR injection persists, in which the rate of newly injected CRs equals that at which others are absorbed.

Numerical Scheme

The final step is to extend the solution for a single, continuously injecting source to a full galactic distribution of sources. Since each source is linearly independent, the method of solution lends itself naturally to a numerical Monte-Carlo (MC) scheme. Equation 4.17 gives the steady-state diffusion/attenuation solution of the transport equation 4.4 for CR protons injected by a discrete source of volume $\mathcal{V}_{\mathrm{S}}$. To extend this to a full spatially-extended distribution of CR injection locations, this individual solution was convolved with a distribution of source locations. For the case of CR protons, the distribution of injection points would presumably follow the population of SN events. A sample of N_{S} points was generated, evenly distributed throughout a spherical volume. A maximum radius of 2 kpc was adopted, above which no further points were placed. The solution 4.17 was applied to each point, and weighted according to the normalised baryonic density profile of the model galaxy (equation 1.5) at each point position.

A characteristic MC point volume $\mathcal{V}_{\mathrm{S}}$, as required in equation 4.17, was specified by allocating an equal fraction of the total simulation (galaxy) volume to each point, such that $\mathcal{V}_{\mathrm{S}} = 4\pi r_{\mathrm{gal}}^3/(3N_{\mathrm{S}})$, where r_{gal} retains its earlier definition as the characteristic protogalaxy size (1 kpc). The resulting full solution due to the distributed CR injection is shown together with that for CR electron secondaries (solved later in section 4.3.2) in Fig. 4.1. This used a sample of $N_{\mathrm{S}} = 10,000$ sources, which gave an acceptable signal-to-noise ratio.[1] This would roughly correspond to the expected number of distinct sources in a galaxy with $\mathcal{R}_{\mathrm{SN}} \approx 1 \ \mathrm{yr}^{-1}$, if the typical active timescale during which a SN remnant can accelerate CR particles were taken to be about 10,000 years.

---

[1]Simulation runs with $N_{\mathrm{S}} = 40,000$ and $N_{\mathrm{S}} = 100,000$ were tested, but did not show any difference from the result calculated using $N_{\mathrm{S}} = 10,000$.
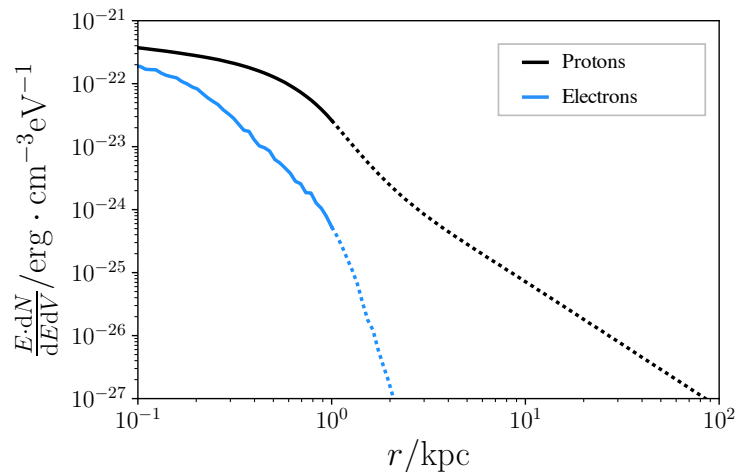
Fig. 4.1: The steady-state CR proton (primary - black line) and electron (secondary - blue line) profile spectral energy densities, integrated over the CR energy spectrum for a SN rate $\mathcal{R}_{\mathrm{SN}} = 0.1 \ \mathrm{yr}^{-1}$, as calculated in sections 4.2 and 4.3 respectively. Note that the solid section of the black line represents the proton distribution in the interstellar medium of the protogalaxy model, in which models of the magnetic field and subsequent CR propagation are more robust. The dashed part of the lines correspond to regions outside the protogalaxy, where the magnetic field is less well understood and the result is best regarded as an upper limit.

Note that Fig. 4.1 shows proton energy density far beyond the actual extent of the host protogalaxy. This is plotted for completeness, and mathematically results from the diffusion of particles into regions of low magnetic energy density. These outer regions, as shown by the dashed part of the line in the figure, are unlikely to be physical due to the complicated non-homogeneous nature of the interfacing magnetic fields between the ISM and the CGM – but the solution at these points may nevertheless be regarded as a generous upper-limit for the external CR proton energy density.

Cosmic Ray Energy Densities

The spectral energy densities attained by the approach outlined here are shown in Fig. 4.1. If the steady-state value of $E \cdot \mathrm{d}N/\mathrm{d}E \, \mathrm{d}V$ (as plotted) is multiplied with the mean CR energy in the proton spectrum, an indication for the CR energy density ϵ_{CR} in a system can be estimated. In the protogalaxy model shown in Fig. 4.1, a SN event rate of $\mathcal{R}_{\mathrm{SN}} = 0.1 \ \mathrm{yr}^{-1}$ was used. The resulting energy density in this case, together with those for models with $\mathcal{R}_{\mathrm{SN}} = 1$ and $10 \ \mathrm{yr}^{-1}$, are shown in Table 4.1.

Comparisons can be made with values for CR (proton) energy densities in nearby starbursts. For example, Yoast-Hull et al. (2016) calculated the CR

energy densities for M82, NGC 253, and Arp 220. These, together with the CR energy density for the Milky Way (data from Ferriere 2001), and M31 (data from Abdo et al. 2010a) are also shown in Table 4.1. It is useful to note that the model with $\mathcal{R}_{\mathrm{SN}} = 0.1$ yr^{-1} is reasonably similar to M82 and NGC 253 (as shown in Table 4.1), where such a SN rate would be appropriate (Lenc and Tingay 2006; Fenech et al. 2010). Moreover, the value calculated for the model with $\mathcal{R}_{\mathrm{SN}} = 1$ yr^{-1} is similar to the derived CR energy density in Arp 220, which Lonsdale et al. (2006) argue may have a SN rate as high as ≈ 4 yr^{-1}. Although the model with the highest SN rate, at 10 yr^{-1}, yields a CR energy density considerably higher than the three nearby starburst galaxies, such an active galaxy may be representative of some of the most violent starburst systems present in the very early Universe. By comparison, the Milky Way and M31 are expected to have very low CR energy densities due to a relatively low level of star-formation activity, corresponding to a SN event rate of ~ 0.015 yr^{-1} (see Adams et al. 2013; Diehl et al. 2006; Hakobyan et al. 2011; Dragicevich et al. 1999). With such a rate, a direct scaling from the model with $\mathcal{R}_{\mathrm{SN}} = 0.1$ yr^{-1} would suggest a Galactic value of $\epsilon_{\mathrm{CR}} \sim 53$ eV cm^{-3}, more than an order of magnitude higher than the actual measured value for the Milky Way, at 1.8 eV cm^{-3}. This discrepancy arises as a scaling is also required to geometrically account for the difference in the sizes of the galaxies.

This issue may be resolved by integrating the steady-state form of equation 4.7, by the divergence theorem (the result of which is actually physically similar to equation 3.31 introduced earlier). It may be rewritten in terms of the diffusive speed as

$$4\pi \ell_{\mathrm{diff}}^2 \left(\frac{D}{\ell_{\mathrm{diff}}} \right) \epsilon_{\mathrm{CR,diff}} = \kappa \, \mathcal{R}_{\mathrm{SN}} \, , \qquad (4.20)$$

in which κ is some arbitrary variable specifying the efficiency of CR production, which encodes the conversion between $L_{\mathrm{CR,eff}}$ and $\mathcal{R}_{\mathrm{SN}}$ (its exact form is not of interest at this point). This allows a scaling relation between CR energy

densities in diffusion-dominated systems to be written as

$$\epsilon_{\text{CR},2} = \epsilon_{\text{CR},1} \left(\frac{\mathcal{R}_{\text{SN},2}}{\mathcal{R}_{\text{SN},1}}\right) \left(\frac{D_1}{D_2}\right) \left(\frac{\ell_{\text{diff},1}}{\ell_{\text{diff},2}}\right) \left(\frac{\kappa_2}{\kappa_1}\right) \left(\frac{\bar{E}_2}{\bar{E}_1}\right) \qquad (4.21)$$

where, for the time being, the CR energy spectrum is neglected such that a characteristic value for the diffusion coefficient and mean CR energy can be used.

To test this scaling relation, consider the Milky Way in comparison to a reference model galaxy with $\ell_{\text{diff},1} = 1$ kpc and $\mathcal{R}_{\text{SN},1} = 0.1$ yr^{-1}, with a CR energy density of $\epsilon_{\text{CR},1} = 350$ eV cm^{-3}. If assuming that diffusion coefficients in the model system and the Milky Way are comparable $D_1 \approx D_2$, that the CR conversion variables $\kappa_1 \approx \kappa_2$, and that the mean CR energies $\bar{E}_1 \approx \bar{E}_2$, then a value of $\epsilon_{\text{CR},2} \approx 1.5$ eV cm^{-3} can be obtained, given that $\ell_{\text{diff},2} = 30$ kpc (see Xu et al. 2015) and $\mathcal{R}_{\text{SN},2} = 0.015$ yr^{-1} for the Milky Way, or similar galaxies like M31 (see Dragicevich et al. 1999; Diehl et al. 2006; Hakobyan et al. 2011; Adams et al. 2013). This value is very close to that inferred for the Milky Way, at 1.8 eV cm^{-3} (Ferriere 2001). At present, the level of CR diffusion or containment in high-redshift galaxies is uncertain. However, comparison between the high-redshift models developed here and values from observations of nearby galaxies does offer some useful insight. By applying the scaling relation 4.21, which is based on the high-redshift models, the present calculations suggest energy densities for these nearby cases which are of similar values to those observed (within a factor of a few). This supports the approach adopted here as a reasonable description of CRs containment and propagation in high-redshift protogalaxies.

4.2.2 Two-Zone Propagation

If an outflow operates in a galaxy, it could substantially reduce the number of CRs that are scattered and contained within its magnetic field. This can be demonstrated by a simple consideration of CR transport timescales: for a diffusion coefficient D of characteristic value 3×10^{28} cm^2 s^{-1} (see equation 3.32) and 1 GeV characteristic CR energy, when the interstellar magnetic field of the galactic host has reached saturation the associated CR diffusion timescale

Source	CR energy density / eV cm^{-3}
Milky Way	1.8±0.5
M31	$0.63^{+0.75}_{-0.50}$
M82	550^{+70}_{-120} [1]
NGC 253	260-350
Arp 220	1100-5100 [2]
Model: 0.1 SN yr^{-1}	350
Model: 1 SN yr^{-1}	3500
Model: 10 SN yr^{-1}	35000

Table 4.1: Estimated values for the CR energy density ϵ_{CR} in model systems and nearby galaxies. Values taken or derived from data in Webber (1998) for the Milky Way (see also Ferriere 2001), and Abdo et al. (2010a) for M31 (when applying their scaling ratio of 0.35 ± 0.25 for the M31 to Milky Way CR energy density ratio). Values for other nearby galaxies were obtained by Yoast-Hull et al. (2016). The model values result from the steady-state CR energy density at the stated SN event rates. [1] Value estimated from γ-ray observations. Note that the value is estimated to be $430 - 620 \, \mathrm{eV \, cm^{-3}}$, if combined with radio data. [2] These values correspond to the full range of values of CR energy densities inferred across the different regions of Arp 220 – see Yoast-Hull et al. (2016).

for a system of characteristic size $\ell \approx 1$ kpc is

$$\tau_{\mathrm{diff}} \approx \frac{\ell^2}{4\,D} \approx 2.5 \text{ Myr} . \tag{4.22}$$

However, in the presence of a galactic outflow, with bulk flow velocity v of around 10^2 to 10^3 km s^{-1} (see Chevalier and Clegg 1985; Seaquist et al. 1985), the corresponding CR advection timescale follows as

$$\tau_{\mathrm{adv}} \approx \frac{\ell}{v} \approx (1 - 10) \text{ Myr} . \tag{4.23}$$

The similarity of these two timescales suggests that these processes operate at comparable rates, and may both be important in governing the dynamics of propagating CRs. The CR absorption rate may be expressed as

$$\frac{\mathrm{d}\,n_{\mathrm{CR,p}}(E_{\mathrm{p}})}{\mathrm{d}t}\bigg|_{\mathrm{p}\pi} = - \left[\mathrm{c} \; \hat{\sigma}_{\mathrm{p}\pi}(E_{\mathrm{p}}) \; n_{\mathrm{H}} \right] \; n_{\mathrm{CR,p}}(E_{\mathrm{p}}) = - \left[\frac{\mathrm{c}}{r_{\mathrm{p}\pi}(E_{\mathrm{p}})} \right] \; n_{\mathrm{CR,p}}(E_{\mathrm{p}}) , \tag{4.24}$$

which leads to a timescale of

$$\tau_{\mathrm{p}\pi}(E_{\mathrm{p}}) = \frac{r_{\mathrm{p}\pi}(E_{\mathrm{p}})}{\mathrm{c}} , \tag{4.25}$$

in which $r_{\mathrm{p\pi}}$ is the pp interaction mean-free-path (see equation 3.24). These timescales can be used to assess the energy-dependence of the various processes in Fig. 4.2, which also takes into account the impact of outflow conditions[2] and CR energies to assess the relative importance for advection and diffusion within an outflow, and how this compares to CR absorption via the pp process. It shows timescales which are calculated according to a 5-μG mean ambient magnetic field (to specify the CR diffusion coefficient, adopted here to be constant – see, e.g. Heesen et al. 2016), an ISM baryonic matter number density (to calculate the CR attenuation) of $n_{\mathrm{H}} = 10$ cm^{-3} in the characteristic case in the upper panel, or as specified by the outflow model (cf. Fig. 2.5) in the lower panels, and a bulk outflow velocity (being the terminal flow velocity established for the CR- and SN-driven wind outflow modelled from section 2.2.1) of 290 km s^{-1}, or as indicated by the flow velocity profile (cf. Fig. 2.4) for the lower panels.

Within the outflow wind, advection would presumably dominate in cases where the wind bulk flow speed is sufficiently high (i.e. greater than the effective diffusion speed) while those parts of the ISM of the host galaxy that are not subject to the influence of the outflow (e.g. as per Zone B of the Two-Zone model) would continue to exhibit diffusive CR propagation overall. However, the presence of these two zones does not necessarily imply that CR propagation must always be different in each. While it is expected that propagation in Zone B (the interstellar zone) would usually be diffusive, CR propagation within the outflow cone (Zone A) may be either advective or diffusive. While it is even theoretically possible for both processes to operate at similar rates throughout the wind, such circumstances would be unlikely, as it would require very finely-tuned conditions to arise throughout the whole profile. Typically large parts of an outflow are observed either to be under advection-dominated conditions, or diffusion-dominated conditions (e.g. Heesen et al. 2016), although

---

[2]Note that there would be a substantial evolution of the matter density within the outflow wind with altitude, as shown in Fig. 2.5. This would mean that the CR attenuation timescale would become substantially larger as the CRs propagate along the outflow cone. This is demonstrated in the lower panels of Fig. 4.2 however, for the purposes of comparison of timescales, the treatment in the characteristic upper panel is sufficiently informative and a good approximation for the system overall, whereby CR attenuation in an outflow would be heavily dominated by that arising at the base of the outflow zone (see, e.g. Farber et al. 2018; Girichidis et al. 2018).
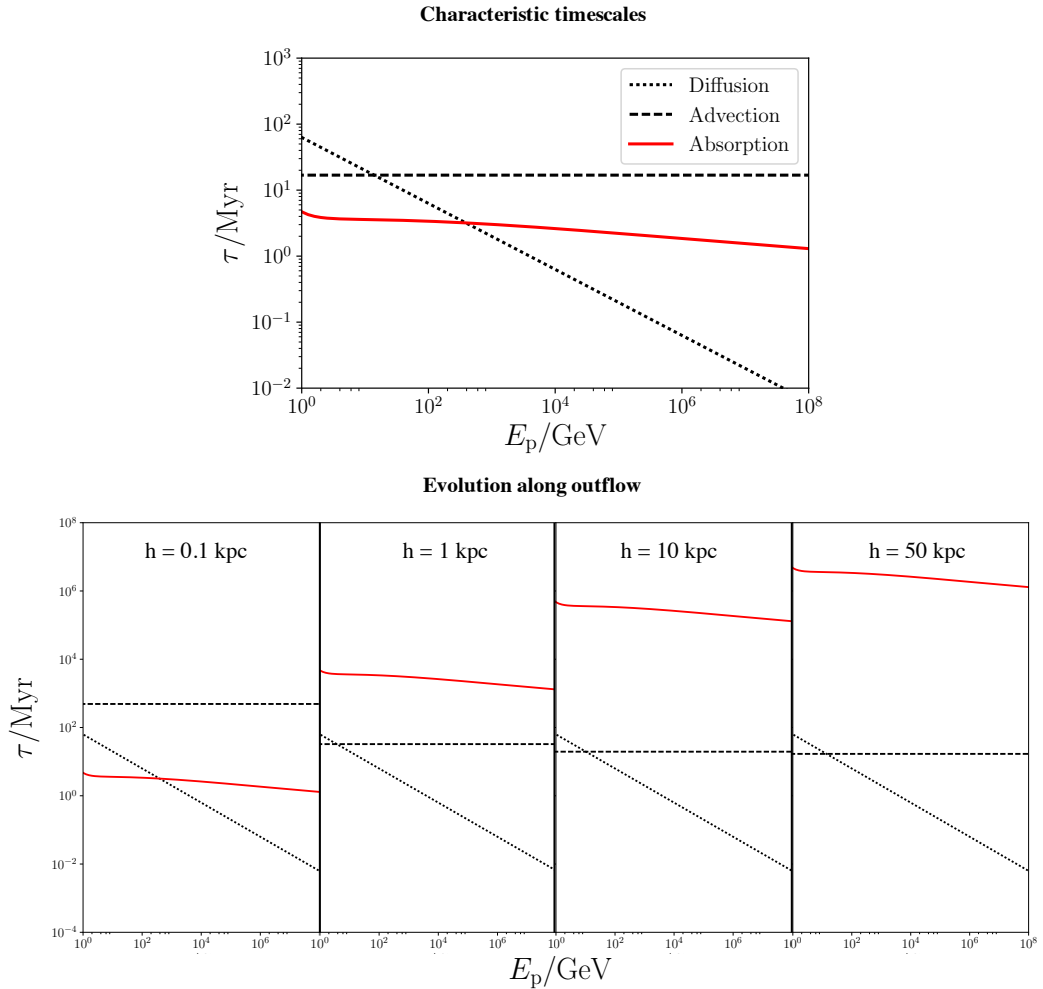
Fig. 4.2: Above: Characteristic timescales for CR proton attenuation due to pp interactions in a medium of density $n_H = 10$ cm^{-3} (solid red line), CR propagation due to diffusion in an interstellar magnetic field of average strength 5 μG (dotted line), and CR propagation due to advection in a bulk flow of 290 km s$^{-1} \approx v_\infty$ (heavy dashed line). Timescales are calculated assuming a characteristic length-scale of $\ell = 5$ kpc, where required and are intended to be characteristic of the full system. The level of internal variation along the flow is shown **below**, with timescales estimated based on the outflow velocity and density properties (from Figs. 2.4 and 2.5) at $h = 0.1, 1, 10$ and 50 kpc, but assuming no variation in the diffusion parameter and retaining the characteristic propagation length-scale of $\ell = 5$ kpc from above.

some transition between the two regimes would be expected – particularly in cases where an outflow is slow at low altitudes.

The Diffusion Limit

In the diffusion limit (e.g. as may arise when the outflow velocity is locally low), the advection term may be neglected in the transport equation 4.1, thus giving

$$-\nabla \cdot [D(E_\mathrm{p})\nabla n_{\mathrm{CR,p}}] = \frac{\partial}{\partial E_\mathrm{p}} [b(E_\mathrm{p}, \mathbf{x})n_{\mathrm{CR,p}}] - S_{\mathrm{CR,p}}(E_\mathrm{p}, \mathbf{x}) \ . \tag{4.26}$$

Using h as the altitude coordinate along an outflow (and adopting a spherical coordinate basis), this may be written as

$$-\frac{D(E_\mathrm{p})}{h^2} \frac{\partial^2 (h^2 n_{\mathrm{CR,p}})}{\partial h^2} = \frac{\partial}{\partial E_\mathrm{p}} [b(E_\mathrm{p}, h)n_{\mathrm{CR,p}}] - \mathrm{c}\ n_{\mathrm{CR,p}}\ \hat{\sigma}_{\mathrm{p\pi}}(E_\mathrm{p})\ n_\mathrm{H}(h) \ . \tag{4.27}$$

A substitution, $Z(E, h) = h^2 n_{\mathrm{CR,p}}(E_\mathrm{p}, h)$ (and, for convenience, $E = E_\mathrm{p}$), may be made, giving:

$$-D(E) \left\{ \frac{\partial^2 Z}{\partial h^2} - \frac{2}{h}\frac{\partial Z}{\partial h} + \frac{2Z}{h^2} \right\} = \frac{\partial}{\partial E} [b(E, h)Z] - \mathrm{c}\ Z\ \hat{\sigma}_{\mathrm{p\pi}}(E)\ n_\mathrm{H}(h) \ , \tag{4.28}$$

and, after some re-arrangement and expansion of the energy-derivative,

$$\frac{\partial^2 Z}{\partial h^2} = -\frac{1}{D(E)} \left\{ Z\frac{\partial b(E, h)}{\partial E} + b(E, h)\frac{\partial Z}{\partial E} \right.$$
$$\left. - \mathrm{c}\ Z\ \hat{\sigma}_{\mathrm{p\pi}}(E)\ n_\mathrm{H}(h) \right\} + \frac{2}{h}\frac{\partial Z}{\partial h} - \frac{2Z}{h^2} \ , \tag{4.29}$$

which may be solved numerically, subject to suitable boundary conditions (BCs).

The first of these BCs is

$$\left.\frac{\mathrm{d}Z}{\mathrm{d}h}\right|_{i,1} = \left.\frac{\mathrm{d}Z}{\mathrm{d}h}\right|_{\substack{E=E_i \\ h=h_0}}$$
$$= \left(\frac{E}{E_0}\right)^{-\Gamma_0} \left(\left.\frac{\mathrm{d}Z}{\mathrm{d}h}\right|_{\substack{E=E_0 \\ h=h_0}} - Z(E_0, h_0)\left(\frac{E}{E_0}\right)^{-1}\left.\frac{\mathrm{d}\Gamma}{\mathrm{d}h}\right|_{h=h_0}\right) \ , \tag{4.30}$$

in which the value of dZ/dh at a boundary ($E = E_0$ and $h = h_0$) is required. In the absence of a full, self-consistent model for the acceleration of CRs when they are injected into the base of an outflow, it can be assumed that the value of dZ/dh for CR protons scales with that for CR electrons at the lower boundary $h = h_0$,

$$\left.\frac{dZ}{dh}\right|_{\substack{E=E_0 \\ h=h_0}} = \left(\left.\frac{dZ_{CRe}}{dh}\right|_{\substack{E=E_0 \\ h=h_0}}\right) R_{cool} \; , \tag{4.31}$$

in which R_{cool} is the scaling factor between the value for electrons (for which there are some observational constraints) and for protons. As radiative cooling processes are typically proportional to the inverse of the fourth order of the ratio of the masses of the charged particles, this scale factor may be set to $R_{cool} = (m_e/m_p)^4$ – see section 3.3.1 for details. This indicates that dZ/dh is practically negligible for protons. Moreover, contributions from adiabatic cooling would not be substantial at the base of an outflow cone. A BC follows from the argument that CR proton flux would be conserved at the lower boundary, i.e. $v_\infty Z(E)|_{h_0} = v_\infty \{n_{CR,p}(E)h^2\}|_{h_0} = $ constant, but a value for dZ_{CRe}/dh is also required at the boundary. This can be determined from the value of dn_{CRe}/dh, which may be estimated from radio observations – for example, based on observations of the nearby starburst outflows NGC 7090 and NGC 7462 in the 6 cm and 22 cm radio bands. For this, Heesen et al. (2016) suggest a value of

$$\left.\frac{dZ_{CR,e}}{dh}\right|_{\substack{E=E_0 \\ h=h_0}} = -0.2 \; . \tag{4.32}$$

The second BC required is $d\Gamma/dh$, i.e. the rate at which the CR spectral index changes at the base of Zone A. Again, a scaling with that for electrons can be used here, with the electron value also determined from NGC 7090 and NGC 7462. Heesen et al. (2016) suggests a value of $\Gamma'_{CR,e} = d\Gamma_{CR,e}/dh = -1.4$, and so, for CR protons, the BC is

$$\left.\frac{d\Gamma}{dh}\right|_{h_0} = \Gamma'_{CR,e} + \log R_{cool} \; . \tag{4.33}$$

Here, the mass scaling is applied once again with R_{cool}. As per the discussion around the previous BC, such a treatment gives negligible variation in the spectral index of the protons at the boundary, consistent with the limited effect that cooling and spectral evolution would be expected to have in this part of the model.

The final BC (which is also applicable to solving the transport equation in the advection limit – see the following subsection) is for $Z(E_0, h_0) = n_{\mathrm{CR,p}}(E_0, h_0) \, v(h_0) \, h_0^2$, where h_0 (the size of the star-forming core region) is specified as 100 pc (cf. Chevalier and Clegg 1985; Tanner et al. 2016), and $n_{\mathrm{CR,p}}$ is set at a reference energy E_0 of 1 GeV. The spectral energy distribution of the protons at the boundary may also be set using a power-law index $\Gamma(h_0) = 2.1$ at h_0. This yields the required BC, calculated as $Z(E, h) \propto E^{-\Gamma(h)} \, h^2 \, v(h)$, for which a velocity profile $v(h)$ can be adopted (in this work, the outflow model in section 2.2.1 was applied). With suitable BCs in place, equation 4.29 may be solved numerically for Z, as outlined below.

Numerical Scheme

An RK4 scheme (Press et al. 2007) was employed to solve equation 4.29 numerically, subject to the previously discussed BCs. This could be done by splitting the second-order PDE into an 'inner' and 'outer' scheme, discretised over a numerical grid over 180 points in energy E_j distributed linearly between $E_0 = 1$ GeV and $E_{\mathrm{max}} = 10^6$ GeV and 10,000 points in position h_i distributed linearly between 0.1 kpc and 100 kpc, indexed by the notation j and i respectively. The first step was to find the numerical solution $\mathrm{d}Z/\mathrm{d}h$ of the 'inner' scheme, according to the difference equation

$$
\begin{aligned}
\left.\frac{\mathrm{d}Z}{\mathrm{d}h}\right|_{i,j+1} = {} & \left.\frac{\mathrm{d}Z}{\mathrm{d}h}\right|_{i,j} + \frac{\Delta h}{D_{i,j}\left(1 - \frac{2}{h}\right)} \left\{ Z_{i,j}\frac{\partial b_{i,j}}{\partial E} + b_{i,j}\frac{Z_{i+1,j} - Z_{i-1,j}}{E_{i+1} - E_{i-1}} \right. \\
& \left. - \mathrm{c}\, Z_{i,j}\, \hat{\sigma}_{\mathrm{p}\pi}(E_i)\, n_{\mathrm{H}}(h_j) \right\} - \frac{2Z_{i,j}}{h}\left(\frac{1}{h-2}\right),
\end{aligned}
\tag{4.34}
$$
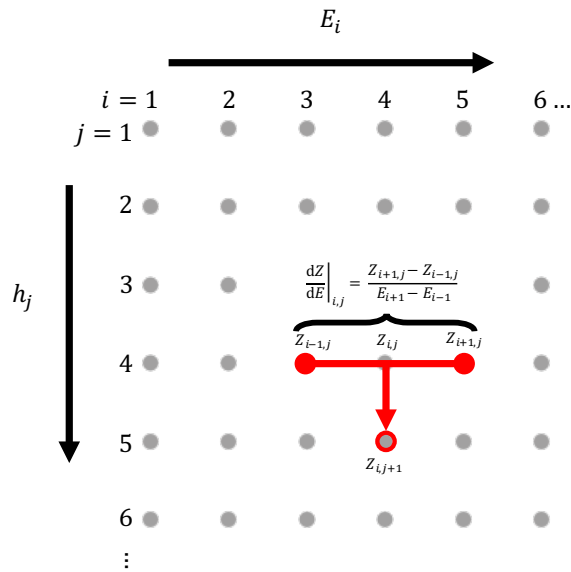
Fig. 4.3: Illustration of the numerical scheme on a grid. The line $j = 1$ is provided by the boundary conditions, and the lines $j = 2$ onwards may then be calculated according to equations 4.34 and 4.35 by use of a 4th order Runge-Kutta scheme. To calculate each point, three adjacent points in the previous h-step are required to estimate the energy-gradient of the solution. This can then be propagated forward to the numerical solution at the desired grid point as indicated by the red arrow. See main text for further details. Cartoon based on schematic in Heesen et al. (2016).

while a further 'outer' step was required to yield the desired numerical result Z, according to the difference equation

$$Z_{i,j+1} = Z_{i,j} + \left.\frac{\mathrm{d}Z}{\mathrm{d}h}\right|_{i,j} \Delta h \; . \qquad (4.35)$$

Every calculated solution $Z_{i,j}$ at a point evidently requires the solution at adjacent points in the previous h-step over three energies to enable the gradient $\partial Z / \partial E$ to be estimated, as illustrated in the cartoon in Fig. 4.3. This allows the gradient at the central point to be propagated forwards (as indicated by the red arrow in the cartoon) so that the next line of solution points can be found. At the edges of the numerical grid, the required three energy points are not available. Instead, it was found that in these 'edge-cases', it was sufficient to simply estimate the energy-gradient using the two available points. In the implementation used to produce the results displayed in this thesis, the energy increments chosen were of sufficiently high resolution such that any small inaccuracies resulting from taking fewer points to calculate the
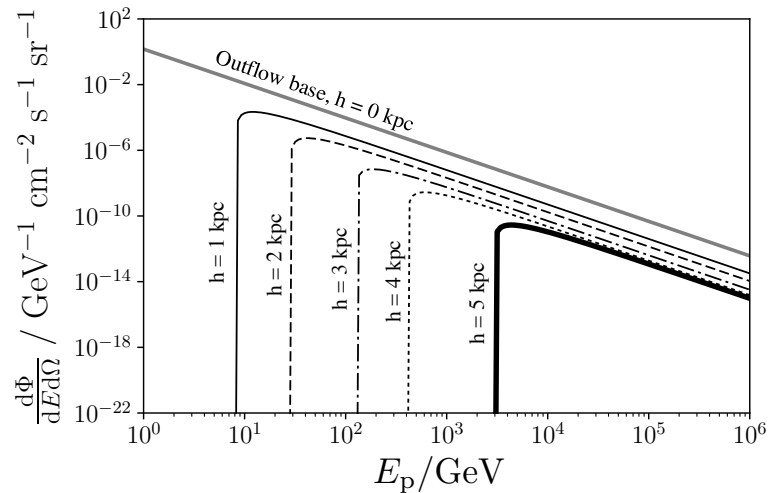
Fig. 4.4: Normalised spectrum of CRs subject to predominantly diffusive propagation at the base of the outflow, (solid grey line), at $h = 1$ kpc (solid black line), $h = 2$ kpc (black dashed line), $h = 3$ kpc (dashed-dotted line) and $h = 4$ kpc (dotted black line) and $h = 5$ kpc (thick black line). The suppression in this case is principally at lower energies, consistent with the lowest energy CRs being absorbed at a rate much faster than they diffuse, mainly depositing their energy near their source.

gradient in the vicinity of the edges were rapidly suppressed. The result of this calculation is shown in Fig. 4.4, up to $h = 5$ kpc in $h = 1$ kpc increments. To ensure stability, tests with higher order difference schemes were implemented to check that results could be reproduced. In these cases, additional Neumann BCs were required for the inner scheme.

The spectral evolution shown in Fig. 4.4 may be understood with the aid of Fig. 4.2. This indicates that at low altitudes lower energy protons, with $E_p < 10^3$ GeV, have a sufficiently long diffusion time such that $\tau_{\text{diff}} \gg \tau_{\text{p}\pi}$. When advection is not operating significantly, these CRs would be easily contained within their source galaxy and would thus eventually be absorbed. Moreover, those protons with $E_p \gg 10^3$ GeV have $\tau_{\text{diff}} < \tau_{\text{p}\pi}$, so could diffuse out of their host galaxy before being absorbed. Indeed, at the highest energies where $\tau_{\text{diff}} \ll \tau_{\text{adv}}$, these CRs could diffuse out of the system regardless of the nature of any outflow (or, indeed, if one was even present at all) – however, such energetic CRs only constitute a very small fraction of the total energy in the CR spectrum, so their astrophysical impacts would be relatively inconsequential.

The Advection Limit

In the advection-dominated regime, when the bulk velocity of an outflow wind is sufficiently fast to transport CRs more quickly than they can diffuse, the diffusion term in equation 4.1 may be neglected to give

$$\nabla \cdot \left\{ \mathbf{v}\, n_{\mathrm{CR,p}} \right\} = \frac{\partial}{\partial E_{\mathrm{p}}} \left\{ b(E_{\mathrm{p}}, \mathbf{x})\, n_{\mathrm{CR,p}} \right\} - S_{\mathrm{CR,p}}(E_{\mathrm{p}}, \mathbf{x}) \ . \qquad (4.36)$$

As before, it may be taken that the flow follows streamlines in the outflow cone region and so, by symmetry, it reduces to an effectively 1-dimensional system, which may be specified by the coordinate h. Thus, equation 4.36 may be written as

$$\frac{1}{h^2} \frac{\partial(h^2\, v(h)\, n_{\mathrm{CR,p}})}{\partial h} = \left\{ \frac{\partial}{\partial E_{\mathrm{p}}} \left\{ b(E_{\mathrm{p}}, h)\, n_{\mathrm{CR,p}} \right\} - \mathrm{c}\, n_{\mathrm{CR,p}}\, \hat{\sigma}_{\mathrm{p}\pi}(E_{\mathrm{p}})\, n_{\mathrm{H}}(h) \right\} \ , \qquad (4.37)$$

with terms retaining their earlier meanings. Again, use of the substitution $Z(E, h) = n_{\mathrm{CR,p}}(E, h)\, v(h)\, h^2$ and $E = E_{\mathrm{p}}$ allows this to be re-written as

$$\frac{\partial Z}{\partial h} = \frac{1}{v(h)} \left\{ Z \frac{\partial b(E, h)}{\partial E} + b(E, h) \frac{\partial Z}{\partial E} - \mathrm{c}\hat{\sigma}_{\mathrm{p}\pi}(E)\, n_{\mathrm{H}}(h) Z \right\} \ , \qquad (4.38)$$

which may be discretised as

$$Z_{i,j+1} = Z_{i,j} + \frac{\Delta h}{v(h_j)} \left\{ Z_{i,j} \frac{\partial b_{i,j}}{\partial E} + b_{i,j} \frac{Z_{i+1,j} - Z_{i-1,j}}{E_{i+1} - E_{i-1}} - \mathrm{c}\, Z_{i,j}\, \hat{\sigma}_{\mathrm{p}\pi}(E_i)\, n_{\mathrm{H}}(h_j) \right\} \ . \qquad (4.39)$$

Once again, this may be solved by use of an RK4 scheme (Press et al. 2007) with 5th order error estimation subject to the boundary condition that $Z(E_0, h_0) = n_{\mathrm{CR,p}}(E_0, h_0)\, v(h_0)\, h_0^2$ with $h_0 = 100$ pc, $E_0 = 1$ GeV and $\Gamma(h_0) = 2.1$. The velocity profile determined in section 2.2.1 was called for each h_j as required by such a numerical scheme, and the result is shown (for h up to 50 kpc) in Fig. 4.5. This demonstrates that there is no apparent spectral evolution along the extent of the outflow. Such behaviour is clearly consistent with the timescales plotted in Fig. 4.2, in which τ_{adv} is not energy-dependent (being due to the intrinsic properties of the outflow, not the CRs) while $\tau_{\mathrm{p}\pi}(E_{\mathrm{p}})$ exhibits only minimal variations with energy across the entire
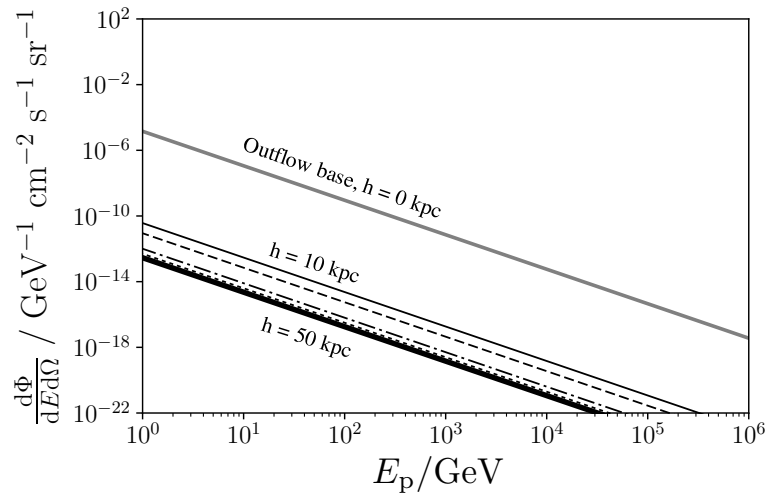
Fig. 4.5: Normalised spectrum of CRs subject to advection at the base of an outflow (solid grey line), at $h = 10$ kpc (solid black line), $h = 20$ kpc (black dashed line), $h = 30$ kpc (dashed-dotted line), $h = 40$ kpc (dotted black line) and $h = 50$ kpc (thick black line).

spectral range adopted. Without any significant energy dependence in these two terms (which are the only timescales relevant to the spectral evolution of this system), substantial spectral evolution of CRs advected by an outflow would not be expected.

It is worth noting that Fig. 4.2 shows that $\tau_{p\pi} < \tau_{adv}$ over all of the energies considered at low altitudes (see the $h = 0.1$ kpc plot). Such timescales would imply that CR protons are heavily attenuated at these low altitudes in the outflow cone. However, over an appropriate length-scale (e.g. a few kpc), the density of the flow rapidly falls to become substantially less than that at its base. Therefore, for much of the flow's extent, $\tau_{p\pi} \gg \tau_{adv}$, and strong CR attenuation could not arise at any distance away from the base of the flow, as is evident in the flow evolution plots of Fig. 4.2 (a conclusion that is also supported by simulation work – see, e.g. Farber et al. 2018; Girichidis et al. 2018).

It is also useful to consider the ratio of the normalised diffusion spectrum, to the normalised advection spectrum to check the self-consistency of the calculated results. This gives an indication of the level of attenuation $\mathcal{A}_{D/A}$ experienced by diffusing CRs, given that it is this attenuation which causes the turn-over in the diffusion spectrum (as can also be seen in Fig. 4.4). The spectral ratios are shown in Fig. 4.6, which again shows the predominant ab-
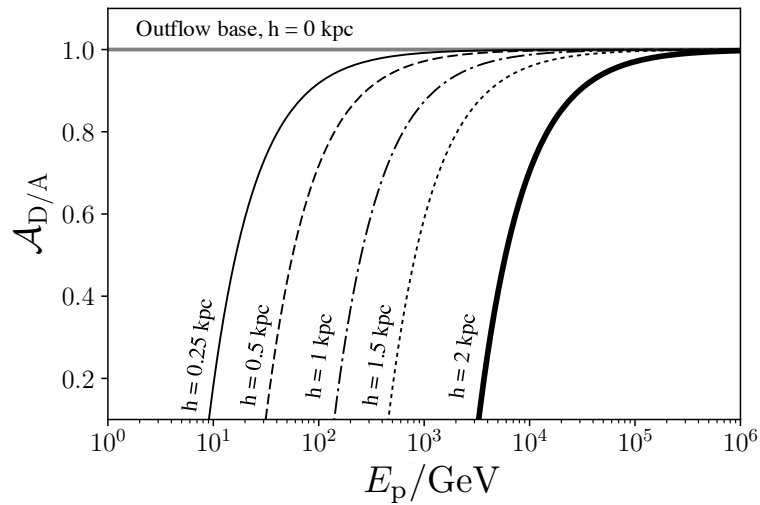
Fig. 4.6: Ratio plot of the normalised CR spectrum in the diffusion-dominated scenario compared to that in the advection-dominated case. This illustrates the level of attenuation $\mathcal{A}_{\mathrm{D/A}}$ experienced by a CR proton at a specified energy as it diffuses (which is regarded as the cause of the turn-over in the spectrum seen at lower energies). Lines are calculated at the base of the outflow (solid grey), $h = 0.25$ kpc (thin solid black), $h = 0.5$ kpc (black dashed), $h = 1$ kpc (dashed-dotted), $h = 1.5$ kpc (dotted black), and $h = 2$ kpc (thick black).

sorption effect experienced by the CR protons up to energies of around 5×10^3 GeV. Beyond this the difference in the normalised spectra subsides, as is consistent with diffusion becoming more important than attenuation at higher energies.

Cosmic Ray Energy Densities

In Zone A of the Two-Zone model, the CR energy density when dominated by advection can be expressed in a similar manner to equation 3.31, but where the diffusive velocity is replaced by the flow velocity. This gives

$$\epsilon_{\mathrm{CR,adv}} = \frac{L_{\mathrm{CR,eff}}}{4\pi \ell_{\mathrm{adv}}^2 \; v(h)} \; , \tag{4.40}$$

where $v(h)$ may be approximated with v_∞, being the terminal velocity of the outflow.

Advective outflows can extend for tens of kpc (see Veilleux et al. 2005; Bland-Hawthorn et al. 2007; Bordoloi et al. 2011; Martin et al. 2013; Rubin et al. 2014; Bordoloi et al. 2016), so an appropriate length-scale of $\ell_{\mathrm{adv}} = 10$ kpc may be adopted. In the case of a Two-Zone galaxy model with $\mathcal{R}_{\mathrm{SN}} = 0.1 \; \mathrm{yr}^{-1}$, in which Zone A harbours an outflow of specifications considered

previously (see section 2.2.1, $v_\infty \approx 290$ km s^{-1}) and Zone B is permeated by an interstellar magnetic field suitable to yield a characteristic diffusion coefficient of $D = 3.0 \times 10^{28}$ cm^2 s^{-1}, the CR energy densities in the two zones can be shown to be $\epsilon_{\mathrm{CR,adv}} \approx 0.59$ eV cm^{-3} and $\epsilon_{\mathrm{CR,diff}} \approx 170.0$ eV cm^{-3} respectively. In this case, the advection of CRs due to the action of the outflow wind reduces their energy density by almost 2 orders of magnitude. These values can be compared with the CR energy densities estimated for M82, $\epsilon_{\mathrm{CR}} \approx 550$ eV cm^{-3}, and NGC 253, $\epsilon_{\mathrm{CR}} \approx 260 - 350$ eV cm^{-3} (Yoast-Hull et al. 2016) which both exhibit comparable SN rates to those adopted in this model (Lenc and Tingay 2006; Fenech et al. 2010), meaning comparisons can be drawn between the CR energy densities. M82 hosts a clear outflow, however its CR energy density is comparatively high, being more consistent with the value estimated in the diffusion case above than for advection. This would indicate that CR propagation in M82 may still be diffusion-dominated overall. Furthermore, by the same argument, NGC 253 is also diffusion-dominated throughout the majority of the regions influenced by its galactic outflows. Advective transport is thought to only become important above a height of around 2 kpc (Heesen et al. 2007). Such a dynamical structure would be consistent with the relatively high CR energy densities inferred for this galaxy.

It is also informative to consider a system that is fully advective, presumably where the outflow velocity is very high. One such example is NGC 3079: this galaxy harbours a remarkably fast outflow wind, with flow velocities reaching somewhere in the range $1,100 - 3,000$ km s^{-1} at its fastest (Filippenko and Sargent 1992; Veilleux et al. 1994a,b, 1999). The galaxy hosts an active nucleus (AGN), which may have some impact on these high outflow velocities – however analysis by Cecil et al. (2001) argues the wind is driven predominantly by the nuclear starburst rather than the AGN. Regardless of the exact driving mechanism, it is difficult to envisage that CR diffusion could keep up with advection under such high bulk velocities, meaning that this system would presumably be advective. Indeed, CR energy densities are found to be relatively low, considering that NGC 3079 has a SN event rate in the range $\mathcal{R}_{\mathrm{SN}} \approx 0.3 - 0.5$ yr^{-1} (Irwin and Seaquist 1988; Condon 1992;

Irwin and Saikia 2003), with radio observations indicating average values of around 8.0 eV cm^{-3} with only small deviations throughout the flow (Irwin and Saikia 2003). This value would be roughly comparable with the level predicted by equation 4.40. If this system were instead solely diffusive, a CR energy density of $1,000 - 2,500$ eV cm^{-3} would be expected, i.e some two orders of magnitude larger than observations can support – so, clearly this system is not diffusion dominated. The CRs here are strongly redistributed by the fast advective flow.

4.3 Propagation of Energetic Electrons

Electrons typically do not propagate as far as protons in interstellar environments (see, e.g. Fig. 3.3 compared to Fig. 3.1). This is because they transfer their energy much more quickly than their hadronic counterparts, which means that their energy is deposited relatively locally to the point at which they are accelerated or injected. It follows, therefore, that most primary CR electrons are unlikely to leave their source environments. Instead, an interstellar energetic electron population is more likely to be mainly injected by the interactions of a non-thermal hadronic CR population. Indeed, a high CR secondary injection fraction in starbursts is argued by Schober et al. (2015), of between 60-80%. The electrons detected in starburst outflows, e.g. those aforementioned in NGC 7090 and NGC 7462 (Heesen et al. 2016), are presumably injected secondaries resulting from hadronic interactions, and are unlikely to be advected to these locations as primary CRs themselves. As such, it is less useful to consider the difference in electron transport in a Two-Zone model, which would not offer any further insight over the One-Zone scenario discussed here.

4.3.1 Electron Cooling

The principal cooling processes of energetic CR electrons in protogalactic environments are shown in Fig. 3.3. These are dominated by inverse Compton processes at higher energies, with Coulomb losses becoming more important at lower energies. Coulomb losses depend on the density of the ambient ISM through which an energetic electron propagates. The ISM density profile in

a galaxy does exhibit some spatial dependence (see equation 1.5), and varies substantially on kpc scales. However, Coulomb cooling of electrons operates over length-scales comparable to that of CR thermalisation, i.e. of order 0.2 kpc (see section 3.4.1). This is much smaller than the size of the protogalaxy, and typically the mean ISM density would not vary much over these distances. As such, in the first instance, the Coulomb contribution to the electron cooling function can be taken to be spatially independent. This is a particularly safe approximation for the calculations shown later in this thesis, whereby the electron distribution and cooling function is not regarded beyond a few hundred parsecs from the centre of a galaxy – beyond this point, uncertainties in the magnetic field structure as it interfaces with the CGM become prohibitive to reasonable modelling.

Fig. 3.4 also demonstrates that the cooling fraction due to inverse Compton losses increases with redshift as the energy density of the CMB (which is up-scattered by the energetic electrons in this process) increases. At high-redshift, low to moderate star-formation rates yield a stellar radiation field of energy density that is easily dominated by the contribution from CMB photons (see section 1.3.4). As the CMB is homogenous and isotropic, the inverse Compton component of the electron cooling function in CMB-dominated cases is likewise. However, if star-formation is sufficiently intense and concentrated, the resulting radiation field may begin to surmount the effect of the CMB so as to introduce a non-negligible position dependence into the resulting inverse Compton cooling function. The following assesses whether this could be the case in any realistic high-redshift star-forming system.

High-Redshift Star-forming Galaxies

Evidence of intense star-forming activity at high-redshift has already been presented in chapter 1 (see section 1.1) for the case of MACS1149-JD1, a star-forming protogalaxy observed at $z = 9.11$ for which there is evidence of a further, previous starburst phase at a much earlier point in its evolutionary history (Watson et al. 2015; Hashimoto et al. 2018). Recent studies have also shown similar characteristics in a several other high-redshift galaxies. These systems typically fall into two categories: (1) galaxies found to be undergoing

an intense starburst episode during the epoch at which they were observed, and (2) galaxies for which there was evidence that a previous starburst episode had been active (e.g. from the identification of an old stellar population alongside a younger population which had formed more recently) but had since been quenched by their observed epoch. 16 high-redshift galaxies were selected (including MACS1149-JD1) from existing observations and studies for which sufficient information was available to determine their redshift, physical size, star-formation activity (or previous starburst activity), stellar mass and stellar population ages. 4 of these systems could be assigned to the first category, while a further 12 (including MACS1149-JD1) could be assigned to the second category. These systems are analysed in much greater depth in chapter 6, where further details are provided. The galaxies in the first category are conventional starbursts, for which the intensity of their stellar radiation field may be estimated based on their stellar population luminosity and the physical size of the system. Those galaxies which fell into the second category are known as 'post-starburst' galaxies, with star-formation histories (SFHs) not unlike those inferred for similar systems found in the less-distant Universe (see e.g. French et al. 2015; Rowlands et al. 2015; French et al. 2018). Although their star-formation was relatively quiescent at the point of observation, their previous starburst phase is of interest here. All 16 of these systems are listed in Table 4.2, where the energy density of the CMB at their observed redshift together with the energy density of their stellar radiation fields (during their starburst phase) is estimated.[3]

---

[3]Stellar radiation energy densities followed from estimated galactic luminosities by $L_{\text{gal}}/4\pi r_{\text{gal}}^2 c$, for which the total stellar luminosities were estimated by scaling against a known baseline system with star-formation rate – see section 5.1, and Leitherer et al. (1999); Hirashita et al. (2003) for details.

Galaxy ID	z	$\mathcal{R}^*_{\rm SB}/{\rm M}_\odot\,{\rm yr}^{-1}$	References[a]	$U^\star/{\rm eV\,cm}^{-3}$ [b]	$U_{\rm CMB}/{\rm eV\,cm}^{-3}$
HDFN-3654-1216	$6.3^{+0.2}_{-0.2}$	$36^{+9.9}_{-23}$	(1)	50	800^{+97}_{-97}
UDF-640-1417	$6.9^{+0.1}_{-0.1}$	47^{+14}_{-19}	(1, 2)	110	$1,000^{+61}_{-61}$
GNS-zD2	$7.1^{+1.5}_{-0.6}$	$10^{+8.0}_{-10}$	(1)	92	$1,200^{+980}_{-390}$
CDFS-3225-4627	$7.1^{+1.5}_{-0.5}$	17^{+11}_{-14}	(1, 3)	120	$1,200^{+980}_{-330}$
GNS-zD4	$7.2^{+0.4}_{-0.2}$	57^{+17}_{-23}	(1)	200	$1,200^{+270}_{-140}$
GNS-zD1	$7.2^{+0.2}_{-0.2}$	63^{+19}_{-25}	(1)	370	$1,200^{+140}_{-140}$
GN-108036	$7.21^\dagger$	100^{+5}_{-2}	(4)	380	$1,200^\dagger$
SXDF-NB1006-2	$7.21^\dagger$	350^{+170}_{-280}	(5)	530	$1,200^\dagger$
UDF-983-964	$7.3^{+0.4}_{-0.3}$	$7.6^{+7.8}_{-7.6}$	(1, 2)	36	$1,300^{+280}_{-210}$
GNS-zD3	$7.3^{+0.9}_{-0.4}$	38^{+12}_{-20}	(1)	150	$1,300^{+630}_{-280}$
GNS-zD5	$7.3^{+0.2}_{-0.2}$	110^{+33}_{-48}	(1)	370	$1,300^{+140}_{-140}$
A1689-zD1	$7.60^\dagger$	$4.9^{+4.7}_{-2.7}$	(6, 7, 8, 9)	11	$1,500^\dagger$
EGS-zs8-1	$7.73^\dagger$	79^{+47}_{-29}	(10, 11)	190	$1,600^\dagger$
UDF-3244-4727	$7.9^{+0.8}_{-0.6}$	35^{+12}_{-30}	(1, 12)	160	$1,700^{+680}_{-510}$
MACS1149-JD1	$9.11^\dagger$	$11^{+9.3}_{-5.4}$	(13, 14)	6.6	$2,800^\dagger$
GN-z11	$11.1^\dagger$	24^{+10}_{-10}	(15)	630	$5,800^\dagger$

Table 4.2: Estimated energy densities of the radiation fields for a sample of 16 high-redshift star-forming galaxies (with stellar radiation energy densities calculated for their starburst phase), compared to the energy density of the CMB radiation field at their observed redshifts. This shows that, in all cases, radiative cooling of the CR electrons would be dominated by the CMB.

Notes:

[a] References: (1) González et al. (2010), (2) Bouwens et al. (2004), (3) Bouwens and Illingworth (2006), (4) Ono et al. (2012), (5) Inoue et al. (2016), (6) Bradley et al. (2008), (7) Watson et al. (2015), (8) Knudsen et al. (2017), (9) Mainali et al. (2018), (10) Oesch et al. (2015), (11) Grazian et al. (2012), (12) Oesch et al. (2009), (13) Hashimoto et al. (2018), (14) Owen et al. (2019), (15) Oesch et al. (2016).

[b] Uncertainties in $U^\star$ could be as large as 100%, due to the poor constraints on galaxy size estimates. These values are only intended as a indicative comparison with CMB energy densities, so such error bounds are sufficient for the present application.

$\dagger$ Uncertainties are not shown for these spectroscopic redshifts and CMB energy densities, as they are substantially less than the precision to which the values are quoted.

When accounting for their size, the values in Table 4.2 show that none of the star-forming galaxies in this sample exhibit an energy density in their stellar radiation fields which would exceed (or would even be comparable to) that of the CMB during their starburst episode, where U_{CMB} is calculated according to equation 1.8 at the specified redshift. It is therefore justified to consider that the inverse Compton cooling function for electrons is dominated by CMB radiation field at high-redshifts, and so may be modelled to be effectively spatially independent. This is not without caveats: caution must be aired for these stellar radiation energy density estimates because they are calculated assuming that star-formation is evenly-distributed throughout the host galaxy. It is unclear whether this is strictly accurate in very extreme systems – particularly in the case of galaxies in the early Universe, for which there are suggestions that starburst activity may be more clumpy in morphology than it is in lower-redshift examples (e.g. Elmegreen et al. 2009; Förster Schreiber et al. 2011; Murata et al. 2014; Tadaki et al. 2014; Kobayashi et al. 2016). This may alter the effective radiation energy-density distribution on a sub-galactic level: for instance, if star-formation were clumped in the inner 1 kpc of a galaxy like SXDF-NB1006-2 (with $\mathcal{R}_{\mathrm{SF}} \approx 350$ M$_\odot$ yr^{-1}), the energy density of the stellar radiation in this clump could be as high as $U^\star \approx 3,300$ eV cm^{-3}, being substantially greater than the CMB at the redshift this system was observed at ($U_{\mathrm{CMB}} \approx 1,200$ eV cm^{-3}). However, such details lie beyond the scope of the present work and would not substantially change the galaxy-wide picture outlined here.

4.3.2 Electron Transport

It was previously shown that, for electrons, the transport equation reduces to the form shown in equation 4.5. The source term in this case, $Q_{\mathrm{e}}(E_{\mathrm{e}}, r)$, is governed by the electrons injected by the CR primary proton interactions, as determined by equation 3.46. For subsequent calculations, the CR electron distribution in its steady state is required. This represents the persisting condition into which the system settles and, as with the CR protons, it is reasonable to assume that the steady-state is reached very rapidly given that the distribution is governed by similar processes operating over comparable

timescales. Thus, enforcing that $\mathrm{d}n_{\mathrm{CR,e}}/\mathrm{d}t = 0$ allows equation 4.5 to be reduced to

$$\frac{\partial(b\,n_{\mathrm{CR,e}})}{\partial E_{\mathrm{e}}} = \frac{1}{r^2}\frac{\partial}{\partial r}\left[r^2 D(E_{\mathrm{e}},r)\frac{\partial n_{\mathrm{CR,e}}}{\partial r}\right] + Q_{\mathrm{CR,e}}(E_{\mathrm{e}},r)\ . \tag{4.41}$$

In a similar manner to the approach invoked to solve equation 4.7, this may be restated as a boundary value problem. The case of a single electron injection event from a source region of size $\mathcal{V}_{\mathrm{s}}$ at a location $\mathbf{r}_i$ thus yields the homogenous PDE

$$\frac{\partial(b\,n_{\mathrm{CR,e}})}{\partial E_{\mathrm{e}}} = \frac{1}{r'^2}\frac{\partial}{\partial r'}\left[r'^2 D(E_{\mathrm{e}},r')\frac{\partial n_{\mathrm{CR,e}}}{\partial r'}\right]\ , \tag{4.42}$$

where r' retains its earlier meaning as the distance between an injection point $\mathbf{r}_i$ and an observation location $\mathbf{r}$. The electron injection specifies the BC as the steady-state number of electrons at the source position, being the product of their total injection rate and cooling rate in a spectral energy interval between E_{e} and $\mathrm{d}E_{\mathrm{e}}$, i.e. $N_{\mathrm{CR,e}}(E,\mathbf{r}_i) = Q_{\mathrm{CR,e}}(E_{\mathrm{e}},\mathbf{r}_i)\mathcal{V}_{\mathrm{S}}\,\tau_{\mathrm{cool}}(E_{\mathrm{e}})$. Physically, this may be regarded as the number of electrons injected by the source point over a characteristic electron cooling timescale. This ignores the contribution from higher-energy electrons cooling into the specified energy interval: indeed, the underlying power-law nature of the injection spectrum means that such cooling would be negligible compared to those electrons which are freshly injected.

Equation 4.42 may be rewritten as

$$\frac{\partial\mathcal{Z}}{\partial E_{\mathrm{e}}} = \frac{1}{r'^2}\frac{\partial}{\partial r'}\left[\frac{D(E_{\mathrm{e}},r')\,r'^2}{b}\frac{\partial\mathcal{Z}}{\partial r'}\right]\ , \tag{4.43}$$

where the substitution $\mathcal{Z} = b\,n_{\mathrm{CR,e}}$ invokes the spatial independence of the electron cooling function (such that b is not dependent on r). The PDE now has a similar structure to that solved previously (see equation 4.12), and the same method may be used to arrive at the solution,

$$\mathcal{Z} = \frac{\mathcal{Z}_0}{[4\pi D(E_{\mathrm{e}},r')\,E_{\mathrm{e}}\,b^{-1}]^{3/2}}\exp\left\{-\frac{r'^2}{4D(E_{\mathrm{e}},r')\,E\,b^{-1}}\right\}\ . \tag{4.44}$$

Here, the normalisation term follows from the BC that $\mathcal{Z}_0 = b\,N_{\mathrm{CR,e}}$, and the

relation $\tau_{\mathrm{cool}}(E_{\mathrm{e}}) = E_{\mathrm{e}}\, b^{-1}$ has been used. The steady-state result for electrons continuously injected at a single point source can be recovered by substituting back $\mathcal{Z} = b\, n_{\mathrm{CR,e}}$, thus giving

$$n_{\mathrm{CR,e}} = \frac{Q_{\mathrm{CR,e}}(E_{\mathrm{e}}, \mathbf{r}_i)\, \mathcal{V}_{\mathrm{S}}}{[4\pi D(E_{\mathrm{e}}, r')]^{3/2}\, \tau_{\mathrm{cool}}^{1/2}(E_{\mathrm{e}})} \exp\left\{ \frac{-r'^2}{4 D(E_{\mathrm{e}}, r')\, \tau_{\mathrm{cool}}(E_{\mathrm{e}})} \right\} . \qquad (4.45)$$

Fig. 4.7 plots this solution, showing various (normalised) electron spectra injected from a single source and being subjected to (spatially independent) inverse Compton and Coulomb cooling. The upper panel plots the electron spectral variation with distance from the injected point, where the dashed light grey line shows the steady-state spectrum expected at the injection point. Note that this is different to the injection spectrum; for instance, CRs may diffuse away, which occurs more readily at higher energies yielding a steeper spectrum than that injected (shown by the marked dashed blue line for comparison). The other lines (solid black through to solid grey) denote the spectrum at 0.1-0.5 kpc in 0.1 kpc increments when adopting a CMB energy density at $z = 7$ and no stellar radiation field. This shows a steepening of the spectrum with distance away from the source, being the result of both the energy dependence of the electron diffusion process, and the energy-dependence of the cooling function (see Fig. 3.3). The middle panel shows electron spectra calculated at 0.2 kpc (black lines) and 0.5 kpc (blue lines) from their injection location, indicating evolution according to no stellar radiation field (solid lines), stellar radiation field consistent with $\mathcal{R}_{\mathrm{SF}} = 3.5$ M$_\odot$ yr^{-1} (dashed lines), $\mathcal{R}_{\mathrm{SF}} = 35$ M$_\odot$ yr^{-1} (dot-dashed lines) and $\mathcal{R}_{\mathrm{SF}} = 350$ M$_\odot$ yr^{-1} (dotted lines) where star-formation is concentrated in a 1 kpc volume.

The most intensely star-forming model here relates to the extreme case in which there is a substantial impact from the stellar radiation field on the electron spectrum. For the less extreme stellar radiation models shown, the impact arising as the spectrum evolves is negligible and indicates that CR electrons must traverse through a substantial fraction of their host galaxy before their spectra differ noticeably between the instances where a strong stellar radiation field is present and where it is not. The lower-most panel
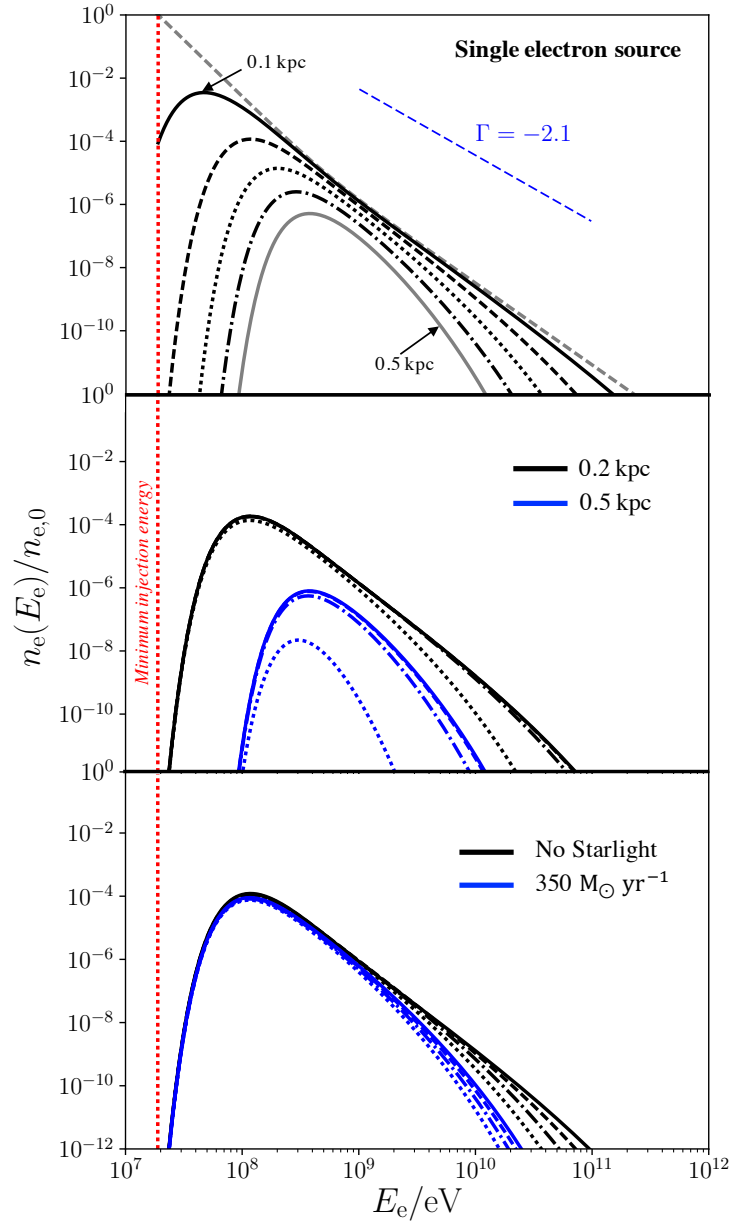
Fig. 4.7: Plots to demonstrate the evolution of CR secondary electron spectra as they propagate away from a single discrete source, demonstrating the impact of variations in the energy densities of the ambient (stellar and CMB) radiation fields. See the main text for details. These are normalised to the injection level at the minimum energy bound $n_{e,0}$, as indicated by the dashed red line (this minimum roughly corresponds to the energy of secondaries injected when a 0.28 GeV CR proton primary undergoes a pp interaction). Note that the injection spectral index is approximately $\Gamma = -2.1$, as indicated by the blue dashed line in the upper panel – subsequent steady-state spectra become progressively steeper than this due to the energy dependence of the electron cooling rate.

of Fig. 3.3 considers this in more detail. Here, all lines are calculated at 0.2 kpc from the injection position. Lines in black relate to the electron spectral evolution in a CMB-only radiation field, while those in blue are for the strong stellar radiation field with $\mathcal{R}_{\mathrm{SF}} = 350~\mathrm{M}_\odot~\mathrm{yr}^{-1}$ in addition to the CMB. These lines are plotted for different redshifts: $z = 6$ (solid line), 7 (dashed line), 8 (dot-dashed line) and 9 (dotted line), and this panel demonstrates that there is no significant contribution from stars to the ambient radiation field (i.e. it is dominated by the CMB energy density), with noticeable resulting differences in cooling arising only for the most energetic electrons (which are of little importance anyway due to the power-law nature of their spectrum).

When considering a distribution of injecting sources, any minor spectral differences that do still arise due to the various stellar radiation field model intensities would typically be 'drowned out' by another source emitting electrons nearby, which would be well within a 0.2 kpc radius. Thus, the earlier assumption that the stellar radiation field contribution to an non-uniform electron cooling function is negligible is further validated.

Numerical Scheme

Equation 4.45 is relevant for the steady-state distribution of electrons when they are injected by a single source. Since each injection solution is linearly independent, the extension of a single source to an ensemble of sources proceeds in a similar fashion to the case for the proton distribution. However, this time a two-stage process is required, such that the varying density profile of the galaxy in determining the level of electron injection at each position (in accordance with equation 3.47) is properly taken into account. The first step of the solution algorithm is to sample an MC points distribution according to the underlying density profile, as was done for the CR protons. From this, the steady-state proton distribution must be determined for each individual MC point, and then a further $N_{\mathrm{S},2}$ points are sampled using the same spherical MC sampling method, but this time weighted by the single-source steady-state proton solution. The resulting distribution is next convolved with the steady-state electron solution for a single source (equation 3.47) to give the resulting CR secondary electron profile for a single primary CR injection point. This re-

sult is then convolved with the original proton source MC point distribution to give the full galactic profile for electrons. The resulting CR energy density (i.e. when integrating over the full resulting electron spectrum) was shown earlier in Fig. 4.1 (blue line), together with that for the CR protons (black line). This was calculated when adopting a SN event rate of $\mathcal{R}_{\mathrm{SN}} = 0.1 \ \mathrm{yr}^{-1}$, and used $N_{\mathrm{S}} = 10,000$ MC points to generate the proton distribution, and a further $N_{\mathrm{S},2} = 1,000$ MC points at each N_{S} point to calculate the electron profile. These MC simulation parameter choices offered an acceptable signal-to-noise ratio.

Chapter 4 summary: *The propagation of charged, energetic CR particles is typically hampered by ambient, turbulent magnetic fields in interstellar environments where continuous random scatterings tend to yield a propagation regime better described as diffusion (or advection if the ambient magnetised fluid is moving sufficiently rapidly as a bulk flow) on macroscopic scales, even though the microscopic speed of the particles is close to the speed of light. In this chapter, the transport equation is introduced as a means by which the advective or diffusive propagation of energetic CRs can be modelled in the previously defined One-Zone and Two-Zone models. Forms of the transport equation for protons and electrons are separately presented, and their solutions – both semi-analytic and fully numerical, as appropriate – are discussed for both the One-Zone (diffusion-dominated) scenario and Two-Zone (diffusion with advection) scenario. The resulting spectra of CR primary protons and secondary electrons are presented in both cases, and the key features and behaviours of the solutions are discussed in various parts of the protogalaxy system.*

Chapter 5

Particle and Radiative Heating in Protogalaxies

Conventional heating processes in local star-forming galaxies often rely on the presence of dust (including polycyclic aromatic hydrocarbons, PAHs) as a medium which may absorb, scatter and reprocess starlight to produce a heating effect (see e.g. Bakes and Tielens 1994; Wolfire et al. 1995; Meijerink and Spaans 2005; Serra et al. 2016; Hu et al. 2017). Indeed, starburst galaxies in the local Universe are rich in dust (see section 1.3) making this a very important avenue by which feedback can operate. In high-redshift ($5 \lesssim z \lesssim 9$) protogalaxies, however, dust would not be as abundant and would therefore be unlikely to play as important a role in catalysing interstellar heating. Instead, the main mechanism by which radiative heating could operate (due to stellar emission and thermal X-ray emission from hot interstellar gases) would be by Thomson (Compton) scattering, which is much less effective. In the absence of strong dust-aided radiative reprocessing effects, other heating processes –

for example, interstellar heating due to CRs – would instead move to play an important role, especially in these actively star-forming environments where it has been shown that CRs would be abundant.

5.1 Heating by Stellar and Thermal Emission

The level of heating experienced due to photon irradiation of a medium at some position r is determined by the tendency of the medium at that position to absorb the incident radiation. This is quantified by the absorption coefficient α (defined in general terms in equation 3.34), which is the product of the local number density of scatterers and the effective scattering cross-section associated with the relevant process. The integrated effect of α over some path between a source location and r quantifies the attenuation experienced by the radiation along its path, and sets the irradiating intensity incident at that location.

The radiative emission from the stellar population of a galaxy has a substantial optical and soft UV component, while thermal emission from hot baryonic interstellar gases would predominantly be comprised of low-energy X-rays (a typical energy of 1 keV is adopted hereafter, where necessary). In the case of the X-rays, the corresponding scattering cross-section can be approximated as $\sigma_{\rm T}$. By contrast, the cross-section appropriate for the stellar radiation in a protogalaxy ISM must account for some energy dependence, given that lower-energy non-ionising photons may additionally be scattered and attenuated by semi-ionised gas, trace metals and the trace quantities of dust. Such semi-ionised regions containing dust and trace metals would presumably be attributed to a denser, cooler ISM component in pressure equilibrium with a hotter and more ionised phase. Like the Milky Way, this may be modelled to be present in some 30% of the ISM of a protogalaxy by volume (see, e.g. Ferriere 2001; Draine 2011). In the following calculation, a dust fraction of 1% of the Milky Way level was adopted in these dense regions, while scattering cross-sections were otherwise informed by Cruddace et al. (1974). The ionising fraction of stellar photons scatter in a similar manner to the thermal X-rays, and so were also allocated a scattering cross-section of $\sigma_{\rm T}$. This ionising com-

ponent of the stellar radiation can be assumed to comprise of photons all at an energy of 13.6 eV, as this is the lowest energy at which they may be ionising. This part of the spectrum is well within the Wien part of the Planck function, whereby most photons are at lower energies – thus, those close to the ionisation threshold would effectively dominate. The non-ionising component of the stellar radiation has a modal energy of $E_\gamma = 2.82\ k_B T_*$, and this was taken to be representative of the photons in this band. The relative intensity of the contributions from these two spectral components was weighted according the integrated Planck function over energy in these two regimes to give a reasonable representation of the ionising and heating power of the stellar radiative emission.

5.1.1 Computational Scheme

The computational scheme to calculate radiative heating rates due to both the thermal X-rays and the stellar emission was essentially the same, however the overall luminosity in each case was modelled differently. The total stellar luminosity was determined by modelling all the stars in the galaxy as a blackbodies of temperature $T_* = 30,000$ K (i.e. type O/B), with their luminosity following from the Stefan-Boltzmann relation (equation 1.9). This was then multiplied by 10^6, the size of a stellar population that would yield a stellar luminosity consistent with that expected for a starburst galaxy exhibiting a SN event rate of $\mathcal{R}_{SN} \approx 0.1\ \mathrm{yr}^{-1}$, e.g. from simulations using Starburst99 (see, e.g. Leitherer et al. 1999; Hirashita et al. 2003, for details).[1] The total stellar luminosity of the entire galaxy thus followed as around 2.8×10^{44} erg s^{-1}. For the soft X-rays, a total galactic luminosity of $L_X = 8.3 \times 10^{38}$ erg s^{-1} was instead directly adopted, corresponding roughly to a system with $\mathcal{R}_{SN} \approx 0.1\ \mathrm{yr}^{-1}$ or $\mathcal{R}_{SF} \approx 16\ \mathrm{M}_\odot\ \mathrm{yr}^{-1}$. This was estimated based on scaling relations in the literature (see, e.g. Li and Wang 2013; Appleton et al. 2015; Sarkar et al. 2016), but is also similar to the diffuse thermal X-ray luminosity of M82 (see, e.g. Watson et al. 1984). Point source contributions to the X-ray emission were

---

[1]These Starburst99 simulations adopted a Salpeter initial mass function, of index -2.35 between 0.1 and 100 $\mathrm{M}_\odot$, with solar metallicity and population age of 10 Myr. While not strictly suitable for a high redshift stellar population, this was sufficient for the rough comparative estimate required here.

ignored given that in protogalaxies, by $z = 7$, many usual X-ray point source candidate objects would not yet have had sufficient time to form.

In the case of both the stellar and thermal X-ray heating calculations, the total galactic luminosity was distributed among a random sphere of $N_{\rm S}$ MC points, spread throughout a sphere of radius $r_{\rm gal} = 1$ kpc and weighted by the underlying density profile of the model protogalaxy (which the hot baryons and stellar population would both presumably trace). Accounting for the inverse square law and attenuation between each source point and some observation point r, the irradiative flux incident at a point r due to each source was calculated. The sum of this was used to find incident flux at r due to the full ensemble of source points, and the absorption coefficient α was then multiplied by this irradiating power in order to determine the level of heating arising at that point. A choice of $N_{\rm S} = 10,000$ points was found to yield a reasonable signal-to-noise ratio.

5.1.2 Stellar Heating

The resulting volumetric heating power due to the stellar photons peaks within the central parts of the protogalactic ISM (where the radiation field is at its most intense), where it reaches a level of around $10^{-25}\,\mathrm{erg\ cm^{-3}s^{-1}}$. The full profile is shown as the blue dashed line in Fig. 5.2, where it is compared to the heating power derived from CRs.

Heating rates due to stellar radiation have also been calculated in previous studies in the context of Galactic and star-forming environments. Applications specifically to protogalaxies are limited, however the literature is well-populated with research that balances cooling rates against heating rates for other irradiated systems that are assumed to be in thermal equilibrium (see, e.g. Baek et al. 2005). Many of these consider specific environments in either local starburst environments or a Galactic settings rather than average ISM conditions, but they offer results which can be scaled to compare with those calculated here. For example, in Glover and Clark (2012), stellar heating rates for Galactic molecular clouds were considered, due to their irradiation by an interstellar radiation field (ISRF) modelled on that of the Milky Way (Draine 1978). These heating rates were calculated for cloud number densities in the

range $n_\mathrm{H} = 10^1 - 10^6$ cm^{-3}, in which the relevant heating mechanisms were specified to be a combination of photo-electric by dust extinction, molecular hydrogen (H$_2$) photodissociation, and the pumping of highly excited vibrational levels of H$_2$ by UV photons – the 'UV pump' (Burton et al. 1990). Of these, photo-electric heating dominated, driving a heating power of around 10^{-25} erg cm^{-3} s^{-1}. In the protogalaxy model considered here, the ISM gas was specified to be mainly ionised, while its dust fraction was negligible compared with the Milky Way. Thus none of the heating mechanisms used in the Glover and Clark (2012) study could be feasible dominant channels in a protogalaxy environment. Moreover, the ISRF would be substantially different in a protogalaxy, typically being much more intense. Despite this, the Glover and Clark (2012) results can still be used as a comparative benchmark by scaling: firstly, the cross-section of photo-electric grain heating is around 1.5×10^{-21} cm^2 (see Draine 1978), i.e. around 10^4 times greater than that for simple Thomson scattering. Moreover, the ISRF luminosity in a protogalaxy is around 10^4 times than that of the Milky Way, based on estimates of the star counts of the host galaxies (10^6 stars in the protogalaxy compared to 10^{11} stars in the Milky Way), the bolometric luminosities of those stars (type O/B stellar luminosities are around 10^6 times greater than those of the lower-mass stars that tend to dominate the Milky Way population – see Lada 2006; Ledrew 2001; Beech 2011) and the volume containing these stars (10^3 times smaller in the protogalaxy). It therefore follows that, in the case of pure Thomson scattering (with the scattering cross-section being smaller by a factor of 10^4), and in a protogalactic ISRF (where the intensity is greater by a factor of 10^4), the stellar heating rate in the protogalaxy should actually be fairly similar to that determined for the molecular cloud (when comparing similar media densities), around 10^{-25} erg cm^{-3} s^{-1}. Indeed, this is broadly in line with the result calculated here.

The stellar heating power in Fig. 5.2 may also be compared with the energy feedback rates adopted in hydrodynamical simulation suites, which offer a better indication of average ISM conditions. A key example of such is the Virgo Consortium's Evolution and Assembly of GaLaxies and their Environ-

ments (hereafter EAGLE) project, which follows the formation and evolution of galaxies in a representative ΛCDM Universe simulation, as introduced in Schaye et al. (2015). The large sizes of these simulations limits the resolution on sub-galactic scales due to computational expense. This means that certain physics on sub-galaxy scales (e.g. associated with feedback or outflows from individual star clusters) is lacking, and self-consistent modelling must be approximated with a so-called 'sub-grid' approach. While pragmatic, this hampers the insight that simulations can provide into the detail of feedback processes at work within galaxies. Moreover, their predictive power is limited for the properties of galaxies, and this necessitates calibration against the observed Universe with fine-tuning of appropriate scaling parameters invoked to make-up for the limitations in the unresolved physics of the simulation. In the EAGLE simulations, the details of such calibration efforts are outlined in Crain et al. (2015), which also discusses the energy feedback from star-formation. This is implemented in a discrete, stochastic manner, with a set quantity of energy being injected per distinct feedback event (instead of a continuous process). The power of this energy feedback is scaled (becoming larger than a physical sub-grid feedback model) to account for artificial numerical losses. Crain et al. (2015) adopts a thermal feedback energy injection of 1.736×10^{49} erg $M_\odot^{-1}$ per stellar mass formed in EAGLE which, if applied to the protogalaxy model considered in this thesis (with $\mathcal{R}_{\mathrm{SF}} \approx 160 \, (\mathcal{R}_{\mathrm{SN}}/\mathrm{yr}^{-1})$ $M_\odot \, \mathrm{yr}^{-1}$ and spherical volume of radius 1 kpc) would imply an average ISM stellar feedback power of $2.265 \times 10^{-22} \, (\mathcal{R}_{\mathrm{SN}}/\mathrm{yr}^{-1})$ erg $\mathrm{cm}^{-3} \, \mathrm{s}^{-1}$, i.e. substantially larger than any of the lines shown in Fig. 5.2. A very similar stellar feedback implementation and power is used in the IllustrisTNG galaxy formation simulation framework (see Pillepich et al. 2018). The discrepancy between the simulations compared to the lines plotted in Fig. 5.2 lies in the vastly different approach they adopt in modelling feedback (stochastic heating in EAGLE/IllustrisTNG compared to the progressive heating in this work), as well as the enhanced feedback power required in the simulations (resulting from calibration to counter artificial numerical losses) compared to 'first-principles' sub-grid physical models.

5.1.3 Thermal X-ray Heating

The peak interstellar heating power due to the X-rays reaches around 10^{-26} erg cm^{-3} s^{-1}, and the full profile is also shown in Fig. 5.2 (the dashed red line). In this plot, it can be seen that the non-ionising stellar radiation is attenuated more effectively than X-rays, meaning that its corresponding heating power falls below that which due to the thermal X-rays away from the central interstellar regions of the protogalaxy.

While direct literature comparisons for X-ray heating in protogalaxies could not be found, scaling comparisons could again be used to corroborate the heating levels calculated here. This time the heating mechanisms attributed to X-rays in low and high-redshift galaxies are unchanged, because the process of X-ray ionisation followed by thermalisation through Coulomb interactions of the emitted electron would presumably arise in any partially-ionised ISM. Moreover, the scattering of the free-electrons (either in a plasma, or when electrons are emitted after ionisation processes) would also persist in any system where free-electrons are present or can emerge. In Meijerink and Spaans (2005) an X-ray heating power of 10^{-24} erg cm^{-3} s^{-1} was quoted as a characteristic value appropriate for a starburst environment (based on NGC 253, with $\mathcal{R}_{SN} \approx 0.1$ yr^{-1} – see Ferriere 2001), with an ISM density of $n_H = 10^3$ cm^{-3}. This value can be used for an immediate scaling comparison, since the heating processes at work are the same (as are the associated cross-sections and radiation fields). The relative density of the ISM target in Meijerink and Spaans (2005) compared to that used here (10 cm^{-3}) can be used to scale the X-ray heating power, which indicates that a level of 10^{-26} erg cm^{-3} s^{-1} should be expected for a protogalaxy with $\mathcal{R}_{SN} = 0.1$ yr^{-1}. This is indeed consistent with the present results (see Fig. 5.2), and indicates that the method used here to calculate radiative heating rates is reasonable.

5.2 Direct Cosmic Ray Heating

The microphysics of the direct Coulomb (DC) cosmic ray heating process relies on the injection of charged pions by the the dominant pp hadronic interaction process (see section 3.4.1). It can be shown that these charged pionic secon-

daries inherit a large fraction of the primary CR energy over a small number of interactions. In a single interaction, around 60% of the CR primary energy is directly passed to pions (when accounting for multiplicities over energy), with the remaining fraction being transferred to secondary neutrons, protons (both of these nucleons can undergo further hadronic interactions) and neutrinos (Blattnig et al. 2000; Dermer and Menon 2009). The proton component adopts around 30% of the remaining energy. This means that, after undergoing a single hadronic interaction, an energy fraction of $f_{pp} \approx 0.3$ is retained by a beam of protons. The effective path-length for a proton beam to lose its energy is therefore given by

$$\bar{r}_{p\pi} \;=\; \frac{\sum_{k=1} k\, r_{p\pi}\, W_k(f_{pp})}{\sum_{k=1} W_k(f_{pp})} \;, \tag{5.1}$$

where $r_{p\pi}$ is the pp interaction mean-free-path (defined by equation 3.24). This uses an energy weighting factor, $W_k = f_{pp}^{k-1}(1-f_{pp})$, which is normalised such that

$$\sum_{k=1} W_k(f_{pp}) \;=\; 1 \;. \tag{5.2}$$

It therefore follows that

$$\begin{aligned}
\bar{r}_{p\pi} \;&=\; r_{p\pi}(1-f_{pp}) + 2\,r_{p\pi} f_{pp}(1-f_{pp}) \\
&\quad + 3\,r_{p\pi} f_{pp}^2(1-f_{pp}) + 4\,r_{p\pi} f_{pp}^3(1-f_{pp}) + \cdots \\
&=\; r_{p\pi}(1-f_{pp})\left(\frac{\mathrm{d}}{\mathrm{d}f_{pp}}\sum_{k=1} f_{pp}^k\right) \\
&=\; r_{p\pi}\,(1-f_{pp})^{-1} \;. \tag{5.3}
\end{aligned}$$

For $f_{pp} = 0.3$, this gives an effective interaction mean free path of $\bar{r}_{p\pi} = 10\, r_{p\pi}/7$. Hence, within just a small number of interaction events, nearly 100% of the original CR primary energy is deposited. Moreover, the interaction timescale is much less than the particle containment timescale, as CRs become entrapped by the magnetic field of their host galaxy ($r_{p\pi}/c \ll t_{con}$). This means that instantaneous energy transfer from the CR primary proton to its

secondaries at the site of the initial interaction can be safely assumed.

Thermalisation in the DC process is governed by Coulomb interactions. Section 3.3.1 showed that energetic electrons can cool and transfer their energy by a number of means, including radiative processes (from inverse Compton and synchrotron emission), free-free losses and, when relevant, adiabatic cooling. The overall thermalisation efficiency of a beam of energetic CR protons of energy E_{p} is quantified by the product of the fractional branching ratio for the formation of charged electron secondaries, f_{e}, and the proportion of electron energy lost to Coulomb processes in the ISM compared to the total energy loss rate, i.e. $f_{\mathrm{therm}}(E_{\mathrm{p}}) = (\mathcal{M} \, f_{\mathrm{C}} \, f_{\mathrm{e}})|_{E_{\mathrm{e}}}$, with $\mathcal{M}$ as the electron production multiplicity (where e.g. $\mathcal{M} = 4$ and $E_{\mathrm{e}} = 0.0375 E_{\mathrm{p}}$ for a 1 GeV primary – see section 3.2.2). The energy fraction lost to Coulomb processes is given by

$$f_{\mathrm{C}}(E_{\mathrm{e}}, n_{\mathrm{H}}) = \left. \frac{\tau_{\mathrm{C}}^{-1}}{\tau_{\mathrm{C}}^{-1} + \tau_{\mathrm{rad}}^{-1} + \tau_{\mathrm{cool}}^{-1}} \right|_{E_{\mathrm{e}}, n_{\mathrm{H}}}, \tag{5.4}$$

with τ_{C}, τ_{rad} and τ_{cool} (see equation 1.2) as the Coulomb, radiative (inverse Compton and synchrotron) and free-free (bremsstrahlung) cooling timescales for the energetic electrons respectively. If adiabatic cooling operates, the associated timescale τ_{ad} is also included in equation 5.4. f_{C} is most strongly influenced by the energy of the cooling electron, E_{e}, and the ambient density of the medium into which it is thermalising, n_{H}. These dependencies are plotted in Fig. 5.1, where the upper panel shows the energy dependence of the timescales (plotted in black) and the resulting impact this has on the Coulomb thermalisation fraction (f_{C}, plotted in red) while the lower panel shows the density dependence. These demonstrate that the lower-energy electrons (which would be injected by primary CRs of energies 1-10 GeV) are far more important in driving DC heating compared to their higher-energy counterparts. By contrast, more energetic electron secondaries are predominantly cooled by radiative processes and are less engaged with Coulomb thermalisation. In media of higher densities, Coulomb thermalisation operates more efficiently, especially if the ionisation fraction is also high. Coulomb thermalisation into lower density environments is much less efficient.
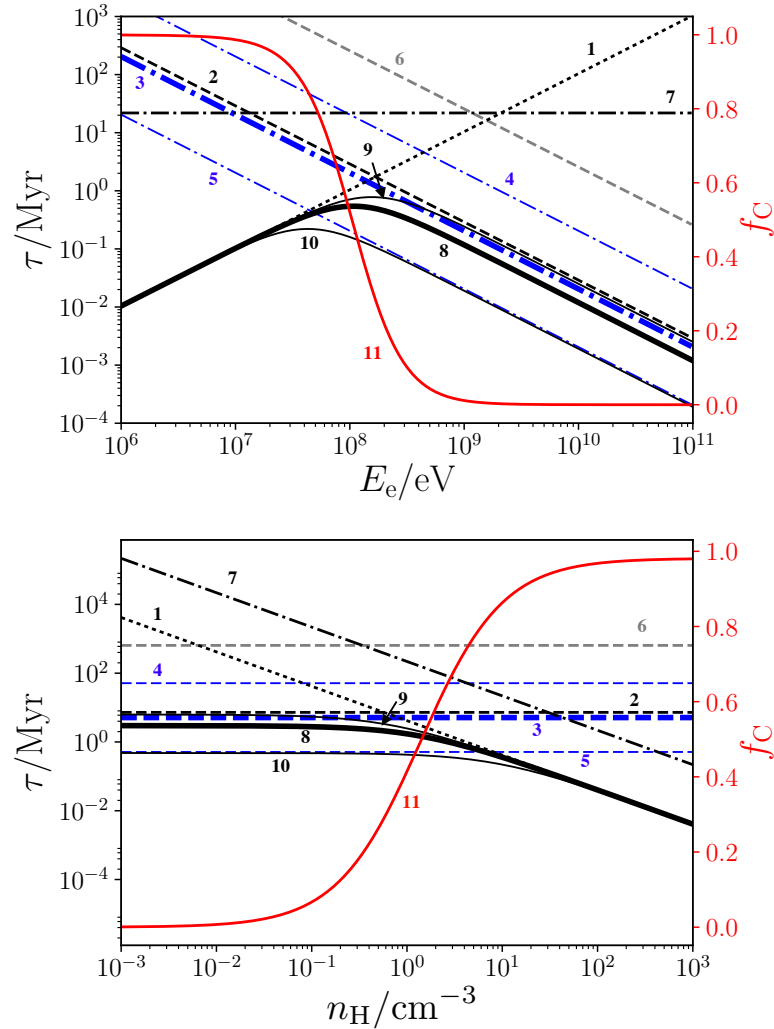
Fig. 5.1: Upper panel: Variation of timescales for energy loss processes of CR secondary electrons over energy, including Coulomb scattering (black dotted line 1), radiative losses due to inverse Compton scattering with the CMB (black dashed line 2), and stellar radiation fields (blue dashed lines – for which the thickest line 3 is due to the stellar radiation field resulting from a star population yielding $\mathcal{R}_{SN} = 1$ yr^{-1}, the upper line 4 is for $\mathcal{R}_{SN} = 0.1$ yr^{-1}, while the lower line 5 is for a system with $\mathcal{R}_{SN} = 10$ yr^{-1}), radiative synchrotron in a 5 μG magnetic field (dashed grey line 6), and free-free bremsstrahlung (black dot-dashed line 7). The resulting total is given by the solid black line, with the thickest (line 8) due to the model corresponding to $\mathcal{R}_{SN} = 1$ yr^{-1} (and thin line 9 for 0.1 yr^{-1} and line 10 for 10 yr^{-1}). An overall estimate for CR electron thermalisation efficiency f_C is plotted by the red line 11 (and corresponding y-axis to the right of the plots). This gives the fraction of CR electron energy transferred by Coulomb scattering, calculated by equation 5.4. An ambient interstellar density field of uniform density $n_H = 10$ cm^{-3} is adopted here. **Lower panel:** As above, but quantities are now calculated for fixed initial electron energy of $E_e = 40$ MeV over varying ambient densities.

5.2.1 One-Zone Model

The volumetric DC heating power imparted by CRs on a medium at some location r is given by

$$\dot{Q}_{\mathrm{DC}}(r) = \int_{E_{\min}}^{E_{\max}} \mathrm{d}E_{\mathrm{p}}\, n_{\mathrm{CR,p}}(E_{\mathrm{p}}, r)\, \mathrm{c}\, f_{\mathrm{C}}(E_{\mathrm{p}}, r)\, \alpha(E_{\mathrm{p}}, r)\,, \qquad (5.5)$$

in which the energy bounds are chosen according to the limits of the adopted CR spectral model, while the product $n_{\mathrm{CR,p}}(E_{\mathrm{p}}, r)\,\mathrm{c}$ gives the CR irradiation through the position at r (being the equivalent CR 'flux' passing through a point from all directions).[2] $f_{\mathrm{C}}(E_{\mathrm{p}}, r)$ follows from the discussion above (equation 5.4) in which the density dependence is absorbed into the position dependency, and $\alpha(E_{\mathrm{p}}, r)$ is given by equation 3.34. Equation 5.5 may alternatively be expressed explicitly in terms of an attenuation factor, i.e. with $\mathcal{A}(E_{\mathrm{p}}, \mathbf{r}; \mathbf{r_i})$ condensed out of equation 4.14 for the CR number density. While this is equivalent to the formulation presented here, it demonstrates how the attenuation of CRs along their propagation may be separately computed and later reinstated to yield the same final result. Computationally, an algorithm that does this would be advantageous in some numerical implementations, e.g. in which repeated calls to an MC routine for the computationally expensive attenuation part of a CR heating calculation may be replaced by a single realisation to be post-applied to many simulation runs.

Fig. 5.2 shows the profiles of the CR heating power calculated for three SN event rates ($\mathcal{R}_{\mathrm{SN}}$ = 0.1, 1 and 10 yr^{-1}). The thick black lines (dot-dashed, dotted and solid) show the heating power once the galactic magnetic field has saturated. An initial free-streaming heating power is also shown for comparison for each of the three SN event rates in grey, corresponding to a time very early in the evolution of the host galaxy at which the intense star-forming burst had not yet been transposed into the rapid magnetisation of the ISM. This indicates that an increase in heating power by around 5 orders of

---

[2] These CRs pass locally through the point at highly relativistic speeds and can be thought of in terms of an isotropic CR 'beam' with effective intensity quantified by the CR local number density $n_{\mathrm{CR,p}}(E_{\mathrm{p}}, r)$. In the case of the One-Zone model, this follows from equation 4.14, but equation 5.5 actually holds generally for any number density of CR protons, so also dictates the required approach in the Two-Zone model (or any other scenario where the volumetric CR distribution is known.
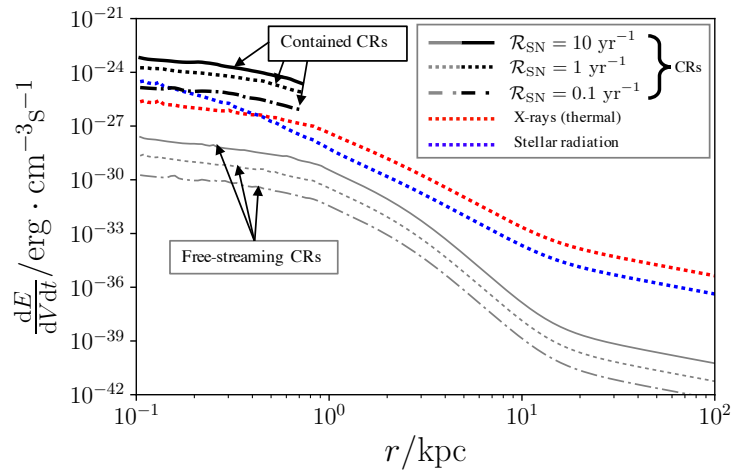
Fig. 5.2: CR heating power in the One-Zone model, when adopting SN event rates of $\mathcal{R}_{SN} = 0.1, 1$ and 10 yr^{-1}, corresponding to the dot-dashed, dotted and solid lines respectively. Heating rates in grey represent the levels expected before the growth of the galactic magnetic field (i.e. when they effectively propagate by free-streaming), while those lines plotted in black are for the heating rates after CR containment by a saturated magnetic field. For comparison, heating profiles due to irradiation by starlight and diffuse soft X-rays are plotted in blue and red respectively, both of which correspond to the radiation field which arises when adopting a galaxy model with $\mathcal{R}_{SN} = 1.0 \text{ yr}^{-1}$. As in Fig. 4.1, for the case of confined CR heating by the magnetic field, only the inner regions of the heating profile are shown. At large distances (e.g. beyond 10 kpc), the corresponding CR heating power would be expected to fall back to levels similar to the free-streaming case.

magnitude would arise due to the magnetisation of the host and the resulting CR containment (this containment arises as the CR transport regime evolves from a free-streaming scenario to diffusion, thus hampering their free escape from the host galaxy). For comparison, the figure also shows the estimated heating power due to starlight and diffuse X-rays, following from the earlier discussion in sections 5.1.2 and 5.1.3. These are both scaled to show the heating power in the intermediate system, with $\mathcal{R}_{SN} = 1.0 \text{ yr}^{-1}$.

For the contained CR heating stage, only the profile segments for the region within the ISM of the protogalaxy are shown. In this region CR transport is facilitated mainly by diffusion, and is strongly governed by the strength and structure of the interstellar magnetic field. Far beyond the central region shown, the CR particles are practically free-streaming, meaning that the heating rate is expected to drop-off to approximately that of the initial free-streaming stage, as shown by the grey lines. In the interfacing regions between the ISM and CGM, the magnetic field and resulting CR propagation is less straightforward to model and not well understood, and any attempts would

have substantial caveats and great uncertainties. Furthermore, an appropriate formulation of a kinetic description of particles when transitioning from a diffusive propagation regime to a free-streaming scenario (as would presumably occur in galactic outskirts) is theoretically challenging. As mentioned before, these matters deserve an independent study in their own right and so are left to future, more thorough investigations.

Heating Power and Energetics

Before the magnetic confinement of CRs can arise (i.e. when the growth of the interstellar magnetic field is still in its early stages), the ISM is predominantly heated by radiation from stars and the diffuse X-rays emitted from hot interstellar baryons. This picture rapidly changes after the onset of star-formation: the development of a galactic magnetic field to μG strengths (perhaps occurring as quickly as within a few Myr) strongly confines CRs and suppresses their free-streaming propagation into circumgalactic/intergalactic space. By the time that CR containment has reached a steady-state distribution, the associated heating power the CRs drive would reach 10^{-25}, 10^{-24} and (almost) 10^{-23} erg cm^{-3} s^{-1} for systems with $\mathcal{R}_{\mathrm{SN}} = 0.1$, 1 and 10 yr^{-1} respectively. It is worth noting that the final CR heating rate achieved is slightly lower than might be expected from a direct scaling with $\mathcal{R}_{\mathrm{SN}}$ in the most intensely star-forming model, with $\mathcal{R}_{\mathrm{SN}} = 10$ yr^{-1}. This is because the resulting boost in the energy density of the starlight increases inverse Compton loss rates to the point that the overall DC heating efficiency is affected. However, in all cases, these CR heating powers exceed the respective levels predicted for starlight and diffuse X-ray heating.

Some caution is required when drawing these comparisons. Fig. 5.2 shows the case where the X-ray heating resulting from a total diffuse X-ray luminosity of 8.3×10^{38} erg s^{-1}, and the normalisation of the profile for diffuse X-ray heating is scaled with the total power of these X-rays. As such, this comparison needs modification when higher values for the total thermal X-ray luminosity of a galaxy is adopted. For example, if the X-ray power were three orders of magnitude higher, at 8.3×10^{41} erg s^{-1}, the resulting X-ray heating would easily come to dominate over the starlight heating in the central regions of the

galaxy. If it were increased another order of magnitude, to 8.3×10^{42} erg s^{-1}, it would even begin to compare to the CR heating power in the inner regions of the ISM for a galaxy of SN event rate $\mathcal{R}_{\mathrm{SN}} = 0.1 \, \mathrm{yr}^{-1}$.

At $\mathcal{R}_{\mathrm{SN}} = 0.1 \, \mathrm{yr}^{-1}$, the total radiative stellar and X-ray powers are set to be 2.8×10^{44} erg s^{-1} and 8.3×10^{38} erg s^{-1} respectively. By contrast, the amount of energy being passed to the CR primaries is much less, at 3.0×10^{40} erg s^{-1}, i.e. 4 orders of magnitude lower than the stellar radiation. These levels of irradiation yield a total power deposited into the ambient medium of 1.9×10^{38} erg s^{-1} and 2.6×10^{37} erg s^{-1} for stellar radiation and X-rays respectively while, for CRs, a contained heating power of 2.1×10^{39} erg s^{-1} develops (from a free-streaming power of 7.5×10^{32} erg s^{-1}). These values all scale directly with the SN event rate (with the exception of CR heating in extremely high SN event rates, as discussed above). In general, this means that the radiative X-ray heating power is around 4 orders of magnitude larger than that due to free-streaming CRs. But, after the initiation of contained CR heating, it consistently follows that the radiative heating power becomes sub-dominant to the CRs, which show an amplification in excess of 5 orders of magnitude in their energy deposition ability compared to the free-streaming case. This results in a CR heating power exceeding that of X-rays by as much as 2 orders of magnitude.

5.2.2 Two-Zone Model

In the Two-Zone model, the total CR luminosity available to fuel CR heating is partitioned according to zone solid angles (cf. equation 2.7 and the corresponding discussion). However, it was argued in section 2.2 that the amount of energy supplied in CRs into Zone A (the outflow cone) is actually lower by a further factor, as given by equation 2.9. Of this energy, some fraction f_{g} is used in pushing the outflow wind from the gravitational potential of the host galaxy, leaving a CR luminosity available to contribute to heating of $L_{\mathrm{CR,eff,A}} = (1 - f_{\mathrm{g}}) \, \nu_{\mathrm{d}} \, L_{\mathrm{CR,eff,A}}$. By contrast, in Zone B where ISM dynamics are less complex, only the solid angle partition is applicable in specifying the CR energy budget available for heating.

Generally, the volumetric heating power by CRs (due to the DC ther-

malisation mechanism) at any given location is given by equation 5.5. In Zone A, $n_{\mathrm{CR,p}}$ is determined from the CR number density/spectral profile for the wind outflow, as calculated in section 4.2.2, for diffusion-dominated or advection-dominated systems. In Zone B, $n_{\mathrm{CR,p}}$ follows from the One-Zone result (but with an appropriate solid angle scaling to account for the different energy budget of the Two-Zone system). In Zone A, it is of physical interest to consider the case in which both diffusion and advection operate within an outflow – either at comparable rates, or with different processes becoming important at different altitudes. This is because the negligible flow velocities at low altitudes of many galactic wind systems (see section 2.2.1, in particular the outflow velocity profile shown in Fig. 2.4, or literature studies/simulations, e.g. Farber et al. 2018) would not advect CRs sufficiently fast to overcome their diffusive propagation. This would be the case up to some 'cross-over' altitude at which the outflow wind would become sufficiently fast to support advection dominance (for a given particle energy), meaning that a typical outflow wind would be unlikely to be dominated by a single process along its full length.

Without losing generality, the relative importance of advection or diffusion in the propagation of CRs in an outflow may be roughly determined by use of timescales. This can be done by weighting the pure diffusion limit (hereafter $n_{\mathrm{CR,p}}^{\mathrm{diff}}$) and pure advection ($n_{\mathrm{CR,p}}^{\mathrm{adv}}$) solutions to the transport equation by their respective timescales at each position h and energy E_{p} (to capture the variation of the flow velocity over position as well as that of the diffusion coefficient over energy) such that a reasonable description of the resulting particle profile can be found by the summed contribution,

$$\bar{n}_{\mathrm{CR,p}}(E_{\mathrm{p}}, h) = \left\{ \omega_{\mathrm{diff}}\, n_{\mathrm{CR,p}}^{\mathrm{diff}}(E_{\mathrm{p}}) + \omega_{\mathrm{adv}}\, n_{\mathrm{CR,p}}^{\mathrm{adv}}(E_{\mathrm{p}}) \right\}\big|_h \ , \qquad (5.6)$$

where

$$\omega_{\mathrm{diff}}(E_{\mathrm{p}}, h) = \left.\frac{\tau_{\mathrm{diff}}^{-1}}{\tau_{\mathrm{diff}}^{-1} + \tau_{\mathrm{adv}}^{-1}}\right|_{\{E_{\mathrm{p}}, h\}} , \qquad (5.7)$$

and

$$\omega_{\mathrm{adv}}(E_{\mathrm{p}}, h) = \left.\frac{\tau_{\mathrm{adv}}^{-1}}{\tau_{\mathrm{diff}}^{-1} + \tau_{\mathrm{adv}}^{-1}}\right|_{\{E_{\mathrm{p}}, h\}} . \qquad (5.8)$$
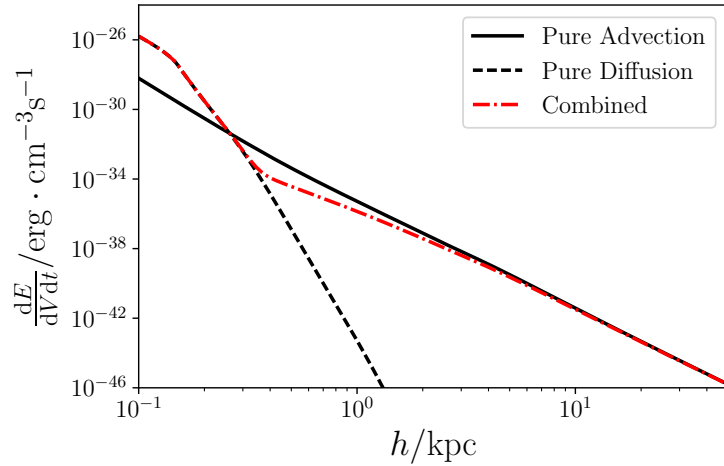
Fig. 5.3: The 'Zone A' CR heating profile along an outflow cone. The diffusion limit result is shown by the black dashed line, while the pure advection result is shown by the solid black line. A parametric combined scaling for the CR heating power when both advection and diffusion operate concurrently is indicated by the dot-dashed red line. The contributions to the advection-limit heating power adopt a model with outflow opening angle 55°, thermalisation efficiency $\mathcal{Q} = 0.01$, and mass loading $\mathcal{P} = 0.1$, driven by a SN event rate of $\mathcal{R}_{\mathrm{SN}} = 0.1 \ \mathrm{yr}^{-1}$.

The two timescales are the position-dependent advection timescale ($\tau_{\mathrm{adv}} = h/v(h)$) and the energy-dependent diffusion timescale ($\tau_{\mathrm{diff}} = h^2/4D(E_{\mathrm{p}})$). The resulting Zone A CR heating profile via the Coulomb thermalisation mechanism is shown by the black dashed (pure diffusion) and solid (pure advection) lines in Fig. 5.3 for a system with a SN-event rate of $\mathcal{R}_{\mathrm{SN}} = 0.1 \ \mathrm{yr}^{-1}$, and a conical outflow of opening angle of 55°. For the outflow wind, the reference model described in section 2.2.1 is invoked (with thermalisation efficiency $\mathcal{Q} = 0.01$, and mass-loading factor $\mathcal{P} = 0.1$), in which a terminal velocity of $v_\infty \approx 290 \ \mathrm{km \ s}^{-1}$ develops. It can be seen that, in the diffusion limit, CRs drive a heating of the ISM of their host galaxy but, when advective transport becomes important, CR energy deposition is redistributed to extend beyond the interior environment of the host. The dot-dashed red line in Fig. 5.3 also shows the CR heating profile calculated for the case of concurrent advection and diffusion. This demonstrates the importance of CR diffusion at low altitudes where outflow velocities are small, while advection overtakes at higher altitudes, above approximately $h \approx 0.4$ kpc, to change the energy deposition pattern which emerges.

The heating profile shown in Fig. 5.3 is suitable for a system with a point-like boundary condition, located at $h = 0$. However, this is in contrast with

many observations of outflows and star-forming regions which show that SN events can arise throughout the disk region of a galaxy, up to at least half their estimated scale-radius (Hakobyan et al. 2012, 2014, 2016). An extension to the model to account for the impact of a more physically extended core region is therefore of physical interest.

This was considered, with the result shown in Fig. 5.4, where lines retain their earlier definitions and where the starburst extended CR injection region is indicated by the light blue shaded region, as marked. To calculate this extended profile, a similar MC scheme to that adopted in the numerical simulations of the One-Zone model was invoked, in which a spherical distribution of $N_S = 1,000$ points up to 0.5 kpc from $h = 0$ (being half the adopted scale-radius for the protogalaxy) was generated. Each point was treated as a linearly independent h_0 boundary condition to specify the resulting CR distribution. More detailed injection distributions beyond a uniform sphere, e.g. the singular isothermal self-gravitating spherical injection weighting proposed by Rodríguez-González et al. 2007 (or, see also Silich et al. 2011; Palouš et al. 2013 for other approaches), were not found to bear any substantial difference to the uniform distribution presented here. Each individual CR distribution associated with every MC point was scaled by $1/N$ and then assigned to each of the MC spherical points distribution. The resulting CR profile from the full distributed source ensemble was then found by superposition of each of these individual contributions, from which the resulting CR heating level could then be calculated. This was done for CRs propagating according to concurrent advection and diffusion (i.e. using equation 5.6 as a basis for the CR distribution along the outflow cone) as well as in the pure diffusion and advection limits.

It is clear from this result that a broadened profile results from the extended CR injection regions, and a clear transition between the advection and diffusion dominated transport zones within the outflow cone arises. A distinct lower 'diffusion' region in the cone emerges with an 'advection' region taking precedence at higher altitudes, where the flow velocities are faster. This structure follows that assumed in models first introduced by e.g. Breitschwerdt et al. 1993 (see also Recchia et al. 2016).
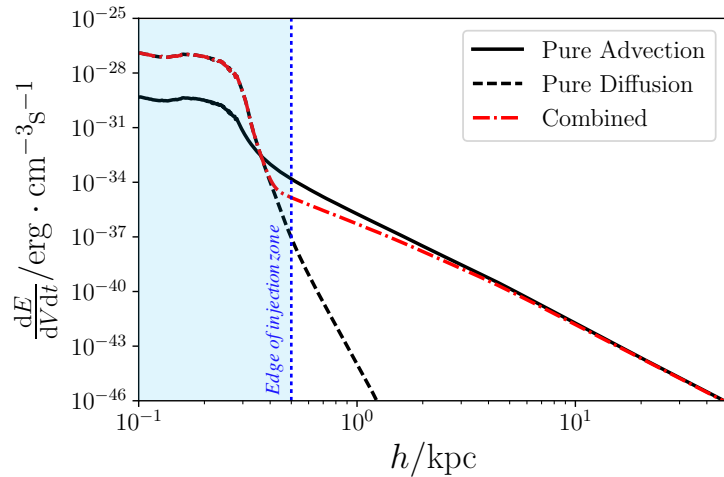
Fig. 5.4: CR heating profile along an outflow cone with an extended CR injection region using a spherical starburst core of radius 0.5 kpc (indicated by the dotted blue line/shaded area). The black lines represent the profile established in the case of pure advection of CRs (solid) and pure diffusion (dashed), while the dot-dashed red line represents concurrent advection and diffusion. A distinct transition between the advection-dominated and diffusion-dominated transport regimes is apparent at around $h \approx 0.3 - 0.4$ kpc.

Energetics

The total integrated CR heating effect (summed over both outflow cones in a galaxy) is shown in Fig. 5.5 up to $h = 50$ kpc, being the characteristic extent of a CR-driven outflow (see, e.g. Veilleux et al. 2005; Bland-Hawthorn et al. 2007, for discussions on the extent of outflows). This indicates that the total heating rate along an outflow due to CR interactions would be around 2.0×10^{35} erg s^{-1}, of which a substantial fraction is focussed in the innermost 0.3 kpc region of the outflow cone – even in the case of an extended CR injection profile throughout a 0.5 kpc starburst core region. This is calculated for the baseline model with a SN event rate of $\mathcal{R}_{\mathrm{SN}} = 0.1$ yr^{-1}, corresponding to a total CR luminosity of 3.0×10^{41} erg s^{-1} (from equation 2.3). Of this, 1.1×10^{39} erg s^{-1} is passed into the outflow cone and is available to engage with hadronic interactions (after the geometry of the system, losses in driving the outflow and energy dissipation have been taken into account, in accordance with equation 2.9).

Fig. 5.5 demonstrates that the DC thermalisation process of CRs is relatively inefficient in typical outflow conditions, with only a small fraction of the initial CR power being released to heat the outflow wind. Indeed, for a mean
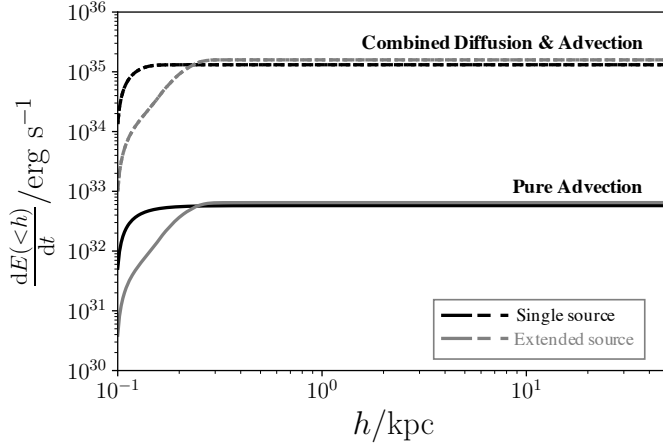
Fig. 5.5: CR heating profiles integrated over outflow cone volume up to 50 kpc ($\mathcal{R}_{\mathrm{SN}} = 0.1\ \mathrm{yr}^{-1}$; opening angle $55°$). The solid lines correspond to pure advective CR transport, while the dashed lines relate to the concurrent advection/diffusion of CRs (in this case, they are indistinguishable from the pure diffusion result which also leads to a majority of CR energy deposition arising in the lower regions of the outflow). The difference between CR injection at a single point boundary location at $h = 0$ (black lines) compared to the extended CR source injection (grey lines) is apparent.

CR primary energy of 8.2 GeV (when weighting for their power-law spectral energy distribution), only a CR energy fraction as small as 1.5×10^{-3} would typically thermalise into the wind fluid. However, this is an average value weighted by the heating profile – some regions of the outflow would attract much more efficient thermalisation (in particular in the denser, lower regions), while CRs would be much less likely to engage and thermalise in more peripheral parts of the flow, in particular the low density regions found at high altitudes. Nevertheless, the mean efficiency would indicate that typically, the total power originally released by the CRs would be around 1.4×10^{38} erg s^{-1} as they interact with the outflow wind environment, corresponding to around 12.0% of the available CR power in the outflow cone. Such an energy-absorption fraction is consistent with that estimated from the numerical models of Girichidis et al. (2018) – between 5 and 25% – which consider a combined transport scenario where outflow velocities close to the mid-plane are small, much like the diffusion limit and combined transport picture considered here. For a pure advection scenario, Farber et al. (2018) find that substantial CR energy is harboured within a few kpc of the galactic plane because outflow velocities are low near $h = 0$. This promotes the rate of hadronic interactions and CR thermalisation near the base of the outflow, enhanced further by the substan-

tially higher densities in these lower regions. Like the results presented here, the Farber et al. (2018) study finds a difference of around 4 orders of magnitude between the density in the medium of the galactic disk compared to the outflow/halo.[3] Pakmor et al. (2016) present contrasting results to Girichidis et al. (2018), Farber et al. (2018) and those shown here. Their simulations show substantial CR energy densities (of order a few eV cm^{-3}) up to altitudes of 5 kpc or more when adopting lower outflow velocities of around 100 km s^{-1} in otherwise comparable systems. However, this tension presumably arises from the Pakmor et al. (2016) study having been predominantly focussed on CR transport, with hadronic interactions (and absorption/energy release) not having been included in their calculations.

Parameter Study

The critical quantity that governs the behaviour of this system is the SN event rate $\mathcal{R}_{\mathrm{SN}}$. The outflow velocity also has some bearing, although this relatively inconsequential. Other parameters, for example the influence of the cone opening angle, are less important. This is demonstrated in Fig 5.6, in which the black line is the result for the standard opening angle of $55°$ while the blue and red lines show a variation of $+10°$ and $-10°$ respectively (i.e. $65°$, blue and $45°$, red). The small variations between these parameter choices that can be discerned indicate that the CR heating rate becomes slightly elevated for larger opening angles. This is due to a greater fraction of the starburst core being subtended by the outflow cone for a larger opening angle, and the associated higher injection rate of CR particles. Although included in the calculation, the varying rates of adiabatic cooling experienced by CRs does not have any noticeable impact on the results.

The outflow velocity is determined by the CR injection model and its hydrodynamical coupling to the SN wind that develops from a concentrated burst of star-formation in the host galaxy. This dictates the resulting outflow velocity profile, as well as its terminal flow speed. However, it is of interest to artificially modify the outflow velocity. This is because different wind-

---

[3]Furthermore, in Farber et al. (2018), when they also invoke CR diffusion and coupling, this density contrast falls to a little under 2 orders of magnitude with more material being propelled along by the outflow wind.
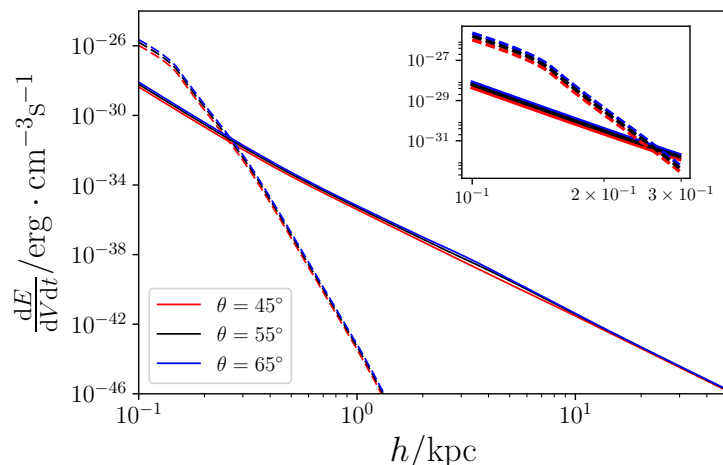
Fig. 5.6: CR heating power in an outflow in the advection limit (solid lines) and diffusion limit (dashed lines) with various opening angles (see legend). Such variation only results in a minimal change in the heating profiles. Up to around 10 kpc, variations in heating power between the different opening angles correspond with the resulting changes in the solid angle subtended by the outflow cone. The inset plot gives a more detailed view of the region between 0.1 and 0.3 kpc.

driving mechanisms can yield vastly different outflow rates (Veilleux et al. 2005), and scaling the results acquired so far can provide some indication as to how these other types of systems may behave. To ensure a reasonably self-consistent estimate, the density profile must be modified an a manner that corresponds to any scaling applied to the velocity profile. From the continuity equation 2.17, the product $\rho\,v(h)\,h^2$ must still hold throughout the flow, as mass must be conserved. Hence, to find a corresponding mass injection rate, a velocity scaled by some factor Ψ also requires a corresponding density scaling of Ψ^{-1}. This would also change the associated mechanical energy of in a wind, being scaled by a factor of Ψ as follows from ρv_∞^2. The effect of crudely scaling the system in this way is shown in Fig. 5.7, where the results essentially follow directly from the initial condition for the CR energy density at the base of the outflow combined with the variation in the outflow density profile.

From equation 4.40, it follows that the energy density of CRs and their resulting heating effect roughly scales inversely with the flow terminal velocity. As such, any reduction in the outflow velocity must be matched with a corresponding increase in the CR energy density which feeds into a scaling of the heating effect. However, the density of the outflow must also be scaled appropriately, increasing by the same factor as the CR energy density. If re-
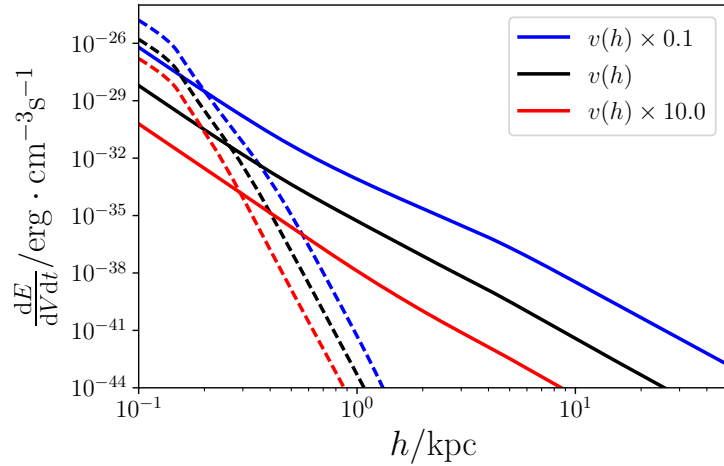
Fig. 5.7: Diffusion-limit and advection-limit heating profiles (dashed and solid lines respectively) resulting from the standard outflow model shown in black ($v_\infty \approx 290$ km s^{-1}) compared to scaled systems: (1) in red, where the velocity profile has been increased 10-fold, with a corresponding reduction applied to the density profile, and; (2) in blue where the velocity profile has been decreased by a factor of 10 (with a corresponding increase applied to the density profile).

ducing the flow velocity by an order of magnitude, there would be an increase in the CR heating power throughout the cone by two orders of magnitude, following from the dependence on CR energy density and the baryon (matter) density of the wind fluid (being the target for the hadronic interactions that drive CR heating). In the pure diffusion limit, the scaling picture is a little more straightforward: now, there would not be any dependence between the CR energy density and the scaling applied to the outflow velocity. The CR heating power would only be affected by the influence on the density of the wind (i.e. it would only increase inversely to the scale factor). The fraction of CRs absorbed in any reasonable scaling of the flow velocity appears to be relatively unchanged. If reducing the velocity by an order of magnitude, the absorption fraction only falls marginally, from 12.0% to 11.9%. If the outflow velocity is instead increased by an order of magnitude, the CR absorption fraction rises slightly to 13.7%. It follows that substantial changes in the patterns of CR energy release in vastly different outflow velocity scenarios would generally not be expected, remaining applicable even to outflows governed by entirely different outflow driving mechanisms.

The SN event rate sets the energy budget of the CRs in the system, and also regulates the level of kinetic energy ultimately passed to the outflow wind.
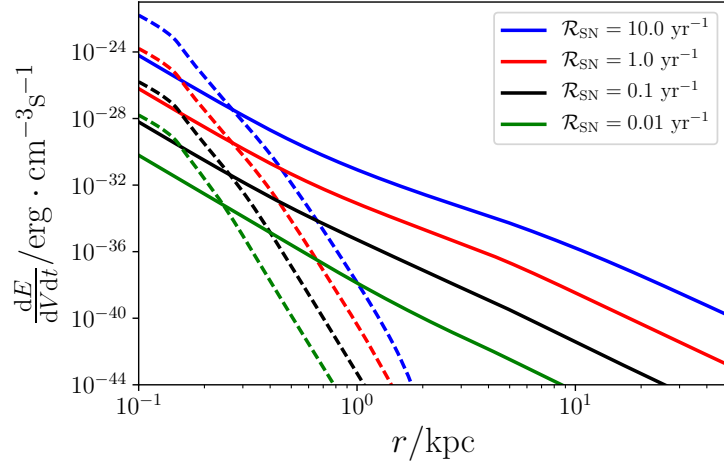
Fig. 5.8: Impact of SN rate on CR heating, showing the profiles in the diffusion (dashed lines) and advection (solid lines) limits, with SN rates $\mathcal{R}_{\mathrm{SN}} = 0.01, 0.1, 1.0$ and 10.0 plotted in green, black, red and blue respectively.

Even in cases when an outflow is not directly SN-driven, the flow dynamics are still impacted by the radiative or thermal output by the stellar population in the core of the host galaxy and this, in turn, scales with the SN event rate. It is therefore not surprising that the SN event rate $\mathcal{R}_{\mathrm{SN}}$ is the most influential parameter in this model. Fig. 5.8 explores this dependency, in which four SN event rates are considered: the three considered previously in the One-Zone model (i.e. $0.1, 1.0$ and 10.0 yr^{-1}) and, additionally 0.01 yr^{-1} to represent a fairly quiescent, barely star-bursting system in a 'normal' (slow) star-forming phase. Such systems would not be obvious candidates for CR calorimetry and/or internal heating and so were of little interest in the One-Zone model – particularly since their low CR energy densities would be unlikely to be able to drive a dominant global heating effect. However, their impact may still be important on extragalactic scales if CRs can be transported beyond the confines of their ISM, and so this low SN rate is of some interest here.

Fig. 5.8 demonstrates that the CR heating power scales with $\mathcal{R}_{\mathrm{SN}}^2$ in the diffusion limit. This follows from the CR heating power being dependent on both the density of the outflow wind (which itself is related to SN event rate via the mass-loading relation) and the CR luminosity. In the pure advection scenario, the $\mathcal{R}_{\mathrm{SN}}^2$ relation can be seen again at low altitudes. However, the heating profile appears to deviate instead towards a scaling with $\mathcal{R}_{\mathrm{SN}}^3$ at high

altitudes, above around 5 kpc. This behaviour is particularly evident in the most active systems. This can be attributed to the varying DC thermalisation efficiency with SN event rate: below $\mathcal{R}_{SN} = 1 \text{ yr}^{-1}$, any inverse Compton losses are dominated by the CMB. However, at this level and above, the starlight starts to become important (even if not dominant), reaching similar energy densities to the CMB (or within an order of magnitude) – but only does so within the ISM where the stellar radiation field is most intense. Higher densities resulting from additional mass-loading should yield improved CR heating efficiencies (see Fig. 5.1), and this improves roughly in proportion to density (and hence SN event rate via mass-loading). This produces an extra dependency on $\mathcal{R}_{SN}$ (on top of the $\mathcal{R}_{SN}^2$ scaling which arises from CR injection and the increased mass-loaded density of the outflow medium). However, when starlight starts to contribute to inverse Compton losses as well as the CMB, heating efficiencies within the lower interstellar regions of the outflow are not similarly enhanced. As such, only the $\mathcal{R}_{SN}^2$ dependence results in the system up to a few kpc in these cases. Once again, the 12% CR absorption fraction is largely independent of SN event rate, as is the outflow velocity profile. This is because those contributing quantities which are dependent on $\mathcal{R}_{SN}$ combine antagonistically.

It was shown in Fig 5.1 that the efficiency of CR thermalisation depends on the rate at which CR secondary electrons lose their energy via various processes compared to Coulomb scattering. These processes are influenced by the ambient environment of the CRs, and are often linked to the SN event rate of a system. For instance, Fig. 5.9 shows the timescales for the various key energy loss processes of secondary CR electrons near the base of an outflow cone at $h = 0.1$ kpc, compared to the corresponding timescales at higher altitudes, at $h = 50$ kpc. This shows the different loss rates in the systems of different activities. Moreover, it shows that thermalisation rates (or loss rates in general) at high altitudes for the CR electrons are low (with long timescales), meaning that any CR secondaries that are able to reach these high altitudes are unlikely to thermalise at all – indeed, CR primary protons, if able to propagate to these heights, would also be unlikely to undergo the initiating
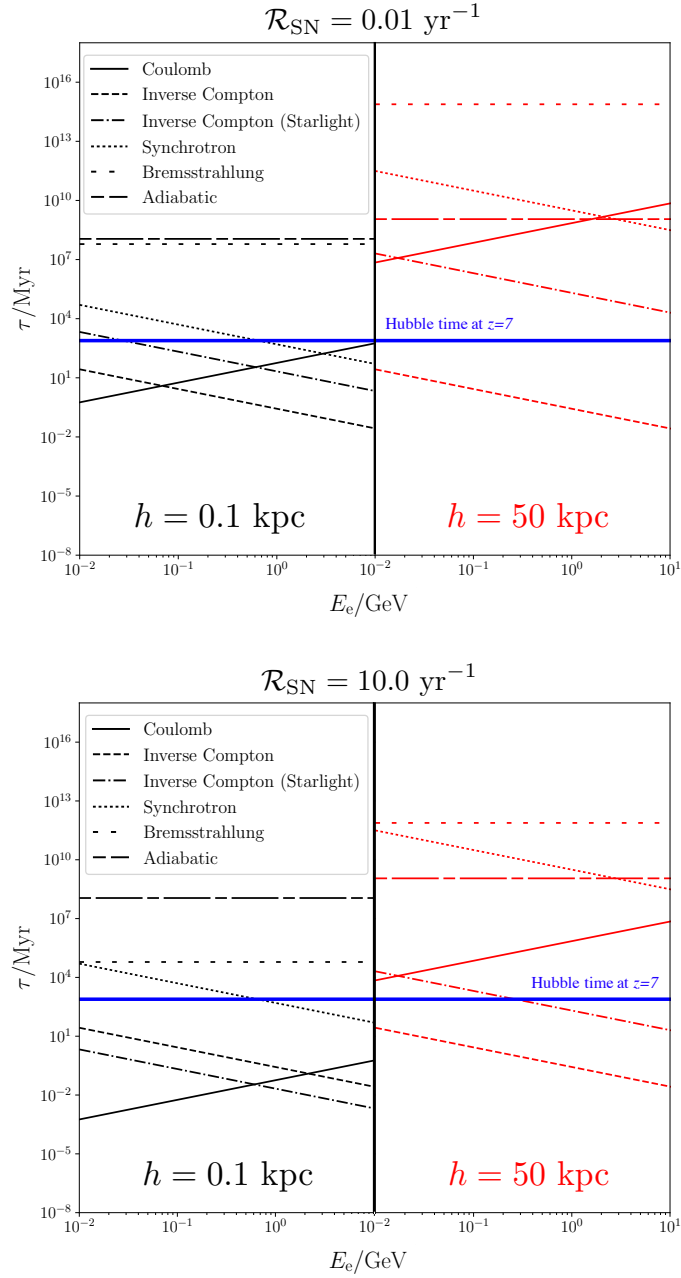
Fig. 5.9: Demonstration of the impact of SN activity $\mathcal{R}_{\mathrm{SN}}$ and position h within an outflow on energetic electron (secondary CRs) loss timescales. With direct (DC) thermalisation arising via Coulomb scattering, the corresponding heating efficiency is higher when the Coulomb timescale is shorter. **Upper panel**: Timescales for a relatively quiescent galaxy ($\mathcal{R}_{\mathrm{SN}} = 0.01$ yr^{-1}). **Lower panel**: Timescales in a strong starburst ($\mathcal{R}_{\mathrm{SN}} = 10.0$ yr^{-1}). For reference, in both panels, the Hubble timescale (evaluated at $z = 7$) is indicated by the blue horizontal line.
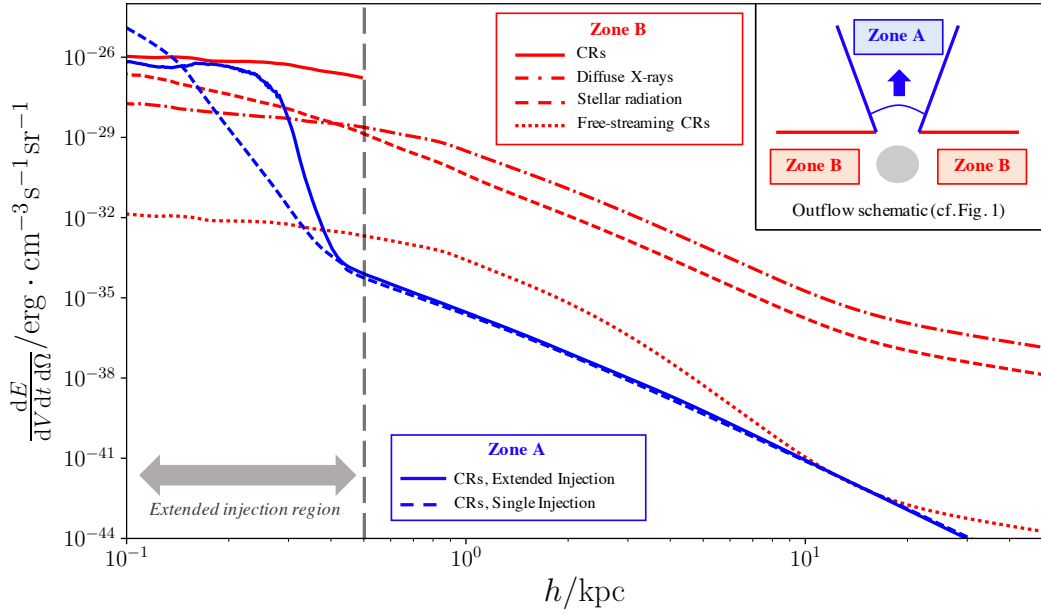
Fig. 5.10: Comparison between the DC cosmic ray heating power which arises in each of the two regions of the Two-Zone model, for a SN event rate of $\mathcal{R}_{\mathrm{SN}} = 0.1 \ \mathrm{yr}^{-1}$ and scaled by the respective zone solid angle. Blue lines show heating rates in Zone A (outflow, advection zone) while Zone B (diffusive ISM zone) heating rates are plotted in red. In the **Zone A** results, the slight dip in the solid blue line at small h is due to the elevated levels of CR attenuation in this part of the model where densities are highest (and reach somewhat larger values than in the stationary Zone B ISM). In the **Zone B** results, heating power due to diffuse X-rays, stellar radiation and free-streaming CRs are included for reference (cf. section 5.1).

hadronic interactions required for substantial heating to take place. Thus, at high flow altitudes, any remaining CRs in the flow may be safely regarded to have fully advected out of the system and will not thermalise. Instead, these CRs adopt a new role, becoming an important agent in regulating the thermal evolution and dynamics of the CGM and beyond.

5.2.3 Zone Comparison

The CR heating power in Zone A (outflow, advection zone) of the Two-Zone model has been calculated, while that in Zone B (diffusive ISM zone) simply follows from the One-Zone model. A comparison between the derived DC heating powers in both cases can be conducted. However, given that the Two-Zone approximation assumes there is negligible transfer of CRs across the zone boundaries, it is necessary to first normalise the heating profile of each of the individual zones by their respective solid angle. This allows the heating power per unit of CR irradiation to be compared. The resulting heating rate per steradian in each of the two zones is shown in Fig. 5.10, with Zone A plotted

in blue and Zone B in red. Both cases adopt the baseline parameter choices (with a 55° opening angle, and SN event rate of $\mathcal{R}_{\text{SN}} = 0.1 \text{ yr}^{-1}$), and the Zone A result follows from the distributed injection model as used earlier in Fig. 5.4.

Fig. 5.10 shows that the CR heating patterns arising in Zone B are similar to those in the inner region of Zone A, where the advective flow is too slow to have any important effect on the redistribution of CRs, and their propagation is diffusive. Presumably, in this region, the Two-Zone model would break-down, with the inner flow ISM being indistinguishable over the zone boundaries. The difference between the advection and diffusion regions only emerges at larger distances from the core of the host galaxy. Within the lower ISM, CR heating always dominates over conventional radiative heating processes. At larger distances, radiative heating may be more important. Note that comparing this with the Zone A results requires caution, because of the large differences in the density profile structures between the two regions.

5.3 Indirect Cosmic Ray Heating

The local intensity of inverse Compton X-rays produced by a population of energetic CR secondary electrons at some position $\mathbf{r}_i$, and spectral luminosity $L_{\text{IX}}(E_\gamma)$ for X-ray photon energy E_γ may be written as:

$$I_{\text{IX}}(E_\gamma, r; \mathbf{r}_i) = \frac{L_{\text{IX}}(E_\gamma)|_{\mathbf{r}_i}}{4\pi r'^2 c} \exp\left\{ -\int_0^{r'} \mathrm{d}\ell\, \sigma_{\text{KN}}(E_\gamma)\, x_i\, n_{\text{H}}(\ell) \right\} , \qquad (5.9)$$

where r' retains its earlier definition as the distance between the source position $\mathbf{r}_i$ and some general location $\mathbf{r}$, and x_i is the local ionisation fraction of the medium. The exponential term encodes the attenuation effect experienced by the X-rays as they propagate from their source, although its impact is small: even in central galaxy ISM conditions of density $n_{\text{H}} = 10 \text{ cm}^{-3}$, the mean free path of a keV photon is of order 100 kpc. In section 3.4.2, it was argued that the spectral distribution of inverse Compton X-rays is not important for the

present application. Thus equation 5.9 reduces to

$$\mathcal{I}_{\mathrm{IX}}(r; \mathbf{r}_i) = \frac{\mathcal{L}_{\mathrm{IX}}|_{\mathbf{r}_i}}{4\pi r'^2 \mathrm{c}} \exp \left\{ -\int_0^{r'} \mathrm{d}\ell\, \sigma_{\mathrm{T}}\, x_i\, n_{\mathrm{H}}(\ell) \right\} , \tag{5.10}$$

where $\mathcal{L}_{\mathrm{IX}}$ is the total inverse Compton X-ray luminosity of a source, being related to its spectral luminosity, $L_{\mathrm{IX}}(E_\gamma)$, by

$$\mathcal{L}_{\mathrm{IX}} = \int_0^\infty \mathrm{d}E_\gamma\, L_{\mathrm{IX}}(E_\gamma) . \tag{5.11}$$

This is calculated according to

$$\mathcal{L}_{\mathrm{IX}}|_{\mathbf{r}_i} = \frac{4}{3}\sigma_{\mathrm{T}} \mathrm{c}\, U_{\mathrm{rad}}\, \mathcal{V}_{\mathrm{S}} \int_{E_{\mathrm{min}}}^{E_{\mathrm{max}}} \mathrm{d}E_{\mathrm{e}} \left(\frac{E_{\mathrm{e}}}{m_{\mathrm{e}}\mathrm{c}^2} \right)^2 n_{\mathrm{CR,e}}(E_{\mathrm{e}}; \mathbf{r}_i) , \tag{5.12}$$

in which $\mathcal{V}_{\mathrm{S}}$ retains its earlier definition as a characteristic source size, with which $N_{\mathrm{CR,e}} = n_{\mathrm{CR,e}} \mathcal{V}_{\mathrm{S}}$ electrons as associated.

For an extended distribution of CR electrons, the resulting X-ray intensity $\mathcal{I}_{\mathrm{IX}}(r)$ can be modelled by use of a distribution of source positions, as per the MC scheme used previously to model extended CR proton and electron distributions (cf. sections 4.3.2 and 4.2.1). Attributing simulated source locations to a set of positions $\mathbf{r}_i$ allows the X-ray intensity profile of the extended system to be modelled by convolving these points with equation 5.10. Once the X-ray intensity profile is known, the indirect cosmic ray inverse Compton X-ray heating rate follows immediately as

$$\dot{Q}_{\mathrm{IX}}(r) = \mathcal{I}_{\mathrm{IX}}(r)\, \alpha_{\mathrm{IX}}(r) , \tag{5.13}$$

where α_{IX} is the attenuation term for X-rays (following from the general form of equation 3.34).

5.3.1 Numerical Method

To calculate the inverse Compton X-ray intensity profile $\mathcal{I}_{\mathrm{IX}}(r)$, the following scheme was adopted: some $N_{\mathrm{S}} = 10,000$ points were sampled by the MC method, with the resulting distribution being weighted according to the CR electron profile determined in section 4.3.2 (Fig. 4.1). This was then con-
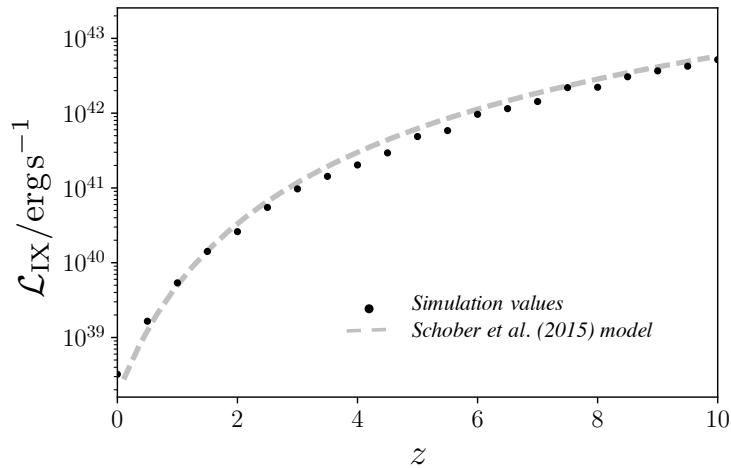
Fig. 5.11: Comparison between the protogalaxy X-ray luminosity (due to inverse Compton scattering of energetic secondary CR electrons) over redshift calculated using the semi-analytical Monte-Carlo simulation detailed in the main text, and the analytical approach introduced by Schober et al. (2015) (dashed grey line). This uses a more intense SN event rate ($\mathcal{R}_{SN} \approx 1\,\mathrm{yr}^{-1}$) than the baseline model to allow comparison with the analytic literature model.

volved with the solution given by equation 5.12 for a point-like X-ray source. From the resulting X-ray intensity profile, the IX heating power followed from equation 5.13.

The inverse Compton X-ray luminosity of starburst galaxies at high-redshift was calculated analytically by Schober et al. (2015) in the 0.2 to 10 keV band, due to the presence of an energetic CR electron population. This was used as the basis for a cross-check of the inverse Compton luminosity determined here. The earlier study adopted a redshift evolution model for the volume of the host galaxy according to $V_{\mathrm{gal}}(z) \propto (1+z)^{-3}$ which is not relevant to the current work, but their model is otherwise comparable, and a spherical protogalactic radius of 1 kpc is sufficiently consistent with the dimensions of the system in Schober et al. (2015) when specified at $z = 7$. Using this as a baseline from which the $(1+z)^{-3}$ scaling could be removed, the resulting inverse Compton X-ray glow in a comparable 0.2 to 10 keV band for a star-forming galaxy was simulated according to the numerical approach detailed above, with $\mathcal{R}_{SN} \approx 1\,\mathrm{yr}^{-1}$. Simulations were performed over a redshift range between $z = 0 - 10$ in 0.25 increments, with the total X-ray luminosity of the system $\mathcal{L}_{IX}$ for each case being compared to the Schober et al. (2015) model at the same redshift, as shown in Fig. 5.11. The simulation results are

plotted in black (dots), while the previous model is shown by the grey dashed line, and it is evident that the approach adopted here is in good agreement with the earlier study.

5.3.2 Implications of Cosmic Ray Heating Mechanisms

The heating power associated with the two CR heating processes, the direct Coulomb (DC) mechanism and the inverse Compton indirect X-ray (IX) mechanism are shown in black and red respectively in Fig. 5.12, when applied to a protogalaxy environment such as that described by the One-Zone model, of characteristic size 1 kpc, central density $n_{\mathrm{H},0} = 10$ cm^{-3}, SN event rate $\mathcal{R}_{\mathrm{SN}} = 0.1$ yr^{-1} and calculated over a range of redshifts, from $z = 0$ to 12, in increments of 2. The Two-Zone prescription is less useful at this point, given that IX heating along an outflow cone would not greatly differ compared to other substructures expected in the circumgalactic environment. Moreover, the radiative transport and X-ray heating in the CGM region would not offer any particular new insight for the present analysis. Details such as the effect of the two CR heating mechanisms with the multiphase structures and sub-structures (e.g. clumps and filaments) within outflows and the CGM fall beyond the present scope of this thesis, instead being left to dedicated follow-up studies (see section 7.3).

Fig. 5.12 shows that the previously calculated DC heating rate is maintained at 10^{-25} erg cm^{-3} s^{-1} when $\mathcal{R}_{\mathrm{SN}} = 0.1$ yr^{-1} over all redshifts considered, being almost completely unaffected by cosmological evolution. This is in stark contrast to the heavily redshift-dependent IX heating effect. A power of around 10^{-26} erg cm^{-3} s^{-1} is attained by $z = 8$, increasing to levels comparable to the DC mechanism at earlier cosmic times within the ISM of the host. This would correspond to a substantial total X-ray luminosity of around 10^{42} erg s^{-1}, or 10^{43} erg s^{-1} by $z = 12$ (see also Fig. 5.11), if the size of the host galaxy is maintained.

The shaded region in Fig. 5.12 shows the IX heating level that would occur if only stellar photons were up-scattered. This means that, for up-scattering of CMB photons to become important, the IX process must operate at a redshift that yields a heating line above this orange shaded area, with the
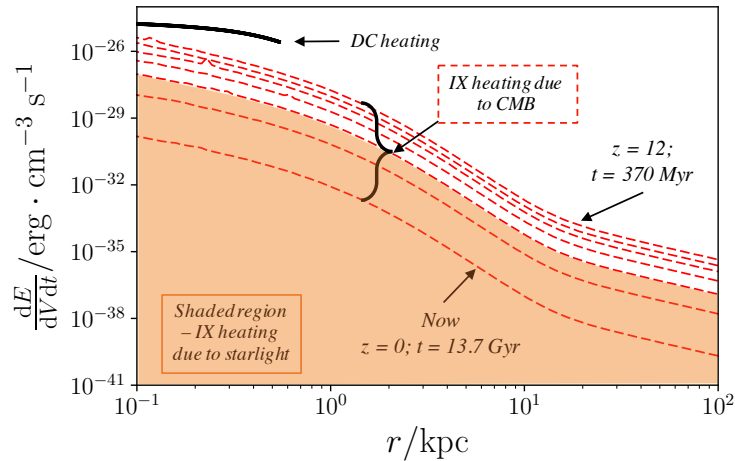
Fig. 5.12: Redshift evolution of CR heating processes: the direct Coulomb heating power is shown in black, while the red lines represent the power via the indirect X-ray channel. These are calculated for the baseline protogalaxy model ($n_{H,0} = 10$ cm^{-3}, $\mathcal{R}_{SN} = 0.1$ yr^{-1}) at redshifts of $z = 0, 2, 4, 6, 8, 10$ and 12. This demonstrates that there is no discernible redshift-evolution in the DC heating power, however the IX heating process is much more susceptible to cosmic evolution (due to the evolution in the energy density of the CMB). At $z = 12$, the heating power by both mechanisms is comparable, around $10^{-24} - 10^{-25}$ erg cm^{-3} s^{-1}. The region shaded orange (which coincides with the $z \approx 4$ IX line) represents the IX 'floor' due to the stellar radiation contribution. When redshift evolution brings the IX line into the shaded area, the contribution from the up-scattering of stellar radiation instead takes precedence.

starlight providing an effective 'floor' for the IX heating at low-redshifts. A cut-off redshift arises at approximately $z = 4$ between stellar-dominated and CMB dominated non-thermal X-ray heating (although note that this value is dependent on the galaxy model and star-formation pattern model adopted).

The IX heating mechanism can only operate at a competitive level with the DC mechanism at high-redshift (which is redshift independent) within the interstellar environment of a galaxy. Given the scales over which both of these processes deposit their energy, this leads to an intriguing conclusion: the DC mechanism predominantly operates within the ISM of the host galaxy (it is regulated by the containment of CRs in the magnetic field, so cannot sustain any notable power outside the confines of the ISM) whereas the IX mechanism is effective over larger scales and is much more instrumental for the thermal evolution of the environment around the host (i.e. the CGM) – particularly at intermediate redshifts (between $4 < z < 7$). It follows from the redshift evolution of the IX effect established above, that CR heating would be split fairly evenly between the interior and exterior environment of a star-forming galaxy in the early Universe, but would become increasingly focussed into the
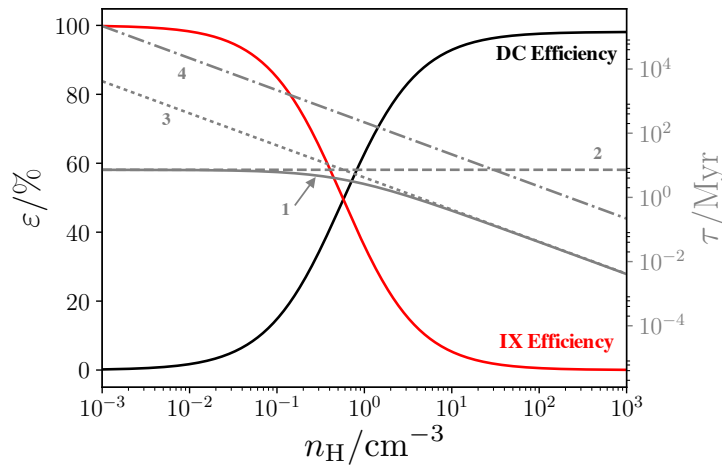
Fig. 5.13: The efficiency of the two CR heating mechanisms for a 40 MeV electron. The red line shows the fraction of energy passed to the IX channel, while the black line shows the fraction passed to the DC channel as a function of the density of the ambient environment. The y-axis on the left corresponds to the heating efficiency value. Timescales (indicated by the grey lines, and y-axis to the right) of the cooling processes affecting the energetic electrons are plotted in grey to illustrate the underlying physics governing the heating efficiency. Total loss timescales are given by the solid line 1, accounting for contributions from inverse Compton (dashed horizontal line 2), Coulomb (dotted line 3) and free-free losses (dot-dashed line 4).

ISM over time. The implication of this is that the CR feedback processes operating in and around star-forming galaxies in the early Universe would be fundamentally different to those at work in the present epoch.

The efficiency of the respective CR heating mechanisms is also dependent on the density of the local environment. Fig. 5.13, which shows how the efficiency of the two CR heating channels depends on ambient density (assuming a fully ionised medium) for a 40 MeV CR secondary electron (resulting from the hadronic interaction of a 1 GeV proton). As with Fig. 5.1, these heating efficiencies are estimated according to the relative timescales of the key loss processes of the CR electrons responsible for driving the heating effects, which are indicated by the lines in grey (inverse Compton, Coulomb losses and synchrotron). The DC and IX processes behave very differently to one another, which further supports the argument above: that CR heating processes operate differently in different astrophysical media and environments (i.e. CR heating is a multi-phase process). The DC mechanism operates effectively in dense pockets of gas (especially if they exhibit a reasonably high ionisation fraction), while the IX channel is more efficient in hot diffuse gas (although it may still operate in higher-density environments over large scales if the ionisa-

tion fraction is sufficiently high). This does not necessarily mean that the IX process would be the dominant heating mechanism in a low-density environment: it will still require dense regions in which the pion-producing hadronic interactions may be initiated to supply electrons. However, in a multi-phase medium, where dense clumps and low density hot plasmas exist together, the IX process may operate particularly effectively and be able to alter the resulting dynamics and ensuing thermal evolution of the system in a manner that has not been considered before. Studies of CR heating in such environments (e.g. in multi-phase galactic outflows) are therefore an important avenue for future enquiry. In terms of feedback, it can similarly be argued that the IX mechanism could play a critical role in regulating the inflow of gas, even presenting a means by which star-forming galaxies are temporarily starved of cool gas by cutting-off filamentary inflows through heating.

Cosmic Ray Escape

The operation of these two distinct CR heating channels hints that feedback may operate in different ways in star-forming galaxies in the high-redshift Universe, as illustrated by the schematic in Fig. 5.14. For instance, the DC channel would act to directly raise the temperature of interstellar gases to the point at which star-formation is suppressed, or even halted entirely, due to the increased pressure support afforded by the heated gas against gravitational collapse (e.g. French et al. 2015). This may be regarded as a *quenching* process. By contrast, the IX channel is better attributed to *stunning* – the process by which star-formation is (temporarily) stopped resulting from the cut-off of the in-falling supply of cold gas required to fuel it, as would result from cold filamentary inflows being heated and evaporated on their approach to the galaxy itself.

As well as the IX process, CRs advected in a galactic outflow may also contribute to stunning star-formation. In section 5.2.2, it was found that almost 90% of CRs within an outflow are transported to the CGM environment (or beyond). It was also demonstrated that this escape fraction of CRs is not particularly sensitive to the choice of model parameters. This corresponds to a CR luminosity of around 3.1×10^{40} erg s^{-1} escaping into the CGM environment
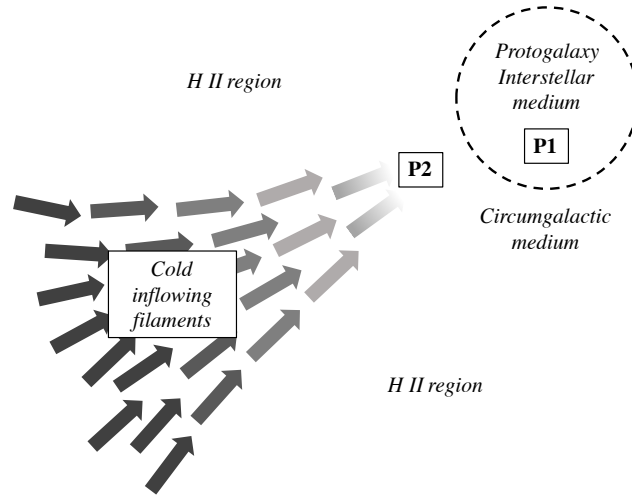
Fig. 5.14: Schematic diagram to illustrate the action of CR feedback processes during a starburst phase in a galaxy. Point **P1** is within the interstellar environment, internal to the galaxy. Here, heating is dominated by the DC channel, with CR primaries (and secondaries) strongly contained by the ambient galactic magnetic field. By contrast, location **P2** is in a filamentary inflow outside the galaxy. Here, the IX heating mechanism is most important, since this does not rely on CR escape – the DC heating effect would be negligible at this point, except in the case of the presence of a galactic outflow.

of a galaxy with $\mathcal{R}_{\mathrm{SN}} = 0.1$ yr^{-1} when outflows operate, which represents a substantial contribution to the external energy budget, exceeding even that expected due to diffuse thermal X-ray emission ($\sim 10^{38}$ erg s^{-1} – e.g. Watson et al. 1984). Such substantial energy injection into the CGM would presumably have implications for the survival of any cold filamentary inflows feeding star-formation in the host, possibly providing as important an effect as the IX process. The ability of these CRs to be retained in the CGM would be governed by the convective flows and magnetic field structures.

Chapter 5 summary: *Average ISM heating rates due to CR-induced mechanisms are calculated in this chapter, and compared against more conventional heating due to starlight and thermal X-rays. In particular, CR heating rates due to the Direct Coulomb (DC) and Inverse-Compton X-ray (IX) processes are presented, where it is shown that the DC process and IX process are of comparable power within the ISM of a galaxy by $z \approx 12$, but that generally the IX process is more effective at redistributing energy to the circumgalactic environment at redshifts below this. The DC process is predominantly an internal regulator of feedback, refocussing CR energy back into interstellar gas. CR heating would have feedback implications on subsequent star-formation in high-redshift galaxies, with two mechanisms being proposed. The first, referred to as a 'quenching' process, relies mainly on the DC process to heat interstellar gas to temperatures at which star-formation is suppressed – or even halted entirely. The second is introduced as 'stunning', whereby the IX process operates to heat the environment around a high-redshift star-forming galaxy, possibly leading to the heating and destruction of filamentary inflows. This starves the gas supply for star-formation until IX heating abates and sufficient cooling can allow them to be reinstated.*

Chapter 6

Feedback in Protogalaxies in the Presence of Energetic Cosmic Rays

Post-starburst galaxies are systems in which star-formation has become quenched after an earlier violent starburst episode (Dressler and Gunn 1983; Couch and Sharples 1987). They have been observed both in the local Universe (see also French et al. 2015; Rowlands et al. 2015; Alatalo et al. 2016; French et al. 2018) and further afield, at high-redshifts (including the aforementioned MACS1149-JD1, Watson et al. 2015; Hashimoto et al. 2018). The work in this thesis has demonstrated that, during their initial starburst phase, the internal media of these galaxies would be rich in CRs that could yield a progressive and long-lasting feedback effect. Indeed, post-starburst galaxies are often found to harbour abundant reservoirs of interstellar molecular gas which, ordinarily, would be able to fuel ongoing vigorous star-formation – but instead appears to be prevented from doing so (French et al. 2015; Rowlands et al. 2015; Alatalo et al. 2016). While the reason for this is under debate, CRs offer a consistent explanation. A tentative clue for this lies in the deficiency of dense molecular gas pockets, as recently detected in low-redshift

post-starburst systems (French et al. 2018). This implies the operation of a mechanism which imparts additional pressure support to the molecular gas reservoir, protecting it from fragmentation and collapse under gravity. This extra support would follow from the additional pressure afforded by the presence of high internal CR energy densities.[1] Not only are they able to directly provide additional pressure support to a semi- or fully-ionised and magnetised interstellar medium (e.g. Salem and Bryan 2014; Zweibel 2016), it has also been shown in this thesis that CRs are also able to drive important interstellar and circumgalactic heating effects (see also Begelman 1995; Zweibel 2013, 2016) which could further support feedback effects. The impact of CR heating, whether by direct or indirect means, could cause a subsequent reduction of star-forming activity of the host galaxy. If strong enough, this would presumably lead to a period during which star-formation is quenched.

CR feedback may operate internally or externally. Externally, IX heating and advected CRs may temporarily 'stun' star-formation by impeding inflowing cold filaments of gas which would otherwise drive (or aid) star-formation in high-redshift starbursts. This has some similarities to the traditional strangulation mechanism in which star-forming galaxies fed by gas inflows are accreted into the hot halo of a more massive host, which permanently cuts off these gas supplies (Larson et al. 1980; Boselli and Gavazzi 2006; Peng et al. 2015) – although with the 'stunning' mechanism inflows are only temporarily halted due to irradiative feedback from the host galaxy, and can be reinstated at a later time. Such external CR driven feedback would presumably operate in conjunction with internal (more direct) feedback mechanisms which, together, provide a compelling hypothesis for the intriguing properties and inferred star-formation history of the high-redshift protogalaxy, MACS1149-JD1, as introduced in chapter 1. CR-driven feedback via internal DC heating and subsequent quenching may arise in this system, aided by the action of outflows which could also draw CRs into the circumgalactic medium where

---

[1]Another explanation would ordinarily be the operation of outflows to remove gas which could otherwise fuel star-formation. However, their action is generally disfavoured in many of these post-starburst systems – partly due to the presence of the large molecular reservoir, but also from the detection of substantial interstellar media in lower redshift examples (Roseboom et al. 2009; Rowlands et al. 2015; Alatalo et al. 2016; French et al. 2018; Smercina et al. 2018).

they could cut off cold inflowing streams of cold gas.[2] However, the concurrent action of the IX heating process removes the requirement for an outflow to be present in this system for stunning to occur. The inferred properties of MACS1149-JD1 can be explained as follows: In this young galaxy, the short lifecycles and fast evolution of the (presumably) metal-poor high-mass stars gave rise to frequent SNe (see Abel et al. 2002; Bromm et al. 2002; Clark et al. 2011), which injected shocks and turbulence into the ISM, and created a rich environment for CR acceleration. The first starburst episode inferred from the Hashimoto et al. (2018) study would have been terminated by continued and progressive CR heating. This caused feedback as CR abundance built up due to the developing galactic magnetic field, via the turbulent dynamo mechanism (Balsara et al. 2004; Balsara and Kim 2005; Beck et al. 2012; Schober et al. 2013), and sustained an extended period of CR heating of interstellar gases.

In order for star-formation to persist for some extended duration of time, feedback processes could not have taken hold immediately. Instead, they would have operated progressively over a timescale comparable to the duration of the star-forming episode of the galaxy. This specifies an upper timescale over which CR feedback is effective and becomes sufficiently entrenched to lead to quenching. Intuitively, it follows that the timescale over which the host's galactic magnetic field saturates must be comparable to the dynamical response to sustained CR heating. As such, the starburst episode would experience two distinct stages – the first being a period of initial magnetic field growth during which CRs are increasingly contained, with their heating power gradually becoming focussed onto the internal interstellar environment (even before magnetic saturation is attained), and a subsequent internal quenching stage due to ongoing CR heating. During the internal quenching stage, the prolonged effect of CR feedback became established to halt the collapse of that gas which is already present in ISM over-densities. This drove the formation of a warm interstellar baryonic reservoir, but the action of cold filamentary

---

[2]Here, 'cold' simply refers to below $T = 10^5$ K. Some cases can be at temperatures as low as 10^4 K – see, e.g. Dayal and Ferrara (2018).

inflows of pristine gas still continued and star-formation was still able to proceed. In turn, magnetic field growth was maintained, with its saturation level being reached at a later time. Star-formation would have continued until external feedback (IX) heating processes caused the temperature of the inflowing filaments to be increased to a point at which they can no longer effectively maintain star-formation. They instead begin to evaporate as they approached the galaxy or may have continued to supply gas, but above a temperature that would be useful for star-formation to continue.

The timescale over which star-formation was halted in this way follows from the virial theorem. This states that there is a cut-off temperature, the virial temperature, above which gravitational collapse of gas in a structure is halted. Moreover, any heating to a temperature above this cut-off would presumably lead to the evaporation of the structure – and would certainly suppress its overall collapse. The virial theorem can be considered in terms of the model introduced in section 1.2.1 for the cold filamentary inflows. For inflows persisting over lengths of up to 50 kpc (Dekel et al. 2009a; Stewart et al. 2013; Goerdt and Ceverino 2015), then to sustain a star-formation rate in a galaxy of $\mathcal{R}_{\mathrm{SF}} \approx 16 \ \mathrm{M_\odot \ yr^{-1}}$ with a 30% mass conversion efficiency (Meier et al. 2002; Turner et al. 2015; Behroozi and Silk 2015; Sun and Furlanetto 2016) and an inflow velocity of 400 km s^{-1} (following from the velocity offset $v_{\mathrm{Ly}\alpha}$ of the Lyman-α line in MACS1149-JD1 – see Hashimoto et al. 2018), the resulting steady-state mass of such structures would be around $6.7 \times 10^7 \ \mathrm{M_\odot}$. If their typical diameter is similar to the galaxy which they are feeding (i.e. around 1 kpc), their resulting virial temperature would be around $T_{\mathrm{vir}} \approx 5,000$ K (Binney and Tremaine 2008). When adopting a characteristic filamentary gas density of order 10 cm^{-3} (as follows from equation 1.3, being comparable to an interstellar environment density), a resulting CR heating power of 10^{-25} erg cm^{-3} s^{-1} would give a heating period of only a few Myr, after which the virial temperature would be exceeded, leading to stunning and pausing/stopping star-formation within a subsequent dynamical timescale τ_{dyn} (this is the free-fall time required for a system to respond to the effect of stunning). The quenching timescale would presumably be even shorter than the stunning timescale,
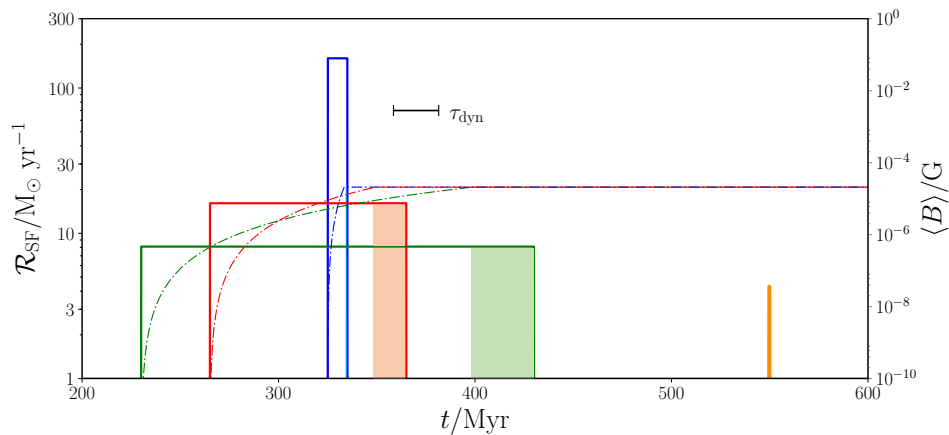
Fig. 6.1: Analysis of the co-evolution of the magnetic field (and subsequent CR containment/heating) and star-formation history in the high-redshift star-forming system MACS1149-JD1. The three Hashimoto et al. 2018 star-formation history models ($\mathcal{R}_{\mathrm{SF}} \approx 8$ M$_\odot$ yr^{-1} for 200 Myr; $\mathcal{R}_{\mathrm{SF}} \approx 16$ M$_\odot$ yr^{-1} for 100 Myr; $\mathcal{R}_{\mathrm{SF}} \approx 160$ M$_\odot$ yr^{-1} for 10 Myr) are plotted by the green, red and blue lines respectively. Moreover, the inferred star-forming activity at the epoch of observation, of $4.2^{+0.8}_{-1.1}$ M$_\odot$ yr^{-1} at $z = 9.11$, is indicated by the line in orange. Star-formation rates $\mathcal{R}_{\mathrm{SF}}$ correspond to values on the left y-axis, while the magnetic field evolution for each of the star-formation models are shown by the dashed-dotted lines (the corresponding axis is on the right of the plot). Regions beneath the star-formation history lines are shaded to indicate the period during which a saturated magnetic field developed (prior to the termination of star-formation). If exposed to prolonged CR heating, star-formation would be stopped within a dynamical timescale, $\tau_{\mathrm{dyn}} \approx 23$ Myr, as indicated by the scale-line annotation.

given that it is governed by more localised and intense heating processes within the interior environment of the host (and gravitationally-bound star-forming clumps would presumably have lower virial temperatures than the inflowing filaments). It thus follows that, with stunning and ISM quenching arising on comparatively short timescales of a system, the magnetic saturation and dynamical timescales together determine how quickly star-forming activities can be brought to a halt.

Returning to the case of MACS1149-JD1, if a starburst of intensity $\mathcal{R}_{\mathrm{SF}} \approx 16$ M$_\odot$ yr^{-1} arose (corresponding to a SN event rate of $\mathcal{R}_{\mathrm{SN}} = 0.1$ yr^{-1}), the galactic magnetic field would saturate at μG levels within around 140 Myr – cf. section 1.3.3. The dynamical timescale for galaxies similar to MACS1149-JD1 can be estimated as $\tau_{\mathrm{dyn}} \approx \sqrt{3\pi/(16G\rho)} \approx 23$ Myr.[3] This sets a minimum timescale over which star-formation can be terminated at around 160 Myr. In Fig. 6.1 this scenario, together with two other possible star-formation

---

[3]Note that this is calculated by using a characteristic ISM density of $n_{\mathrm{H}} = 10$ cm^{-3} rather than by directly using the dynamical mass. This is because the dynamical mass quoted in Hashimoto et al. 2018 has large uncertainties through their lensing parameter μ_{L}.

histories for the first starburst phase of MACS1149-JD1, are considered (as proposed by Hashimoto et al. 2018). These are plotted alongside the corresponding evolution of the galactic magnetic field, according to the turbulent dynamo amplification model introduced in Schober et al. (2013) and applied to a system similar to MACS1149-JD1, using the parameters obtained by Hashimoto et al. (2018). When imposing the requirement for a delayed response to the quenching of star-formation after CR containment, the most intense starburst scenario among those proposed by Hashimoto et al. (2018) may immediately be ruled out. This is because it would require the termination of star-formation to occur long before the system can actually respond to any quenching or stunning process. Moreover, this requirement also sets an upper star-formation rate limit of 20 $M_\odot$ yr^{-1}, as well as a latest bound for the initiation of star-forming activity of before 260 Myr after the Big Bang (i.e. at redshift $z \approx 15.4$). After the quenching of the initial starburst phase, a period of relative quiescence would follow for around 100 Myr. However a later, more moderate star-formation phase of rate $4.2^{+0.8}_{-1.1}$ $M_\odot$ yr^{-1} at $z = 9.11$ was identified in MACS1149-JD1. This apparent rejuvenation of star-formation was considered in section 1.1, being attributed to interstellar and circumgalactic gas cooling, as well as the reinstatement of cold inflows from distances beyond the range of feedback influence (being possible after the decline of CR feedback).

6.1 Protogalactic Star-Formation Histories

Further examples of high-redshift galaxies which also present indications of burst-like star-formation histories can be identified in the literature, as previously introduced in Table 4.2. 12 of these (including MACS1149-JD1) were found to show evidence of a former burst of intense star-formation, despite being relatively quiescent by their observational epoch. These examples are not an exhaustive literature sample of systems with such properties, but were selected as those where sufficient information was readily available for key characteristics of the galaxies to be known (or inferred), including the star-formation rate, star-formation rate during the earlier burst, stellar population

(estimated) age, stellar mass and the approximate physical size of each system (as required for the following analysis). For comparison, and to consider systems which may be representative of protogalaxies undergoing their initial starburst episode (i.e. in an earlier progenitor state to the post-starburst systems of principal interest here), a further 4 high-redshift galaxies were found in previous literature studies for which useful information could be derived – in particular their mass, size and star-formation rates. The star-formation histories of these starburst and post-starburst galaxies are explored in this section, which discusses how estimates were made to build up a picture of their possible evolutionary histories and the impact that CR feedback may have had.

6.1.1 Protogalaxies in a Post-Starburst Phase

Table 6.1 outlines the key details of the 12 post-starburst high-redshift protogalaxies identified in the literature. These were selected based on the size of their Balmer break, and/or because they notably demonstrated a relatively high stellar mass combined with a relatively low inferred star-formation rate at their observational epoch, as would be consistent with them being high-redshift protogalaxies in a post-starburst, quenched stage of their evolution. If enforcing the assumption of a burst-like star-formation history on this sample of 12 galaxies, the timescale over which their rapid star-formation episode progressed can be estimated if an upper estimate for the redshift of formation of their first stars in these galaxies, z_f, is also adopted. Recent studies (e.g. Hashimoto et al. 2018) suggest this redshift to be around $z_\mathrm{f} = 15^{+2.7}_{-2.0}$ (see also Thomas et al. 2017 which finds a similar but slightly lower redshift of formation of $z_\mathrm{f} = 14.8$). This would correspond to a time around 250-300 Myr after the Big Bang (Wright 2006). This may well prove to be an extreme limit for the formation of the earliest galaxies, with many galaxies forming their first stars at later times – for example, evidence actually suggests a later $z_\mathrm{f} \approx 9$ for A1689-zD1 is more appropriate (Mainali et al. 2018).[4] However, for the current purposes, adopting an earlier limit in this way yields a more conservative analysis which may be refined in future work.

---

[4]Indeed, this later redshift is adopted for z_f for A1689-zD1 (only) in the analysis here.

The timescale over which the initial starburst phase in a post-starburst system was active can be crudely estimated by

$$t_{\mathrm{SB}} \approx [t(z_{\mathrm{obs}}) - \tau_*] - t(z_{\mathrm{f}}), \tag{6.1}$$

i.e. the difference between the approximate time since the starburst ended, t_{end} (Note that $t_{\mathrm{end}} \approx \tau^*$, the characteristic stellar population age), and the estimated lower limit of the formation time of the galaxy, at redshift z_{f}. This gives a rough upper limit to the plausible timescale over which the starburst phase continued, and may be justified by considering that t_{SB} is considerably smaller than $t(z_{\mathrm{obs}}) - t(z_{\mathrm{f}})$, such that the starburst is bound to be triggered near the $t(z_{\mathrm{f}})$ end of the timeline. A lower bound for the starburst phase star-formation rate $\mathcal{R}_{\mathrm{SB}}^*$ now follows as

$$\mathcal{R}_{\mathrm{SB}}^* \approx \frac{(M_*/M_\odot)}{(t_{\mathrm{SB}}/\mathrm{yr})} \ \mathrm{M}_\odot \ \mathrm{yr}^{-1} \ , \tag{6.2}$$

which holds if the vast majority of the stellar mass of a galaxy forms within the starburst period, and does not substantially evolve after the end of the starburst. This can be justified as follows: while some fraction of the more massive stars in these systems would have gone through their evolutionary lifecycle by the time these galaxies are observed, the number of stars with masses sufficiently large to yield a SN within a few hundred Myr would only comprise a relatively small fraction of the total stellar population, and so their evolution would not have a large impact on the overall galaxy stellar mass.

The quantities $\mathcal{R}_{\mathrm{SB}}^*$ and t_{SB} are calculated in Table 6.1 for each of the 12 post-starburst galaxies (listed in order from lowest to highest inferred burst-phase star-formation rates), with literature references indicated. In all cases, redshift, star-formation rate, stellar mass, stellar population age and dynamical timescale had been measured in previous work (as cited) or could be inferred from information already available in the literature. The dynamical timescale, $\tau_{\mathrm{dyn}} = (\pi/2)\sqrt{r^3/\mathrm{G}M_{\mathrm{dyn}}}$ (e.g. Binney and Tremaine 2008) is estimated by use of the dynamical mass, M_{dyn}. This can be quantified in one of two ways. Either, an estimate can be made in which the stellar mass is taken

as a lower bound for the galaxy's dynamical mass (presumably there would be components in the galaxy other than stars, e.g. interstellar gas, which means the true dynamical mass would be larger) to allow an upper bound on τ_{dyn} to be found. Alternatively, the velocity dispersion of emission or absorption lines in an observed spectrum may be used, if available (Binney and Tremaine 2008; Förster Schreiber et al. 2009; Epinat et al. 2009; Gnerucci et al. 2011) which, in conjunction with the virial theorem gives an estimate for the dynamical mass of a galaxy as

$$M_{\mathrm{dyn}} = f_{\mathrm{dyn}} \frac{(\mathrm{FWHM})^2 \, r_{\mathrm{gal}}}{\mathrm{G}} \; , \tag{6.3}$$

(Gnerucci et al. 2011) where $f_{\mathrm{dyn}} \approx 2.25$ (Binney and Tremaine 2008; Förster Schreiber et al. 2009; Epinat et al. 2009), r_{gal} is the approximate radius of the galaxy (inferred from the half-light radius) and G is the Newtonian gravitational constant. The FWHM is the full width of half-maximum of the line profile, being a proxy to the velocity dispersion of the system. This accounts for the difference in relative velocity due to the orbiting motion of the gases around the galaxy from which the spectral line in question is emitted. In general, some caution is required in the interpretation of results derived by this technique: absorption and emission lines would presumably probe different components of a multi-phase medium, and these may be impacted by different dynamical effects and influences. This could lead to alternative interpretations of the same system when probed with absorption lines compared to emission lines. Moreover, in this case, the FWHM of the gas-phase emission lines used to estimate M_{dyn} may not strictly represent the gravitational velocity dispersion required to estimate the dynamical mass of the system – contributions from, e.g., bulk flows of gas or turbulence could also influence the FWHM of an emitted line, and thus distort the inferred value of the dynamical mass.

Galaxy ID	Literature Values				Estimated Quantities			References^f
	z^a	$\mathcal{R}_{SF}/M_\odot\,yr^{-1}$	$M_*/10^9\,M_\odot$	τ_*/Myr^b	t_{SB}/Myr^c	$\mathcal{R}^*_{SB}/M_\odot\,yr^{-1\,d}$	τ_{dyn}/Myr^e	
A1689-zD1	7.60	$2.7^{+0.3}_{-0.3}$	$1.7^{+0.7}_{-0.5}$	81^{+67}_{-34}	350^{+300}_{-160}	$4.9^{+4.7}_{-2.7}$	$13^{+6.4}_{-6.2}$	$(1,2,3,4)$
UDF-983-964	$7.3^{+0.4}_{-0.3}$	$7.4^{+2.4}_{-1.4}$	$2.2^{+2.0}_{-1.5}$	170^{+70}_{-120}	290^{+140}_{-210}	$7.6^{+7.8}_{-7.6}$	26^{+17}_{-15}	$(5,6)$
GNS-zD2	$7.1^{+1.5}_{-0.6}$	$5.9^{+6.4}_{-1.6}$	$2.5^{+1.8}_{-2.2}$	250^{+70}_{-120}	240^{+85}_{-130}	$10^{+8.0}_{-10}$	$15^{+8.6}_{-9.4}$	(5)
MACS1149-JD1^g	9.11	$4.2^{+0.8}_{-1.1}$	$1.1^{+0.5}_{-0.2}$	$3.0^{+2.0}_{-1.0}$ / 290^{+190}_{-120}	100^{+69}_{-46}	$11^{+9.3}_{-5.4}$	23^{+25}_{-23}	$(7,8)$
CDFS-3225-4627	$7.1^{+1.5}_{-0.5}$	$7.4^{+5.2}_{-1.8}$	$3.5^{+2.0}_{-2.3}$	280^{+70}_{-120}	210^{+70}_{-100}	17^{+11}_{-14}	$16^{+8.5}_{-8.9}$	$(5,9)$
UDF-3244-4727^h	$7.9^{+0.8}_{-0.6}$	$5.4^{+2.0}_{-1.2}$	$2.8^{+0.5}_{-2.1}$	320^{+70}_{-120}	80^{+25}_{-34}	35^{+12}_{-30}	24^{+11}_{-14}	$(5,10)$
HDFN-3654-1216	$6.3^{+0.2}_{-0.2}$	$9.8^{+1.7}_{-0.9}$	$6.9^{+0.3}_{-3.8}$	430^{+70}_{-120}	190^{+52}_{-66}	$36^{+9.9}_{-23}$	38^{+17}_{-20}	(5)
GNS-zD3	$7.3^{+0.9}_{-0.4}$	$7.1^{+2.0}_{-1.1}$	$4.2^{+0.4}_{-1.5}$	350^{+70}_{-120}	110^{+33}_{-44}	38^{+12}_{-20}	22^{+10}_{-11}	(5)
UDF-640-1417	$6.9^{+0.1}_{-0.1}$	$10.5^{+0.7}_{-0.7}$	$6.6^{+0.3}_{-0.9}$	380^{+70}_{-120}	140^{+40}_{-53}	47^{+14}_{-19}	26^{+12}_{-12}	$(5,6)$
GNS-zD4	$7.2^{+0.4}_{-0.2}$	$11.2^{+1.4}_{-1.2}$	$6.8^{+0.3}_{-0.7}$	360^{+70}_{-120}	120^{+35}_{-47}	57^{+17}_{-23}	$19^{+8.6}_{-8.6}$	(5)
GNS-zD1	$7.2^{+0.2}_{-0.2}$	$12.6^{+1.2}_{-1.1}$	$7.6^{+0.4}_{-0.5}$	360^{+70}_{-120}	120^{+35}_{-47}	63^{+19}_{-25}	$12^{+5.4}_{-5.4}$	(5)
GNS-zD5	$7.3^{+0.2}_{-0.2}$	$20.9^{+1.5}_{-1.4}$	$12.3^{+0.3}_{-2.1}$	350^{+70}_{-120}	110^{+32}_{-44}	110^{+33}_{-48}	$14^{+6.3}_{-6.4}$	(5)

Table 6.1: High-redshift systems which have relatively suppressed star-formation rates but, despite this, show evidence of a developed stellar population consistent with a previous episode of (possibly intense) star-formation. **Caption continues on following page.**

Table 6.1 [cont.]: The objects listed in this table are the most distant for which sufficient information is available about their stellar populations and star-formation rates.

Notes:

[a] Redshifts: these are calculated spectroscopically, unless in italics which indicates a photometric redshift. For spectroscopic redshifts, uncertainties are not quoted as these were less than the precision to which these values are stated. Uncertainties are only shown for photometric redshifts, as these measurements are less precise, with uncertainties having a much greater impact on the analysis.

[b] Stellar population ages: only best-fit stellar ages are quoted here – this is because constraints depend strongly on the adopted star-formation history model.

[c] Starburst timescale: this is calculated for a redshift of galaxy formation of $z_f = 15.4$, being the highest value suggested in the literature (see Hashimoto et al. 2018) – however, A1689-zD1 is an exception as there is evidence that a later epoch of formation ($z = 9$) is more appropriate (see Mainali et al. 2018). This approach is intended to yield an over-estimate in the starburst timescale, so conservative star-formation rates would result. Thus these timescales should be regarded as an upper limit (although for an indication of accuracy, propagated Gaussian errors are shown).

[d] Star-formation rate in the starburst phase: estimated from the starburst timescale and stellar mass, so should be regarded as a lower-limit (propagated Gaussian errors are shown).

[e] Dynamical timescales: typically, the stellar mass was used as a minimum mass here, to estimate the maximum plausible value of τ_{dyn}, as values for the galaxy masses were not stated and/or could not be reasonably determined from information in the literature – as such, quoted values for τ_{dyn} should be regarded as an upper limit. There are two exceptions, being MACS1149-JD1 and A1689-zD1. In these cases, a mean density/size as derived was used (Hashimoto et al. 2018), or the full-width of half maximum of the C III (Mainali et al. 2018) line was used (respectively) to estimate dynamical masses. The required values for the sizes of systems (i.e. their radial estimates) were estimated either based on their detected half-light radius, or were available directly in the literature source – however, note that values for GNS-zD1, GNS-zD1, GNS-zD3, GNS-zD4, GNS-zD5, CDFS-3225-4627 and HDFN-3654-1216 needed to be estimated by eye using half-light radii of photometric images in González et al. (2010) and so should be treated with some caution (propagated Gaussian errors are indicated).

[f] References: (1) Bradley et al. (2008), (2) Watson et al. (2015), (3) Knudsen et al. (2017), (4) Mainali et al. (2018), (5) González et al. (2010), (6) Bouwens et al. (2004), (7) Hashimoto et al. (2018), (8) Owen et al. (2019), (9) Bouwens and Illingworth (2006), (10) Oesch et al. (2009).

[g] Stellar population modelling by spectral fitting suggests the stars in MACS1149-JD1 can be separated into two distinct stellar populations by age, one young and the other much older – see Hashimoto et al. (2018). In the table, the young component of the best-fit stellar population ages are quoted in the top line, with that for the older component below.

[h] Also has the designation HUDF-708 in Oesch et al. (2009).

From Table 6.1, it can be seen that quenching does not occur immediately after the onset of star-formation (by comparing values for t_{SB} with τ_{dyn}). Instead, it takes several dynamical timescales to reduce star-formation to a relatively quiescent state, suggesting that feedback is a gradual process rather than instantaneous – as was also indicated in the analysis of MACS1149-JD1 and corresponding discussion.

The table also highlights an outlier in this sample: A1689-zD1. This galaxy seems to exhibit a particularly long starburst period, with a corresponding low starburst star-formation rate. Moreover, it has also been found to harbour a large amount of interstellar dust – at a level of around 1% of its stellar mass (Watson et al. 2015; Knudsen et al. 2017). Dust in galaxies is thought to be built up over time due to the evolution of stellar populations (see section 1.3), but can be destroyed by the intense shocks from frequent SN activity in a starburst (Bianchi and Schneider 2007; Nozawa et al. 2007; Nath et al. 2008; Silvia et al. 2010; Yamasawa et al. 2011). In this case, it would seem that the SN rate is insufficient to destroy dust on a timescale competitive with its formation, given that the dust destruction time would be of the order 0.1 - 1 Gyr for a star-formation rate of $\mathcal{R}_{\mathrm{SF}} \approx 5.0$ M$_\odot$ yr^{-1} (Temim et al. 2015; Aoyama et al. 2017). It may be argued that this system may actually have followed a different evolutionary path, and does not properly fit into the bust-mode star-formation history which is more compatible with the behaviour of other galaxies in this sample.

6.1.2 Protogalaxies with Ongoing Starburst Activity

The 4 high-redshift systems with an ongoing starburst episode at the redshift of observation are listed in Table 6.2 in order of their star-formation rates, with literature references indicated. These systems provide some insight about pre-quenched systems to compliment that of their quenched counterparts in section 6.1.1. Stellar ages, star-formation rates, and the timescales over which each starburst has been ongoing, as well as associated dynamical timescales, are shown. These data are found by spectral fitting methods (as outlined in e.g. Robertson et al. 2010; Stark et al. 2013; Oesch et al. 2014; Mawatari et al. 2016). The length of the starburst phase of these systems is estimated as

$$t_{\mathrm{SB}} \approx \frac{(M_*/\mathrm{M}_\odot)}{(\mathcal{R}_{\mathrm{SF}}/\mathrm{M}_\odot \ \mathrm{yr}^{-1})} \ \mathrm{yr} \ , \tag{6.4}$$

where M_* is the stellar mass of the respective system, and $\mathcal{R}_{\mathrm{SF}}$ is the estimated star-formation rate (at the observational epoch).

Galaxy ID	Literature Values				Estimated Quantities		References[c]
	z^a	$\mathcal{R}_{\mathrm{SF}}/M_\odot\,\mathrm{yr}^{-1}$	$M_*/10^9\,M_\odot$	τ_*/Myr	$t_{\mathrm{SB}}/\mathrm{Myr}$	$\tau_{\mathrm{dyn}}/\mathrm{Myr}^b$	
GN-z11	11.1	24^{+10}_{-10}	$1.0^{+1.5}_{-0.6}$	40^{+60}_{-24}	42^{+140}_{-30}	$11^{+9.6}_{-5.9}$	(1)
EGS-zs8-1^d	7.73	79^{+47}_{-29}	$7.9^{+4.7}_{-2.9}$	100^{+220}_{-68}	100^{+150}_{-60}	23^{+12}_{-11}	(2, 3)
GN-108036	7.21	$100^{+5.0}_{-2.0}$	$0.58^{+0.14}_{-0.14}$	$5.8^{+1.5}_{-1.4}$	$5.8^{+1.6}_{-5.8}$	61^{+28}_{-28}	(4)
SXDF-NB1006-2	7.21	350^{+170}_{-280}	$0.35^{+1.8}_{-0.14}$	$1.0^{+9.0}_{-0.0}$	$1.0^{+33}_{-1.0}$	$13^{+34}_{-6.4}$	(5)

Table 6.2: High-redshift star-forming galaxy sample in which a starburst episode appears to be in progress during the observational epoch of these objects. z is observed redshift, $\mathcal{R}_{\mathrm{SF}}$ is the derived/inferred star-formation rate, M_* is the total stellar mass estimate, τ_* is the characteristic stellar population age, t_{SB} is the star-formation timescale (i.e. the time over which the ongoing starburst appears to have been active for) and τ_{dyn} is the dynamical timescale of the system (an estimated upper limit). The galaxies in this sample are among the furthest away in the known Universe for which sufficient information is available (or may be determined) regarding the star-formation rate, stellar mass and stellar population. Notes:

^{a} Redshifts: all these are determined spectroscopically, and their uncertainty is substantially less than the precision to which the redshift values are quoted.

^{b} Dynamical timescales: note that these estimated values should be considered as upper limits because the stellar mass was used as a minimum mass to estimate the maximum plausible value of τ_{dyn} when values for the dynamical galaxy mass were not available and/or could not be derived from the available information. However, to indicate accuracy, Gaussian errors were propagated from uncertainties in contributing quantities. SDXF-NB1006-2 is an exception for which the dynamical mass estimate quoted in Inoue et al. (2016) could be directly used. The required values for galaxy size in calculating the dynamical timescale were either estimated using the half-light radius of the observed system, or simply used the stated galaxy radius (if available).

^{c} References: (1) Oesch et al. (2016), (2) Oesch et al. (2015), (3) Grazian et al. (2012), (4) Ono et al. (2012), (5) Inoue et al. (2016).

^{d} Also identified as EGSY-0348800153 and EGS 8053.

Table 6.2 shows that the estimated stellar population ages in the two most actively star-bursting systems of the sample (GN-108036 and SXDF-NB1006-2) are substantially lower than their dynamical timescales. This would indicate that insufficient time has passed since the initiation of their starburst phases for the impacts of any feedback/quenching process to have taken hold. Such an interpretation would be consistent with their ongoing high star-formation rates. By contrast, the dynamical timescale for the other two star-forming systems (GN-z11 and EGS-zs8-1) is shorter than the estimated timescale over which their observed starburst appears to have been ongoing ($\tau_{\mathrm{dyn}} < t_{\mathrm{SB}}$). Thus, in these cases it is reasonable to expect that feedback impacts may now be starting to influence the ongoing star-forming evolution of these systems, which could account for their comparatively lower star-formation intensities.

6.2 Internal Heating and Quenching

The heating of interstellar gases by CRs is governed by the DC mechanism, which can lead to quenching if it causes the temperature of the molecular clouds in which stars form to exceed their characteristic virial temperature. This is the point at which gravitational collapse can no longer proceed in a cloud, because the additional outward thermal pressure is able to overcome (or at least balance) the inward pull of gravity. Other processes may operate alongside CR heating in clouds, such as radiative heating and conduction from the surrounding hot ISM phases. However, these would typically either not be as powerful at the effect imparted by CRs (see chapter 5), or would only occur with reasonable speeds in specific scenarios – e.g. conduction of heat into dense clouds and clumps is fast for relatively low cloud densities and when submerged into a hot plasma (e.g. Wu et al. 2019), but for an interstellar molecular cloud, the conduction timescale would be of order Gyrs, and so would not be comparatively important (Draine 2011).

Calculating the individual heating rates due to the DC heating by CRs by invoking a full MC realisation (as was done in chapter 5) in a simulated multi-phase interstellar medium is computationally demanding, therefore it is useful to consider a scaling relation in which a reasonable characteristic heating power

may be estimated from a baseline model. A first approximation can be made whereby the average density of interstellar gases and their average heating rate can be used in order to set an upper limit to the CR heating timescales. A conservative estimate determined in this way is sufficient for the present purpose, given that much greater uncertainties surrounding the properties of the interstellar environment (e.g. clumping substructure, mass distribution and composition) and CR injection fractions would make any more refined timescale calculations redundant at this time. Detailed sub-grid theoretical work to understand the heating of molecular clouds and star-forming cores in high-redshift environments will be necessary in future work to properly understand the feedback response of these environments to patterns of CR heating (see section 7.3), and will be critical to inform future observations of high-redshift starbursts in coming years using, e.g. the *Atacama Large Millimetre Array (ALMA)* and the *James Webb Space Telescope (JWST)* which will study these high-redshift protogalactic environments in unprecedented detail.

The virial temperature of a star-forming molecular cloud is proportional to its enclosed mass and size, i.e. $T_{\mathrm{vir}} \propto M_{\mathrm{cl}}/r_{\mathrm{cl}}$ (Binney and Tremaine 2008). It can be related to the virial temperature of its host galaxy by use of a scaling relation (which assumes a uniform density in the cloud), i.e.

$$T_{\mathrm{vir,gal}} = \left(\frac{\bar{n}_{\mathrm{H,gal}}}{\bar{n}_{\mathrm{H,cl}}} \right) \left(\frac{r_{\mathrm{gal}}}{r_{\mathrm{cl}}} \right)^2 T_{\mathrm{vir,cl}} \; , \tag{6.5}$$

where the mean ISM gas density $\bar{n}_{\mathrm{H,gal}}$ is 10 cm^{-3}, and the host galaxy size is $r_{\mathrm{gal}} = 1$ kpc. By comparison, a molecular cloud (which must undergo gravitational collapse to trigger star-formation) has a typical density of between $\bar{n}_{\mathrm{H,cl}} = 10^2$ cm^{-3} to $\bar{n}_{\mathrm{H,cl}} = 10^5$ cm^{-3}, with size ranging between a few to a few tens of parsecs (Draine 2011). This gives a ratio $\bar{n}_{\mathrm{H,gal}}/\bar{n}_{\mathrm{H,cl}} = 10^{-4}$ (if using extreme values in the respective cases, i.e. $\bar{n}_{\mathrm{H,cl}} = 10^5$ cm^{-3} and $r_{\mathrm{cl}} = 10$ pc , to yield a conservative result), and $r_{\mathrm{gal}}/r_{\mathrm{cl}} = 10^2$. Applying these ratios to the scaling relation 6.5 indicates an approximate relation of $T_{\mathrm{vir,gal}} \gtrsim T_{\mathrm{vir,cl}}$, which means that if $T_{\mathrm{vir,gal}}$ is reached, then $T_{\mathrm{vir,cl}}$ must also have been reached (or exceeded) on average, and the associated heating timescale can be regarded

as an upper limit to that required for quenching. Note that although these are average characteristic values specified across the entire galaxy, DC cosmic ray feedback would be particularly concentrated in the most dense regions of the interstellar environment (i.e. the molecular clouds and star-forming cores), where the CR heating and resulting temperature rise would be much faster than the galactic average. This further ensures that the treatment here yields a conservative upper-bound on the heating timescale. The condition for quenching can thus be regarded in terms of the virial temperature for the entire galaxy. It is defined as:

$$T_{\text{vir}} \approx 6.8 \times 10^4 \left(\frac{M_{\text{dyn}}}{10^9 \, M_\odot} \right) \left(\frac{1 \, \text{kpc}}{r_{\text{gal}}} \right) \, \text{K} \tag{6.6}$$

(Binney and Tremaine 2008). The following analysis uses this as a basis to estimate CR heating and quenching timescales.

6.2.1 Internal Heating Parameterisation and Application

In the case of the DC heating power, the rate is principally governed by the input CR power (i.e. via the star-formation rate $\mathcal{R}_{\text{SF}}$ or $\mathcal{R}_{\text{SN}}$ of the system) and the interstellar density, which provides the target for the underlying hadronic interactions. As such, it may reasonably be parameterised and scaled as

$$\dot{Q}_{\text{DC},2} \approx \dot{Q}_{\text{DC},1} \left(\frac{\mathcal{R}_{\text{SF},2}}{\mathcal{R}_{\text{SF},1}} \right) \left(\frac{n_{\text{H},2}}{n_{\text{H},1}} \right) \, , \tag{6.7}$$

where reference values are $\dot{Q}_{\text{DC},1} = 1.7 \times 10^{-25}$ erg cm^{-3} s^{-1}, $\mathcal{R}_{\text{SF},1} = 16 \, M_\odot$ yr^{-1} and $n_{\text{H},1} = 10$ cm^{-3}. Subscript '2' denotes the scaled values. Note that the star-formation rate has been adopted here as the scaling parameter instead of the SN event rate. This is simply because the available quantity for these galaxies is the star-formation rate itself, even though the SN event rate is the more physically appropriate parameter. This treatment requires that $\dot{Q}_{\text{DC},2}$ and $\dot{Q}_{\text{DC},1}$ are computed for systems where the ISM is of comparable density such that the CR heating efficiency (see Fig. 5.13) is similar – this would usually be the case for the current purposes, given that DC heating operates within the host galaxy and is largely unaffected by variations

that might arise in the external circumgalactic environment.

Using the virial temperature T_{vir} as a cut-off, a quenching timescale τ_{Q} can be assigned to a galaxy. This is defined as the time required for the virial temperature to be attained by interstellar gas subjected to a given heating rate. However, the full CR heating power only develops after the magnetic field of the host galaxy has saturated. To estimate τ_{Q}, this magnetic field evolution must be taken into account such that the quenching time would be the magnetic saturation time t_{sat} plus the time taken for entrenched CR heating to raise the ISM temperature above T_{vir}. The magnetic saturation time may be estimated as

$$t_{\mathrm{sat}} \approx 140 \, \left(\frac{\mathcal{R}_{\mathrm{SF}}}{16\,\mathrm{M}_\odot} \right)^{-1} \mathrm{Myr} \; , \tag{6.8}$$

which is scaled from the results shown in section 1.3.3, and are governed only by the SN event rate of the host galaxy (or the star-formation rate, according to the conversion relation specified in section 1.3.1). The time taken for the virial temperature to be reached due to the DC heating channel then follows as

$$\tau_{\mathrm{Q}} \approx t_{\mathrm{sat}} + \frac{n_{\mathrm{H}} \, k_{\mathrm{B}} \, T_{\mathrm{vir}}}{\dot{Q}_{\mathrm{DC}}} \; , \tag{6.9}$$

in which the second term gives the timescale for this temperature to be reached under a DC heating power of $\dot{Q}_{\mathrm{DC}}$, and where $n_{\mathrm{H}} = \langle n_{\mathrm{H}} \rangle$ is the mean interstellar gas (number) density for the host galaxy.

Using the literature or derived values for the key parameters in the sample of observed high-redshift starburst and post-starburst galaxies introduced in Tables 6.1 and 6.2, the resulting DC heating power operating within the ISM for each system during its starburst phase was estimated using the scaling approach in equation 6.7. The resulting values are quoted in the column $\dot{Q}_{\mathrm{DC}}$ in Table 6.3, later in section 6.4. From this, the above approach was used to estimate the associated quenching timescale in Myr, shown by column τ_{Q} in the same table. These are discussed and analysed in section 6.4.

6.3 External Heating and Stunning

The IX channel typically operates over larger scales than the DC heating mechanism with its impacts being principally felt in the circumgalactic medium and the structures therein, where the DC process cannot reach. However, at high-redshift, its effect can also be important in the internal environment of a galaxy. IX heating is pertinent in influencing the development of the inflowing filaments (Dekel et al. 2009a; Stewart et al. 2013; Goerdt and Ceverino 2015; Goerdt et al. 2015) which supply the cold gas required to feed star-formation in the host galaxy (Dijkstra et al. 2006; Sancisi et al. 2008; Ribaudo et al. 2011; Sánchez Almeida et al. 2014; Peng et al. 2015) via e.g. cold mode accretion (Birnboim and Dekel 2003; Kereš et al. 2005). If sufficiently strong, heating and evaporation of these filaments can lead to the stunning of a galaxy, if they are prevented from delivering a supply of cold gas its ISM – see Fig. 5.14.

6.3.1 External Heating Parameterisations

Like the DC heating power, the internal IX heating effect can be estimated using a parametrised scaling. The power with which it operates depends on the star-formation rate, the ISM density, and the intensity of the non-thermal X-rays emitted by a galaxy, which itself is governed by the redshift (due to its dependence on the CMB energy density). This leads to the following parameterisation:

$$\dot{Q}_{\mathrm{IX},2} \approx \dot{Q}_{\mathrm{IX},1} \left(\frac{1+z_2}{1+z_1} \right)^4 \left(\frac{\mathcal{R}_{\mathrm{SF},2}}{\mathcal{R}_{\mathrm{SF},1}} \right) \left(\frac{n_{\mathrm{H},2}}{n_{\mathrm{H},1}} \right) \ , \qquad (6.10)$$

which is normalised to $\dot{Q}_{\mathrm{IX},1} = 6.4 \times 10^{-27}$ erg cm^{-3} s^{-1}, $z_1 = 7$, $\mathcal{R}_{\mathrm{SF},1} = 16$ yr^{-1} and $n_{\mathrm{H},1} = 10$ cm^{-3} (this is assumed to be equal to the electron number density in the medium).

In regions where the circumgalactic medium density is not greatly influenced by the density profile of the host protogalaxy, the distance from the host is sufficiently large that it may be regarded as an effective point source of X-rays. Over such length-scales, the above parametrisation 6.10 additionally

has a distance dependence. This gives

$$\dot{Q}_{\mathrm{IX},2} \approx \dot{Q}_{\mathrm{IX},1} \left(\frac{1+z_2}{1+z_1}\right)^4 \left(\frac{\mathcal{R}_{\mathrm{SF},2}}{\mathcal{R}_{\mathrm{SF},1}}\right) \left(\frac{r_2}{r_1}\right)^{-2} \left(\frac{n_{\mathrm{e},2}}{n_{\mathrm{e},1}}\right) , \qquad (6.11)$$

where $\dot{Q}_{\mathrm{IX},1} = 7.9 \times 10^{-37}$ erg cm^{-3} s^{-1}.[5] The distance dependence here is introduced using a scaling location of $r_1 = 100$ kpc and r_2 as the distance of the required point from the centre of the protogalaxy. Furthermore, $n_{\mathrm{e},1} = x_i\, n_{\mathrm{H},1} = 10^{-2}$ cm^{-3} is the number density of electrons, with x_i being the characteristic ionisation fraction of the system.

6.3.2 Heating of Filamentary Inflows and Stunning

To analyse the impact of external IX heating, and to determine the resulting stunning timescale, a suitable approximation for the virial temperature of a cold filament is needed. Consider the temperature required to prevent a segment of filamentary cloud from collapsing. This sets the minimum temperature above which the cloud begins to disperse (giving a lower limit for the stunning timescale for a given heating rate). Thus, for a spherical region of cloud with radius $r_{\mathrm{f}} = \sqrt{0.1}\, r_{\mathrm{gal}}$ (which reflects a 10% covering fraction of the filament – see section 1.2.1), the mass of a filamentary region follows as

$$M_{\mathrm{fil}} \approx \frac{4\pi}{3} r_{\mathrm{f}}^3 n_{\mathrm{H}}\, m_{\mathrm{p}} , \qquad (6.12)$$

where n_{H} is the baryon density of the filamentary media, as determined by equation 1.3. For a galaxy exhibiting $\mathcal{R}_{\mathrm{SF}} = 16$ M$_\odot$ yr^{-1}, this would indicate a filamentary region mass of around 6×10^7 M$_\odot$ (which is similar to the total steady-state filament mass). The corresponding virial temperature follows as $T_{\mathrm{vir}} \approx 1.2 \times 10^4$ K. This is roughly consistent with the expectation for the temperature range of these structures (i.e between $10^4 - 10^5$ K – see Dekel and Birnboim 2006; Dekel et al. 2009a). The stunning timescale is calculated in a similar manner to the quenching timescale in the previous section, i.e the sum of the magnetic containment time (required for the X-ray glow to develop)

---

[5]Note that the normalisation here is substantially lower than a direct scaling of that for equation 6.10 might suggest. This is because the previous parameterisation additionally takes account of the interstellar density 'foreground', which is much higher than the CGM density and not required here.

and the heating timescale: $\tau_{\mathrm{S}} = t_{\mathrm{sat}} + \tau_{\mathrm{IX}}$, where the IX heating timescale is given by

$$\tau_{\mathrm{IX}} = \frac{x_i\, n_{\mathrm{H}}\, k_{\mathrm{B}}\, T_{\mathrm{vir}}}{\overline{Q}_{\mathrm{IX}}} \ , \tag{6.13}$$

Here, $\overline{Q}_{\mathrm{IX}}$ is introduced as the effective IX heating rate throughout the filament. The true IX heating power along the length of the filament would be subject to the inverse square law along its length, meaning its value would vary substantially at different points along the structure's extent. However, adopting an effective heating power, $\overline{Q}_{\mathrm{IX}}$, for the inflow allows an approximate timescale associated with the heating process to be estimated. $\dot{Q}_{\mathrm{IX}}$ varies as distance squared (r^{-2}) away from the galaxy. Thus, consider a point R_{eq} along a radial line, at which the total (integrated) heating rate up to some distance $r = R_{\mathrm{eq}}$ is equal to that above $r = R_{\mathrm{eq}}$, being an effective midpoint, i.e.

$$\dot{Q}_{\mathrm{IX}}|_0 \int_{r_{\mathrm{in}}}^{R_{\mathrm{eq}}} r^{-2}\, \mathrm{d}r = \dot{Q}_{\mathrm{IX}}|_0 \int_{R_{\mathrm{eq}}}^{R} r^{-2}\, \mathrm{d}r \ , \tag{6.14}$$

where r_{in} is the innermost radius of the filament, R is its outermost extent and $\dot{Q}_{\mathrm{IX}}|_0$ is an effective central volumetric heating power.[6] Taking $R = 50$ kpc, beyond which inflows are not clearly evident in simulations (see Dekel et al. 2009a; Stewart et al. 2013; Goerdt and Ceverino 2015), and $r_{\mathrm{in}} \sim r_{\mathrm{gal}} = 1$ kpc gives $R_{\mathrm{eq}} = 1.96$ kpc. For an inflowing filament, the gas would (approximately) experience a comparable amount of heating on either side of R_{eq}. Here, the proximity of R_{eq} to r_{in} suggests a rapid evaporation of the inflow filament as it nears the galaxy, with much more gentle IX heating arising further out.

Using the parameterisation above (equation 6.11), the characteristic IX heating power at R_{eq} can be estimated by applying an inverse-square law scaling to equation 6.10. Given the continuous density profile along the filament and into the ISM, a scaling of this internal IX heating parametrisation is presumably more meaningful than a re-scaling of the external IX heating power. This yields $\overline{Q}_{\mathrm{IX}} = \dot{Q}_{\mathrm{IX}}|_{R_{\mathrm{eq}}} \approx 3.0 \times 10^{-27}$ erg cm^{-3} s^{-1} for a system with $\mathcal{R}_{\mathrm{SF}} = 16$ M$_\odot$ yr^{-1} and $\overline{n}_{\mathrm{H}} = 20$ cm^{-3} at $z = 7$. The corresponding

---

[6]This approximates the heating profile to follow $\dot{Q}_{\mathrm{IX}}|_0/4\pi r^2$, which yields the form of these integrals.

stunning timescale of around 200 Myr (when also accounting for the magnetic containment time) for an inflow traversing a distance of 50 kpc at a velocity of 400 km s^{-1}, which compares to an infall timescale of over 100 Myr. The filament's dynamical timescale is around $\tau_{\mathrm{dyn}} \approx 20$ Myr, so this paints a picture of a cold inflowing filament being destroyed by the X-ray glow of the host galaxy, providing a reasonable expectation that a galaxy could indeed be stunned by the IX heating process at high-redshift. This procedure is applied to the sample of observed high-redshift systems to determine the resulting IX heating rate and their associated stunning timescales during their burst phase, as presented in Table 6.3.

6.4   Indications of Cosmic Ray Feedback

Derived information for the full sample of high-redshift quenched post-starburst and starburst systems (cf. Tables 6.1 and 6.2) is shown in Table 6.3, which introduces estimates for t_{qui} as the time for which a post-starburst galaxy has remained relatively quiescent after its initial violent star-formation episode (this is estimated from the age of the stellar population and starburst timescale – here, it is sufficient to approximate this to be comparable to the stellar population ages, such that $t_{\mathrm{qui}} \approx \tau_*$[7]). Table 6.3 also shows values for the heating rate via the DC process in the interstellar medium of the host, $\dot{Q}_{\mathrm{DC}}$, the heating rate via the IX process in the inflowing filaments at an estimated average X-ray irradiation intensity, $\overline{Q}_{\mathrm{IX}}$, the estimated timescales for star-formation quenching τ_{Q} and stunning τ_{S}, and the cooling timescale for the inflowing gas, τ_{cool} (this is estimated by assuming a CGM number density of 10^{-2} cm^{-3}, and $T = T_{\mathrm{vir}}$ to give an indication of the timescale over which inflows may be able to be reinstated in the CGM).

The timescales presented in Table 6.3 provide support for the argument that CR feedback operates in all these systems via both the direct quenching and stunning mechanisms, with some competition between them. This is evident from the similarity between the starburst timescales, t_{SB} and the

---

[7]This argument follows from the idea that the age of the stars would correspond to their age by the end of the starburst plus the quiescent time. More correctly, this value should be determined by considering the point during the starburst episode that stars formed *on average*, but such a calculation is not trivial, and is deserving of a dedicated study.

quenching and/or stunning timescales, τ_Q and τ_S. There are three scenarios for these galaxies, which can broadly be categorised as follows:

- **Low** $\mathcal{R}_{SB}^*$, $t_{SB} \leq \{\tau_Q, \tau_S\}$: Here, t_{sat} dominates for both τ_S and τ_Q – for example, in A1689-zD1 and UDF-983-964. From equation 6.8, magnetic saturation arises in A1689-zD1 over a timescale of 440 Myr, while in UDF-983-964 it takes around 320 Myr. Thus, quenching can only occur over timescales comparable to this (at its fastest). The low rates of star-formation seen in these cases could be due to a limited supply of cold gas reaching the galaxies. In such a scenario, it would not take much to heat the local reservoir of gas (being the only supply for star-formation), quickly leading to quenching. Alternatively, gas of a sufficiently low temperature may persist in pockets throughout these galaxies which would then be heated and/or exhausted rapidly, or moderately warm gases (close to the local virial temperature of a star-forming system) may be abundant throughout the host, but only cooling inefficiently. This would produce low star-formation rates overall, which may readily be quenched with little requirement for feedback. In circumstances where star-formation was arising just below some temperature threshold, it may be argued that quenching may even be achieved before complete magnetic saturation has been reached. This would also account for a starburst period which is shorter even than the quenching timescale.

- **Moderate** $\mathcal{R}_{SB}^*$, $t_{SB} \simeq \tau_Q$: Now, in systems with moderate star-formation activity, t_{sat} is less important to t_{SB} (cf. equation 6.8). In these circumstances, both the quenching τ_Q and starburst t_{SB} timescales are consistent and comparable with one another. It might be argued that this would suggest such processes are more dependent on their cold gas reservoirs to form stars than they are on inflows, with feedback principally driven by quenching. Before the termination of star-formation can happen, CRs must heat much of the cold gas reservoir (after magnetic saturation has been achieved). The action of stunning is less important in these systems, but is effective over longer timescales to maintain quench-

ing throughout the quiescent period (until new flows can be established and/or CGM gas can cool).

- **High** $\mathcal{R}_{\mathrm{SB}}^{*}$, $t_{\mathrm{SB}} \simeq \tau_{\mathrm{S}}$: Here, collapsing and fragmentation of interstellar gas reservoirs may not be sufficient to maintain star-formation at the intense level estimated for a prolonged period (with correspondingly short quenching timescales). Systems, including examples like GNS-zD1 and GNS-zD5, presumably would depend instead on the injection of cold gas by filamentary inflows to sustain their extreme starburst episodes. This can then be maintained until stunning stops this external gas supply, thus accounting for the similarity between t_{SB} and τ_{S} in such cases.

Galaxy ID	z	$\mathcal{R}^*_{\mathrm{SB}}$ /M$_\odot$ yr^{-1}	t_{SB} /Myr[a]	t_{qui} /Myr[b]	$\log\left[\dfrac{\dot{Q}_{\mathrm{DC}}}{/\mathrm{erg\ cm}^{-3}\ \mathrm{s}^{-1}}\right]^c$	τ_{Q} /Myr[d]	$\log\left[\dfrac{\overline{Q}_{\mathrm{IX}}}{/\mathrm{erg\ cm}^{-3}\ \mathrm{s}^{-1}}\right]^e$	τ_{S} /Myr[f]	τ_{cool} /Myr[g]	τ_{dyn} /Myr
					QUENCHED POST-STARBURSTS, HIGH-REDSHIFT					
A1689-zD1	7.60	$4.9^{+4.7}_{-2.7}$	350^{+300}_{-160}	81^{+67}_{-34}	-25.28	510	-27.07	540	76	$13^{+6.4}_{-6.2}$
UDF-983-964	$7.3^{+0.4}_{-0.3}$	$7.6^{+7.8}_{-7.6}$	290^{+140}_{-210}	170^{+70}_{-120}	-25.09	350	-27.43	390	100	26^{+17}_{-15}
GNS-zD2	$7.1^{+1.5}_{-0.6}$	$10^{+8.0}_{-10}$	240^{+85}_{-130}	250^{+70}_{-120}	-24.97	280	-27.09	330	120	$15^{+8.6}_{-9.4}$
MACS1149-JD1	9.11	$11^{+9.3}_{-5.4}$	100^{+69}_{-46}	290^{+190}_{-120}	-24.93	210	-27.68	250	43	23^{+25}_{-23}
CDFS-3225-4627	$7.1^{+1.5}_{-0.5}$	17^{+11}_{-14}	210^{+70}_{-100}	280^{+70}_{-120}	-24.74	180	-26.63	240	140	$16^{+8.5}_{-8.9}$
UDF-3244-4727	$7.9^{+0.8}_{-0.6}$	35^{+12}_{-30}	80^{+25}_{-34}	320^{+70}_{-120}	-24.43	80	-26.02	140	110	24^{+11}_{-14}
HDFN-3654-1216	$6.3^{+0.2}_{-0.2}$	$36^{+9.9}_{-23}$	190^{+52}_{-66}	430^{+70}_{-120}	-24.42	83	-26.86	230	130	38^{+17}_{-20}
GNS-zD3	$7.3^{+0.9}_{-0.4}$	38^{+12}_{-20}	110^{+33}_{-44}	350^{+70}_{-120}	-24.39	79	-26.11	160	140	22^{+10}_{-11}
UDF-640-1417	$6.9^{+0.1}_{-0.1}$	47^{+14}_{-19}	140^{+40}_{-53}	380^{+70}_{-120}	-24.30	67	-26.25	170	150	26^{+12}_{-12}
GNS-zD4	$7.2^{+0.4}_{-0.2}$	57^{+17}_{-23}	120^{+35}_{-47}	360^{+70}_{-120}	-24.22	57	-26.00	140	150	$19^{+8.6}_{-8.6}$
GNS-zD1	$7.2^{+0.2}_{-0.2}$	63^{+19}_{-25}	120^{+35}_{-47}	360^{+70}_{-120}	-24.17	59	-25.67	140	190	$12^{+5.4}_{-5.4}$
GNS-zD5	$7.3^{+0.2}_{-0.2}$	110^{+33}_{-48}	110^{+32}_{-44}	350^{+70}_{-120}	-23.93	40	-25.25	120	230	$14^{+6.3}_{-6.4}$
					STARBURSTS, HIGH-REDSHIFT					
GN-z11	11.1	24^{+10}_{-10}	42^{+140}_{-30} *	—	-24.59	110	-25.07	120	110	$11^{+9.6}_{-5.9}$
EGS-zs8-1	7.73	79^{+47}_{-29}	100^{+150}_{-60} *	—	-24.08	34	-26.35	110	110	23^{+12}_{-11}
GN-108036	7.21	$100^{+5.0}_{-2.0}$	$5.8^{+1.6}_{-5.8}$ *	—	-23.97	23	-25.30	120	51	61^{+28}_{-28}
SXDF-NB1006-2	7.21	350^{+170}_{-280}	$1.0^{+33}_{-1.0}$ *	—	-23.43	6.4	-26.02	110	14	$13^{+34}_{-6.4}$

Table 6.3: Derived values for high-redshift quenched post-starburst and starburst systems, for the sample introduced in Tables 6.1 and 6.2. **Caption continues on the following page.**

Table 6.3 [cont.]: Columns show redshift z, star-formation rate (during burst) $\mathcal{R}^*_{\mathrm{SB}}$, estimated duration of the starburst period t_{SB} and estimated dynamical timescale τ_{dyn} (upper limit, although Gaussian propagated errors are shown to indicate accuracy), all from previous tables (for reference). This table also introduces estimated values of t_{qui} (quiescent timescale since end of starburst), the heating power via the DC mechanism, $\dot{Q}_{\mathrm{DC}}$, the heating power via the IX mechanism (at an estimated average level along an inflowing filament – see main text for details), $\overline{Q}_{\mathrm{IX}}$, quenching timescale τ_{Q}, stunning timescale τ_{S}, and the cooling timescale for the CGM (and hence in-falling gas), τ_{cool}. Where uncertainties are not shown, value should be taken as a (conservative) upper limit.

Notes:

[a] Starburst time, t_{SB}: estimated timescale over which the starburst phase has persisted – an asterisk * indicates that starburst activity is ongoing at the observational epoch.

[b] Quiescence timescale, t_{qui}: estimated time since the end of the starburst phase, which is found using the stellar population age, such that $t_{\mathrm{qui}} \approx \tau_*$ – see footnote 7 in text for details.

[c] Coulomb heating rate, $\dot{Q}_{\mathrm{DC}}$: log10 of DC heating power in the interstellar medium is shown (responsible for the quenching process).

[d] Quenching timescale, τ_{Q}: Quenching timescale is estimated from the virial temperature of the host galaxy.

[e] Characteristic filament inverse Compton heating rate, $\overline{Q}_{\mathrm{IX}}$: log10 of a characteristic IX heating rate in inflowing filaments (responsible for stunning).

[f] Stunning timescale τ_{S}: Stunning timescale is estimated from the virial temperature of the inflowing filaments (not of the total system). This is best regarded as an upper limit.

[g] Cooling timescale, τ_{cool}: Cooling timescale of the circumgalactic gases – this is the minimum time needed for star-formation to resume after its termination by CR feedback (following quenching and/or stunning).

6.4.1 Discussion and Analysis

At the end of the starburst phase of a galaxy in the early Universe, quiescence would set in and persist until the conditions which enabled star-formation were reinstated. The cooling timescale τ_{cool} indicates the time required for cold filamentary inflows to be reinstated, after CR heating by the IX process in the external environment has abated. For many of the galaxies, it can be seen that the cooling timescale and the quiescent time, t_{qui}, are similar. This may suggest a connection between the two processes, and indicates that the quiescence period in a galaxy's star-formation history is brought to an end when inflows of gas are able to resume.

Although the quiescent timescale is interpreted simply as the time elapsed since the end of a starburst episode, it may alternatively be regarded as a measure of the degree of star-formation feedback in a system. Indeed, this may be the case if post-starburst galaxies only tend to exceed detection thresholds once they resume star-formation, so that the high-redshift post-starburst galaxies observed are be preferentially those which have emerged from their quiescent phase, thus being the only ones which can be detected with the current generation of instruments available. Such an interpretation of t_{qui} is actually supported by the suggestion of two stellar populations found in MACS1149-JD1, where the youngest population is attributed to the observed lower star-formation rate, being only a few Myr old (Hashimoto et al. 2018). Consider how t_{qui} relates to other system parameters, as plotted in Fig. 6.2 for size r_{gal}, stellar mass M_* (both directly derived/estimated quantities), and dynamical timescale τ_{dyn}, quenching timescale τ_{Q} and stunning timescale τ_{S} (calculated quantities)[8].

---

[8]The system MACS1149-JD1 is highlighted here in red (and in subsequent plots). This is because it is at a much higher redshift than the other galaxies in the sample – despite this, its properties and behaviour do not otherwise appear to be exceptional.
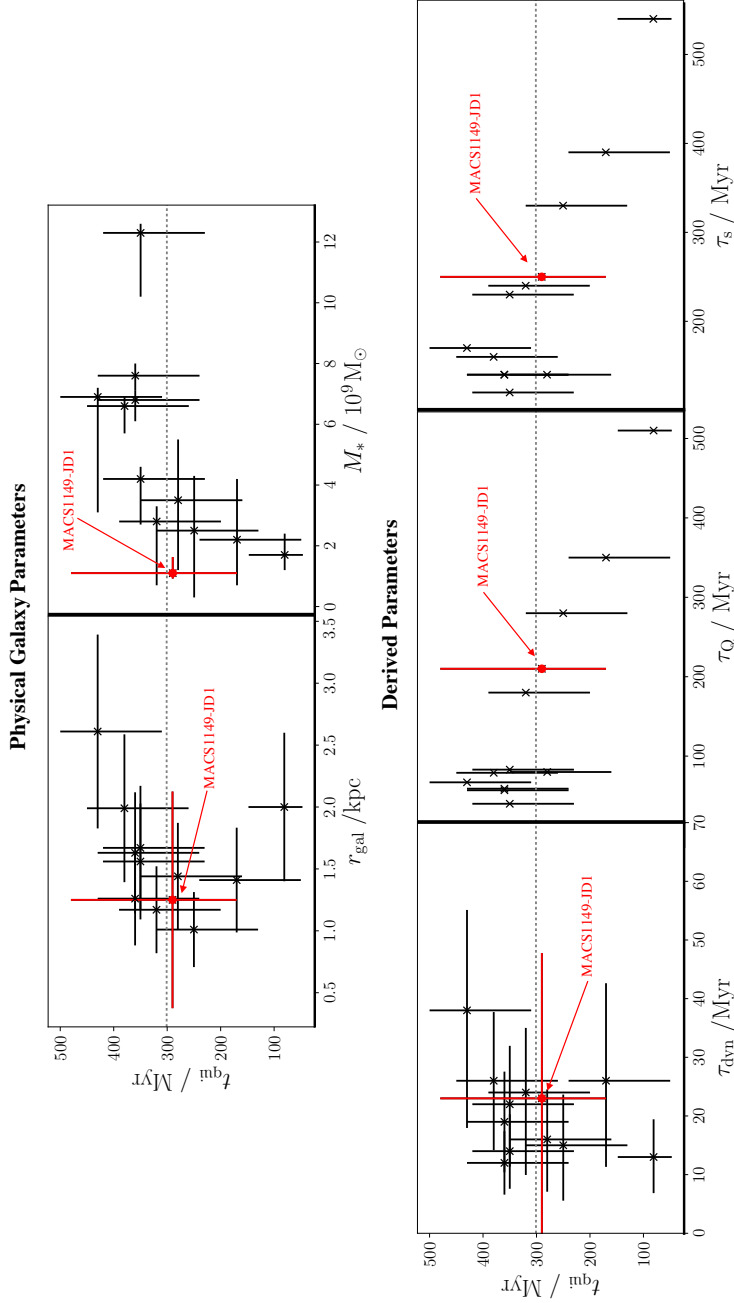
Fig. 6.2: Parameter plots to established the response of the quiescence timescales to physical (upper row) and derived (lower row) galactic parameters. Points representing MACS1149-JD1 are highlighted in red as this galaxy is at much higher redshift than the others in the sample (but does not otherwise seem to be an outlier). The average t_{qui} value is shown by the horizontal dashed grey line for comparison. **Upper Left:** Plot against estimated galaxy radius, which demonstrates that the quiescent time scale is independent of galaxy size, with an associated Pearson correlation coefficient of 0.15 (weighted appropriately by error bars). Error bars in r_{gal} are as quoted in the literature (A1689-zD1 at 50% and MACS1149-JD1 at 71%), or are otherwise set to be 30%. **Upper Right:** Plot against stellar mass, with a positive correlation (coefficient of 0.58). **Lower Left:** Plot against galaxy dynamical timescales, which appears to show that t_{qui} is not dependent on τ_{dyn} (correlation of 0.06). **Lower Centre:** Plot against quenching timescale, τ_Q, with a strong negative correlation (coefficient of -0.81), as would be consistent with t_{qui} indicating the strength of feedback felt by the system – i.e. the longer time required taken to quench star-formation, the weaker the feedback (and the shorter the quiescence timescale). Uncertainties in τ_Q are not known, and so are not plotted or included in the analysis. **Lower Right:** As per the lower centre panel, but against the stunning time, τ_S which again shows a negative correlation (of coefficient -0.78) as would also be consistent with t_{qui} having been influenced by feedback (shorter quiescence time periods for longer stunning times). As with τ_Q, uncertainties in τ_S are not known and so are omitted.

The panels in the figure demonstrate a moderate positive correlation between t_{qui} and stellar mass (Pearson coefficient of 0.58), but a strong negative correlation between t_{qui} and both τ_{Q} (-0.81) and τ_{S} (-0.78). These negative correlations are particularly telling, and are consistent with t_{qui} being an effective tracer for the level of feedback experienced by a system: for longer quenching or stunning timescales (i.e. when the feedback effect by CR heating effects would be weak), the quiescent time which results is shorter. The positive correlation between t_{qui} and stellar mass M_* also supports such an interpretation, given that the systems with higher stellar mass seem to yield more intense starburst episodes (with respect to their size). This is shown in Fig. 6.3, which plots the dependence of the star-formation rate surface density of galaxies during their burst phase, Σ_{SB}^*, against stellar mass, where

$$\Sigma_{\mathrm{SB}}^* = \frac{\mathcal{R}_{\mathrm{SB}}^*}{4\pi r_{\mathrm{gal}}^2} \, , \tag{6.15}$$

which illustrates the moderate correlation between these quantities. Comparing this with Fig. 6.4 shows that the specific star-formation rate during the quiescent period exhibits a similar dependence on stellar mass, however this appears to simply scale with the star-formation rate surface density during the burst. No notable correlation between t_{qui} and galaxy size r_{gal} or dynamical timescale τ_{dyn} emerges in this analysis but, in a feedback model, no such correspondence would be expected between these parameters. Overall, these plots show that there is no strong dependency of t_{qui} on extensive system quantities, only intensive ones relating to the level of feedback, i.e. τ_{Q} and τ_{S}. Such results are consistent with the quiescence being strongly influenced by feedback from star-formation.

The additional four systems observed with ongoing starburst activity are also shown in grey in the upper panel of Fig. 6.3. These weakly indicate some inverse trend with stellar mass, and such behaviour would follow from the depletion of gas supplies as stunning takes hold – however it is difficult to draw strong conclusions with this current small data set and the large associated uncertainties.
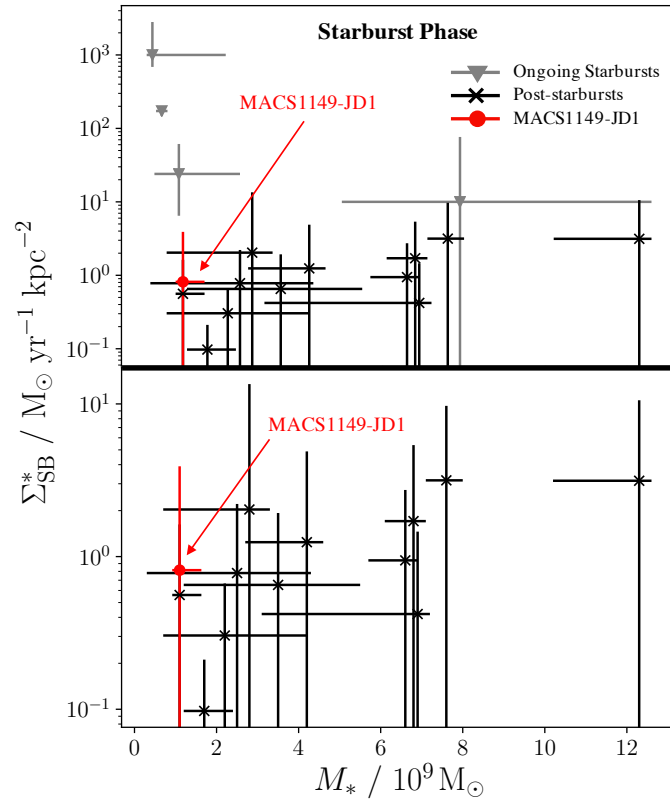
Fig. 6.3: Plots for the correlation between star-formation rate surface density and galaxy stellar mass. These generally support a moderate positive correlation (with a weighted Pearson coefficient of 0.71 for post-starburst systems). **Upper Panel:** Σ_{SB}^* for the four galaxies observed during their starburst phase (see Table 6.2), which are plotted in grey, together with the post-starbursts systems as shown in black (see Table 6.1). **Lower Panel:** As above, but without the 4 ongoing starbursts so as to more clearly show the distribution of the post-starburst systems.
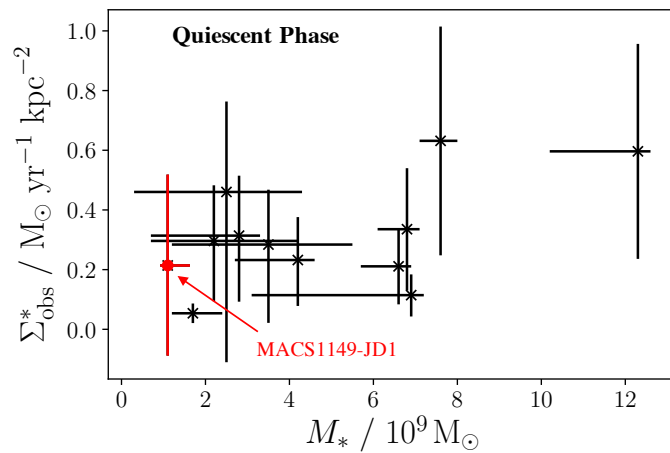
Fig. 6.4: Plots to study the correlation between observed star-formation rate surface densities for the post-starburst galaxy sample, and stellar mass. This shows a moderate positive correlation between these quantities (with a weighted Pearson coefficient of 0.55).

Reinstatement of Star-formation

The sample of post-starburst galaxies considered in this work have been observed at a point in their evolution where there is still some ongoing star-formation activity, albeit much lower than that inferred for their former burst phase. It is unclear whether this is residual star-formation, or re-instated star-formation – but evidence for either case would indicate a smoother star-formation history than the binary burst-mode evolution initially adopted in this research.

The reinstatement of star-formation after a complete (or almost complete) stoppage would arise when inflows slowly begin to return the cold gas fuel supply to the host galaxy. In such a scenario, higher rates of star-formation for systems observed at a greater time after the onset of quenching would be expected, allowing more time for the recovery of inflows. Indeed, a first view of the data would appear to support this, as seen in the upper panel of Fig. 6.5 in which the star-formation rate $\mathcal{R}_{\mathrm{SF}}$ at the epoch of observation (i.e. not during the burst) for each of the high-redshift galaxies is plotted against the time elapsed since the estimated end of their starburst episode, t_{qui}, and some positive correlation can be seen (with Pearson coefficient of 0.93). However, degeneracies with other effects may be responsible for this trend: the middle panel shows the star-formation rate surface density, $\Sigma^*_{\mathrm{obs}} = \mathcal{R}_{\mathrm{SF}}/4\pi r^2_{\mathrm{gal}}$ while the specific star-formation rate, $\mathrm{SSFR} = \mathcal{R}_{\mathrm{SF}}/M_*$ is plotted in the lower panel. The observed post-starburst Σ^*_{obs} shows a more complicated behaviour: up to around $t_{\mathrm{qui}} \approx 350 \ \mathrm{M}_\odot \ \mathrm{yr}^{-1} \ \mathrm{kpc}^{-2}$, Σ^*_{obs} increases with t_{qui}. Conversely, for larger t_{qui} values, the star-formation surface density subsides again. This could result from the compactness of some of the galaxies: the behaviour of the SSFR in the lower panel (which does not depend on the physical extent of the system) is different and shows that the longer the time elapsed since the end of star-formation, the lower the observed SSFR. Such behaviour would be more consistent with t_{qui} being a marker for the level of feedback experienced by a system, rather than offering any real insight into the processes behind the re-establishment and/or the retention of star-forming activity.

It is also worth considering the star-formation rate surface density during
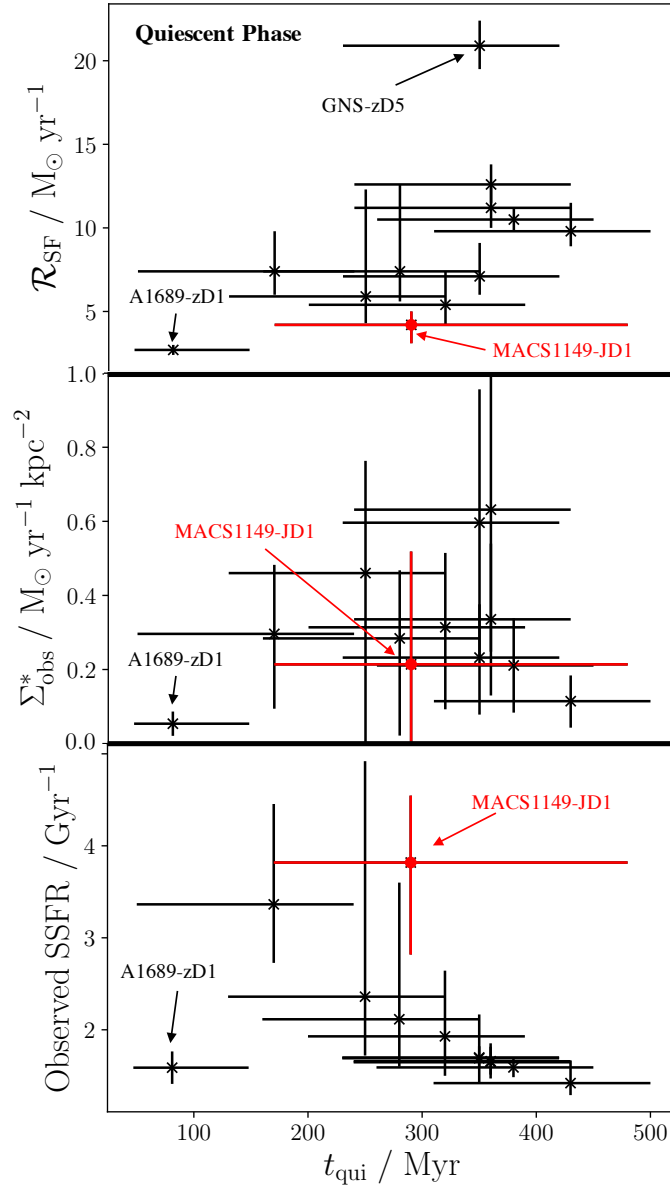
Fig. 6.5: Star-formation rates for the 12 post-starburst galaxies. **Upper Panel**: Quiescent star-formation rate $\mathcal{R}_{SF}$ (at observational epoch) plotted against the length of quiescence period, t_{qui}, which is measured up to the point of observation (i.e. t_{qui} gives an indication of the time elapsed since the end of starburst activity). This demonstrates a strong positive correlation, with a Pearson coefficient (weighted by the error bounds) of 0.93. **Middle Panel**: As above, except the y-axis is star-formation rate surface density ($\Sigma^{*}_{obs} = \mathcal{R}_{SF}/4\pi r^{2}_{gal}$), which all but removes the correlation seen in the upper panel, with a Pearson coefficient of -0.02 (if the outlier is removed – A1689-zD1, as labelled). **Lower Panel**: As above, but with the y-axis as specific star-formation rate, i.e. normalised by galaxy mass where SSFR $= \mathcal{R}_{SF}/M_*$. If again removing the labelled outlier galaxy A1689-zD1, a non-negligible negative correlation of weighted Pearson coefficient -0.64 emerges.

the starburst episode, $\mathcal{R}_{\text{SB}}^*$ – see Fig. 6.6, which might also be a useful tracer for the behaviour of this system. In this case, note that $\mathcal{R}_{\text{SB}}^*$ is derived from M_* rather than measured independently. Thus, the SSFR is not considered here in Fig. 6.6 as it would not be physically meaningful – instead, only $\mathcal{R}_{\text{SB}}^*$ and Σ_{SB}^* are plotted. Intriguingly, these quantities appear to follow a similar behaviour to their counterparts during the quiescent phase in Fig. 6.5: $\mathcal{R}_{\text{SB}}^*$ also correlates with the quiescence timescale, as does the star-formation surface density during the burst – although, in the latter case, the behaviour is once again complicated (cf. middle panel of Fig. 6.5), with a similar trend emerging to its counterpart. It is unclear whether this pattern is physical in origin, due to random fluctuations with the limited data points, or whether it is a mathematical feature resulting from the way $\mathcal{R}_{\text{B}}^*$ and associated quantities were calculated.[9] On the other hand, such behaviour cannot be attributed to these analysis caveats in the earlier plot, Fig. 6.5, in which star-formation rates were determined independently to t_{qui}. This points towards a physical origin.

---

[9]The star-formation rate during the burst is inversely related to t_{SB} which itself is estimated by $[t(z_{\text{obs}}) - t(z_{\text{f}})] - t_{\text{qui}}$ (see equation 6.4). This implies an inverse proportionality between $\mathcal{R}_{\text{SB}}^*$ (as well as quantities derived from this) and t_{SB} when $t_{\text{qui}} > t(z_{\text{obs}}) - t(z_{\text{f}})$, i.e. after around 350 Myr (which is indeed the location of the peaks in Fig. 6.6).
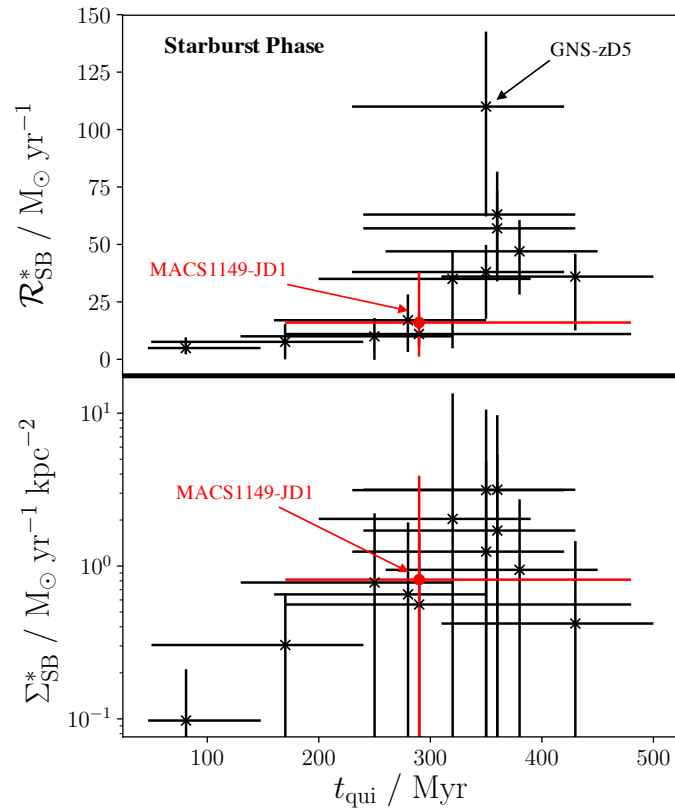
Fig. 6.6: As per Fig. 6.5, but values shown for the starburst period of each system instead. The top panel shows a weighted Pearson correlation value of 0.71, while the lower panel presents more complicated behaviour with a less clear overall trend (correlation of 0.39) – see text for details. As SSFR is estimated during the burst phase using t_{SB} and M_* (rather than being determined independently) it is not physically insightful to include it here.

Chapter 6 summary: *This chapter applies the CR heating and feedback models to 16 observed high-redshift $7 \lesssim z \lesssim 9$ starburst and post-starburst galaxies from the literature and assesses the timescales over which star-formation could be stopped – either by the DC heating internal quenching mechanism or by the IX heating external stunning mechanism as introduced in earlier chapters. Relations between intensive and extensive system parameters are explored and no notable correlation between t_{qui} and galaxy size r_{gal} or dynamical timescale τ_{dyn} was found to emerge. However, in a feedback model, no such dependence on these extensive system quantities would be expected. Instead, a relatively smooth negative correlation is found between t_{qui}, the quiescent timescale between starburst episodes, and intensive system parameters relating to the level of feedback, i.e. the quenching timescale τ_{Q} and the stunning timescale τ_{S}. This indicates that post-starburst quiescence is strongly influenced by feedback from star-formation in these selected galaxies and, moreover, it is consistent with the CR-mediated feedback models explored in this thesis.*

Chapter 7

Conclusions

7.1 Summary

The research presented in this thesis investigates the heating and feedback impacts of energetic particles in and around high-redshift protogalaxies and starbursts. Such systems are expected to be rich in energetic CR protons. This is because their high star-formation rates produce frequent SN events, and these are important source environments for accelerating charged particles up to PeV energies. Moreover, local observations of star-forming galaxies reveal a distinctive γ-ray glow (e.g. that observed from M82) which is a characteristic signature for the abundant presence of interacting, energetic hadrons (see, e.g. Abdo et al. 2010b; Wang and Fields 2014; Yoast-Hull et al. 2016; Heckman and Thompson 2017; Wang and Fields 2018).

As charged CR particles propagate within an interstellar environment, their escape into circumgalactic space is hampered by galactic magnetic fields. It has been argued in the literature that these magnetic fields are amplified rapidly after the onset of star-formation in a galaxy to μG levels by a turbulent dynamo mechanism (Beck et al. 2012; Schober et al. 2013; Latif et al. 2013). Indeed, such growth would be consistent with observations that suggest galactic magnetic fields develop quickly alongside violent star-forming activity, and that they saturate early in the evolutionary timescale of the host system (Bernet et al. 2008; Beck et al. 2012; Hammond et al. 2012; Rieder and Teyssier 2016; Sur et al. 2017). These fields are non-uniform, and their complicated turbulent structure leads to substantial, continuous deflection and scattering

of propagating charged CRs within them, which can be well described as diffusion. The slower diffusion speed of CRs compared to their free-streaming propagation (which would occur at nearly the speed of light) means that they become entangled within their source environment, leading to their effective containment as the environment becomes magnetised.

Above a GeV, energetic CR protons can undergo pion-producing interactions though channels which are not open to their lower energy counterparts. The resulting injection of charged and neutral pions leads to both γ-ray emission close to the interaction site (due to the decay of a neutral pion $\pi^0 \to 2\gamma$), and the injection of leptons ($\pi^+ \to \mu^+ + \nu_\mu$ or $\pi^- \to \mu^- + \bar{\nu}_\mu$). These leptons are predominantly muons, which decay quickly into electrons and positrons (via the processes $\mu^+ \to e^+ + \nu_e + \bar{\nu}_\mu$ and $\mu^- \to e^- + \bar{\nu}_e + \nu_\mu$), and these end-products can interact with the ambient interstellar medium to thermalise via Coulomb interactions over a length-scale of around 0.2 kpc. They may also cool radiatively to emit non-thermal X-rays (predominantly via inverse Compton scattering with CMB photons). The effects of such electron cooling and energy deposition are two-fold:

(i) Their thermalisation via Coulomb interactions eventually yields an internal heating effect of greater power than conventional photonic heating processes. This is aided by the containment of CRs by the magnetic field, which focusses their heating internally and makes CR Coulomb heating particularly effective. By contrast, the lack of dust in protogalaxies makes photonic heating processes – e.g. dust scattering/reprocessing – particularly ineffective.

(ii) Their radiative cooling contributes to a powerful non-thermal X-ray glow, which can cause an indirect heating effect of the internal galaxy environment as well as the circumgalactic region beyond.

The direct Coulomb thermalisation channel can operate at any point within the interstellar medium of a strongly star-forming galaxy and, once the internal magnetic field has strengthened, it can attain a power of around 10^{-25} erg cm^{-3} s^{-1} in a system in which SN events occur at an average rate of

$\mathcal{R}_{SN} = 0.1$ yr^{-1}. This work has shown that such heating levels would be able to increase the average temperature of interstellar gases to above their virial temperature (and hence decisively quench star-formation) within just a few tens to hundreds of Myr in realistic models – but its impacts would largely only be felt within the internal medium of a galaxy.

The indirect non-thermal X-ray emission channel can operate both inside and outside the host galaxy, but it relies on high energy densities of ambient radiation fields. For instance, its influence would be particularly important in and around high-redshift environments when the energy density of the CMB was substantially higher than it is in the present Universe. This heating process could attain a similar internal power to the direct Coulomb channel by redshift $z = 12$ – although its effects are actually more likely to be important in the circumgalactic environment of the host galaxy, where the implications are more substantial. This is because, at high-redshift, there is an increasing bank of circumstantial evidence (e.g. Mandelker et al. 2018) to suggest that bursts of star-formation are predominantly driven by the action of cold, inflowing filaments of chemically pristine primordial gas. It has been shown in this work that the X-ray heating of these filaments can lead to their destruction, ultimately stunning galaxies by cutting off the flow of cold gas which they supply. If caused by the non-thermal X-ray emission, the work presented in this thesis has demonstrated that such a feedback mechanism could terminate star-formation in the host within just a few hundred Myr. Both this and internal Coulomb thermalisation driven feedback presumably operate together in any given star-forming galaxy at high-redshift. This work has shown that, for more intensely star-forming galaxies, estimated timescales preferentially support the action of CR heating and feedback through stunning. However, in less active systems, internalised Coulomb driven heating seems more important, with quenching of star-formation arising before it could be stunned. Stunning must still operate over longer timescales in these less active systems in order to account for the post-starburst quiescent phase – this occurs because of the time taken for circumgalactic gases to sufficiently cool so as to enable the reinstatement of cold inflows.

At low-redshift, there is less evidence to support the ongoing action of cold inflows in driving star-formation. Moreover, the important non-thermal X-ray heating process could not operate in the later Universe due to the lower energy density of the CMB. Indeed, after around $z \approx 4$ the inverse Compton effect due to the up-scattering of CMB photons may not even be able to compete with that due to the up-scattering of stellar photons, and certainly would not be able to bring about an important feedback impact compared to other mechanisms. This promotes the idea that high-redshift galaxies are actually very different environments to their low-redshift descendants and, on galactic scales, gives some insight into how feedback in these systems may have evolved.

7.2 Astrophysical Implications

A frequent implication of sustained, concentrated starburst activity in a galaxy is the emergence of a galactic-scale outflow. These are ubiquitous among starburst galaxies in the nearby Universe (e.g. Arp 220, M82, and NGC 253). Further afield, in the more distant Universe, outflows are also found to be an important feature arising in star-forming galaxies and protogalaxies (Frye et al. 2002; Ajiki et al. 2002; Benítez et al. 2002; Rupke et al. 2005a,b; Bordoloi et al. 2011; Arribas, S. et al. 2014). In this thesis, the model introduced by Samui et al. (2010) was adopted to study the impact that outflows may have on redistributing CRs in and around high-redshift protogalaxies, and what impact their advection may have on the resulting heating and feedback effects.

In the presence of these large-scale bulk movements of the media in which CRs are entrapped, both the energetic particles and ambient magnetic fields can be advected by the flow. In outflows, CR energy density can be redistributed, depositing substantial numbers of CRs (amounting to as much as 10% of the total CR power originally supplied by SN events) into the circumgalactic environment, where they may contribute to thermalisation and could support the feedback effects leading to stunning by e.g. aiding the heating of filamentary inflows. Some of the advected energetic particles would be able to escape into intergalactic space and, if contributed by sufficient numbers

of early star-forming galaxies, they may have the ability to inject substantial CR energy density into the primordial IGM at high-redshift. This could influence pre-heating and ionisation processes in the wider Universe (Nath and Biermann 1993; Sazonov and Sunyaev 2015; Leite et al. 2017), and alter its thermal and ionisation history. This opens up new questions about the role CRs could have played in amplifying intra-cluster and/or intergalactic magnetic fields (e.g. Miniati and Bell 2011; Beck et al. 2013; Lacki 2015), and the ability for such processes to be maintained. In fact, the influence of the advected CRs may be even more important than this. Typically clusters, proto-clusters, and groups/pairs of protogalaxies are supported by outward pressure gradients (see, e.g. Suto et al. 2013; Biffi et al. 2016) against their gravitational potentials. If as much as 10% of CRs are indeed able to escape from highly star-forming galaxies in the presence of outflows, the balance of hydrostatic equilibrium may be changed in the host galaxy's surroundings due to the additional pressure gradients these CRs would introduce. In larger-scale groups and assemblies of galaxies and clusters containing one or more actively star-forming systems, a non-negligible addition to the CR pressure (if maintained for a sufficient length of time) could start to distort nearby large-scale structures if CR pressure started to become significant (see, e.g. Ginzburg and Syrovatskii 1963; Lacki 2015; Butsky and Quinn 2018).

In terms of internal implications, the work presented in this thesis also found that, if outflows operate, the contained Coulomb thermalisation heating effect of the secondary electrons within the internal environment of the host galaxy could still be maintained at a similar power to a situation without outflows, of around 10^{-26} erg cm^{-3} s^{-1} (when adopting a SN event rate of $\mathcal{R}_{\mathrm{SN}} = 0.1$ yr^{-1}). However, typically outflows are bi-conical in structure (Veilleux et al. 2005). This means that their characteristic fast-flowing hot gas would be present only within the upper outflow cone regions, while the remainder of the interstellar environment of the galaxy would actually be left relatively unaffected by the outflow itself.

In general, the internal interstellar heating effect of CRs can have implications for the subsequent star-formation in a galaxy, beyond simply quenching

it. CRs (in particular via the direct Coulomb mechanism) particularly target denser regions of the ISM, and these are typically the regions most likely to be forming new generations of stars. The energy deposited by CRs within dense star-forming clouds and cores could severely affect their ability to fragment and collapse. This is because the enhanced heating and pressure support would effectively raise the Jeans' masses of such cores. Even if this action is insufficient to immediately quench star-formation, it could still substantially increase the initial mass function of stars which form subsequently to a more top-heavy form (see discussions in Kuwabara and Ko 2006; Ko and Lo 2009; Hanawa and Tomisaka 2015; Hanawa and Tomisakar 2015; Kuwabara and Ko 2015). Further to this, CRs may heat proto-stellar clumps throughout the host galaxy more effectively than radiation is able to, due to higher levels of energy deposition at the point of interaction, and the possibility that they may even be guided into star-forming regions by 'hourglass' shaped magnetic field structures threaded through them (see e.g. Jokipii 1966; Ferland 2009). When compared to soft (thermal) X-rays and ultraviolet (e.g. stellar) radiation, CRs are less prone to shielding by any neutral material present in dense star-forming clouds and cores. This makes them a particularly effective means by which feedback impacts from star-formation may be delivered and targeted onto these environments.

The action of CRs may offer an explanation for the quenching of so-called 'red nuggets' in the more local Universe, at redshifts of $z \sim 1 - 3$ (although recently these have also been observed at $z \approx 0$ – see Walsh et al. 2017). These galaxies arise as part of the formation/evolutionary scenario of giant ellipticals in which a fast starburst phase forms a concentrated core of radius 1-2 kpc and stellar mass around 10^{11} M$_\odot$ (see, e.g. Trujillo et al. 2014; Walsh et al. 2017; Ferré-Mateu et al. 2017; Werner et al. 2018) over a period of around 1 Gyr (thus indicating a rate of $\mathcal{R}_{\mathrm{SF}} \sim 100$ M$_\odot$ yr^{-1} during the burst). This star-forming episode ends, and is followed by a slow accretion phase which persists as the galaxy undergoes mergers with lower mass galaxies to build up the disc without affecting the previously formed central core (Oser et al. 2010; Rodriguez-Gomez et al. 2016). The second disc-building stage is stochastic in

nature. As such, a fraction of these systems should exist which would not have undergone any mergers, thus leaving the quenched, massive concentrated core untouched and without a disc, to be observed in the later Universe as 'red nuggets' (Quilis and Trujillo 2013). The quenching process from the starburst core region progenitors (sometimes referred to as 'blue nuggets' during their star-forming episode – see Barro et al. 2013; Williams et al. 2014; Barro et al. 2014)[1] has been argued to be driven by two types of mechanisms: *bulge quenching* caused by feedback from the concentrated star-formation episode itself (see, e.g. Murray et al. 2005), and *halo quenching* caused by halo-related feedback processes which may operate more slowly and progressively – this would include processes like infall heating (Khochfar and Ostriker 2008), or virial shock heating (Birnboim and Dekel 2003; Kereš et al. 2009). The work in this thesis has also introduced two other potential mechanisms that could operate in and around the extreme, concentrated starburst conditions that would arise in red nugget progenitors, and could contribute to (or even dominate) the quenching process. The internal DC heating mechanism (referred to as 'quenching' in this thesis) could act as an effective bulge quenching mechanism, while the IX 'stunning' mechanism could operate as a progressive halo quenching process.

The research presented in this thesis also has implications for simulation work. Current implementations of cosmological hydrodynamical galaxy formation and evolution simulations (e.g. IllustrisTNG and EAGLE – see Schaye et al. 2015; Pillepich et al. 2018 for information) invoke feedback from star particles on a sub-grid level as a simple parameterised stochastic process (Crain et al. 2015; Pillepich et al. 2018) with adjustments and calibrations made against observations to ensure realistic results are produced on large-scales. These simulations have been used in recent years to study the evolution and feedback impacts of star-forming galaxies both in the low-redshift evolved Universe (e.g. Wilkinson et al. 2018; Starkenburg et al. 2019), as well as in more

---

[1]Simulation work has also been done, which follows the evolution of stream-fed blue nuggets at $z = 2 - 4$ to compact quiescent red nuggets by $z \sim 2$ – Zolotov et al. (2015). Moreover, the masses, kinematics and abundances of blue nuggets are consistent with those of red nuggets (Barro et al. 2014; Bruce et al. 2014; Nelson et al. 2014; Williams et al. 2014), supporting the evolutionary link between the two populations where blue nuggets are progenitors of red nuggets.

primordial conditions (e.g. Sharma et al. 2017). On the sub-grid level, the findings of the research in this thesis would suggest that a progressive heating/feedback implementation may actually be more appropriate and physically representative of the feedback physics on sub-galactic scales. The analyses of section 6.4 indicated that CR feedback may be an important regulator of star-formation in some star-forming galaxies, perhaps of similar or comparable importance to discrete mechanical feedback events like SNe. Moreover, it might also be argued that the relatively smooth correlations seen in Fig. 6.2 between t_{qui} and τ_{Q}, and between t_{qui} and τ_{S} could be more consistent with a progressive feedback effect operating (as would be the case with CR-mediated feedback), which is in contrast to the stochastic, discrete feedback currently assumed at the sub-grid level in large-scale simulations, which would not be guaranteed to yield such a correlation. This motivates the need to consider progressive feedback mechanisms on sub-grid scales (including CR-induced mechanisms) in simulation frameworks.

7.3 Future Work

The work in this thesis has identified energetic particles as an important agent by which star-formation in protogalaxies can be regulated, and this opens up new research directions. First and foremost is the detailed action of CR feedback processes. To be properly assessed and modelled in detail, it is essential to develop models by which the detailed propagation and interactions of CRs in multi-phase interstellar environments can be properly studied (i.e. the relevant sub-grid physics). It was mentioned before that the sustained, enhanced CR heating experienced by a galaxy could lead to an increased Jeans' mass in stellar nurseries. This, in turn, would result in either a quenching of star-formation activity, or an increasingly top-heavy distorted initial mass function of subsequently forming stars. However, the magnetic fields of star-forming regions could heavily influence the local level of CR heating that would actually be experienced. Observations of magnetic fields in and around star-forming cores in the Milky Way, via Zeeman effect measurements (see e.g. Bergin and Tafalla 2007; Koch, P.M. et al. 2015; Ching et al. 2017) and dust emission

polarimetry (e.g. see Planck Collaboration 2016) have revealed complex magnetic features threaded through stellar nurseries. The alignment and spatial structure of such magnetic fields is very diverse. Their orientation and structure over different length-scales is shown to vary within the same system (see Rao et al. 2009; Alves et al. 2011; Chen et al. 2012; Wang et al. 2015; Hull et al. 2017) and presumably a similar variety (if not more) would also be present in the star-forming regions of galaxies in the early Universe. Star-forming clouds and cores exhibit relatively strong magnetic field strengths – enhanced by the dragging of magnetic field lines by the collapsing gases from which they originally formed. In the densest parts of some molecular clouds, where stars are spawned, the local magnetic field can reach strengths as high as $\sim 1\,\mathrm{mG}$ (Crutcher et al. 2010), and this would be strong enough to substantially modify the propagation and diffusion patterns of energetic CRs compared to the average ISM representation adopted in this thesis. This could lead to shielding of star-forming regions if magnetic fields were appropriately aligned, protecting them somewhat from the excesses of CR heating and allowing star-formation to persist in pockets despite substantial feedback being felt globally across a galaxy. By contrast, if magnetic field vectors are arranged in a way so as to preferentially direct diffusing CRs into denser star-forming regions, quenching of internal star-formation may instead be more readily achieved due to the extremely targeted nature of CR feedback in this case. Although complicated and challenging from a modelling perspective, it is essential that these details are properly explored as they could substantially change the overall response of a galaxy to CR feedback. Moreover, other environmental factors and their role in this process should be considered – for example, the X-ray irradiation (which would be associated with the high non-thermal X-ray luminosities of high-redshift starbursts) and partial ionisation enhancement of a magnetised star-forming region could change the way in which permeating magnetic fields evolve (e.g. by modifying the rate at ambipolar diffusion occurs – see e.g. Draine 2011). In turn, this could affect the ability for CR feedback to be delivered in such a scenario.

This work has also demonstrated that CRs would be present in the circum-

galactic environment of high-redshift star-forming protogalaxies – especially in cases where a galactic outflow operates. The CGM, and the media of outflows in local starburst galaxies, are known to be multi-phase. They are comprised of hot, low density gases in which cool dense clumps are entrained. These clumps may have been deposited into the CGM by the action of a galactic outflow: indeed, observations of nearby starburst galaxies (e.g. M82) indicate that filaments and clump-like structures are present and are being pushed along by the outflow wind, with clump velocities approaching 600 km s^{-1} (see Strickland and Heckman 2009). This multi-phase structure is likely responsible for the charge-exchange lines observed in emission from the outflow cones of M82 (Liu et al. 2011, 2012; Wang and Liu 2012; Wu et al. 2019). These clumps and clouds may fall back towards the host galaxy as structures similar to the high-velocity clouds seen in the Milky Way (see Putman et al. 2012). They may become entrained into a persisting galactic outflow, and may even enable the recycling of galactic material, or could contribute to the fuelling of star-formation cycles. However, since CR heating is focussed on denser regions, these clumps would be particularly targeted by CR feedback effects. This may act to evaporate and destroy them, either within a galactic outflow, or within the circumgalactic environment. This could suppress the recycling of material in and around the host system, and begin to suppress the flow of metals in and around star-forming galaxies. Such a process would influence the ability for interstellar gases to cool and collapse, perhaps distorting the mass distribution of stars which would subsequently form. If these entrained CGM clumps and clouds are a useful sink of CR energy, their presence may even be key to understanding the phenomenology of the convective flows in and around galaxies. These flows may be suppressed if CR feedback can indeed operate to heat/evaporate clumps, with implications for the subsequent evolution of the host galaxy (e.g. its ability to re-establish star-formation).

Such matters may be investigated in follow-up studies by use of Monte-Carlo based semi-analytical modelling (SAM) as outlined in Somerville and Primack 1999 (see also Kauffmann et al. 1993; Cole et al. 1994), which can be used to unlock the main features of the large-scale physics more quickly than

full computationally-expensive hydrodynamical simulations. In this approach, SAMs are built into an appropriate cosmological framework including an initial matter power spectrum and structure growth model, and they allow the inclusion of a physically-motivated yet simple treatment of processes such as gas cooling, star-formation, feedback and galaxy interactions/merging. The work presented in this thesis has shown that CR induced feedback can be readily parameterised, which means that it would lend itself to be conveniently studied with SAMs. Simplified models based on SN event rate (or star-formation rate), mean ISM density, a quantification of a multi-phase structure (via, e.g. a clumping factor – see Leroy et al. 2013), stellar and gas/dust distribution and magnetic field configuration within a galaxy ISM would be sufficient to inform a SAM to study the CR feedback physics in galaxies quickly, with many realisations.

CR heating is governed by the rate at which pp hadronic interactions can occur and, subsequently, by the relative fraction of charged pions compared to neutral pions that they injected. The charged pions ultimately decay to the electrons required to mediate the heating process, however neutral pions instead decay to form γ-rays. These freely stream away with minimal further interaction or attenuation (except by GZK effects with the CMB over cosmological distances – see Greisen 1966; Zatsepin and Kuz'min 1966 for details), so can be useful as a tracer for interacting CR protons.[2] This γ-ray production may be related to the extragalactic γ-ray background (EGRB) which, as yet, is not fully understood. γ-ray emission from star-forming galaxies is a feasible contributor, and can be modelled in a similar way to the electron injection rate considered in this work. Thus, the γ-ray emission from starburst galaxies and protogalaxies can be calculated without substantial changes to the approach adopted in this thesis, and could even be extended to populations of galaxies to model the evolution of their γ-ray emission over redshift. Indeed, development of SAMs may provide an accessible means of doing this in future, once the CR interaction and γ-ray propagation physics is properly established

---

[2]Such emission has already been detected from nearby starbursts, including NGC 253, M82, Arp 220 and M31 (VERITAS Collaboration et al. 2009; Abdo et al. 2010a; Rephaeli and Persic 2014; Yoast-Hull et al. 2017).

and parameterised. Research looking into this matter is an essential step towards modelling and understanding the EGRB, and may even unlock details about its evolution over cosmic time. Indeed, studies of the EGRB have been identified as a key science goal of up-coming missions and observatories. Chief among these is the Cherenkov Telescope Array, which is due to begin its operations in 2022. This research direction is therefore timely, and would naturally pertain to ongoing observational efforts.

Appendix A

Cosmic Ray Acceleration

The favoured mechanism for accelerating CRs is first order Fermi acceleration (Fermi 1949; Bell 1978), in which energetic particles gain energy through elastic scattering in magnetised shocks and irregularities. This is found to yield an energy spectrum of particles consistent with the power law index of the observed Galactic UHECR spectrum (Bell 1978). This appendix summarises how the power-law spectrum results from such a mechanism (see also, e.g. Dermer and Menon 2009; Schlickeiser 2002; Longair 2011).

Consider a strong magnetic shock in which the compression factor across the front (i.e. the ratio of densities of the pre-shocked upstream medium to post-shock downstream medium) is given by

$$R_{\mathrm{C}} = \frac{\gamma_{\mathrm{g}} + 1}{\gamma_{\mathrm{g}} - 1} \, , \tag{A.1}$$

where $\gamma_{\mathrm{g}} = 5/3$ is the adiabatic index for an assumed monatomic ideal gas, such that $R_{\mathrm{C}} \approx 4$. The Euler equations give the ratio of velocities as $\rho_1 v_1 = \rho_2 v_2$ on either side of the shock front so, for the case of a head-on collision, the resultant velocity of a particle viewed from either the frame of the shock (denoted by primed quantities) or the frame of the particle encountering the shock (denoted as the unprimed frame) is given by

$$v = v_1 - v_2 = v_1 \left(1 - \frac{1}{R_{\mathrm{C}}} \right) \, . \tag{A.2}$$

The fractional energy gain of a particle as it interacts (i.e. crosses) the

shock may be written as

$$\eta_{\mathrm{E}} = \frac{E_2 - E_1}{E_1} = \frac{E_2}{E_1} - 1 \;, \tag{A.3}$$

which can be transformed into the shock frame by the Lorentz transformations

$$E_1' = \gamma_{\mathrm{L}} E_1 (1 - \beta \cos \theta_1) \tag{A.4}$$
$$E_2 = \gamma_{\mathrm{L}} E_2' (1 + \beta \cos \theta_2') \;,$$

where the Lorentz factor, γ_{L}, is defined as

$$\gamma_{\mathrm{L}} = \frac{1}{\sqrt{1 - \beta^2}} \tag{A.5}$$

for $\beta = v/c$, and θ_1 and θ_2 are introduced as the angles between the normal to the shock front and the angle at which a particle enters the shock and exits the shock respectively (in the indicated frame). The energy gain of the particle, as per equation A.3 can be written in terms of the energy gain in the frame of the magnetic shock by the transformations A.4, i.e.

$$\eta_{\mathrm{E}} = \frac{E_2}{E_1} - 1 = \left(\frac{E_2'}{E_1'} \right) \gamma_{\mathrm{L}}^2 \, (1 - \beta \cos \theta_1)(1 + \beta \cos \theta_2') - 1 \;, \tag{A.6}$$

however the magnetic field itself does not do work, so $E_1' = E_2'$. This leaves the fractional energy gain per interaction as

$$\eta_{\mathrm{E}} = \frac{1 - \beta \cos \theta_1 + \beta \cos \theta_2' - \beta^2 \cos \theta_1 \cos \theta_2'}{1 - \beta^2} - 1 \;. \tag{A.7}$$

The average energy gain $\langle \eta_{\mathrm{E}} \rangle$ for particles as they cross the magnetic shock can be found by averaging over each of the terms in equation A.7. In the shock frame, there should be no preferred direction for the ejection of particles after they scatter - i.e. the shock 'sees' outgoing particles leaving the front isotropically. The average $\langle \cos \theta_2' \rangle$ must therefore be zero.

In the frame of the particle, the probability that it approaches the shock between an angle θ_1 and $\theta_1 + \mathrm{d}\theta_1$ is $\sin \theta_1 \mathrm{d}\theta_1$. The rate at which interactions arise is proportional to the component of the particle velocity normal to the

shock, i.e $v_x \approx -c\cos\theta_1$, where the negative sign is introduced to indicate that the particle 'sees' the shock moving towards it. The probability distribution of particles approaching a shock with an angle θ_1 is then given by the product of the rate at which the particles approach and the probability of arrival from a given direction θ, i.e.

$$P(\theta_1) \propto -c\cos\theta_1 \sin\theta_1 \mathrm{d}\theta_1 \tag{A.8}$$

and so the average of the cosine of the angles of approach is given by

$$\langle\cos\theta_1\rangle = \frac{1}{N_{\theta_1}} \int_{-\frac{\pi}{2}}^{\frac{\pi}{2}} \cos\theta_1 \; P(\theta_1) \; \mathrm{d}\theta_1 = -\frac{2}{N_{\theta_1}} \int_0^{\frac{\pi}{2}} \cos^2\theta_1 \; \sin\theta_1 \; \mathrm{d}\theta_1 \;, \tag{A.9}$$

where the normalisation N_{θ_1} is defined as

$$N_{\theta_1} = \int_{-\frac{\pi}{2}}^{\frac{\pi}{2}} |P(\theta_1)| \; \mathrm{d}\theta_1 = 2\int_0^{\frac{\pi}{2}} \sin\theta_1 \; \cos\theta_1 \; \mathrm{d}\theta_1 \;, \tag{A.10}$$

and the integration range is set by the range of angles possible for particle approach, i.e. between $-\pi/2$ and $\pi/2$. Making the substitution $\mu = \cos\theta_1$,

$$\langle\cos\theta_1\rangle = -\frac{1}{N_{\theta_1}} \int_0^1 \mu^2 \; \mathrm{d}\mu = -\frac{1}{3N_{\theta_1}} \;, \tag{A.11}$$

and

$$N_{\theta_1} = \int_0^1 \mu \; \mathrm{d}\mu = \frac{1}{2} \;, \tag{A.12}$$

so $\langle\cos\theta_1\rangle = -2/3$. A similar argument can be made for the particles leaving the shock after crossing, with the only difference being that the sign of the velocity is reversed (this follows from the shock moving away from the particle after a crossing event). The result in this case is therefore $\langle\cos\theta_2\rangle = +2/3$.

Putting these angle-averaged values back into the equation A.6 for η_E yields the fractional energy gain per interaction as

$$\langle\eta_E\rangle \simeq \frac{4}{3}\beta > 0 \;. \tag{A.13}$$

This is positive, which guarantees that, on average, particles in an ensem-

ble receive an energy boost every time they interact with a magnetic shock. However, during each crossing, the particle is confined by scattering off self-generated Alfvén waves, redirecting it back towards the shock front after having crossed it and received an energy boost. This means that a particle can cross the shock back and forth a large number of times, which offers a stochastic means by which the particles can be accelerated to very high energies - up to a point where they cannot reasonably be contained and reaccelerated any further. It follows that, for a particle of initial energy E_{init}, after n crossings, its energy will be

$$E = E_{\mathrm{init}} \langle \eta_{\mathrm{E}} \rangle^n \ . \tag{A.14}$$

There is some non-zero probability that an interacting charged energetic particle may escape from a system after a scattering event, meaning that not all of an original ensemble of X_0 particles is continually re-accelerated by ongoing scatterings. If P_{esc} is the chance of a particle escaping the system in a single scattering event, then $P_{\mathrm{cont}} = 1 - P_{\mathrm{esc}}$ is the (complimentary) containment probability, i.e. the chance that the particle remains contained by the system after a single scattering event to be scattered again. After n scatterings, the number of particles remaining to be re-scattered follows as

$$X = X_0 P_{\mathrm{cont}}^n \ . \tag{A.15}$$

Equations A.14 and A.15 can be combined and rearranged to give the particle energy spectrum

$$\frac{X}{X_0} = \left(\frac{E}{E_{\mathrm{init}}} \right)^{\frac{\log(P_{\mathrm{cont}})}{\log\langle \eta_{\mathrm{E}} \rangle}} = \left(\frac{E}{E_{\mathrm{init}}} \right)^{-\Gamma} \ , \tag{A.16}$$

which yields the distinctive power-law expected in the case of stochastic acceleration (e.g. Bell 1978). The value of this index can be calculated theoretically as $\Gamma = \log(P_{\mathrm{cont}})/\log\langle \eta_{\mathrm{E}} \rangle$, for which the containment probability P_{cont} and average energy boost per particle per crossing $\langle \eta_{\mathrm{E}} \rangle$ must be well understood. The true values of the energy boost and containment probability are, however, very uncertain and also widely variable between individual sources in

a galactic-wide CR accelerating source population. This is because they are strongly influenced by the geometry and local conditions of the accelerator. While values for these parameters could theoretically be determined for a single well-defined source, finding a suitable representation for a broad range of source types and geometries is not reasonable, even if the same acceleration process operates within. Instead, a representative value for the index can be estimated empirically. γ-ray observations of the galactic ridge of the Milky Way (thought to be rich in high-energy environments suitable for accelerating CRs) indicate a value of $\Gamma = 2.0 - 2.4$. Assuming conditions in protogalaxies are similar in terms of accelerating CRs to those of the galactic ridge, a value of $\Gamma = 2.1$ is adopted for the models and calculations presented in this thesis – see, e.g. Ackermann et al. (2013); Kotera and Olinto (2011), and also chapter 2.

Second order Fermi acceleration is a less efficient process, but is continuous. It may arise in magnetic clouds of the ISM of a host galaxy, in which particles scatter off turbulence and irregularities. If a cloud is moving with a non-relativistic speed β, the resulting particle acceleration can be determined by the repeated scattering with gain

$$\Delta E \propto \beta^2 \ . \tag{A.17}$$

While this will also lead to a power-law distribution in the resulting CR spectrum, the index would be flatter than that expected from first order Fermi acceleration. Comparison of the β^2 to the β^1 in the first order case (see equation A.13) for each energy gain per scattering accounts for the slower acceleration in second order acceleration as compared to first order (see, e.g. Rieger et al. 2007).

Appendix B

Cosmological Context

Cosmology forms a core aspect of modern astrophysics and is relevant to much of the background physics of this thesis. As such, this appendix provides a brief discussion and introduction of some key ideas to support the main text. It is informed primarily by the lecture notes Peiris (2012a,b), and by the comprehensive book on the subject, Peacock (1999).

B.1 The Cosmological Principle

The most fundamental principle of modern cosmology is that an observer is not special: there are no 'special' locations in the Universe, and the Universe is not arranged in any particular manner to accommodate the existence of an observer. This idea can be encompassed by what has come to be known as the cosmological principle, which states that the Universe is *homogeneous* (on large scales, $\gtrsim 100$ Mpc) and *isotropic*. Essentially, it looks roughly the same in every direction, from every point. This doesn't hold as well for smaller scale systems within the Universe, which are gravitationally bound and effectively de-coupled from the cosmic flow: locally, these have come to form structures that are highly inhomogeneous due to the collapse of matter, structure formation, feedback and other more local astrophysical processes. However, the cosmological argument is that, even though such structure and inhomogeneity exists on small scales, the overall distribution of these small scale systems (like galaxies and galaxy clusters) is still homogeneous and isotropic throughout the Universe.

B.2 A Brief History of the Universe

The evolution of the Universe, from the Big Bang to the present day, arose over the course of around 14 billion years. Shortly after the Big Bang, it expanded very rapidly in a period known as inflation. This lasted for the first few 10^{-30} seconds, after which expansion proceeded much more slowly and consistently (until late times). The very early Universe, after inflation, was comprised of a very hot and dense primordial 'soup'. The high energy densities allowed for easy interactions between particles, and scattering between particles and radiation. This energetic environment cooled as the Universe expanded adiabatically, allowing baryonic matter and nucleons to form in Big Bang Nucleosynthesis (BBN). It eventually reached temperatures of around 3000 K, at which point neutral matter was able to form for the first time. This process, known as recombination, enabled photons to freely stream to produce a last-scattering radiation field – this has now been redshifted into the microwave part of the spectrum and can be observed as cosmological microwave background radiation (CMB). After recombination, the expansion of the Universe endured, with the energy density (temperature) of its constituents continuing to fall. After last-scattering, radiation and matter effectively became decoupled. This meant that any instabilities formerly present in the primordial plasma were now free to collapse under gravity, thus seeding all of the large-scale structure that can be observed in the Universe today.

The formation and collapse of structure enabled the emergence of irradiating sources – e.g. early stars/galaxies, and quasars. These caused the Universe to began to heat up again after a period of sustained cooling (even though its expansion persisted). This re-heating culminated in a period known as the Epoch of Reionisation (EoR) wherein the feedback from the newly formed ionising radiative sources throughout the Universe returned the intergalactic gases to an ionised state. The Universe continued to evolve and expand at a roughly uniform rate, with its energy density dominated by radiation (and later by matter). However at late times, in the last few billion years, its expansion rate appears to have accelerated. This is attributed to a new emerging

dominant component governing its evolution, dark energy, which is attributed to driving such accelerated expansion.

Late-time expansion due to dark energy is built into the currently popular and widely accepted cosmological model – ΛCDM. Here, Λ refers to a cosmological constant term, necessary to represent dark energy. CDM refers to cold dark matter, which is invoked to account for the stability of bound systems such as galaxies (and e.g. their rotation curves) in the context of accelerating cosmic expansion. Under this model, the total energy density of the Universe in the current era can be considered in terms of its constituent parts, with most parameter estimates derived from observations indicating that the Universe is comprised of around 68% dark energy, 27% dark matter and only 5% baryons (with all conventional matter in galaxies, stars, and the Earth falling into the latter component).

B.3 Geometry

The geometry of a space can be described in terms of an interval, ds, being an infinitesimal line element on a manifold (such as a surface in space, or a line in a surface), defined by the metric tensor $g_{\mu\nu}$. For a simple plane under a cartesian coordinate system, the Euclidean metric takes the simple form of

$$ds^2 = dx^2 + dy^2 \; , \tag{B.1}$$

or, in spherical coordinates this may instead expressed as

$$ds^2 = dr^2 + r^2 d\theta^2 \; . \tag{B.2}$$

The mathematics of metric tensors and their representation of various spaces within manifolds is an extensive field of study in its own right. For the purposes of discussion here, only the very basics are required: the key points are that the metric tensor turns observer-dependent coordinates into invariant quantities (such as ds^2), and for the purposes of cosmology, incorporating both space and time components into a metric tensor provides a means of representing the effects of gravity through its association, by General Relativity (GR),

with the curvature of space time. Thus, in GR, the invariant metric must also contain a time interval as well as spatial intervals, and may be expressed in Einstein implicit summation notation as

$$\mathrm{d}s^2 = g_{\alpha\beta}\mathrm{d}x^\alpha\mathrm{d}x^\beta \ , \tag{B.3}$$

where the summation indices $\alpha, \beta \in \{0, 1, 2, 3\}$, and the index $\{0\}$ relates to a time-like interval while $\{1, 2, 3\}$ relate to three space-like intervals. The most simple of spacetimes (flat and stationary) is described by the *Minkowski* metric.

Minkowski Metric

The metric describing a flat, static space-time is that presented in Special Relativity (SR). This is the Minkowski metric, which is uniform across space and time and may be represented by the line element

$$\mathrm{d}s^2 = \mathrm{d}t^2 - \mathrm{d}x^2 - \mathrm{d}y^2 - \mathrm{d}z^2 \ , \tag{B.4}$$

or by the metric tensor $g_{\alpha\beta} = \mathrm{diag}(1, -1, -1, -1)$. The Minkowski metric describes inertial frames falling freely in a gravitational field, but is only locally equivalent such that, in general, there is no frame for which $\mathrm{d}s^2 = 0$. To transform to other coordinates which do not require the free-fall assumption, a more general case is required. Gravitational fields must be accounted for to do this (i.e. to transform from a free-fall frame to a non-free-fall frame), and thus GR requires that this is done by modelling the curvature of space-time in response to the presence of matter and energy.

This can be done by linking the concept of a geodesic with that of space-time, where a geodesic is a straight line *as seen by the space-time*. In essence, a straight line would be the shortest line followed to cover the distance between two points on the manifold. In Euclidean space, this would be a straight line in the usual sense – simply the shortest physical spatial distance between two points on a plane. In spherical space, the geodesic would follow an arc between the two points, which is the shortest distance between them over the surface of a sphere. Similarly, in some other curved space, the geodesic would

curve according to the shape of the manifold upon which it is defined. In GR, this is extended one step further, and the geodesic is defined to be the shortest distance between two points on the manifold accounting for both its spatial curvature and temporal components of the manifold. The metric is the tool that provides this link, demonstrating how the interval (the geodesic) ds^2 corresponds to the manifold described by the metric $g_{\alpha\beta}$. There are three types of intervals. When $ds^2 = 0$, the interval is that followed by massless particles (such as photons), and is described as *null* or a *light-like* interval. When $ds^2 > 0$, the interval is time-like, while when $ds^2 < 0$, the interval is described to be space-like.

Flat Expanding Metric

To describe a simple expanding spacetime, the Minkowski metric can be modified by multiplying all its spatial components with a time-dependent scale-factor $a(t)$, leaving

$$g_{\alpha\beta} = \text{diag}(1, -a^2(t), -a^2(t), -a^2(t)) \ . \tag{B.5}$$

This is a physically useful away from high-density regions of significant curvature - i.e. regions of the Universe where gravitational fields are weak and space-time can be assumed to be approximately flat. Such a metric to describe an expanding space-time is called the *Friedmann-Robertson-Walker* metric, which can be generalised case to account for the cosmological principle and large-scale spatial curvature.

General Friedmann-Robertson-Walker Metric

The General Friedmann-Robertson-Walker (FRW) metric is intended to describe a maximally symmetric space with allowance for large-scale curvature, in line with the cosmological principle (introduced earlier) and the *Copernican principle* (i.e. that the observer is not at the centre of the Universe). The derivation of the metric itself is described comprehensively throughout the literature (e.g. Peacock 1999), but is beyond the scope of the current outline.

The resulting General FRW metric is described by the interval

$$ds^2 = dt^2 - a^2(t) \left[\frac{dr^2}{1 - \kappa r^2} + r^2 d\Omega^2 \right] \ , \tag{B.6}$$

where $d\Omega^2 = d\theta^2 + \sin^2 \theta \, d\phi^2$ is the metric on a 2-sphere, and κ is a curvature parameter for which positive values revert the metric to that of a 3-sphere, negative values revert it to the metric of a hyperboloid space and a zero-value reverts the metric to a flat Minkowski spacetime.

B.3.1 The Einstein and Friedmann Equations

The Einstein equations allow the Friedmann equations describing the dynamics of an evolving FRW Universe to be derived. The Einstein equations form the crux of GR and outline how geometry and energy are inter-related. In implicit summation (Einstein) notation, they are given by

$$G_{\alpha\beta} \equiv R_{\alpha\beta} - \frac{1}{2} g_{\alpha\beta} R_{\rm S} = 8\pi G T_{\alpha\beta} \ , \tag{B.7}$$

where $G_{\alpha\beta}$ is the Einstein tensor, $R_{\alpha\beta}$ is the Ricci tensor (which describes curvature of the metric), $R_{\rm S}$ is the Ricci scalar (a contraction of the Ricci tensor such that $R_{\rm S} \equiv g^{\alpha\beta} R_{\alpha\beta}$) and $T_{\alpha\beta}$ is the energy-momentum tensor, a symmetric tensor to describe the constituents of the Universe. The Ricci tensor is defined as

$$R_{\alpha\beta} = \Gamma^\mu{}_{\alpha\beta,\mu} - \Gamma^\mu{}_{\nu\mu} \Gamma^\nu{}_{\alpha\beta} - \Gamma^\mu{}_{\nu\beta} \Gamma^\nu{}_{\alpha\mu} \ , \tag{B.8}$$

for which comma denotes differentiation with respect to the quantity with index stated after the comma, and Γ^a_{bc} are Christoffel symbols (of the second kind), as defined by

$$\Gamma^a_{bc} = \frac{g^{a\alpha}}{2} \left[\frac{\partial g_{b\alpha}}{\partial x^c} + \frac{\partial g_{c\alpha}}{\partial x^b} - \frac{\partial g_{bc}}{\partial x^\alpha} \right] \ . \tag{B.9}$$

The general energy-momentum tensor for a perfect fluid is

$$T^{\alpha\beta} = (\rho + P)U^\alpha U^\beta - P g^{\alpha\beta} \ , \tag{B.10}$$

where U^α is a 4-velocity and ρ and P is the density and pressure of the perfect fluid, respectively.

For the FRW metric defined in equation B.6, the non-zero components of the Ricci tensor are (using over-dot to represent differentiation with respect to coordinate time t)

$$R_{00} = -3\frac{\ddot{a}}{a}$$
$$R_{11} = \frac{a\ddot{a} + 2\dot{a}^2 + 2\kappa}{1 - \kappa r^2}$$
$$R_{22} = r^2(a\ddot{a} + 2\dot{a}^2 + 2\kappa)$$
$$R_{33} = r^2(a\ddot{a} + 2\dot{a}^2 + 2\kappa)\sin^2\theta \ ,$$

and the Ricci scalar becomes

$$R_{\rm S} = -6\left[\left(\frac{\ddot{a}}{a}\right) + \left(\frac{\dot{a}}{a}\right)^2 + \frac{\kappa}{a^2}\right] \ .$$

Lowering the energy-momentum tensor with the metric and substituting terms into the Einstein equation B.7 yields two results (the three spatial components each yield the same outcome), being the first and second Friedmann equations:

$$\left(\frac{\dot{a}}{a}\right)^2 = \frac{8\pi G}{3}\rho - \frac{\kappa}{a^2} \ , \tag{B.11}$$

$$\frac{\ddot{a}}{a} = -\frac{4\pi G}{3}(\rho + 3P) \ . \tag{B.12}$$

Together, these two equations can describe the dynamics of an FRW Universe with a given curvature and energy density.

B.3.2 Cosmological Distance Measures

From the discussion about the topology of the Universe, it is evident that the concept of a distance measurement in a physical universe is less clear than it is in a flat, Euclidean topology. One obvious consideration is whether the expansion of the Universe should be taken into account when defining a distance - this is particularly important when considering an expanding

manifold from a higher dimensional space: should the distance between two points A_1 and A_2 be defined in terms of their relative distance on the metric, or their physical distance on the manifold? The distinction between these measures is the difference between using *comoving* distances (in which the distance accounts for the expansion of the Universe and so remains the same as the Universe evolves) compared to *physical* distances, which do reflect the increased distance between the two points on a manifold, as observed from some higher dimensional space.

A necessary complication to this picture is the consideration of how time fits into distance measurement definitions. An analogous time-like quantity to comoving distance can be defined as the comoving distance light travels since $t = 0$. Using a system of units in which c, the speed of light is 1, light can travel a distance $\mathrm{d}x = \mathrm{d}t/a$ in a time $\mathrm{d}t$, such that the total distance light travels since $t = 0$ is

$$\eta_\mathrm{t} \equiv \int_0^t \frac{\mathrm{d}t'}{a(t')} \ . \tag{B.13}$$

From this, the *particle horizon* may be specified as the associated distance, being the radius travelled by light since $t = 0$, such that regions separated by larger distances than this are not causally connected, i.e.

$$d_H \equiv a(t) \int_0^t \frac{\mathrm{d}t'}{a(t')} = a(\eta_\mathrm{t})\eta_\mathrm{t} \ . \tag{B.14}$$

Since η_t increases monotonically with *coordinate time*, t, can also be considered to be a time variable, and thus the *conformal time* can be defined as η_t, under which the FRW metric becomes

$$\mathrm{d}s^2 = a^2(\eta_\mathrm{t}) \left[\mathrm{d}\eta_\mathrm{t}^2 - \frac{\mathrm{d}r^2}{1 - \kappa r^2} - r^2 \mathrm{d}\Omega^2 \right] \ . \tag{B.15}$$

With these ideas in mind, some of the conventional means of measuring distances in cosmology can be specified.

Metric Distance

The metric distance, sometimes referred to as the *lookback distance*, is the comoving distance between an observer and a source. The comoving distance to a source at scale factor a, or redshift $z = 1/(a - 1)$, is defined as

$$d_{\mathrm{m}} = d_{\mathrm{lookback}}(a) = \int_{t(a)}^{t_0} \frac{\mathrm{d}t'}{a(t')} = \int_a^1 \frac{\mathrm{d}a'}{a^2(t')H(a')} \; , \qquad (\text{B.16})$$

where H is the Hubble parameter, defined as $H(z) = \dot{a}a$, which depends on the matter content of the Universe, as further discussed in section B.4.

Instantaneous Physical Distance

A further useful distance measure is that between an observer and some object at the same t-ordinate - i.e. the distance to the object on the current spatial surface. This is called the *instantaneous physical distance*, and can be determined by considering the displacement as a radial distance and applying equation B.6. In such a case, the distance is measured by the passage of light, a massless particle such that $\mathrm{d}s = 0$, and a flat Universe is assumed such that $\kappa = 0$. Integrating the result yields

$$d_{\mathrm{IPD}} = a(t)\, R_{\mathrm{d}} \qquad (\text{B.17})$$

for some coordinate distance R_{d}. This is useful to find the distance of objects that are comoving, from which peculiar velocity corrections may be added. At low-redshifts, it is found that $v = \dot{d}_{\mathrm{IPD}} = \dot{a}R_{\mathrm{d}} = d_{\mathrm{IPD}}\dot{a}/a$, which yields Hubble's law $v = H_0\, d_{\mathrm{IPD}}$, where H_0 is the Hubble parameter $\dot{a}a$ as measured in the current epoch.

Luminosity Distance

The use of standard candles in cosmology motivates the use of the *luminosity distance*. This is essentially an extension of the flux/luminosity inverse square law (for Euclidean space), extended to an FRW space-time. In making the transition from the Euclidean case to the FRW case, there are two effects to consider. The first is that the arrival rate of photons is lower by a redshift factor $(1 + z)$ than the rate at which they were emitted. The second is that

the energy of these photons will be lower than when they were emitted, by the same redshift factor. Thus the Euclidean inverse square law is modified to

$$F_{\mathrm{L}} = \frac{L}{4\pi d_{\mathrm{m}}^2 (1+z)^2} \equiv \frac{L}{4\pi d_{\mathrm{L}}^2} \ , \tag{B.18}$$

for a source flux of F_{L}, where the luminosity distance d_L is thus defined as

$$d_{\mathrm{L}} = d_{\mathrm{m}}(1+z) \ , \tag{B.19}$$

with d_{m} as the metric distance, or look-back distance, as defined in equation B.16.

Angular Diameter Distance

The final commonly used cosmological distance measure is the *angular diameter distance*. This indicates the physical size of an object compared to the size of the region it subtends on the sky. In Euclidean space, the angular diameter distance d_{A} of an object of size D_{A} and angular size on the sky $\delta\theta$ is simply $d_{\mathrm{A}} = D_{\mathrm{A}}/\delta\theta$. Extending this to FRW space-time, a $(1+z)$ correction to the distance D_{A} term can be applied, as before, to account for the expansion of the Universe as light from the object travels towards an observer. This yields a relation between the physical size of the object and the angle it subtends on the sky as

$$d_{\mathrm{m}} = \frac{D_{\mathrm{A}}(1+z)}{\delta\theta} \tag{B.20}$$

for the metric distance to the object d_{m}. Comparing to the Euclidean definition of angular diameter distance, an FRW version can be written as

$$d_{\mathrm{A}} = \frac{d_{\mathrm{m}}}{1+z} \ , \tag{B.21}$$

or, alternatively it may be expressed in terms of the luminosity distance, by comparison with equation B.19, as

$$d_{\mathrm{A}} = \frac{d_{\mathrm{L}}}{(1+z)^2} \ . \tag{B.22}$$

B.4 Dynamics and Evolution

The evolution and ultimate fate of the Universe is essentially governed by its contents (i.e. its energy density). This counts together all constituents of the Universe in terms of their energy, and its total value will determine whether the Universe is flat (with no curvature), open (with a negative curvature) or closed (with a positive curvature). In the case of a closed Universe, the energy density would eventually dominate, causing it to reverse its expansion and collapse back towards a single point under gravity. In an open Universe, expansion continues forever, unstopped and unstoppable by the effects of gravity. With a dark energy component, the expansion accelerates, ultimately leading to the heat death of the Universe. If the Universe is flat, with zero curvature, the end result is much the same as with the open case – but without dark energy, expansion would begin to be countered by the effects of gravity, asymptotically bringing the expansion of the Universe to zero. Observations appear to suggest that the Universe is flat, or indistinguishably close to it.

The critical density of the Universe is defined to be a mean density which leads to a flat cosmology,

$$\rho_{\text{crit}} = \frac{3H^2}{8\pi G} \tag{B.23}$$

and, from this, the density parameter Ω may be defined as the fractional density of a universe compared to ρ_{crit},

$$\Omega = \frac{\rho}{\rho_{\text{crit}}} = \frac{8\pi G \rho}{3H^2} \; . \tag{B.24}$$

$\Omega_{\text{m}}, \Omega_{\kappa}$ and Ω_{Λ} can also be specified as density parameters for the energy densities associated with matter, curvature and dark energy respectively, being the fraction that these energy densities represent of the critical density ρ_{crit}.

B.4.1 Dynamics

Returning to the Friedmann equations, B.11 and B.12, then equation B.11 can be differentiated with respect to time, t. Substituting both Friedmann

equations into the result gives the continuity equation,

$$\frac{d\rho}{dt} + 3H(\rho + P) = 0 \ . \tag{B.25}$$

Defining the equation of state, $\omega_{\mathrm{EoS}} = P/\rho$, the result B.25 may then be integrated with respect to time to give a proportionality between ρ and a as

$$\rho \propto a^{-3(1+\omega_{\mathrm{EoS}})} \ . \tag{B.26}$$

The contents of the Universe can be described by the equation of state, which has the values $0, 1/3, -1/3, -1$ for matter, radiation, curvature and dark energy, such that their energy density evolves as $a^{-3}, a^{-4}, a^{-2}, a^0$ respectively. The definition B.24 (and the associated quantities for each constituent component of the Universe) such that the notation $\Omega_{i,0}$ (where i is matter, radiation, curvature or dark energy, and subscript 0 represents the present value) can be modified to indicate the evolution of the contents of the Universe with redshift, for instance $\Omega_r = \Omega_{r,0} \, a^{-4}$ for radiation. By this convention, the Friedmann equations B.11 and B.12 may be rewritten as

$$\left(\frac{H}{H_0}\right)^2 = \Omega_{r,0}a^{-4} + \Omega_{m,0}a^{-3} + \Omega_{\kappa,0}a^{-2} + \Omega_{\Lambda,0} \ , \tag{B.27}$$

$$\left(\frac{\ddot{a}}{a}\right)_{t=t_0} = -\frac{H_0^2}{2}\left(2\Omega_r + \Omega_m - 2\Omega_\Lambda\right) \ . \tag{B.28}$$

From these evolution equations, particularly B.27, it is clear that different constituents of the Universe come to dominate at different epochs. For instance, radiation (thought to dominate at early epochs) density decreased as a factor of a^{-4}. It was quickly overwhelmed by matter density which, in turn, became dominated by dark energy (in a flat cosmology). Intriguingly, it is found that $\Omega_{m,0} \approx \Omega_{\Lambda,0}$ in the present Universe. This indicates that the Universe is currently in a state where the transition from matter to dark energy domination can be observed (as manifested by late-time acceleration).

B.5 The Perturbed Universe

The development and growth of structure in the Universe can be described in terms of Newtonian perturbation theory. Newtonian dynamics are generally appropriate for most cosmological (the large-scale, weak field regime of gravity) applications, and structure growth is best considered from the point of view of fluid dynamics.

It should first be noted that the fluid equations are derived in the context of a static spacetime. It is therefore necessary to modify them appropriately for the ΛCDM paradigm, i.e. accounting for the expansion of the Universe. Comoving coordinates can be used, where $r = a(t)x$ for which x is the comoving coordinate, and r is the static-space Euclidean coordinate. This imposes that, for density, $\rho \rightarrow \rho/a^3$ and, for velocity, $\vec{u} = \dot{\vec{r}} = \dot{a}\vec{x} + a\dot{\vec{x}}$. When transforming the fluid equations to comoving coordinates, comoving time also introduces a factor of a^{-1} to any appearance of the gradient operator ∇. The fluid equations thus become:

$$\frac{\partial \rho}{\partial t} + \nabla \cdot (\rho \vec{u}) = 0 \tag{B.29}$$

$$\frac{\partial \vec{v}}{\partial t} + (\vec{u} \cdot \nabla)\vec{u} = -\frac{1}{\rho}\nabla P - \nabla \Phi$$

$$a^{-2}\nabla^2 \Phi = 4\pi G\rho$$

for the continuity, momentum and Poisson equations respectively. Perturbations of the relevant quantities about their background levels can now be applied, for density, pressure, velocity (of the IGM flow) and gravitational potential (where the over-bar notation represents the average, background value of each quantity), i.e. $\rho \rightarrow \bar{\rho}(t) + \delta\rho$, $P \rightarrow \bar{P}(t) + \delta P$, $\vec{u} \rightarrow \vec{u}(t) + \vec{v}$, and $\Phi \rightarrow \bar{\Phi}(\vec{x}, t) + \phi$, where $\delta\rho$ is a fractional over-density in the IGM (the fluid), ϕ is the gravitational potential perturbation and $\vec{v}$ is the velocity perturbation of the fluid (IGM) flow. To first order, substitution of the perturbed quantities back into the modified fluid equations yields (with substitution of H), the

Newtonian perturbation equations:

$$\frac{\partial \delta}{\partial t} + \frac{1}{a} \nabla \cdot \vec{v} = 0 \tag{B.30}$$

$$\frac{\partial \vec{v}}{\partial t} + H\vec{v} = -\frac{1}{a\bar{\rho}} \nabla \delta P - \frac{1}{a} \nabla \phi$$

$$\nabla^2 \phi = 4\pi G a^2 \delta \rho \ .$$

These are the basic equations by which the evolution of perturbations in a ΛCDM universe can be described, to first order. To understand their impact on the growth of structure, the time derivative of the perturbed continuity equation can be taken,

$$\frac{\partial^2 \delta}{\partial t^2} - a^{-1} H \nabla \cdot \vec{v} + a^{-1} \nabla \cdot \frac{\partial \vec{v}}{\partial t} = 0 \ . \tag{B.31}$$

This, combined with the perturbed momentum equation and Poisson equation, gives

$$\frac{\partial^2 \delta}{\partial t^2} + 2H \frac{\partial \delta}{\partial t} - 4\pi G \bar{\rho} \delta - \frac{1}{a^2 \bar{\rho}} \nabla^2 \delta P = 0 \ . \tag{B.32}$$

Assuming the IGM to be a barotropic fluid, $\delta P \equiv c_s^2 \delta \rho$, with c_s as the sound speed, equation B.32 can be Fourier expanded (such that ∇^2 becomes $-k^2$), giving

$$\frac{\partial^2 \delta}{\partial t^2} + 2H \frac{\partial \delta}{\partial t} - \left[a^{-2} c_s^2 k^2 - 4\pi G \bar{\rho} \right] \delta = 0 \ . \tag{B.33}$$

Consider the case of perturbations which exceed the Jean's mass within a proper wavelength, so that the matter term dominates (i.e. relating to the growing solution of δ in B.33). The result B.33 now becomes

$$\frac{\partial^2 \delta}{\partial t^2} + 2H \frac{\partial \delta}{\partial t} - 4\pi G \delta \rho = 0 \ , \tag{B.34}$$

which has growing mode solutions of $\delta(t)$, demonstrating that over-densities above the Jean's mass within a comoving wavelength will grow over time - leading to the formation of large-scale structure.

Appendix C

Lists of Symbols, Constants and Abbreviations

Physical Constants

c	Speed of light	2.998×10^{10} cm s^{-1}
G	Newtonian gravitational constant	6.673×10^{-8} dyn cm^{-2} g^{-2}
k$_B$	Boltzmann constant	1.381×10^{-16} erg K^{-1}
h	Planck constant	6.626×10^{-27} erg s
$\hbar$	Atomic unit of angular momentum ($= h/2\pi$)	1.054×10^{-27} g
σ_B	Stefan-Boltzmann constant	5.671×10^{-5} erg cm^{-2} s^{-1} K^{-4}
α_f	Fine structure constant	7.297×10^{-3}
σ_T	Thomson cross section	6.653×10^{-25} cm^2
λ_C	Compton wavelength	3.862×10^{-11} cm
m_e	Electron rest mass	0.511 MeV/c^2
m_p	Proton rest mass	938.27 MeV/c^2
m_n	Neutron rest mass	939.57 MeV/c^2
m_{π^0}	Pion rest mass (neutral)	134.96 MeV/c^2
$m_{\pi^\pm}$	Pion rest mass (charged)	139.57 MeV/c^2
e	Electron charge	4.8×10^{-10} e.s.u
eV	Energy of 1 electron-volt	1.602×10^{-12} erg

Astrophysical Quantities

pc	Parsec	3.086×10^{18} cm
yr	Year	3.154×10^{7} s
$L_\odot$	Solar luminosity	3.90×10^{33} erg s^{-1}
$M_\odot$	Solar mass	1.989×10^{33} g
$Z_\odot$	Solar metallicity fraction (by mass)	0.0134
T_0	Current temperature of the CMB	2.725 K

Symbols and Parameters

Symbols used throughout this thesis are listed below alphabetically. A brief meaning or definition is given for each, with (if relevant) a typical value or parameter choice. The location of either the first use or defining equation in the thesis is also noted for reference. Note that substitution terms used in equations in self-contained sections are not included in this list.

$\mathcal{A}(E_\mathrm{p}, \mathbf{r}; \mathbf{r}_i)$	Attenuation experienced by a beam of hadronic CRs of energy E_p as they propagate between a source at $\mathbf{r}_i$ and some position $\mathbf{r}$	Eq. 4.11, Chap. 4
a	Scale-factor of the Universe	Eq. B.5, App. B
$\mathcal{B}_\mathrm{e}$	Fitting function introduced by Kelner et al. (2006) for use in determining F_e (the number of electrons released per pp interaction per energy interval)	Eq. 3.39, Chap. 3
$b_{\gamma\mathrm{e}}$	Electron cooling rate due to photo-pair losses	Eq. 3.23, Chap. 3
b_ad	Particle cooling rate due to adiabatic losses	Eq. 3.54, Chap. 3
b_IC	Electron cooling rate due to inverse Compton losses	Eq. 3.48, Chap. 3
B_ISM	Magnetic field strength at the base of an outflow cone (in the ISM of the host)	Eq. 2.8, Chap. 2
$B_\mathrm{L,sat}$	Large scale (galactic) magnetic field saturation strength	Eq. 1.6, Chap. 1
B_L	Large scale (galactic) magnetic field	Eq. 1.6, Chap. 1
b_synch	Electron cooling rate due to synchrotron losses	Eq. 3.48, Chap. 3
b_TPP	Electron cooling rate due to triplet pair production processes	Eq. 3.53, Chap. 3
$B_\mathrm{v,sat}$	Small-scale viscous magnetic field saturation strength	Sec. 1.3.3, Chap. 1
B_v	Small-scale viscous magnetic field	Sec. 1.3.3, Chap. 1
B_0	Seed magnetic field strength	Sec. 1.3.3, Chap. 1
b	Total CR electron cooling term	Eq. 4.3, Chap. 4
B	Magnetic field strength (general)	Sec. 1.3.3, Chap. 1
c_*	Effective sound speed in an outflow	Eq. 2.29, Chap. 2

c_g	Galaxy concentration parameter	Eq. 2.14, Chap. 2
c_s	Sound speed (in the IGM)	Eq. B.33, App. B
d_A	Angular diameter distance	Eq. B.21, App. B
D_A	Object size in defining the angular diameter distance	Eq. B.20, App. B
d_IPD	Instantaneous physical distance	Eq. B.17, App. B
d_L	Luminosity distance	Eq. B.19, Chap. B
$d_\mathrm{m}, d_\mathrm{lookback}$	Metric distance, or lookback distance	Eq. B.20 and Eq. B.16, App. B
D_N	Radiation field correction factor for a distributed source ensemble	Eq. 1.17, Chap. 1
D_0	Reference value for the diffusion coefficient for a 1-GeV CR proton in a 5-μG mean magnetic field ($D_0 = 3.0 \times 10^{28}$ cm^2 s^{-1})	Eq. 3.32, Chap. 2
d_H	Particle horizon (radius travelled by light since $t = 0$)	Eq. B.14, App. B
D	Diffusion coefficient	Eq. 3.32, Chap. 2
E_γ	Photon energy	Eq. 3.29, Chap.2
$E_{\pi^\pm}$	Energy transferred to pions from proton of energy E_p	Eq. 3.45, Chap. 3
E_e	Electron energy (secondary)	Sec. 3.1, Chap. 3
$\dot{E}_\mathrm{e}^\mathrm{x}$	CR electron energy transfer rate due to a process x	Sec. 3.3.1, Chap. 3
E_init	Seed CR energy (before acceleration processes)	Eq. A.14, App. A
E_kin	Total kinetic energy of interacting CR proton (contracted notation)	Eq. 3.42, Chap. 3
E_max	Maximum bound for model CR energy spectrum, 10^{15} eV	Eq. 2.6, Chap. 2
E_p^th	Threshold energy for π^0 production in the pp interaction	Eq. 3.10, Chap. 3
E_p	CR proton energy	Sec. 3.1, Chap. 3
E_SN	Energy of a core collapse SN event	Sec. 1.3.1, Chap. 1
E_0	Minimum bound for model CR energy spectrum 10^9 eV	Eq. 2.5, Chap. 2
$E(k)$	Energy in turbulence spectrum for waves of wavenumber k	Eq. 3.33, Chap. 2
E	Energy (general)	Sec. 2.1, Chap. 2
$F_{\pi^\pm}$	Charged pion flux per energy interval	Eq. 3.42, Chap. 3
f_A	Solid angle fraction of 4π subtended by Zone A	Eq. 2.7, Chap. 2
f_B	Solid angle fraction of 4π subtended by Zone B	Eq. 2.7, Chap. 2
f_C	Cosmic ray Coulomb heating efficiency fraction	Eq. 5.4, Chap. 5
f_dyn	Estimation factor for dynamical mass, approximately $f_\mathrm{dyn} = 2.25$	Eq. 6.3, Chap. 6

F_{e}	Number of electrons released per CR interaction, per energy interval	Eq. 3.38, Chap. 3
f_{g}	Fraction of CR energy lost in driving an outflow wind	Eq. 2.13, Chap. 2
$\mathcal{F}_{\gamma\mathrm{e}}$	Function specifying the photo-pair production rate for CR protons	Eq. 3.17, Chap. 3
F_{L}	Radiative flux emitted from a point source	Eq. B.18, App. B
f_{PP}	Fraction of energy retained by protons in a baryon beam after undergoing a single pp interaction event	Eq. 5.1, Chap. 5
f_{turb}	Fraction of turbulent kinetic energy transferred to magnetic energy	Eq. 1.6, Chap. 1
F	Correction factor ($F/\sqrt{2} \sim 1$) to account for minor differences between rotation velocity measures	Eq. 2.32, Chap. 2
$g_{\alpha\beta}$	General notation for the metric tensor	Eq. B.5, App. B
$G_{\alpha\beta}$	Einstein tensor	Eq. B.7, App. B
h_{B}	Characteristic length-scale over which the ISM magnetic field retains an approximately uniform strength within the interstellar environment of the host galaxy ($h_{\mathrm{B}} = 1.5$ kpc)	Eq. 2.8, Chap. 2
h_{inj}	Maximum injection altitude of CRs in an outflow	Condition on eq. 2.21, Chap. 2
h_{*}	Location of the critical point in an outflow solution where the flow velocity transitions from subsonic to supersonic	Fig. 2.4, Chap. 2
h_0	Lower outflow altitude boundary condition	Eq. 4.30, Chap. 4
H	Hubble parameter, current value $\mathrm{H}_0 = (67.8 \pm 0.9)$ km s^{-1} Mpc^{-1}	Eq. 3.25, App. 3
I	Total energy exchange term between thermal and non-thermal components of an outflow wind	Eq. 2.16, Chap. 2
$\mathcal{I}_{\mathrm{p}}$	Total (energy-integrated) local volumetric injection rate of CR protons	Eq. 2.4, Chap. 2
$\mathcal{I}_{\mathrm{IX}}(r)$	The bolometric intensity of inverse Compton X-rays at r produced by a population of energetic CR secondary electrons	Sec. 3.4.2, Chap. 3
$\bar{K}$	Overall effective energy transfer efficiency for the production of CR secondary electrons from CR protons ($\bar{K} = K_{\mathrm{e}}K_{\pi\pm}$)	Eq. 3.46, Chap. 3
$K_{\pi\pm}$	Fraction of energy passed from the CR proton to secondary pions (typically, $K_{\pi\pm} = 0.6$)	Eq. 3.42, Chap. 3
$K_{\gamma\pi}$	Inelasticity coefficient for the photo-pion interaction	Eq. 3.4, Chap. 3

$k_{\gamma e}$	Fitting parameter for effective photo-pair production and triplet pair-production interaction cross-sections ($k_{\gamma e} = 6.7$)	Eq. 3.14, Chap. 3
K_e	Efficiency of energy transfer from pions to electrons ($K_e = 0.265$)	Eq. 3.45, Chap. 3
$\mathcal{K}_e$	Fitting function introduced by Kelner et al. (2006) for use in determining F_e (the number of electrons released per pp interaction per energy interval)	Eq. 3.40, Chap. 3
$\mathcal{L}_0$	Spectral normalisation term for CRs	Eq. 2.6, Chap. 2
L_*	Stellar luminosity	Eq. 1.9, Chap. 1
$L_{\mathrm{CR,eff,A}}$	CR luminosity passed to outflow cone (Zone A)	Eq. 2.7 and Eq. 2.9, Chap. 2
$L_{\mathrm{CR,eff,B}}$	CR luminosity passed to ISM (Zone B)	Eq. 2.7, Chap. 2
$L_{\mathrm{CR,eff}}$	Effective total CR luminosity	Eq. 2.3, Chap. 2
$\mathcal{L}_{\mathrm{CR}}(E)$	Energy spectrum of the freshly accelerated CR hadronic particles	Eq. 2.5, Chap. 2
L_f	Driving scale of ISM turbulence	Sec. 1.3.3, Chap. 1
L_{IX}	Total luminosity of inverse Compton X-rays due to CR electrons in a galaxy	Eq. 5.9, Chap. 5
$\mathcal{L}_{\mathrm{IX}}$	Total (bolometric) inverse Compton X-ray luminosity of a source	Eq. 5.11, Chap. 5
L_{X}	Total (galactic) luminosity in thermal X-rays due to hot baryons/ISM gas	Sec. 5.1, Chap. 5
L	Energy parameter notation $L = m_{\mathrm{p}}\mathrm{c}^2 + \frac{E_{\pi\pm}}{K_{\pi\pm}}$	Eq. 3.44, Chap. 3
M_*	Stellar mass of galaxy	Sec. 6.1, Chap. 6
M_{cl}	Mass of star-forming molecular cloud	Eq. 6.5, Chap. 6
M_{dyn}	estimated dynamical mass of galaxy	Eq. 6.3, Chap. 6
M_{fil}	Characteristic mass of a filamentary inflow region	Eq. 6.12, Chap. 6
M_{inj}	Injected mass per SN event into an outflow	Eq. 2.15, Chap. 2
M_{tot}	Total system (galaxy) mass, including dark matter, gas and stellar components	Eq. 2.14, Chap. 2
$M(< r)$	Contained (integrated) mass to r	Sec. 1.3.2, Chap. 1
m	Diffusion geometrical parameter	Eq. 4.13, Chap. 4
$\mathcal{M}$	Number of electron secondary CRs produced by a hadronic CR primary	Eq. 3.45, Chap. 3
n_γ^{BB}	Blackbody spectrum photon number density	Section 1.3.4, Chap. 1
n_γ^{CMB}	CMB photon number density	Eq. 1.7, Chap. 1
$n_\gamma^\star$	Stellar photon number density	Eq. 1.17, Chap. 1
n_γ	General photon number density in a radiation field	Eq. 3.6, Chap. 3

$n_{\mathrm{CR,e}}$	Differential number density of CR electrons (secondaries) per energy interval	Eq. 4.5, Chap. 4
$N_{\mathrm{CR,e}}$	Injection rate of CRs from a source volume	BC for Eq. 4.42, Chap. 4
$n_{\mathrm{CR,p}}^{\mathrm{adv}}$	Differential number density of CR protons per energy interval under pure advective propagation	Eq. 5.6, Chap. 5
$n_{\mathrm{CR,p}}^{\mathrm{diff}}$	Differential number density of CR protons per energy interval under pure diffusive propagation	Eq. 5.6, Chap. 5
$n_{\mathrm{CR,p}}$	Differential number density of CR protons per energy interval	Eq. 4.4, Chap. 4
n_{CR}	General differential number density of energetic CRs per energy interval	Eq. 4.2, Chap. 4
n_{e}	Thermal electron number density (note that $n_{\mathrm{e}} = x_{\mathrm{i}} n_{\mathrm{H}}$)	Eq. 1.2, Chap. 1
$n_{\mathrm{H,0}}$	Peak interstellar medium density in a protogalaxy	Eq. 1.5, Chap. 1
n_{H}	Medium number density (or hydrogen number density)	Eq. 1.3, Chap. 1
$\bar{n}_{\mathrm{H,cl}}$	Characteristic number density of medium in a molecular cloud or ISM clump	Eq. 6.5, Chap. 6
$\bar{n}_{\mathrm{H,gal}}$	Characteristic number density of a galactic ISM	Eq. 6.5, Chap. 6
N_{p}	Number of CR protons	Eq. 3.37, Chap.3
N_{S}, $N_{\mathrm{S,2}}$	Number of discrete points used in Monte-Carlo numerical scheme	Sec. 4.2.1, Chap. 4
N	Estimated number of discrete points in an ensemble where the effective point size and total distribution extent are known	Eq. 1.13, Chap. 1
$\dot{N}_{\gamma\pi,\mathrm{abs}}$	Rate of CR collisions that successfully yield pion-production and subsequent hadronic CR absorption due to photo-pion interactions	Eq. 3.6, Chap. 3
$\dot{N}_{\gamma\pi,\mathrm{coll}}$	Rate of CR collisions due to photo-pion interactions	Eq. 3.6, Chap. 3
$\dot{N}_{\mathrm{p}\pi,\mathrm{abs}}$	CR absorption rate due to pp-pion production	Eq. 3.11, Chap. 3
P_{C}	CR pressure	Eq. 2.18, Chap. 2
P_{cont}	Probability a particle remains confined in a system after a scattering event (in an a magnetic shock)	Eq. A.15, App. A
P_{esc}	Probability a particle escapes from a system after a scattering event (in an a magnetic shock)	Eq. A.15, App. A
P_{IC}	Inverse-Compton power due to the scattering of a single electron	Eq. 3.59, Chap. 3
P	Pressure (gas)	Eq. 2.18, Chap. 2
$\mathcal{P}$	Outflow mass-loading factor	Eq. 2.15, Chap. 2

$\dot{Q}_{\rm DC}$	Volumetric heating power imparted by CRs on a medium due to the direct (Coulomb) mechanism	Eq. 5.5, Chap. 5
$Q_{\pi\pm}$	Volumetric local charged pion injection rate at energy $E_{\pi\pm}$	Eq. 3.44, Chap. 3
$Q_{\rm e}$	Volumetric local CR electron injection rate at energy $E_{\rm e}$	Eq. 3.36, Chap. 3
$q_{\rm inj}$	Mass injection rate to an outflow by SN activity	Eq. 2.15, Chap. 2
$\dot{Q}_{\rm IX}$	Volumetric heating power imparted by CRs on a medium due to the indirect (inverse Compton emitted X-rays) mechanism	Eq. 5.13, Chap. 5
$Q_{\rm p}$	Volumetric local CR proton injection rate at energy $E_{\rm p}$	Eq. 4.4, Chap. 4, also see Eq. 2.4, Chap. 1
$q_{\rm t}$	Parameterisation of turbulence spectrum in ISM	Eq. 3.33, Chap. 2
q	Charge on particle	Eq. 2.1, Chap. 2
Q	CR source term (general), local CR volumetric injection rate	Sec. 2.1, Chap. 2
$\mathcal{Q}$	Outflow thermalisation efficiency	Eq. 2.10, Chap.2
R_*	Stellar radius	Eq. 1.9, Chap. 1
R_ℓ	Scale length of a galaxy (defined as the ratio of the virial radius to the concentration parameter, i.e. $R_{\rm vir}/c_{\rm g}$)	Eq. 2.14, Chap. 2
$r_{\gamma\pi}$	Interaction path length due to CR photo-pion production	Eq. 3.21, Chap. 3
$r_{\gamma{\rm e}}$	Interaction path length due to CR photo-pair production	Eq. 3.23, Chap. 3
$r_{\rm p\pi}$	Interaction path length due to CR proton-proton pion production	Eq. 3.24, Chap. 3
$R_{\rm C}$	Compression factor across a strong magnetic shock front	Eq. A.1, App. A
$r_{\rm c}$	Protogalaxy core radius (in defining density profile)	Eq. 1.5, Chap. 1
$r_{\rm cl}$	Size of star-forming molecular cloud	Eq. 6.5, Chap. 6
$R_{\rm cool}$	Scaling factor to account for the ratio of cooling rates of protons compared to electrons, where $R_{\rm cool} = (m_e/m_p)^4$	Eq. 4.31, Chap. 4
$R_{\rm cut}$	Maximum radius of extended stellar distribution	Sec. 1.3.4, Chap. 1
$R_{\rm d}$	Coordinate distance	Eq. B.17, App. B
$R_{\rm eq}$	Point at which half of the total integrated IX heating in an inflow has been experienced by the gas	Eq. 6.14, Chap. 6
$r_{\rm exp}$	CR particle path length due to adiabatic losses during expansion	Eq. 3.25, Chap. 3

r_{f}	Characteristic radius of a cold filamentary inflow	Eq. 1.3, Chap. 1
r_{gal}	Characteristic radius of (host) galaxy	Sec. 1.3.3, Chap. 1
r_{h}	Protogalaxy halo radius (in defining density profile)	Eq. 1.5, Chap. 1
r_{in}	Innermost radius of the inflow ($\sim r_{\mathrm{gal}}$)	Eq. 6.14, Chap. 6
r_{int}	Characteristic path-length of a CR over which it loses its energy due to interactions with its environment	Eq. 3.18, Chap. 3
$r_{\mathrm{L},0}$	Larmor radius for a 1 GeV proton in a 5-μG magnetic field (reference value)	Eq. 3.32, Chap. 2
r_{L}	Larmor (gyro) radius of a charged particle moving in a uniform magnetic field	Eq. 2.1, Chap. 2
$\bar{r}_{\mathrm{p}\pi}$	Effective path length for a hadron beam to lose its energy due to multiple scatterings	Eq. 5.1, Chap.5
$r_{\mathrm{p}\pi}$	Interaction path length due to pp pion production	Eq. 3.24, Chap. 3
R_{S}	Ricci scalar	Eq. B.7, App. B
$\mathcal{R}_{\mathrm{SB}}^{*}$	Star-formation rate during starburst episode	Eq. 6.2, Chap. 6
$\mathcal{R}_{\mathrm{SB}}^{*}$	Star-formation rate surface density during the starburst phase of a galaxy	Fig. 6.6, Chap. 6
$\mathcal{R}_{\mathrm{SF}}$	Star-formation rate (at observational epoch if distinction is relevant, as per use in chapter 6)	Eq. 1.3, Chap. 1
$\mathcal{R}_{\mathrm{SN}}$	SN event rate	Sec. 1.3.1, Chap. 1
r_{sph}	General radius of extended source	Eq. 1.17, Chap. 1
r_{sys}	Characteristic length-scale of a system acting as a CR accelerator	Eq. 2.2, Chap. 2
R_{vir}	Virial radius	Eq. 2.14, Chap. 2
$R_S N, 0$	Reference SN event rate in scaling relation	Eq. 2.8, Chap. 2
R	Maximum extent of inflowing filaments	Sec. 1.2.1, Chap. 1
$S_{\mathrm{CR,p}}$	CR proton 'sink' (absorption) term	Eq. 4.4, Chap. 4
S	General particle sink term	Eq. 4.1, Chap. 4
$\mathcal{S}$	Equipartition constant term, $\mathcal{S} = \sqrt{4\pi\rho}\ v_{\mathrm{f}}$	Sec. 1.3.3, Chap. 1
$T_{\alpha\beta}$	Energy-momentum tensor	Eq. B.7, Chap. B
T_{*}	Stellar temperature	Eq. 1.9, Chap. 1
t_{con}	Containment timescale for CRs (comparable to the magnetic saturation timescale of the host galaxy)	Sec. 5.2, Chap. 5
T_{e}	Electron temperature	Eq. 1.2, Chap. 1
t_{end}	Approximate time since the end of star-formation burst	Eq. 6.4, Chap. 6
t_{int}	General interaction timescale i.e. the time taken for a characteristic energy-loss path length due to an interaction process to be traversed by a CR undergoing that interaction	Eq. 3.19, Chap. 3

t_{qui}	The timescale over which a post-starburst galaxy has remained relatively quiescent after its initial violent star-formation episode	Sec. 6.4, Chap. 6
t_{sat}	Timescale over which the large-scale protogalactic magnetic, B_{L}, field saturates	Eq. 1.6, Chap. 1
t_{SB}	The timescale over which the initial starburst phase in a post-starburst system was active	Eq. 6.4, Chap. 6
$T_{\mathrm{vir,cl}}$	Virial temperature of star-forming cloud/clump	Eq. 6.5, Chap. 6
$T_{\mathrm{vir,gal}}$	Virial temperature of entire galaxy	Eq. 6.5, Chap. 6
T_{vir}	Virial temperature of a system	Sec. 6.2, Chap. 6
T_0	CMB temperature in the current epoch	Eq. 1.7, Chap. 1
$t(z_{\mathrm{f}})$	Age of the Universe at redshift of initiation of starburst activity in a galaxy	Eq. 6.4, Chap. 6
$t(z_{\mathrm{obs}})$	Age of Universe at the redshift a galaxy is observed	Eq. 6.4, Chap. 6
T	Temperature (general); partially ionised and/or neutral gas temperature; radiation field temperature	Chap. 1 and throughout
U_{B}	General magnetic field energy density	Eq. 3.48, Chap. 3
U_{CMB}	CMB energy density	Eq. 1.8, Chap. 1
U_{rad}	General radiation field energy density	Eq. 3.48, Chap. 3
$U^{\star}$	radiation energy density	Sec. 1.3.4, Chap. 1
U^{i}	4-velocity, with index i	Eq. B.10, App. B
v_{∞}	Terminal outflow velocity	Sec. 2.2.1, Chap. 2
v_{A}	Alfvén velocity	Sec. 2.2, Chap. 2
$V_{\mathrm{c,vir}}$	Circular velocity at virial radius	Eq. 2.32, Chap. 2
$V_{\mathrm{c},*}$	Circular velocity at the critical point h_*	Sec. 2.2, Chap. 2
v_{f}	Turbulent velocity of interstellar gas	Sec. 1.3.3, Chap. 1
V_{gal}	Characteristic galaxy volume at redshift z	Sec. 5.3, Chap. 5
$v_{\mathrm{Ly}\alpha}$	Lyman-α velocity offset in observations (compared to other emission lines)	Eq. 1.3, Chap. 1
v	Velocity	Used throughout
$\mathcal{V}_{\mathrm{S}}$	Characteristic assigned source size for a discrete injection point of particles in an extended distribution	Eq. 4.14, Chap. 4
$\mathcal{W}$	Growth rate of small-scale (viscous) galactic magnetic field	Sec. 1.3.3, Chap. 1
x_i	Ionisation fraction	Sec. 1.2.1, Chap. 1; Eq. 5.9, Chap. 5
X (also X_0)	Number of particles engaging in scattering acceleration events (initial value)	Eq. A.15, App. A
z_{f}	Redshift of the initiation of star-formation in a galaxy	Sec. 6.1.1, Chap. 6
z_{obs}	Redshift of the observational epoch of a galaxy	Eq. 6.4, Chap. 1

$Z_\odot$	Solar metallicity	Sec. 1.2.2, Chap. 1
z	Redshift, $z = (a-1)^{-1}$	App. B and throughout
$\alpha^\star$	Conversion fraction between star-formation rate and SN event rate	Eq. 1.4, Chap. 1
α	Effective absorption coefficient (for CRs attenuated by photo-pion production pp-pion production)	Eq. 3.34, Chap. 3
$\beta_{\rm p}$	CR proton speed normalised to the speed of light	Sec. 3.1, Chap. 3
β	Fraction of SN energy transferred into ISM turbulence ($\beta = 0.05$)	Sec. 1.3.3, Chap. 1
χ	Energy parameter for the pp interaction cross-section	Eq. 3.10, Chap. 3
δ	Over-density in the intergalactic fluid	Eq. B.31, App. B
$\dot\epsilon_{\rm CR}^{\rm outflow}$	Energy injection rate into an outflow by SN events via CRs	Eq. 2.9, Chap. 2
$\dot\epsilon_{\rm th}^{\rm outflow}$	Thermal/SN energy injection rate into an outflow by SN events	Eq. 2.10, Chap. 2
$\dot\epsilon$	Total SN injection power into an outflow wind	Eq. 2.11, Chap. 2
$\ell_{\rm adv}$	Advection length-scale	Eq. 4.40, Chap. 2
$\ell_{\rm diff}$	Diffusion length-scale	Eq. 3.31, Chap. 2
$\ell_{\rm p}$	The scale of peak energy of the ISM (turbulent) magnetic field	Eq. 1.6, Chap. 1
$\ell_{\rm th}$	CR thermalisation length-scale (by Coulomb energy transfer)	Eq. 3.57, Chap. 3
$\ell_{\rm v}$	Viscous (small) length-scale of the ISM magnetic field	Sec. 1.3.3 Chap. 1
$\epsilon_{\rm CR,adv}$	CR energy density under advective propagation	Eq. 4.40, Chap. 2
$\epsilon_{\rm CR,diff}$	CR energy density under diffusive propagation	Eq. 3.31, Chap. 2
$\epsilon_{\rm CR}$	General CR energy density	Eq. 3.30, Chap. 2
$\epsilon_{\rm p}$	CR proton energy normalised to electron mass	Sec. 3.1, Chap. 3
$\epsilon_{\rm r}$	Invariant energy of an interaction normalised to electron mass	Sec. 3.1, Chap. 3
ϵ	Photon energy normalised to electron mass	Sec. 3.1, Chap. 3
$\eta_{\rm E}$	Fractional energy gain of a charged particle as it interacts with a shock during stochastic particle acceleration	Eq. A.3, Chap. A
$\eta_{\rm SNe}$	Combined SN energy efficiency term (in powering an outflow wind)	Eq. 2.12, Chap. 2
$\eta_{\rm t}$	Conformal time: total distance travelled by light since $t = 0$	Eq. B.13, App. B
$\eta_{\rm inflow}^\star$	Star-formation efficiency of inflowing gas from cold filaments ($\eta_{\rm inflow}^\star = 0.3$)	Eq. 1.3, Chap. 1
$\gamma_{\rm C}$	Adiabatic index for a relativistic gas, CRs ($\gamma_{\rm C} = 4/3$)	Eq. 2.20, Chap. 2

$\Gamma_{\mathrm{CR,e}}$	CR power law spectral index boundary condition for electrons	Eq. 4.33, Chap. 4
γ_{e}	CR electron Lorentz factor	Sec. 3.1, Chap. 3
γ_{g}	Adiabatic index for a monatomic ideal gas ($\gamma_{\mathrm{g}} = 5/3$)	Eq. 2.19, Chap. 2
γ_{L}	Lorentz factor (general)	Eq. A.5, App. A
γ_{p}	CR proton Lorentz factor	Sec. 3.1, Chap. 3
Γ_{w}	Magnetic field (small-scale) growth rate	Sec. 1.3.3, Chap. 1
$\Gamma^i_{j,k}$	Christoffel symbol of the second kind	Eq. B.9, App. B
Γ	CR spectral index (resulting from diffusive shock acceleration processes)	Eq. A.16, App. A
$\hat{\sigma}_{\gamma\pi}$	Inelastic cross-section of the photo-pion interaction, note: $\sigma_{\gamma\pi}(\epsilon_{\mathrm{r}})K_{\gamma\pi}$, and approximated value is $\hat{\sigma}^*_{\gamma\pi}$	Eq. 3.3, Chap. 3
$\hat{\sigma}_{\gamma\mathrm{e}}$	Analytic fit to the cross-section for photo-electron pair production	Eq. 3.13, Chap. 3
$\hat{\sigma}_{\mathrm{p}\pi}$	Effective total inelastic cross-section for the pp interaction	Eq. 3.29, Chap. 2; also see Eq. 3.10, Chap. 3
$\hat{\sigma}_{\mathrm{TPP}}$	Approximation for the triplet pair production cross-section	Eq. 3.51, Chap. 3
κ	Curvature parameter of the Universe	Eq. B.6, Chap. B
λ_{C}	Compton wavelength ($\lambda_{\mathrm{C}} = h/m_{\mathrm{e}}c$)	Eq. 1.7, Chap. 1
Λ_{cool}	Thermal free-free cooling rate of an ionised hot gas	Eq. 1.1, Chap. 1
μ_{L}	Lensing parameter used in Hashimoto et al. (2018) for MACS1149-JD1	See also 6 introduction
μ	Cosine of the angle between the momentum vectors of interacting species	Sec. 3.1, Chap. 3
ν_{d}	Fraction of thermal energy injected by SN events lost to driving an outflow wind ($\nu_{\mathrm{d}} = 0.1$)	Eq. 2.10, Chap. 2
ν	Photon frequency	Sec. 3.1, Chap. 3
Ω_{κ}	Effective curvature density parameter (current value denoted by $\Omega_{\kappa,0}$)	Eq. B.28, App. 3
Ω_{Λ}	Effective dark energy density parameter (current value denoted by $\Omega_{\Lambda,0}$)	Eq. B.28, App. 3
ω_{adv}	Weighting factor for advection solution contribution to combined CR number density	Eq. 5.8, Chap. 5
ω_{diff}	Weighting factor for diffusion solution contribution to combined CR number density	Eq. 5.7, Chap. 5
Ω_A	Solid angle subtended by Zone A	Eq. 2.7, Chap. 2
Ω_B	Solid angle subtended by Zone B	Eq. 2.7, Chap. 2
Ω_{m}	Matter density of the Universe (current value denoted by $\Omega_{m,0}$)	Eq. B.28, App. 3

Ω_{r}	Effective radiation density parameter (current value, denoted by $\Omega_{r,0}$ is negligible)	Eq. B.28, App. 3
ω_{EoS}	Equation of state of the Universe ($\omega_{\mathrm{EoS}} = P/\rho$)	Eq. B.26, App. B
Ω	Density parameter: density of the Universe compared to the critical density	Eq. B.24, App.B
ω	Weighting function for stellar population sampling for a model galaxy (based on underlying density profile)	Eq. 1.10, Chap. 1
Φ_{p}	CR proton differential energy density	Eq. 3.37, Chap. 3
Φ	Gravitational potential	Eq. 2.19, Chap. 2
Ψ	Scaling factor used in outflow solution parameter study	Sec. 5.2.2, Chap. 5
ρ_{crit}	Critical density of the Universe (which leads to a flat Universe)	Eq. B.23, Chap. B
ρ	Mass density of medium	Eq. 1.3.3, Chap. 1
σ_{π^0}	Cross-section for the formation of neutral pions	Eq. 3.29, Chap. 2
σ_{f}	Cross-sectional area of a filamentary cold inflow, $\sigma_{\mathrm{f}} = \pi r_{\mathrm{f}}^2$	Eq. 1.3, Chap. 1
σ_{KN}	Klein-Nishina (relativistic) scattering cross-section	Sec. 3.4.2, Chap. 3
Σ_{obs}^*	Star-formation rate surface density of a galaxy at the epoch of its observation	Fig. 6.5, Chap. 6; see also Chap. 1
$\tau_{\gamma\pi,\mathrm{abs}}$	Timescale associated with the CR absorption rate resulting from photo-pion interactions	Eq. 3.6, Chap. 3
$\tau_{\gamma\pi,\mathrm{coll}}$	Timescale associated with the CR collision rate leading to photo-pion interactions	Eq. 3.6, Chap. 3
τ_{ad}	Adiabatic cooling timescale	Relates to eq. 5.4, Chap. 5
τ_{adv}	CR advection timescale	Eq. 4.23, Chap. 4
τ_{C}	Coulomb electron cooling timescale	Eq. 5.4, Chap. 5
τ_{cool}	Thermal free-free (bremsstrahlung) cooling timescale for a hot ionised gas	Eq. 1.2, Chap. 1
τ_{diff}	CR diffusion timescale	Eq. 4.22, Chap. 4
τ_{dyn}	Dynamical timescale (of a galaxy)	Throughout Chap. 6
τ_{IX}	Indirect X-ray (IX) CR heating timescale	Eq. 6.13, Chap. 6
$\tau_{\mathrm{p}\pi}$	CR proton absorption timescale due to pp interactions	Eq. 4.25, Chap. 4
τ_{Q}	Quenching timescale	Eq. 6.9, Chap. 6
τ_{rad}	Radiative (inverse Compton and synchrotron) electron cooling timescale	Eq. 5.4, Chap. 5
τ_{S}	Stunning (of star-formation) timescale	Sec. 6.3.2, Chap. 6

τ_{th}	CR secondary electron thermalisation timescale (by Coulomb scattering)	Eq. 3.56, Chap. 3
τ^*	Characteristic age of stellar population	Eq. 6.4, Chap. 6
θ_{Turb}	Slope of the turbulent velocity spectrum	Eq. 3.32, Chap. 2
Θ	Dimensionless temperature (for a radiation field)	Sec. 1.3.4, Chap.3
θ	Opening angle of galactic outflow cone	Eq. 2.7, Chap. 2
Υ	Index for Salpeter IMF, value 2.35	Eq. 1.4, Chap. 1
ε	Fraction of SN power converted into to CR power ($\varepsilon \sim 0.1$)	Eq. 2.3, Chap. 2
$\varkappa_{\text{e}}$	Energy-depending fitting parameter for F_{e} introduced by Kelner et al. 2006 (eq. 3.38)	Eq. 3.41, Chap. 3
ς	Ratio of free-streaming to diffusive CR proton propagation path lengths	Eq. 4.10, Chap. 4
$\vec{v}$	Velocity perturbation of IGM fluid flow	Eq. B.31, Chap. B
$\xi_{\pm}$	Charged pion production multiplicity	Eq. 3.9, Chap. 3
ξ_{c}	Reduced core radius parameter, $\xi_{\text{c}} = (r/r_{\text{c}})^2$	Eq. 1.5, Chap. 1
ξ_{h}	Reduced halo radius parameter, $\xi_{\text{h}} = (r/r_{\text{h}})^2$	Eq. 1.5, Chap. 1
ξ_0	Neutral pion production multiplicity	Eq. 3.9, Chap. 3
ξ	SN energy fraction retained after accounting for neutrino losses ($\xi = 0.01$)	Eq. 2.3, Chap. 2

List of parameters used in the thesis with their adopted value.

D_0	Reference value for the diffusion coefficient for a 1-GeV CR proton in a 5-μG mean magnetic field	3.0×10^{28} cm^2 s^{-1}
E_{max}	Maximum energy for CR spectrum	10^{15} eV
E_0	Minimum energy for CR spectrum	10^9 eV
E_{SN}	Typical energy of a core collapse SN event	10^{53} erg
h_{B}	Characteristic length-scale over which the ISM magnetic field retains an approximately uniform strength within the interstellar environment of its host galaxy	1.5 kpc
H_0	Current value of the Hubble parameter	(67.8 ± 0.9) km s^{-1} Mpc^{-1}
K_{e}	Efficiency of energy transfer from pions to electrons	0.265
$k_{\gamma\text{e}}$	Fitting parameter for effective photo-pair production and triplet pair-production interaction cross-sections	6.7

$K_{\pi^\pm}$	Fraction of energy passed from the CR proton to the produced pions	0.6
M_{cut}	Minimum stellar mass in a forming population	$1\mathrm{M}_\odot$
$M_{\max}$	Maximum stellar progenitor mass to yield a SN event (core collapse)	$50\mathrm{M}_\odot$
M_{SN}	Minimum stellar progenitor mass to yield a SN event (core collapse)	$8.5\mathrm{M}_\odot$
β	Fraction of SN energy transferred into ISM turbulence	0.05
ε	Fraction of SN power converted into to CR power	0.1
$\eta^\star_{\mathrm{inflow}}$	Star-formation efficiency of inflowing gas from cold filaments	0.3
ν_{d}	Fraction of thermal energy injected by SN events lost to driving an outflow wind	0.1
$\Omega_{\mathrm{m},0}$	Current matter density of the Universe, from Planck Collaboration et al. (2018)	0.314
$\Omega_{\Lambda,0}$	Current dark energy density of the Universe, from Planck Collaboration et al. (2018)	0.689
Υ	Salpeter index for stellar initial mass function	2.35
ξ	SN energy fraction retained after accounting for neutrino losses	0.01

Abbreviations

Definitions of abbreviations used in this thesis for reference.

AGB	Asymptotic giant branch
AGN	Active galactic nucleus
ALMA	*Atacama Large-Millimetre Array*
BBN	Big Bang nucleosynthesis
BC	Boundary condition
CGM	Circumgalactic medium
CMB	Cosmological microwave background
CR	Cosmic ray
DC	Direct Coulomb heating

DSA	Diffusive shock acceleration
EBL	Extragalactic background light
EGCR	Extragalactic cosmic ray
EoR	Epoch of (cosmic) reionisation
Fermi-LAT	*Fermi* Large Area Telescope
FRW	Friedman-Robertson-Walker (cosmological metric)
FWHM	Full width at half-maximum
GCR	Galactic cosmic ray
GR	General relativity
GRR	Galactic ridge region
GZK	Gresisen-Zatsepin-Kuzmin cut-off (energy)
HAWC	*High altitude water Cherenkov experiment*
HESS	*High energy stereoscopic system*
HIM	Hot ionised medium
IGM	Intergalactic medium
IMF	Initial mass function
ISM	Interstellar medium
ISRF	Interstellar radiation field
IVP	Initial value problem
IX	Indirect X-ray heating
JWST	*James Webb Space Telescope*
KN	Klein-Nishina (cross-section)
LAB	Lyman alpha break galaxy
ΛCDM	Λ (cosmological constant) Cold Dark Matter (cosmological model)
MC	Monte Carlo
NFW	Navarro-Frenk-White (dark matter profile)
PAH	Poly-aromatic hydrocarbon
PDE	Partial differential equation
RK4	4th order Runge-Kutta scheme
SAM	Semi-analytic model
SFH	Star-formation history
SN/SNe	Supernova/Supernovae (pl.)
SSFR	Specific star-formation rate
TPP	Triplet pair-production
UHECR	Ultra-high energy cosmic ray
UV	Ultraviolet (radiation)
WHIM	Warm-hot intergalactic medium

Bibliography

Abbasi, R. U. et al. (2004), Measurement of the Flux of Ultrahigh Energy Cosmic Rays from Monocular Observations by the High Resolution Fly's Eye Experiment, *Physical Review Letters* **92**(15), 151101.

Abbasi, R. U. et al. (2008a), An Upper Limit on the Electron-Neutrino Flux from the HiRes Detector, *ApJ* **684**, 790–793.

Abbasi, R. U. et al. (2008b), First Observation of the Greisen-Zatsepin-Kuzmin Suppression, *Physical Review Letters* **100**(10), 101101.

Abdo, A. A. et al. (2010a), Fermi Large Area Telescope observations of Local Group galaxies: detection of M 31 and search for M 33, *A&A* **523**, L2.

Abdo, A. A. et al. (2010b), Observations of the Large Magellanic Cloud with Fermi, *A&A* **512**, A7.

Abe, F. et al. (1990), Pseudorapidity distributions of charged particles produced in pp interactions at $\sqrt{s}$ =630 and 1800 GeV, *Phys. Rev. D* **41**, 2330–2333.

Abel, T., Bryan, G. L. and Norman, M. L. (2002), The Formation of the First Star in the Universe, *Science* **295**(5552), 93.

Abraham, J. et al. (2010), Measurement of the energy spectrum of cosmic rays above 10^{18} eV using the Pierre Auger Observatory, *Physics Letters B* **685**, 239–246.

Ackermann, M. et al. (2013), Detection of the Characteristic Pion-Decay Signature in Supernova Remnants, *Science* **339**(6121), 807.

Adams, S. M. et al. (2013), Observing the Next Galactic Supernova, *ApJ* **778**, 164.

Adebahr, B. et al. (2013), M82 A radio continuum and polarisation study - I. Data reduction and cosmic ray propagation, *A&A* **555**, A23.

Adelberger, K. L. et al. (2003), Galaxies and Intergalactic Matter at Redshift z∼3: Overview, *ApJ* **584**(1), 45.

Adrián-Martínez, S. et al. (2016), Constraints on the neutrino emission from the Galactic Ridge with the ANTARES telescope, *Physics Letters B* **760**, 143–148.

Aguirre, A. et al. (2001a), Metal Enrichment of the Intergalactic Medium at z = 3 by Galactic Winds, *ApJ* **560**(2), 599.

Aguirre, A. et al. (2001b), Metal Enrichment of the Intergalactic Medium in Cosmological Simulations, *ApJ* **561**(2), 521.

Aguirre, A. et al. (2004), Metallicity of the Intergalactic Medium Using Pixel Statistics. III. Silicon, *ApJ* **602**, 38–50.

Aguirre, A. et al. (2005), Confronting Cosmological Simulations with Observations of Intergalactic Metals, *ApJ* **620**(1), L13.

Aguirre, A. and Schaye, J. (2007), How Did the IGM become Enriched?, *in* E. Emsellem et al. (eds.), *EAS Publications Series*, Vol. 24, pp.165–175.

Aharonian, F. A. and Atoyan, A. M. (2000), Broad-band diffuse gamma ray emission of the galactic disk, *A&A* **362**, 937–952.

Aharonian, F. et al. (2006), Discovery of very-high-energy γ-rays from the Galactic Centre ridge, *Nature* **439**, 695–698.

Aharonian, F. et al. (2012), Cosmic Rays in Galactic and Extragalactic Magnetic Fields, *Space Sci. Rev.* **166**(1), 97.

Aharonian, F. et al. (2013), *Astrophysics at Very High Energies: Saas-Fee Advanced Course 40. Swiss Society for Astrophysics and Astronomy*, Saas-Fee Advanced Course, Springer Berlin Heidelberg.

Ajiki, M. et al. (2002), A New High-Redshift Lyα Emitter: Possible Superwind Galaxy at z = 5.69, *The Astrophysical Journal Letters* **576**(1), L25.

Alatalo, K. et al. (2016), Shocked POststarburst Galaxy Survey. II. The Molecular Gas Content and Properties of a Subset of SPOGs, *ApJ* **827**, 106.

Albajar, C. et al. (1990), A study of the general characteristics of proton-antiproton collisions at $\sqrt{s}$=0.2 to 0.9 TeV, *Nuclear Physics B* **335**, 261–287.

Albini, E. et al. (1976), Mean charged hadron multiplicities in high-energy collisions, *Nuovo Cimento A Serie* **32**, 101–124.

Alexopoulos, T. et al. (1998), The role of double parton collisions in soft hadron interactions, *Physics Letters B* **435**, 453–457.

Allard, D. et al. (2005), UHE nuclei propagation and the interpretation of the ankle in the cosmic-ray spectrum, *A&A* **443**, L29–L32.

Allard, D., Parizot, E. and Olinto, A. (2007), On the transition from galactic to extragalactic cosmic-rays: Spectral and composition features from two opposite scenarios, *Astroparticle Physics* **27**(1), 61 – 75.

Almeida, S. P. et al. (1968), pp Interactions at 10 GeV/ c, *Phys. Rev.* **174**, 1638.

Alner, G. J. et al. (1984), Scaling violation favouring high multiplicity events at 540 GeV CMS energy, *Physics Letters B* **138**, 304–310.

Alner, G. J. et al. (1985), Multiplicity distributions in different pseudorapidity intervals at a CMS energy of 540 GeV, *Physics Letters B* **160**, 193–198.

Aloisio, R., Berezinsky, V. and Gazizov, A. (2012), Transition from galactic to extragalactic cosmic rays, *Astroparticle Physics* **39**, 129–143.

Alonso, M. S. et al. (2004), Galaxy pairs in the 2dF survey - II. Effects of interactions on star formation in groups and clusters, *MNRAS* **352**, 1081–1088.

Alvarez-Muniz, J., Engel, R. and Stanev, T. (2002), Ultrahigh-Energy Cosmic-Ray Propagation in the Galaxy: Clustering versus Isotropy, *ApJ* **572**(1), 185.

Alves, F. O. et al. (2011), The Magnetic Field in the NGC 2024 FIR 5 Dense Core, *ApJ* **726**(2), 63.

Amenomori, M. et al. (2008), New Estimation of the Spectral Index of High-Energy Cosmic Rays as Determined by the Compton-Getting Anisotropy, *ApJ* **672**(1), L53.

Ansorge, R. E. et al. (1989), Charged Particle Multiplicity Distributions at 200-GeV and 900-GeV Center-Of-Mass Energy, *Z. Phys.* **C43**, 357.

Aoyama, S. et al. (2017), Galaxy simulation with dust formation and destruction, *MNRAS* **466**, 105–121.

Appleton, P. N. et al. (2015), X-Ray Emission from the Taffy (VV254) Galaxies and Bridge, *ApJ* **812**, 118.

Arnison, G. et al. (1983), Charged particle multiplicity distributions in proton-antiproton collisions at 540 GeV centre of mass energy, *Physics Letters B* **123**, 108–114.

Arribas, S. et al. (2014), Ionized gas outflows and global kinematics of low-z luminous star-forming galaxies, *A&A* **568**, A14.

Atoyan, A. M. and Dermer, C. D. (2003), Neutral Beams from Blazar Jets, *ApJ* **586**(1), 79.

Baek, C. H. et al. (2005), Three-dimensional Numerical Simulations of Thermal-Gravitational Instability in the Protogalactic Halo Environment, *ApJ* **630**, 689–704.

Bakes, E. L. O. and Tielens, A. G. G. M. (1994), The photoelectric heating mechanism for very small graphitic grains and polycyclic aromatic hydrocarbons, *ApJ* **427**, 822–838.

Baldini, A. et al. (1987), *Total Cross-Sections for Reactions of High Energy Particles*, Landolt-Börnstein: Numerical Data and Functional Relationships in Science and Technology - New Series / Elementary Particles, Nuclei and Atoms, Springer.

Balsara, D. S. et al. (2004), Amplification of Interstellar Magnetic Fields by Supernova-driven Turbulence, *ApJ* **617**(1), 339.

Balsara, D. S. and Kim, J. (2005), Amplification of Interstellar Magnetic Fields and Turbulent Mixing by Supernova-driven Turbulence. II. The Role of Dynamical Chaos, *ApJ* **634**, 390–406.

Barcos-Muñoz, L. et al. (2018), Fast, Collimated Outflow in the Western Nucleus of Arp 220, *ApJ* **853**, L28.

Barro, G. et al. (2013), CANDELS: The Progenitors of Compact Quiescent Galaxies at z ˜ 2, *ApJ* **765**, 104.

Barro, G. et al. (2014), CANDELS+3D-HST: Compact SFGs at z ~2-3, the Progenitors of the First Quiescent Galaxies, *ApJ* **791**(1), 52.

Bartos, I. and Marka, S. (2015), Spectral Decline of PeV Neutrinos from Starburst Galaxies, *ArXiv e-prints* .

Bastian, N., Covey, K. R. and Meyer, M. R. (2010), A Universal Stellar Initial Mass Function? A Critical Look at Variations, *ARA&A* **48**(1), 339.

Beall, J. H. and Bednarek, W. (2002), Neutrinos from Early-Phase, Pulsar-driven Supernovae, *ApJ* **569**, 343–348.

Beck, A. M. et al. (2012), Origin of strong magnetic fields in Milky Way-like galactic haloes, *MNRAS* **422**, 2152–2163.

Beck, A. M. et al. (2013), On the magnetic fields in voids, *MNRAS* **429**, L60–L64.

Beck, R. et al. (2005), Magnetic fields in barred galaxies - IV. NGC 1097 and NGC 1365, *A&A* **444**(3), 739.

Beck, R. and Wielebinski, R. (2013), *Magnetic Fields in Galaxies*, Springer: Dordrecht, p.641.

Becker, J. K. (2008), High-energy neutrinos in the context of multimessenger astrophysics, *Phys. Rep.* **458**, 173–246.

Beech, M. (2011), Since When Was the Sun a Typical Star?, *JRASC* **105**, 232.

Begelman, M. C. (1995), Cosmic Ray Heating of the Interstellar Gas, *in* A. Ferrara et al. (eds.), *The Physics of the Interstellar Medium and Intergalactic Medium*, Vol. 80 of *Astronomical Society of the Pacific Conference Series*, p.545.

Behroozi, P. S. and Silk, J. (2015), A Simple Technique for Predicting High-redshift Galaxy Evolution, *ApJ* **799**, 32.

Bekki, K. and Meurer, G. R. (2013), Evolution of the High-mass End of the Stellar Initial Mass Functions in Starburst Galaxies, *ApJ* **765**(1), L22.

Bell, A. R. (1978), The acceleration of cosmic rays in shock fronts. I, *MNRAS* **182**, 147–156.

Bell, A. R. (2013), Cosmic ray acceleration, *Astroparticle Physics* **43**, 56–70.

Bell, A. R. et al. (2013), Cosmic-ray acceleration and escape from supernova remnants, *MNRAS* **431**(1), 415–429.

Benhabiles-Mezhoud, H. et al. (2013), De-excitation Nuclear Gamma-Ray Line Emission from Low-energy Cosmic Rays in the Inner Galaxy, *ApJ* **763**, 98.

Benítez, N. et al. (2002), Observing z > 4 Galaxies Through a Cosmic Lens, *in* M. Gilfanov, R. Sunyeav and E. Churazov (eds.), *Lighthouses of the Universe: The Most Luminous Celestial Objects and Their Use for Cosmology*, p.239.

Benson, A. J. and Bower, R. (2011), Accretion shocks and cold filaments in galaxy formation, *MNRAS* **410**, 2653–2661.

Berezinskii, V., Gazizov, A. and Grigorieva, S. (2006), On astrophysical solution to ultrahigh energy cosmic rays, *Phys. Rev. D* **74**, 043005.

Berezinskii, V. S. et al. (1990), *Astrophysics of cosmic rays*, Amsterdam: North-Holland.

Berezinskii, V. S. and Gazizov, A. Z. (1993), Production of high-energy cosmic neutrinos in $p\gamma$ and $n\gamma$ scattering. I. Neutrino yields for power-law spectra of protons and neutrons, *Phys. Rev. D* **47**, 4206.

Berezinskii, V. S. and Grigor'eva, S. I. (1988), A bump in the ultra-high energy cosmic ray spectrum, *A&A* **199**, 1.

Bergin, E. A. and Tafalla, M. (2007), Cold Dark Clouds: The Initial Conditions for Star Formation, *ARA&A* **45**, 339.

Bernet, M. L. et al. (2008), Strong magnetic fields in normal galaxies at high redshift, *Nature* **454**, 302.

Bertone, S., Stoehr, F. and White, S. D. M. (2005), Semi-analytic simulations of galactic winds: volume filling factor, ejection of metals and parameter study, *MNRAS* **359**(4), 1201.

Bertone, S., Vogt, C. and Enβlin, T. (2006), Magnetic field seeding by galactic winds, *MNRAS* **370**(1), 319.

Bethe, H. A. and Maximon, L. C. (1954), Theory of Bremsstrahlung and Pair Production. I. Differential Cross Section, *Physical Review* **93**, 768.

Bethe, H. and Heitler, W. (1934), On the Stopping of Fast Particles and on the Creation of Positive Electrons, *Proc. R. Soc. A* **146**(856), 83.

Bianchi, S. and Schneider, R. (2007), Dust formation and survival in supernova ejecta, *MNRAS* **378**, 973–982.

Biermann, L. (1950), Über den Ursprung der Magnetfelder auf Sternen und im interstellaren Raum (miteinem Anhang von A. Schlüter), *Zeitschrift Naturforschung Teil A* **5**, 65.

Biffi, V. et al. (2016), On the Nature of Hydrostatic Equilibrium in Galaxy Clusters, *ApJ* **827**, 112.

Binney, J. and Tremaine, S. (2008), *Galactic Dynamics: Second Edition*, Princeton University Press.

Bird, D. J. et al. (1993), Evidence for correlated changes in the spectrum and composition of cosmic rays at extremely high energies, *Physical Review Letters* **71**, 3401–3404.

Birnboim, Y. and Dekel, A. (2003), Virial shocks in galactic haloes?, *MNRAS* **345**, 349–364.

Bland-Hawthorn, J., Veilleux, S. and Cecil, G. (2007), Galactic winds: a short review, *Ap&SS* **311**(1), 87–98.

Blasi, P. (2014), Origin of very high- and ultra-high-energy cosmic rays, *Comptes Rendus Physique* **15**, 329–338.

Blattnig, S. R. et al. (2000), Parametrizations of inclusive cross sections for pion production in proton-proton collisions, *Phys. Rev. D* **62**(9), 094030.

Blumenthal, G. R. (1970), Energy Loss of High-Energy Cosmic Rays in Pair-Producing Collisions with Ambient Photons, *Phys. Rev. D* **1**, 1596.

Bocchio, M. et al. (2016), Dust grains from the heart of supernovae, *A&A* **587**, A157.

Bolatto, A. D. et al. (2013), Suppression of star formation in the galaxy NGC 253 by a starburst-driven molecular wind, *Nature* **499**, 450.

Booth, C. M. et al. (2012), The filling factor of intergalactic metals at redshift z=3, *MNRAS* **420**, 1053–1060.

Bordoloi, R. et al. (2011), The Radial and Azimuthal Profiles of Mg II Absorption around 0.5 < z < 0.9 zCOSMOS Galaxies of Different Colors, Masses, and Environments, *ApJ* **743**(1), 10.

Bordoloi, R. et al. (2016), Spatially resolved galactic wind in lensed galaxy RCSGA 032727-132609, *MNRAS* **458**(2), 1891.

Borsellino, A. (1947), Sulle coppie di elettroni create da raggi γ in presenza di elettroni, *Il Nuovo Cimento (1943-1954)* **4**(3), 112–130.

Boselli, A. and Gavazzi, G. (2006), Environmental Effects on Late-Type Galaxies in Nearby Clusters, *PASP* **118**, 517–559.

Bothwell, M. S. et al. (2013), A fundamental relation between the metallicity, gas content and stellar mass of local galaxies, *MNRAS* **433**, 1425–1435.

Bouché, N. et al. (2013), Signatures of Cool Gas Fueling a Star-Forming Galaxy at Redshift 2.3, *Science* **341**, 50–53.

Bouché, N. et al. (2016), Possible Signatures of a Cold-flow Disk from MUSE Using a z∼1 Galaxy-Quasar Pair toward SDSS J1422-0001, *ApJ* **820**, 121.

Bouwens, R. J. et al. (2004), Galaxies at z∼7-8: z_{850}-Dropouts in the Hubble Ultra Deep Field, *ApJ* **616**, L79–L82.

Bouwens, R. J. et al. (2016), ALMA Spectroscopic Survey in the Hubble Ultra Deep Field: The Infrared Excess of UV-Selected z = 2-10 Galaxies as a Function of UV-Continuum Slope and Stellar Mass, *ApJ* **833**, 72.

Bouwens, R. J. and Illingworth, G. D. (2006), Rapid evolution of the most luminous galaxies during the first 900 million years, *Nature* **443**, 189–192.

Bradamante, F., Matteucci, F. and D'Ercole, A. (1998), The influence of stellar energetics and dark matter on the chemical evolution of dwarf irregulars, *A&A* **337**, 338.

Bradley, L. D. et al. (2008), Discovery of a Very Bright Strongly Lensed Galaxy Candidate at z ≃ 7.6, *ApJ* **678**, 647–654.

Braginskii, S. I. (1965), Transport Processes in a Plasma, *Reviews of Plasma Physics* **1**, 205.

Branch, D. (2010), Supernovae: New explosions of old stars?, *Nature* **465**(7296), 303.

Brandenburg, A. et al. (1993), Vertical Magnetic Fields above the Discs of Spiral Galaxies, *A&A* **271**, 36.

Breakstone, A. et al. (1984), Charged multiplicity distribution in pp interactions at CERN ISR energies, *Phys. Rev. D* **30**, 528–535.

Breitschwerdt, D., McKenzie, J. F. and Voelk, H. J. (1991), Galactic winds. I - Cosmic ray and wave-driven winds from the Galaxy, *A&A* **245**, 79–98.

Breitschwerdt, D., McKenzie, J. F. and Voelk, H. J. (1993), Galactic winds. II - Role of the disk-halo interface in cosmic ray driven galactic winds, *A&A* **269**, 54–66.

Breitschwerdt, D., McKenzie, J. F. and Volk, H. J. (1987), Cosmic Ray and Wave Driven Galactic Wind Solutions, *International Cosmic Ray Conference* **2**, 115.

Bromm, V., Coppi, P. S. and Larson, R. B. (2002), The Formation of the First Stars. I. The Primordial Star-forming Cloud, *ApJ* **564**(1), 23.

Bruce, V. A. et al. (2014), The bulge-disc decomposed evolution of massive galaxies at 1 < z < 3 in CANDELS, *MNRAS* **444**, 1001–1033.

Brunetti, G. and Jones, T. W. (2014), Cosmic Rays in Galaxy Clusters and Their Nonthermal Emission, *IJMPD* **23**(04), 1430007.

Burgers, J. (1948), A Mathematical Model Illustrating the Theory of Turbulence, Vol. 1 of *Advances in Applied Mechanics*, Elsevier, pp.171–199.

Burton, M. G., Hollenbach, D. J. and Tielens, A. G. G. M. (1990), Line emission from clumpy photodissociation regions, *ApJ* **365**, 620–639.

Bustard, C., Zweibel, E. G. and D'Onghia, E. (2016), A Versatile Family of Galactic Wind Models, *ApJ* **819**, 29.

Butsky, I. and Quinn, T. R. (2018), The Role of Cosmic Ray Transport in Shaping the Simulated Circumgalactic Medium, *ArXiv e-prints* .

Bykov, A. M., Paerels, F. B. S. and Petrosian, V. (2008), Equilibration Processes in the Warm-Hot Intergalactic Medium, *Space Sci. Rev.* **134**, 141–153.

Capak, P. L. et al. (2015), Galaxies at redshifts 5 to 6 with systematically low dust content and high [C II] emission, *Nature* **522**, 455–458.

Caprioli, D. (2012), Cosmic-ray acceleration in supernova remnants: non-linear theory revised, *J. Cosmology Astropart. Phys.* **7**, 038.

Cecil, G., Bland-Hawthorn, J. and Veilleux, S. (2002a), Tightly Correlated X-Ray/Hα-emitting Filaments in the Superbubble and Large-Scale Superwind of NGC 3079, *ApJ* **576**(2), 745.

Cecil, G. et al. (2001), Jet- and Wind-driven Ionized Outflows in the Superbubble and Star-forming Disk of NGC 3079, *ApJ* **555**, 338–355.

Cecil, G., Ferruit, P. and Veilleux, S. (2002b), Bubbles, Bow-Shocks, and Bullets over Broadlines: Three Ionized Outflows Resolved with HST, *Revista Mexicana de Astronomia y Astrofisica Conference Series* **13**, 170.

Cen, R. (2010), The State of Star Formation and the Intergalactic Medium at z∼6, *ApJ* **725**(1), 115.

Ceverino, D., Dekel, A. and Bournaud, F. (2010), High-redshift clumpy discs and bulges in cosmological simulations, *MNRAS* **404**, 2151–2169.

Chabrier, G., Hennebelle, P. and Charlot, S. (2014), Variations of the Stellar Initial Mass Function in the Progenitors of Massive Early-type Galaxies and in Extreme Starburst Environments, *ApJ* **796**(2), 75.

Chen, J., Bryan, G. L. and Salem, M. (2016), Cosmological Simulations of Dwarf Galaxies with Cosmic Ray Feedback, *MNRAS* **460**(3), 3335.

Chen, W. P. et al. (2012), Magnetic Field Structure in Molecular Clouds by Polarization Measurements, *Proceedings of the International Astronomical Union* **10**(H16), 390.

Chevalier, R. A. and Clegg, A. W. (1985), Wind from a starburst galaxy nucleus, *Nature* **317**(6032), 44.

Ching, T.-C. et al. (2017), Magnetic Fields in the Massive Dense Cores of the DR21 Filament: Weakly Magnetized Cores in a Strongly Magnetized Filament, *ApJ* **838**(2), 121.

Christiansen, H. R., Orellana, M. and Romero, G. E. (2006), High-energy neutrino emission from X-ray binaries, *Phys. Rev. D* **73**(6), 063012.

Chyży, K. T. et al. (2006), Large-scale magnetized outflows from the Virgo Cluster spiral NGC 4569. A galactic wind in a ram pressure wind, *A&A* **447**, 465–472.

Clark, P. C. et al. (2011), The Formation and Fragmentation of Disks Around Primordial Protostars, *Science* **331**, 1040.

Coc, A. (2016), Primordial Nucleosynthesis, *in Journal of Physics Conference Series*, Vol. 665 of *Journal of Physics Conference Series*, p.012001.

Cole, S. et al. (1994), A recipe for galaxy formation., *MNRAS* **271**, 781–806.

Combes, F. (2013), Dark matter distribution and its impact on the evolution of galaxy disks , *Memorie della Societa Astronomica Italiana Supplementi* **25**, 45.

Compiégne, M. (2010), Interstellar Dust, *in* R. Kothes, T. L. Landecker and A. G. Willis (eds.), *The Dynamic Interstellar Medium: A Celebration of the Canadian Galactic Plane Survey*, Vol. 438 of *Astronomical Society of the Pacific Conference Series*, p.55.

Condon, J. J. (1992), Radio emission from normal galaxies, *ARA&A* **30**, 575–611.

Cooper, J. L. et al. (2008), Three-Dimensional Simulations of a Starburst-driven Galactic Wind, *ApJ* **674**, 157–171.

Cornuault, N. et al. (2018), Are cosmological gas accretion streams multiphase and turbulent?, *A&A* **610**, A75.

Côté, B., Martel, H. and Drissen, L. (2015), Cosmological Simulations of the Intergalactic Medium Evolution. II. Galaxy Model and Feedback, *ApJ* **802**, 123.

Couch, W. J. and Sharples, R. M. (1987), A spectroscopic study of three rich galaxy clusters at z = 0.31, *MNRAS* **229**, 423–456.

Crain, R. A. et al. (2015), The EAGLE simulations of galaxy formation: calibration of subgrid physics and model variations, *MNRAS* **450**, 1937–1961.

Crighton, N. H. M., Hennawi, J. F. and Prochaska, J. X. (2013), Metal-poor, Cool Gas in the Circumgalactic Medium of a z = 2.4 Star-forming Galaxy: Direct Evidence for Cold Accretion?, *ApJ* **776**, L18.

Cruddace, R. et al. (1974), On the opacity of the interstellar medium to ultrasoft X-rays and extreme-ultraviolet radiation., *ApJ* **187**, 497.

Crutcher, R. M. et al. (2010), Magnetic Fields in Interstellar Clouds from Zeeman Observations: Inference of Total Field Strengths by Bayesian Analysis, *ApJ* **725**(1), 466.

Danovich, M. et al. (2015), Four phases of angular-momentum buildup in high-z galaxies: from cosmic-web streams through an extended ring to disc and bulge, *MNRAS* **449**, 2087–2111.

Dar, A. and de Rújula, A. (2008), A theory of cosmic rays, *Phys. Rep.* **466**, 179.

Davé, R. (2008), The galaxy stellar mass-star formation rate relation: evidence for an evolving stellar initial mass function?, *MNRAS* **385**, 147.

Davé, R. et al. (1998), Constraining the Metallicity of the Low-Density Lyα Forest Using O VI Absorption, *ApJ* **509**, 661–677.

Dayal, P. and Ferrara, A. (2018), Early galaxy formation and its large-scale effects, *Phys. Rep.* **780**, 1–64.

de Cea del Pozo, E., Torres, D. F. and Rodriguez Marrero, A. Y. (2009), Multimessenger Model for the Starburst Galaxy M82, *ApJ* **698**, 1054–1060.

De Young, D. S. (1992), Galaxy-driven turbulence and the growth of intracluster magnetic fields, *ApJ* **386**, 464–472.

Dehnen, W. (1993), A family of potentialdensity pairs for spherical galaxies and bulges, *MNRAS* **265**(1), 250.

Dekel, A. et al. (2009a), Cold streams in early massive hot haloes as the main mode of galaxy formation, *Nature* **457**, 451–454.

Dekel, A. and Birnboim, Y. (2006), Galaxy bimodality due to cold flows and shock heating, *MNRAS* **368**, 2–20.

Dekel, A. and Silk, J. (1986), The origin of dwarf galaxies, cold dark matter, and biased galaxy formation, *ApJ* **303**, 39–55.

Dekel, A., Sari, R. and Ceverino, D. (2009b), Formation of Massive Galaxies at High Redshift: Cold Streams, Clumpy Disks, and Compact Spheroids, *ApJ* **703**, 785–801.

Dermer, C. D. and Menon, G. (2009), *High energy radiation from black holes: gamma rays, cosmic rays, and neutrinos*, Princeton series in astrophysics, Princeton University Press, Princeton, NJ.

Dermer, C. D. and Powale, G. (2013), Gamma rays from cosmic rays in supernova remnants, *A&A* **553**, A34.

Dermer, C. D. and Schlickeiser, R. (1991), Effects of triplet pair production on ultrarelativistic electrons in a soft photon field, *A&A* **252**, 414.

Díaz-Rodríguez, M. et al. (2018), Progenitor Mass Distribution for Core-collapse Supernova Remnants in M31 and M33, *ApJ* **861**, 92.

Dib, S. et al. (2011), Star formation efficiency as a function of metallicity: from star clusters to galaxies, *MNRAS* **415**, 3439–3454.

Diehl, R. et al. (2006), Radioactive ^{26}Al from massive stars in the Galaxy, *Nature* **439**, 45.

Dijkstra, M., Haiman, Z. and Spaans, M. (2006), Lyα Radiation from Collapsing Protogalaxies. II. Observational Evidence for Gas Infall, *ApJ* **649**, 37–47.

Dijkstra, M. and Loeb, A. (2008), Lyα-driven outflows around star-forming galaxies, *MNRAS* **391**, 457–466.

Dijkstra, M. and Loeb, A. (2009), Lyα blobs as an observational signature of cold accretion streams into galaxies, *MNRAS* **400**, 1109–1120.

Dolag, K., Bartelmann, M. and Lesch, H. (1999), SPH simulations of magnetic fields in galaxy clusters, *A&A* **348**, 351.

Dolag, K., Bartelmann, M. and Lesch, H. (2002), Evolution and structure of magnetic fields in simulated galaxy clusters, *A&A* **387**(2), 383.

Domingo-Santamaría, E. and Torres, D. F. (2005), High energy γ-ray emission from the starburst nucleus of NGC 253, *A&A* **444**, 403–415.

Dragicevich, P. M., Blair, D. G. and Burman, R. R. (1999), Why are supernovae in our Galaxy so frequent?, *MNRAS* **302**, 693–699.

Draine, B. T. (1978), Photoelectric heating of interstellar gas, *ApJS* **36**, 595–619.

Draine, B. T. (2011), *Physics of the Interstellar and Intergalactic Medium*, Princeton University Press.

Dressler, A. and Gunn, J. E. (1983), Spectroscopy of galaxies in distant clusters. II - The population of the 3C 295 cluster, *ApJ* **270**, 7–19.

Durrer, R. and Neronov, A. (2013), Cosmological magnetic fields: their generation, evolution and observation, *A&A Rev.* **21**, 62.

Efstathiou, G. (2000), A model of supernova feedback in galaxy formation, *MNRAS* **317**, 697–719.

Ellison, S. L. et al. (2000), The Enrichment History of the Intergalactic Medium-Measuring the C IV/H I Ratio in the Lyα Forest, *AJ* **120**, 1175–1191.

Elmegreen, D. M. et al. (2009), Clumpy Galaxies in Goods and Gems: Massive Analogs of Local Dwarf Irregulars, *ApJ* **701**, 306–329.

Enßlin, T. A. et al. (2007), Cosmic ray physics in calculations of cosmological structure formation, *A&A* **473**, 41–57.

Epinat, B. et al. (2009), Integral field spectroscopy with SINFONI of VVDS galaxies. I. Galaxy dynamics and mass assembly at $1.2 < z < 1.6$, *A&A* **504**, 789–805.

Everett, J. E. et al. (2008), The Milky Way's Kiloparsec-Scale Wind: A Hybrid Cosmic-Ray and Thermally Driven Outflow, *ApJ* **674**, 258–270.

Falgarone, E. et al. (2017), Large turbulent reservoirs of cold molecular gas around high-redshift starburst galaxies, *Nature* **548**, 430–433.

Farber, R. et al. (2018), Impact of Cosmic-Ray Transport on Galactic Winds, *ApJ* **856**, 112.

Faucher-Giguère, C.-A. et al. (2010), Lyα Cooling Emission from Galaxy Formation, *ApJ* **725**, 633–657.

Faucher-Giguère, C.-A. and Kereš, D. (2011), The small covering factor of cold accretion streams, *MNRAS* **412**, L118–L122.

Fazzini, T. et al. (1958), Electron Decay of the Pion, *Phys. Rev. Lett.* **1**, 247–249.

Federrath, C. et al. (2011), Mach Number Dependence of Turbulent Magnetic Field Amplification: Solenoidal versus Compressive Flows, *Phys. Rev. Lett.* **107**, 114504.

Fenech, D. et al. (2010), Wide-field Global VLBI and MERLIN combined monitoring of supernova remnants in M82, *MNRAS* **408**, 607.

Fensch, J. et al. (2017), High-redshift major mergers weakly enhance star formation, *MNRAS* **465**, 1934–1949.

Ferguson, H. C. et al. (2004), The Size Evolution of High-Redshift Galaxies, *ApJ* **600**, L107–L110.

Ferland, G. J. (2009), Magnetic fields, stellar feedback, and the geometry of H II regions, *in* K. G. Strassmeier, A. G. Kosovichev and J. E. Beckman (eds.), *Cosmic Magnetic Fields: From Planets, to Stars and Galaxies*, Vol. 259 of *IAU Symposium*, p.25.

Fermi, E. (1949), On the Origin of the Cosmic Radiation, *Phys. Rev.* **75**, 1169.

Ferrara, A., Pettini, M. and Shchekinov, Y. (2000), Mixing metals in the early Universe, *MNRAS* **319**, 539–548.

Ferrara, A., Viti, S. and Ceccarelli, C. (2016), The problematic growth of dust in high-redshift galaxies, *MNRAS* **463**, L112–L116.

Ferré-Mateu, A. et al. (2017), Two new confirmed massive relic galaxies: red nuggets in the present-day Universe, *MNRAS* **467**, 1929–1939.

Ferriere, K. M. (2001), The interstellar environment of our galaxy, *Rev. Mod. Phys.* **73**, 1031.

Fields, B. D. et al. (2001), Standard cosmic ray energetics and light element production, *A&A* **370**, 623–634.

Fiete Grosse-Oetringhaus, J. and Reygers, K. (2010), Topical Review: Charged-particle multiplicity in proton-proton collisions, *Journal of Physics G Nuclear Physics* **37**(8), 083001.

Filippenko, A. V. and Sargent, W. L. W. (1992), The kinematics of a violent outflow from the nucleus of the SC galaxy NGC 3079, *AJ* **103**, 28–40.

Fletcher, A. et al. (2011), Magnetic fields and spiral arms in the galaxy M51, *MNRAS* **412**(4), 2396.

Fontaine, G., Brassard, P. and Bergeron, P. (2001), The Potential of White Dwarf Cosmochronology, *PASP* **113**, 409–435.

Forbes, J. C. et al. (2014), On the origin of the fundamental metallicity relation and the scatter in galaxy scaling relations, *MNRAS* **443**, 168–185.

Ford, A. B. et al. (2014), Tracing inflows and outflows with absorption lines in circumgalactic gas, *MNRAS* **444**, 1260–1281.

Förster Schreiber, N. M. et al. (2009), The SINS Survey: SINFONI Integral Field Spectroscopy of z∼2 Star-forming Galaxies, *ApJ* **706**, 1364–1428.

Förster Schreiber, N. M. et al. (2011), Constraints on the Assembly and Dynamics of Galaxies. II. Properties of Kiloparsec-scale Clumps in Rest-frame Optical Emission of z∼2 Star-forming Galaxies, *ApJ* **739**, 45.

French, K. D. et al. (2015), Discovery of Large Molecular Gas Reservoirs in Post-starburst Galaxies, *ApJ* **801**, 1.

French, K. D. et al. (2018), Why Post-starburst Galaxies Are Now Quiescent, *ApJ* **861**, 123.

Frye, B., Broadhurst, T. and Benitez, N. (2002), Spectral Evidence for Widespread Galaxy Outflows at z<4, *ApJ* **568**(2), 558.

Fryer, C. L. (1999), Mass Limits For Black Hole Formation, *ApJ* **522**, 413–418.

Fuente, A. et al. (2008), On the chemistry and distribution of HOC^+ in M 82. More evidence for extensive PDRs, *A&A* **492**, 675–684.

Fumagalli, M. et al. (2011), Absorption-line systems in simulated galaxies fed by cold streams, *MNRAS* **418**, 1796–1821.

Furlanetto, S. R. and Loeb, A. (2003), Metal Absorption Lines as Probes of the Intergalactic Medium Prior to the Reionization Epoch, *ApJ* **588**, 18–34.

Gaggero, D. (2012), *Cosmic Ray Diffusion in the Galaxy and Diffuse Gamma Emission*, Springer Theses, Springer: Berlin.

Gaggero, D. et al. (2017), Diffuse Cosmic Rays Shining in the Galactic Center: A Novel Interpretation of H.E.S.S. and Fermi-LAT γ-Ray Data, *Physical Review Letters* **119**(3), 031101.

Gaisser, T. K. (2007), Cosmic Rays at the Knee, *in* K. Sato and J. Hisano (eds.), *Energy Budget in the High Energy Universe*, pp.45–55.

Gaisser, T. K., Halzen, F. and Stanev, T. (1995), Particle astrophysics with high energy neutrinos, *Phys. Rep.* **258**, 173–236.

Gall, C., Hjorth, J. and Andersen, A. C. (2011), Production of dust by massive stars at high redshift, *ARA&A* **19**, 43.

Gao, J. et al. (2015), Physical Dust Models for the Extinction toward Supernova 2014J in M82, *ApJ* **807**, L26.

Gargiulo, I. D. et al. (2015), Chemoarchaeological downsizing in a hierarchical universe: impact of a top-heavy IGIMF, *MNRAS* **446**(4), 3820.

Genel, S., Dekel, A. and Cacciato, M. (2012), On the effect of cosmological inflow on turbulence and instability in galactic discs, *MNRAS* **425**, 788–800.

Giammanco, C. and Beckman, J. E. (2005), Temperature fluctuations in H II regions: Ionization by cosmic rays as a key mechanism, *A&A* **437**, L11.

Ginolfi, M. et al. (2018), Where does galactic dust come from?, *MNRAS* **473**, 4538–4543.

Ginzburg, V. L. and Syrovatskii, S. I. (1963), Cosmic Rays in Metagalactic Space, *Soviet Ast.* **7**, 357.

Girichidis, P. et al. (2018), Cooler and smoother - the impact of cosmic rays on the phase structure of galactic outflows, *MNRAS* **479**, 3042–3067.

Glover, S. C. O. and Clark, P. C. (2012), Is molecular gas necessary for star formation?, *MNRAS* **421**, 9–19.

Gnerucci, A. et al. (2011), A dynamical mass estimator for high z galaxies based on spectroastrometry, *A&A* **533**, A124.

Goerdt, T. et al. (2010), Gravity-driven Lyα blobs from cold streams into galaxies, *MNRAS* **407**, 613–631.

Goerdt, T. et al. (2012), Detectability of cold streams into high-redshift galaxies by absorption lines, *MNRAS* **424**, 2292–2315.

Goerdt, T. et al. (2015), Distribution of streaming rates into high-redshift galaxies, *MNRAS* **454**, 637–648.

Goerdt, T. and Ceverino, D. (2015), Inflow velocities of cold flows streaming into massive galaxies at high redshifts, *MNRAS* **450**, 3359–3370.

Goldshmidt, O. and Rephaeli, Y. (1993), Turbulent generation of intracluster magnetic fields and Faraday rotation measurements, *ApJ* **411**, 518.

González-López, J. et al. (2014), Search for [C II] Emission in z = 6.5-11 Star-forming Galaxies, *ApJ* **784**, 99.

González, V. et al. (2010), The Stellar Mass Density and Specific Star Formation Rate of the Universe at z∼7, *ApJ* **713**, 115–130.

Gould, R. J. (1975), Energy loss of relativistic electrons and positrons traversing cosmic matter, *ApJ* **196**, 689.

Gould, R. J. and Burbidge, G. R. (1965), High energy cosmic photons, *Annales d'Astrophysique* **28**, 171.

Grazian, A. et al. (2012), The size-luminosity relation at z = 7 in CANDELS and its implication on reionization, *A&A* **547**, A51.

Greisen, K. (1966), End to the Cosmic-Ray Spectrum?, *Phys. Rev. Lett.* **16**, 748.

Guo, F. and Oh, S. P. (2008), Feedback heating by cosmic rays in clusters of galaxies, *MNRAS* **384**(1), 251.

Hakobyan, A. A. et al. (2011), Five supernova survey galaxies in the southern hemisphere. II. The supernova rates, *Astrophysics* **54**, 301.

Hakobyan, A. A. et al. (2012), Supernovae and their host galaxies. I. The SDSS DR8 database and statistics, *A&A* **544**, A81.

Hakobyan, A. A. et al. (2014), Supernovae and their host galaxies - II. The relative frequencies of supernovae types in spirals, *MNRAS* **444**, 2428–2441.

Hakobyan, A. A. et al. (2016), Supernovae and their host galaxies - III. The impact of bars and bulges on the radial distribution of supernovae in disc galaxies, *MNRAS* **456**, 2848–2860.

Hammond, A. M., Robishaw, T. and Gaensler, B. M. (2012), A New Catalog of Faraday Rotation Measures and Redshifts for Extragalactic Radio Sources, *ArXiv e-prints* .

Hanawa, T. and Tomisaka, K. (2015), Structure and Stability of Filamentary Clouds Supported by Lateral Magnetic Field, *ApJ* **801**(1), 11.

Hanawa, T. and Tomisakar, K. (2015), Structure and Stability of Filamentary Clouds Supported by Lateral Magnetic Field, *Proceedings of the International Astronomical Union* **11**(S315).

Harayama, Y., Eisenhauer, F. and Martins, F. (2008), The Initial Mass Function of the Massive Star-forming Region NGC 3603 from Near-Infrared Adaptive Optics Observations, *ApJ* **675**(2), 1319.

Hashimoto, T. et al. (2018), The onset of star formation 250 million years after the Big Bang, *Nature* **557**(7705), 392–395.

Haug, E. (1981), Simple Analytic Expressions for the Total Cross Section for y-e Pair Production, *Z. Naturforsch* **36**, 413–414.

Hayward, C. C. et al. (2013), Submillimetre galaxies in a hierarchical universe: number counts, redshift distribution and implications for the IMF, *MNRAS* **428**(3), 2529.

Heckman, T. M., Armus, L. and Miley, G. K. (1990), On the nature and implications of starburst-driven galactic superwinds, *ApJS* **74**, 833.

Heckman, T. M. and Thompson, T. A. (2017), A Brief Review of Galactic Winds, *ArXiv e-prints* .

Heesen, V. et al. (2007), The radio halo of the nearby starburst galaxy NGC253, *Astronomische Nachrichten* **328**, 637.

Heesen, V. et al. (2016), Advective and diffusive cosmic ray transport in galactic haloes, *MNRAS* **458**(1), 332.

Heger, A. et al. (2003), How Massive Single Stars End Their Life, *ApJ* **591**, 288–300.

Hennebelle, P. (2012), Formation of proto-clusters and star formation within clusters: apparent universality of the initial mass function?, *A&A* **545**, A147.

H.E.S.S. Collaboration (2018), Characterising the VHE diffuse emission in the central 200 parsecs of our Galaxy with H.E.S.S., *A&A* **612**, A9.

Hillas, A. M. (1984), The Origin of Ultra-High-Energy Cosmic Rays, *ARA&A* **22**, 425–444.

Hirashita, H., Buat, V. and Inoue, A. K. (2003), Star formation rate in galaxies from UV, IR, and Hα estimators, *A&A* **410**, 83–100.

Hirschmann, M. et al. (2012), Galaxy formation in semi-analytic models and cosmological hydrodynamic zoom simulations, *MNRAS* **419**, 3200–3222.

Howard, A. M. and Kulsrud, R. M. (1997), The Evolution of a Primordial Galactic Magnetic Field, *ApJ* **483**(2), 648.

Hu, C.-Y. et al. (2017), Variable interstellar radiation fields in simulated dwarf galaxies: supernovae versus photoelectric heating, *MNRAS* **471**, 2151–2173.

Hull, C. L. H. et al. (2017), Unveiling the Role of the Magnetic Field at the Smallest Scales of Star Formation, *ApJ* **842**(2), L9.

Hummel, E., Beck, R. and Dahlem, M. (1991), The magnetic field structure in the radio halos of NGC 891 and NGC 4631, *A&A* **248**, 23–29.

Hummel, E. et al. (1988), The radio halo of NGC 4631: Ordered magnetic fields far above the plane, *A&A* **197**, L29–L31.

Hussein, M. and Shalchi, A. (2014), Parallel and perpendicular diffusion coefficients of energetic particles interacting with shear Alfvén waves, *MNRAS* **444**, 2676–2684.

Hutton, S., Ferreras, I. and Yershov, V. (2015), Variations of the dust properties of M82 with galactocentric distance, *MNRAS* **452**, 1412–1420.

Inoue, A. K. et al. (2016), Detection of an oxygen emission line from a high-redshift galaxy in the reionization epoch, *Science* **352**, 1559–1562.

Ipavich, F. M. (1975), Galactic winds driven by cosmic rays, *ApJ* **196**, 107–120.

Irwin, J. A. and Saikia, D. J. (2003), Giant Metrewave Radio Telescope observations of NGC 3079, *MNRAS* **346**, 977–986.

Irwin, J. A. and Seaquist, E. R. (1988), Nuclear jets in the radio lobe spiral galaxy, NGC 3079, *ApJ* **335**, 658–667.

Iwamoto, K. and Kunugise, T. (2006), Neutrino Emission from Type Ia Supernovae, *AIP Conference Proceedings* **847**(1), 406.

Jacob, S. et al. (2018), The dependence of cosmic ray-driven galactic winds on halo mass, *MNRAS* **475**, 570–584.

Jacobsen, I. B. (2015), personal communication.

Jacobsen, I. B. et al. (2015), High-energy neutrino fluxes from AGN populations inferred from X-ray surveys, *MNRAS* **451**(4), 3649.

Janka, H.-T. (2012), Explosion Mechanisms of Core-Collapse Supernovae, *Annual Review of Nuclear and Particle Science* **62**, 407.

Jennings, Z. G. et al. (2014), The Supernova Progenitor Mass Distributions of M31 and M33: Further Evidence for an Upper Mass Limit, *ApJ* **795**, 170.

Jermyn, A. S., Steinhardt, C. L. and Tout, C. A. (2018), The cosmic microwave background and the stellar initial mass function, *MNRAS* **480**, 4265–4272.

Jing, Y. P. (2000), The Density Profile of Equilibrium and Nonequilibrium Dark Matter Halos, *ApJ* **535**, 30–36.

Jokipii, J. R. (1966), Cosmic-Ray Propagation. I. Charged Particles in a Random Magnetic Field, *ApJ* **146**, 480.

Joseph, J. and Rohrlich, F. (1958), Pair Production and Bremsstrahlung in the Field of Free and Bound Electrons, *Rev. Mod. Phys.* **30**, 354–368.

Joseph, R. D. and Wright, G. S. (1985), Recent star formation in interacting galaxies. II - Super starburst in merging galaxies, *MNRAS* **214**, 87–95.

Jost, R., Luttinger, J. M. and Slotnick, M. (1950), Distribution of Recoil Nucleus in Pair Production by Photons, *Phys. Rev.* **80**, 189.

Kacprzak, G. G. et al. (2010), Halo Gas and Galaxy Disk Kinematics Derived from Observations and ΛCDM Simulations of Mg II Absorption-selected Galaxies at Intermediate Redshift, *ApJ* **711**, 533–558.

Kacprzak, G. G. et al. (2012), Discovery of multiphase cold accretion in a massive galaxy at z = 0.7, *MNRAS* **427**, 3029–3043.

Kacprzak, G. G. et al. (2016), Cold-mode Accretion: Driving the Fundamental Mass-Metallicity Relation at z ~ 2, *ApJ* **826**, L11.

Kafexhiu, E. et al. (2014), Parametrization of gamma-ray production cross sections for p p interactions in a broad proton energy range from the kinematic threshold to PeV energies, *Phys. Rev. D* **90**(12), 123014.

Kamae, T. et al. (2006), Parameterization of γ, e^{pm}, and Neutrino Spectra Produced by p-p Interaction in Astronomical Environments, *The Astrophysical Journal* **647**(1), 692.

Karlsson, N. (2008), Hadronic Production of Gamma Rays and Starburst Galaxies, *AIP Conference Proceedings* **1085**(1), 561.

Kauffmann, G., White, S. D. M. and Guiderdoni, B. (1993), The Formation and Evolution of Galaxies Within Merging Dark Matter Haloes, *MNRAS* **264**, 201.

Kazantsev, A. P. (1968), Enhancement of a Magnetic Field by a Conducting Fluid, *JETP* **26**, 1031.

Kelner, S. R., Aharonian, F. A. and Bugayov, V. V. (2006), Energy spectra of gamma rays, electrons, and neutrinos produced at proton-proton interactions in the very high energy regime, *Phys. Rev. D* **74**(3), 034018.

Kereš, D. et al. (2005), How do galaxies get their gas?, *MNRAS* **363**, 2–28.

Kereš, D. et al. (2009), Galaxies in a simulated ΛCDM Universe - I. Cold mode and hot cores, *MNRAS* **395**, 160–179.

Khanna, R. (1998), Generation of magnetic fields by a gravitomagnetic plasma battery, *MNRAS* **295**, L6–L10.

Khochfar, S. and Ostriker, J. P. (2008), Adding Environmental Gas Physics to the Semianalytic Method for Galaxy Formation: Gravitational Heating, *ApJ* **680**(1), 54–69.

Khochfar, S. and Silk, J. (2009), Modeling the Star-Forming Universe at z = 2: Impact of Cold Accretion Flows, *ApJ* **700**, L21–L24.

Klein, O. and Nishina, T. (1929), Über die Streuung von Strahlung durch freie Elektronen nach der neuen relativistischen Quantendynamik von Dirac, *Zeitschrift fur Physik* **52**, 853–868.

Klein, S. R. (2006), e^+e^- Pair production from 10 GeV to 10 ZeV, *Radiation Physics and Chemistry* **75**, 696.

Knudsen, K. K. et al. (2016), [C II] emission in z∼6 strongly lensed, star-forming galaxies, *MNRAS* **462**(1), L6.

Knudsen, K. K. et al. (2017), A merger in the dusty, z = 7.5 galaxy A1689-zD1?, *MNRAS* **466**, 138–146.

Ko, C.-M. (2017), personal communication.

Ko, C.-M. and Lo, Y.-Y. (2009), Stability of a Cosmic-Ray-Magnetohydrodynamic System, *ApJ* **691**(2), 1587.

Kobayashi, M. A. R. et al. (2016), Morphological Properties of Lyα Emitters at Redshift 4.86 in the Cosmos Field: Clumpy Star Formation or Merger?, *ApJ* **819**, 25.

Koch, P.M. et al. (2015), Local Magnetic Field Role in Star Formation, *EAS Publications Series* **75-76**, 159.

Kolmogorov, A. N. (1941a), Dissipation of Energy in Locally Isotropic Turbulence, *Akademiia Nauk SSSR Doklady* **32**, 16.

Kolmogorov, A. N. (1941b), On the degeneration of isotropic turbulence in an incompressible viscous fluid, *Dokl. Akad. Nauk SSSR* **31**(6), 319–323.

Kolmogorov, A. N. (1962), A refinement of previous hypotheses concerning the local structure of turbulence in a viscous incompressible fluid at high Reynolds number, *Journal of Fluid Mechanics* **13**(1), 8285.

Kotera, K., Allard, D. and Olinto, A. V. (2010), Cosmogenic neutrinos: parameter space and detectabilty from PeV to ZeV, *J. Cosmology Astropart. Phys.* **10**, 013.

Kotera, K. and Olinto, A. V. (2011), The Astrophysics of Ultrahigh-Energy Cosmic Rays, *ARA&A* **49**, 119.

Kraichnan, R. H. (1959), The structure of isotropic turbulence at very high Reynolds numbers, *Journal of Fluid Mechanics* **5**(4), 497543.

Kraichnan, R. H. (1965), Inertial-Range Spectrum of Hydromagnetic Turbulence, *Physics of Fluids* **8**, 1385–1387.

Kraichnan, R. H. (1971), Inertial-range transfer in two- and three-dimensional turbulence, *Journal of Fluid Mechanics* **47**(3), 525535.

Kronberg, P. P., Lesch, H. and Hopp, U. (1999), Magnetization of the Intergalactic Medium by Primeval Galaxies, *ApJ* **511**, 56–64.

Kulpa-Dybeł, K. et al. (2011), Global Simulations of the Magnetic Field Evolution in Barred Galaxies Under the Influence of the Cosmic-ray-driven Dynamo, *ApJ* **733**, L18.

Kulsrud, R. and Pearce, W. P. (1969), The Effect of Wave-Particle Interactions on the Propagation of Cosmic Rays, *ApJ* **156**, 445.

Kulsrud, R. M. (2005), *Plasma physics for astrophysics*, Princeton University Press.

Kulsrud, R. M. and Cesarsky, C. J. (1971), The Effectiveness of Instabilities for the Confinement of High Energy Cosmic Rays in the Galactic Disk, *Astrophys. Lett.* **8**, 189.

Kusakabe, M. et al. (2014), Revised Big Bang Nucleosynthesis with Long-lived, Negatively Charged Massive Particles: Updated Recombination Rates, Primordial ^{9}Be Nucleosynthesis, and Impact of New ^{6}Li Limits, *ApJS* **214**, 5.

Kuwabara, T. and Ko, C.-M. (2006), Parker-Jeans Instability of Gaseous Disks Including the Effect of Cosmic Rays, *ApJ* **636**(1), 290.

Kuwabara, T. and Ko, C.-M. (2015), Analysis of Magnetorotational Instability with the Effect of Cosmic-Ray Diffusion, *ApJ* **798**(2), 79.

Lacey, C. G. et al. (2008), Galaxy evolution in the infrared: comparison of a hierarchical galaxy formation model with Spitzer data, *MNRAS* **385**(3), 1155.

Lacey, C. and Cole, S. (1993), Merger rates in hierarchical models of galaxy formation, *MNRAS* **262**, 627–649.

Lacki, B. C. (2015), The ultimate fate of cosmic rays from galaxies and their role in the intergalactic medium, *MNRAS* **448**, L20–L24.

Lacki, B. C. et al. (2011), On the GeV and TeV Detections of the Starburst Galaxies M82 and NGC 253, *ApJ* **734**, 107.

Lacki, B. C. and Beck, R. (2013), The equipartition magnetic field formula in starburst galaxies: accounting for pionic secondaries and strong energy losses, *MNRAS* **430**, 3171–3186.

Lada, C. J. (2006), Stellar Multiplicity and the Initial Mass Function: Most Stars Are Single, *ApJ* **640**, L63–L66.

Lambas, D. G. et al. (2003), Galaxy pairs in the 2dF survey - I. Effects of interactions on star formation in the field, *MNRAS* **346**, 1189–1196.

Larson, R. B. (1974), Effects of supernovae on the early evolution of galaxies, *MNRAS* **169**, 229–246.

Larson, R. B. and Tinsley, B. M. (1978), Star formation rates in normal and peculiar galaxies, *ApJ* **219**, 46–59.

Larson, R. B., Tinsley, B. M. and Caldwell, C. N. (1980), The evolution of disk galaxies and the origin of S0 galaxies, *ApJ* **237**, 692–707.

Latif, M. A. et al. (2013), The small-scale dynamo and the amplification of magnetic fields in massive primordial haloes, *MNRAS* **432**, 668–678.

Laursen, P., Sommer-Larsen, J. and Razoumov, A. O. (2011), Intergalactic Transmission and Its Impact on the Lyα Line, *ApJ* **728**, 52.

Ledrew, G. (2001), The Real Starry Sky, *JRASC* **95**, 32.

Leite, N. et al. (2017), Do cosmic rays heat the early intergalactic medium?, *MNRAS* **469**(1), 416.

Leitherer, C. et al. (1999), Starburst99: Synthesis Models for Galaxies with Active Star Formation, *ApJS* **123**, 3–40.

Lemoine-Goumard, M. et al. (2012), Constraints on cosmic-ray efficiency in the supernova remnant RCW 86 using multi-wavelength observations, *A&A* **545**, A28.

Lenc, E. and Tingay, S. J. (2006), The Subparsec-Scale Radio Properties of Southern Starburst Galaxies. I. Supernova Remnants, the Supernova Rate, and the Ionized Medium in the NGC 253 Starburst, *AJ* **132**, 1333.

Leroy, A. K. et al. (2013), Clumping and the Interpretation of kpc-scale Maps of the Interstellar Medium: Smooth H I and Clumpy, Variable H_2 Surface Density, *ApJ* **769**(1), L12.

Li, J.-T. and Wang, Q. D. (2013), Chandra survey of nearby highly inclined disc galaxies - II. Correlation analysis of galactic coronal properties, *MNRAS* **435**, 3071–3084.

Libeskind, N. I. et al. (2018), Tracing the cosmic web, *MNRAS* **473**, 1195–1217.

Linsley, J. (1963), Evidence for a Primary Cosmic-Ray Particle with Energy 10^{20} eV, *Physical Review Letters* **10**, 146–148.

Lipari, P. (2003), Introduction to neutrino physics, *in* N. Ellis and B. Maréchal (eds.), *2001 CERN - CLAF School of High-energy Physics Proceedings*, Vol. 3, p.283.

Liu, J., Mao, S. and Wang, Q. D. (2011), Charge-exchange X-ray emission of M82: Kα triplets of O VII, Ne IX and Mg XI, *MNRAS* **415**, L64–L68.

Liu, J., Wang, Q. D. and Mao, S. (2012), Charge-exchange X-ray emission of nearby star-forming galaxies, *MNRAS* **420**, 3389–3395.

Lockhart, K. E. et al. (2015), HST/WFC3 Observations of an Off-nuclear Superbubble in Arp 220, *ApJ* **810**(2), 149.

Loeb, A. and Waxman, E. (2006), The cumulative background of high energy neutrinos from starburst galaxies, *J. Cosmology Astropart. Phys.* **5**, 003.

Longair, M. S. (2011), *High Energy Astrophysics*, Cambridge University Press.

Lonsdale, C. J. et al. (2006), VLBI Images of 49 Radio Supernovae in Arp 220, *ApJ* **647**, 185.

Mac Low, M.-M. and Ferrara, A. (1999), Starburst-driven Mass Loss from Dwarf Galaxies: Efficiency and Metal Ejection, *ApJ* **513**(1), 142.

Madau, P., Ferrara, A. and Rees, M. J. (2001), Early Metal Enrichment of the Intergalactic Medium by Pregalactic Outflows, *ApJ* **555**, 92–105.

Maier, C. et al. (2015), Mass-metallicity relation of zCOSMOS galaxies at z ≃ 0.7, its dependence on star formation rate, and the existence of massive low-metallicity galaxies, *A&A* **577**, A14.

Mainali, R. et al. (2018), Spectroscopic constraints on UV metal line emission at z ≃ 6-9: the nature of Lyα emitting galaxies in the reionization era, *MNRAS* **479**, 1180–1193.

Maiolino, R. et al. (2015), The assembly of 'normal' galaxies at z∼7 probed by ALMA, *MNRAS* **452**, 54–68.

Mandelker, N. et al. (2018), Cold Filamentary Accretion and the Formation of Metal-poor Globular Clusters and Halo Stars, *ApJ* **861**, 148.

Maness, H. et al. (2007), Evidence for a Long-standing Top-heavy Initial Mass Function in the Central Parsec of the Galaxy, *ApJ* **669**(2), 1024.

Mannucci, F. et al. (2010), A fundamental relation between mass, star formation rate and metallicity in local and high-redshift galaxies, *MNRAS* **408**, 2115–2127.

Martel, H. and Shapiro, P. (2001), *Revista Mexicana de Astronomia y Astrofisica Conference Series* **10**, 101.

Martin, C. L. et al. (2013), Scattered Emission from z∼1 Galactic Outflows, *ApJ* **770**(1), 41.

Martin, C. L., Kobulnicky, H. A. and Heckman, T. M. (2002), The Metal Content of Dwarf Starburst Winds: Results from Chandra Observations of NGC 1569, *ApJ* **574**, 663–692.

Matsuda, Y. et al. (2006), A Keck/DEIMOS Spectroscopy of Lyα Blobs at Redshift z = 3.1, *ApJ* **640**, L123–L126.

Matsuda, Y. et al. (2011), The Subaru Lyα blob survey: a sample of 100-kpc Lyα blobs at z=3, *MNRAS* **410**, L13–L17.

Matthee, J. et al. (2018), Confirmation of double peaked Lyα emission at z = 6.593. Witnessing a galaxy directly contributing to the reionisation of the Universe, *A&A* **619**, A136.

Mawatari, K. et al. (2016), Possible identification of massive and evolved galaxies at z∼5, *PASJ* **68**, 46.

McCrady, N., Gilbert, A. M. and Graham, J. R. (2003), Kinematic Masses of Super-Star Clusters in M82 from High-Resolution Near-Infrared Spectroscopy, *ApJ* **596**(1), 240.

McCray, R. and Buff, J. (1972), Cosmic-Ray Heating of Low-Density Interstellar H II Regions, *ApJ* **175**, L65.

Meier, D. S., Turner, J. L. and Beck, S. C. (2002), Molecular Gas and the Young Starburst in NGC 5253 Revisited, *AJ* **124**, 877–885.

Meijerink, R. and Spaans, M. (2005), Diagnostics of irradiated gas in galaxy nuclei. I. A far-ultraviolet and X-ray dominated region code, *A&A* **436**, 397–409.

Miniati, F. and Bell, A. R. (2011), Resistive Magnetic Field Generation at Cosmic Dawn, *ApJ* **729**, 73.

Miranda, O. D., Opher, M. and Opher, R. (1998), Seed magnetic fields Generated by Primordial Supernova Explosions, *MNRAS* **301**, 547–550.

Mo, H. J. et al. (2005), Pre-heating by pre-virialization and its impact on galaxy formation, *MNRAS* **363**, 1155–1166.

Mohan, N. R., Goss, W. M. and Anantharamaiah, K. R. (2005), Multi-density model of the ionised gas in NGC 253 using radio recombination lines, *A&A* **432**, 1–14.

Mora, S. C. and Krause, M. (2013), Magnetic field structure and halo in NGC 4631, *A&A* **560**, A42.

Morlino, G. and Caprioli, D. (2012), Strong evidence for hadron acceleration in Tycho's supernova remnant, *A&A* **538**, A81.

Moster, B. P. et al. (2011), The effects of a hot gaseous halo in galaxy major mergers, *MNRAS* **415**, 3750–3770.

Mücke, A. et al. (1999), Photohadronic Processes in Astrophysical Environments, *PASA* **16**, 160.

Muno, M. P. et al. (2006), A Neutron Star with a Massive Progenitor in Westerlund 1, *ApJ* **636**, L41–L44.

Murata, K. L. et al. (2014), Evolution of the Fraction of Clumpy Galaxies at 0.2 < z < 1.0 in the COSMOS Field, *ApJ* **786**, 15.

Murray, N., Quataert, E. and Thompson, T. A. (2005), On the Maximum Luminosity of Galaxies and Their Central Black Holes: Feedback from Momentum-driven Winds, *ApJ* **618**, 569–585.

Naab, T. and Ostriker, J. P. (2017), Theoretical Challenges in Galaxy Formation, *ARA&A* **55**, 59–109.

Nagano, M. et al. (1992), Energy spectrum of primary cosmic rays above $10^{17.0}$ eV determined from extensive air shower experiments at Akeno, *Journal of Physics G Nuclear Physics* **18**, 423–442.

Nagataki, S. (2004), High-Energy Neutrinos Produced by Interactions of Relativistic Protons in Shocked Pulsar Winds, *The Astrophysical Journal* **600**(2), 883.

Nath, B. B. and Biermann, P. L. (1993), Did cosmic rays reionize the intergalactic medium?, *MNRAS* **265**, 421.

Nath, B. B. and Silk, J. (2009), Starburst-driven galactic outflows, *MNRAS* **396**, L90–L94.

Nath, B. B. and Trentham, N. (1997), On the enrichment of the intergalactic medium by galactic winds, *MNRAS* **291**, 505.

Nath, B. B., Laskar, T. and Shull, J. M. (2008), Dust Sputtering by Reverse Shocks in Supernova Remnants, *ApJ* **682**, 1055–1064.

Navarro, J. F., Frenk, C. S. and White, S. D. M. (1996), The Structure of Cold Dark Matter Halos, *ApJ* **462**, 563.

Nelson, E. et al. (2014), A massive galaxy in its core formation phase three billion years after the Big Bang, *Nature* **513**(7518), 394–397.

Nicastro, F. et al. (2018), Observations of the missing baryons in the warm-hot intergalactic medium, *Nature* **558**, 406–409.

Nicastro, F., Mathur, S. and Elvis, M. (2008), Missing Baryons and the Warm-Hot Intergalactic Medium, *Science* **319**, 55.

Nikolic, B., Cullen, H. and Alexander, P. (2004), Star formation in close pairs selected from the Sloan Digital Sky Survey, *MNRAS* **355**, 874–886.

Nozawa, T. et al. (2007), Evolution of Dust in Primordial Supernova Remnants: Can Dust Grains Formed in the Ejecta Survive and Be Injected into the Early Interstellar Medium?, *ApJ* **666**, 955–966.

Oesch, P. A. et al. (2009), The UDF05 Follow-Up of the Hubble Ultra Deep Field. II. Constraints on Reionization from Z-Dropout Galaxies, *ApJ* **690**, 1350–1357.

Oesch, P. A. et al. (2014), The Most Luminous z~9-10 Galaxy Candidates Yet Found: The Luminosity Function, Cosmic Star-formation Rate, and the First Mass Density Estimate at 500 Myr, *ApJ* **786**, 108.

Oesch, P. A. et al. (2015), A Spectroscopic Redshift Measurement for a Luminous Lyman Break Galaxy at z = 7.730 Using Keck/MOSFIRE, *ApJ* **804**, L30.

Oesch, P. A. et al. (2016), A Remarkably Luminous Galaxy at z=11.1 Measured with Hubble Space Telescope Grism Spectroscopy, *ApJ* **819**, 129.

Ohyama, Y. et al. (2002), Decomposition of the Superwind in M 82, *PASJ* **54**, 891–898.

Ono, Y. et al. (2012), Spectroscopic Confirmation of Three z-dropout Galaxies at z = 6.844-7.213: Demographics of Lyα Emission in z~7 Galaxies, *ApJ* **744**, 83.

Ono, Y. et al. (2013), Evolution of the Sizes of Galaxies over $7 < z < 12$ Revealed by the 2012 Hubble Ultra Deep Field Campaign, *ApJ* **777**, 155.

Oppenheimer, B. D. and Davé, R. (2008), Mass, metal, and energy feedback in cosmological simulations, *MNRAS* **387**, 577–600.

Oser, L. et al. (2010), The Two Phases of Galaxy Formation, *ApJ* **725**, 2312–2323.

Ostriker, E. C. and Shetty, R. (2011), Maximally Star-forming Galactic Disks. I. Starburst Regulation Via Feedback-driven Turbulence, *ApJ* **731**, 41.

Ota, K. et al. (2014), ALMA Observation of 158 μm [C II] Line and Dust Continuum of a $z = 7$ Normally Star-forming Galaxy in the Epoch of Reionization, *ApJ* **792**, 34.

Ouchi, M. et al. (2013), An Intensely Star-forming Galaxy at $z \sim 7$ with Low Dust and Metal Content Revealed by Deep ALMA and HST Observations, *ApJ* **778**, 102.

Owen, E. R. et al. (2019), Hadronic interactions of energetic charged particles in protogalactic outflow environments and implications for the early evolution of galaxies, *MNRAS* **484**(2), 1645–1671.

Page, M. (2018), personal communication.

Paglione, T. A. D. et al. (1996), Diffuse Gamma-Ray Emission from the Starburst Galaxy NGC 253, *ApJ* **460**, 295.

Pakmor, R. et al. (2016), Galactic Winds Driven by Isotropic and Anisotropic Cosmic-Ray Diffusion in Disk Galaxies, *ApJ* **824**, L30.

Palouš, J. et al. (2013), Young Stellar Clusters with a Schuster Mass Distribution. I. Stationary Winds, *ApJ* **772**, 128.

Patrignani, C. et al. (2016), Review of Particle Physics, *Chin. Phys.* **C40**(10), 100001.

Peacock, J. A. (1999), *Cosmological Physics*, Cambridge University Press.

Peiris, H. V. (2012a), Lecture notes: Cosmology Part I: The Homogenous Universe.

Peiris, H. V. (2012b), Lecture notes: Cosmology Part II: The Perturbed Universe.

Peng, Y., Maiolino, R. and Cochrane, R. (2015), Strangulation as the primary mechanism for shutting down star formation in galaxies, *Nature* **521**, 192–195.

Perets, H. B. et al. (2010), A faint type of supernova from a white dwarf with a helium-rich companion, *Nature* **465**(7296), 322.

Persic, M., Rephaeli, Y. and Arieli, Y. (2008), Very-high-energy emission from M 82, *A&A* **486**, 143–149.

Pettini, M. et al. (2003), The C IV Mass Density of the Universe at Redshift 5, *ApJ* **594**, 695–703.

Pfrommer, C. et al. (2007), Simulating cosmic rays in clusters of galaxies - I. Effects on the Sunyaev-Zel'dovich effect and the X-ray emission, *MNRAS* **378**, 385–408.

Pieri, M. M., Martel, H. and Grenon, C. (2007), Anisotropic Galactic Outflows and Enrichment of the Intergalactic Medium. I. Monte Carlo Simulations, *ApJ* **658**(1), 36.

Pierre Auger Collaboration (2007), Correlation of the Highest-Energy Cosmic Rays with Nearby Extragalactic Objects, *Science* **318**, 938.

Pillepich, A. et al. (2018), Simulating galaxy formation with the IllustrisTNG model, *Monthly Notices of the Royal Astronomical Society* **473**(3), 4077–4106.

Pinzke, A. and Pfrommer, C. (2010), Simulating the γ-ray emission from galaxy clusters: a universal cosmic ray spectrum and spatial distribution, *MNRAS* **409**, 449–480.

Planck Collaboration (2016), Planck intermediate results - XXXV. Probing the role of the magnetic field in the formation of structure in molecular clouds, *A&A* **586**, A138.

Planck Collaboration et al. (2018), Planck results. VI. Cosmological parameters, *arXiv e-prints* .

Pollack, J. B. and Fazio, G. G. (1963), Production of π Mesons and Gamma Radiation in the Galaxy by Cosmic Rays, *Phys. Rev.* **131**, 2684.

Press, W. H. et al. (2007), *Numerical Recipes 3rd Edition: The Art of Scientific Computing*, 3 edition, Cambridge University Press.

Press, W. H. and Schechter, P. (1974), Formation of Galaxies and Clusters of Galaxies by Self-Similar Gravitational Condensation, *ApJ* **187**, 425–438.

Protheroe, R. J. and Johnson, P. A. (1996), Propagation of ultra high energy protons and gamma rays over cosmological distances and implications for topological defect models, *Astroparticle Physics* **4**, 253.

Putman, M. E., Peek, J. E. G. and Joung, M. R. (2012), Gaseous Galaxy Halos, *ARA&A* **50**, 491–529.

Quilis, V. and Trujillo, I. (2013), Expected Number of Massive Galaxy Relics in the Present Day Universe, *ApJ* **773**, L8.

Rao, R. et al. (2009), IRAS 16293: A "Magnetic" Tale of Two Cores, *ApJ* **707**(2), 921.

Rauch, M. et al. (2011), Filamentary infall of cold gas and escape of Lyα and hydrogen ionizing radiation from an interacting high-redshift galaxy, *MNRAS* **418**, 1115–1126.

Recchia, S., Blasi, P. and Morlino, G. (2016), Cosmic ray driven Galactic winds, *MNRAS* **462**, 4227–4239.

Rees, M. J. (1987), The origin and cosmogonic implications of seed magnetic fields, *QJRAS* **28**, 197.

Rephaeli, Y., Arieli, Y. and Persic, M. (2010), High-energy emission from the starburst galaxy NGC 253, *MNRAS* **401**, 473–478.

Rephaeli, Y. and Persic, M. (2014), Nonthermal Emission in the Starburst Galaxies M 82 & NGC 253, **256**.

Ribaudo, J. et al. (2011), Evidence for Cold Accretion: Primitive Gas Flowing onto a Galaxy at z∼0.274, *ApJ* **743**, 207.

Riechers, D. A. et al. (2014), ALMA Imaging of Gas and Dust in a Galaxy Protocluster at Redshift 5.3: [C II] Emission in "Typical" Galaxies and Dusty Starbursts ≃1 Billion Years after the Big Bang, *ApJ* **796**, 84.

Rieder, M. and Teyssier, R. (2016), A small-scale dynamo in feedback-dominated galaxies as the origin of cosmic magnetic fields - I. The kinematic phase, *MNRAS* **457**, 1722.

Rieger, F. M., Bosch-Ramon, V. and Duffy, P. (2007), Fermi acceleration in astrophysical jets, *Ap&SS* **309**, 119–125.

Rieke, G. H. et al. (1993), Starburst modeling of M82 - Test case for a biased initial mass function, *ApJ* **412**, 99.

Rimondi, F. (1993), Multiplicity distributions in $\bar{p}p$ interactions at $\sqrt{s} = 1800$-GeV, *in 23rd International Symposium on Ultra-High Energy Multiparticle Phenomena Aspen, Colorado, September 12-17, 1993*, pp.0400–404.

Robertson, B. E. et al. (2010), Early star-forming galaxies and the reionization of the Universe, *Nature* **468**, 49–55.

Robitaille, T. P. and Whitney, B. A. (2010), The Present-Day Star Formation Rate of the Milky Way Determined from Spitzer-Detected Young Stellar Objects, *ApJ* **710**, L11–L15.

Rodriguez, E. L. (2018), SOFIA/HAWC+ Polarization in Galaxies: Its all about the magnetic fields (press release).

Rodriguez-Gomez, V. et al. (2016), The stellar mass assembly of galaxies in the Illustris simulation: growth by mergers and the spatial distribution of accreted stars, *MNRAS* **458**, 2371–2390.

Rodríguez-González, A. et al. (2007), Winds from clusters with non-uniform stellar distributions, *MNRAS* **380**, 1198–1206.

Roseboom, I. G., Oliver, S. and Farrah, D. (2009), Spitzer IRS Observations of k+a Galaxies: A Link Between Polycyclic Aromatic Hydrocarbon Emission Properties and Active Galactic Nucleus Feedback?, *ApJ* **699**, L1–L4.

Rowlands, K. et al. (2015), The evolution of the cold interstellar medium in galaxies following a starburst, *MNRAS* **448**, 258–279.

Rubin, K. H. R. et al. (2014), Evidence for Ubiquitous Collimated Galactic-scale Outflows along the Star-forming Sequence at z∼0.5, *ApJ* **794**(2), 156.

Rupke, D. S., Veilleux, S. and Sanders, D. B. (2003), Keck AbsorptionLine Spectroscopy of Galactic Winds in Massive InfraredLuminous Galaxies, *AIP Conference Proceedings* **666**(1), 195.

Rupke, D. S., Veilleux, S. and Sanders, D. B. (2005a), Outflows in Infrared-Luminous Starbursts at z< 0.5. I. Sample, Na I D Spectra, and Profile Fitting, *ApJS* **160**(1), 87.

Rupke, D. S., Veilleux, S. and Sanders, D. B. (2005b), Outflows in Infrared-Luminous Starbursts at z< 0.5. II. Analysis and Discussion, *ApJS* **160**(1), 115.

Ruszkowski, M., Yang, H.-Y. K. and Reynolds, C. S. (2017), Cosmic-Ray Feedback Heating of the Intracluster Medium, *ApJ* **844**, 13.

Rybicki, G. B. and Lightman, A. P. (1979), *Radiative processes in astrophysics*, Wiley.

Salem, M. and Bryan, G. L. (2014), Cosmic ray driven outflows in global galaxy disc models, *MNRAS* **437**, 3312–3330.

Salvadori, S. et al. (2014), Metals and ionizing photons from dwarf galaxies, *MNRAS* **437**, L26–L30.

Samui, S., Subramanian, K. and Srianand, R. (2005), Can Cosmic Rays Heat the Intergalactic Medium?, *International Cosmic Ray Conference* **9**, 215.

Samui, S., Subramanian, K. and Srianand, R. (2008), Constrained semi-analytical models of galactic outflows, *MNRAS* **385**, 783–808.

Samui, S., Subramanian, K. and Srianand, R. (2009), Models of high redshift luminosity functions and galactic outflows: The dependence on halo mass function, *New A* **14**, 591–603.

Samui, S., Subramanian, K. and Srianand, R. (2010), Cosmic ray driven outflows from high-redshift galaxies, *MNRAS* **402**, 2778–2791.

Sánchez Almeida, J. et al. (2014), Star formation sustained by gas accretion, *A&A Rev.* **22**, 71.

Sancisi, R. et al. (2008), Cold gas accretion in galaxies, *A&A Rev.* **15**, 189–223.

Sarkar, K. C. et al. (2016), Diffuse X-Ray Emission from Star-forming Galaxies, *ApJ* **818**, L24.

Sazonov, S. and Sunyaev, R. (2015), Preheating of the Universe by cosmic rays from primordial supernovae at the beginning of cosmic reionization, *MNRAS* **454**, 3464.

Scannapieco, E. (2005), What Can the Distribution of Intergalactic Metals Tell Us about the History of Cosmological Enrichment?, *ApJ* **624**, L1–L4.

Scannapieco, E., Ferrara, A. and Madau, P. (2002), Early Enrichment of the Intergalactic Medium and Its Feedback on Galaxy Formation, *ApJ* **574**, 590–598.

Schaye, J. et al. (2003), Metallicity of the Intergalactic Medium Using Pixel Statistics. II. The Distribution of Metals as Traced by C IV, *ApJ* **596**, 768–796.

Schaye, J. et al. (2015), The EAGLE project: simulating the evolution and assembly of galaxies and their environments, *Monthly Notices of the Royal Astronomical Society* **446**(1), 521–554.

Schlickeiser, R. (2002), *Cosmic Ray Astrophysics*, Berlin: Springer.

Schober, J., Schleicher, D. R. G. and Klessen, R. S. (2013), Magnetic field amplification in young galaxies, *A&A* **560**, A87.

Schober, J., Schleicher, D. R. G. and Klessen, R. S. (2015), X-ray emission from star-forming galaxies - signatures of cosmic rays and magnetic fields, *MNRAS* **446**(1), 2.

Schure, K. M. and Bell, A. R. (2013), Cosmic ray acceleration in young supernova remnants, *MNRAS* **435**, 1174–1185.

Seaquist, E. R., Bell, M. B. and Bignell, R. C. (1985), Radio studies of the ionized gas in the nucleus of M82, *ApJ* **294**, 546.

Seaquist, E. R. and Clark, J. (2001), Observations of CO J=3-2 in the Outflow of the Starburst Galaxy M82, *ApJ* **552**, 133–143.

Serra, P., Doré, O. and Lagache, G. (2016), Dissecting the High-z Interstellar Medium through Intensity Mapping Cross-correlations, *ApJ* **833**, 153.

Shalchi, A. et al. (2004), Nonlinear Parallel and Perpendicular Diffusion of Charged Cosmic Rays in Weak Turbulence, *ApJ* **616**, 617–629.

Shalchi, A. et al. (2006), Parallel and Perpendicular Transport of Heliospheric Cosmic Rays in an Improved Dynamical Turbulence Model, *ApJ* **642**, 230–243.

Sharma, M. et al. (2017), Winds of change: reionization by starburst galaxies, *MNRAS* **468**, 2176–2188.

Shen, S., Wadsley, J. and Stinson, G. (2010), The enrichment of the intergalactic medium with adiabatic feedback - I. Metal cooling and metal diffusion, *MNRAS* **407**, 1581–1596.

Sigl, G., Olinto, A. V. and Jedamzik, K. (1997), Primordial magnetic fields from cosmological first order phase transitions, *Phys. Rev. D* **55**, 4582.

Silich, S. et al. (2011), The Steady-state Wind Model for Young Stellar Clusters with an Exponential Stellar Density Distribution, *ApJ* **743**, 120.

Silvia, D. W., Smith, B. D. and Shull, J. M. (2010), Numerical Simulations of Supernova Dust Destruction. I. Cloud-crushing and Post-processed Grain Sputtering, *ApJ* **715**, 1575–1590.

Simcoe, R. A. (2006), High-Redshift Intergalactic C IV Abundance Measurements from the Near-Infrared Spectra of Two z ˜ 6 QSOs, *ApJ* **653**, 977–987.

Skorodko, T. et al. (2008), Excitation of the Roper resonance in single- and double-pion production in nucleon-nucleon collisions, *European Physical Journal A* **35**, 317.

Slattery, P. (1972), Evidence for the Onset of Semi-inclusive Scaling in Proton-Proton Collisions in the $50 - 300 - \mathrm{GeV}/c$ Momentum Range, *Phys. Rev. Lett.* **29**, 1624–1627.

Smartt, S. J. (2009), Progenitors of Core-Collapse Supernovae, *ARA&A* **47**, 63.

Smartt, S. J. et al. (2009), The death of massive stars - I. Observational constraints on the progenitors of Type II-P supernovae, *MNRAS* **395**, 1409–1437.

Smercina, A. et al. (2018), After the Fall: The Dust and Gas in E+A Post-starburst Galaxies, *ApJ* **855**, 51.

Smith, N. et al. (2011), Observed fractions of core-collapse supernova types and initial masses of their single and binary progenitor stars, *MNRAS* **412**, 1522.

Smith, N., Hinkle, K. H. and Ryde, N. (2009), Red Supergiants as Potential Type IIn Supernova Progenitors: Spatially Resolved 4.6 μm CO Emission Around VY CMa and Betelgeuse, *AJ* **137**, 3558–3573.

Smith, N., Vink, J. S. and de Koter, A. (2004), The Missing Luminous Blue Variables and the Bistability Jump, *ApJ* **615**, 475–484.

Socrates, A., Davis, S. W. and Ramirez-Ruiz, E. (2008), The Eddington Limit in Cosmic Rays: An Explanation for the Observed Faintness of Starbursting Galaxies, *ApJ* **687**(1), 202.

Sofue, Y. and Rubin, V. (2001), Rotation Curves of Spiral Galaxies, *ARA&A* **39**, 137–174.

Soida, M. et al. (2011), The large scale magnetic field structure of the spiral galaxy NGC 5775, *A&A* **531**, A127.

Somerville, R. S. and Primack, J. R. (1999), Semi-analytic modelling of galaxy formation: the local Universe, *MNRAS* **310**(4), 1087–1110.

Songaila, A. and Cowie, L. L. (1996), Metal enrichment and Ionization Balance in the Lyman Alpha Forest at $z = 3$, *AJ* **112**, 335.

Stark, D. P. et al. (2013), Keck Spectroscopy of 3<z<7 Faint Lyman Break Galaxies: The Importance of Nebular Emission in Understanding the Specific Star Formation Rate and Stellar Mass Density, *ApJ* **763**(2), 129.

Starkenburg, T. K., Tonnesen, S. and Kopenhafer, C. (2019), What Is Inside Matters: Simulated Green Valley Galaxies Have too Centrally Concentrated Star Formation, *ApJ* **874**, L17.

Stecker, F. W., Malkan, M. A. and Scully, S. T. (2006), Intergalactic Photon Spectra from the Far-IR to the UV Lyman Limit for $0 < z < 6$ and the Optical Depth of the Universe to High-Energy Gamma Rays, *ApJ* **648**, 774.

Stecker, F. W., Tsuruta, S. and Fazio, G. G. (1968), The Effects of the Decay of Nucleon Isobars and Hyperons on the Cosmic Gamma-Ray Spectrum, *ApJ* **151**, 881.

Steidel, C. C. et al. (2000), Lyα Imaging of a Proto-Cluster Region at <z>=3.09, *ApJ* **532**, 170–182.

Steidel, C. C. et al. (2002), The Kinematic Connection between absorbing Gas toward QSOs and Galaxies at Intermediate Redshift, *ApJ* **570**, 526–542.

Stepney, S. and Guilbert, P. W. (1983), Numerical FITS to important rates in high temperature astrophysical plasmas, *MNRAS* **204**, 1269.

Stewart, K. R. et al. (2013), Angular Momentum Acquisition in Galaxy Halos, *ApJ* **769**, 74.

Stolte, A. et al. (2005), The Arches Cluster: Evidence for a Truncated Mass Function?, *ApJ* **628**(2), L113.

Strickland, D. K. et al. (2000), Chandra Observations of NGC 253: New Insights into the Nature of Starburst-driven Superwinds, *AJ* **120**(6), 2965.

Strickland, D. K. and Heckman, T. M. (2007), Iron Line and Diffuse Hard X-Ray Emission from the Starburst Galaxy M82, *ApJ* **658**, 258–281.

Strickland, D. K. and Heckman, T. M. (2009), Supernova Feedback Efficiency and Mass Loading in the Starburst and Galactic Superwind Exemplar M82, *ApJ* **697**, 2030–2056.

Strömgren, B. (1939), The Physical State of Interstellar Hydrogen., *ApJ* **89**, 526.

Sukumar, S. and Allen, R. J. (1990), Linearly polarised radio emission from M83 (NGC 5236) and NGC 891, *in* R. Beck, P. P. Kronberg and R. Wielebinski (eds.), *Galactic and Intergalactic Magnetic Fields*, Vol. 140 of *IAU Symposium*, pp.215–217.

Sukumar, S. and Allen, R. J. (1991), Polarized radio emission from the edge-on spiral galaxies NGC 891 and NGC 4565, *ApJ* **382**, 100–107.

Sun, G. and Furlanetto, S. R. (2016), Constraints on the star formation efficiency of galaxies during the epoch of reionization, *MNRAS* **460**, 417–433.

Sur, S., Bhat, P. and Subramanian, K. (2017), Faraday rotation signatures of fluctuation dynamos in young galaxies, *ArXiv e-prints* .

Sutherland, R. S. and Dopita, M. A. (1993), Cooling functions for low-density astrophysical plasmas, *ApJS* **88**, 253–327.

Suto, D. et al. (2013), Validity of Hydrostatic Equilibrium in Galaxy Clusters from Cosmological Hydrodynamical Simulations, *ApJ* **767**, 79.

Tadaki, K.-I. et al. (2014), The Nature of Hα-selected Galaxies at z > 2. II. Clumpy Galaxies and Compact Star-forming Galaxies, *ApJ* **780**, 77.

Tanner, R., Cecil, G. and Heitsch, F. (2016), Starburst-driven Galactic Superbubbles Radiating to 10 K, *ApJ* **821**, 7.

Temim, T. et al. (2015), Dust Destruction Rates and Lifetimes in the Magellanic Clouds, *ApJ* **799**, 158.

Thomas, R. et al. (2017), The extended epoch of galaxy formation: Age dating of 3600 galaxies with 2 < z < 6.5 in the VIMOS Ultra-Deep Survey, *A&A* **602**, A35.

Thome, W. et al. (1977), Charged Particle Multiplicity Distributions in pp Collisions at ISR Energies, *Nucl. Phys.* **B129**, 365.

Thompson, T. A. et al. (2006), Magnetic Fields in Starburst Galaxies and the Origin of the FIR-Radio Correlation, *ApJ* **645**, 186–198.

Thompson, T. A. et al. (2015), Dynamics of dusty radiation-pressure-driven shells and clouds: fast outflows from galaxies, star clusters, massive stars, and AGN, *MNRAS* **449**, 147–161.

Tominaga, N. et al. (2008), The Peculiar Type Ib Supernova 2006jc: A WCO Wolf-Rayet Star Explosion, *ApJ* **687**, 1208–1219.

Torres, D. F. (2004), Theoretical Modeling of the Diffuse Emission of Gamma Rays from Extreme Regions of Star Formation: The Case of ARP 220, *ApJ* **617**, 966–986.

Tremaine, S. et al. (1994), A family of models for spherical stellar systems, *AJ* **107**, 634.

Trujillo, I. et al. (2014), NGC 1277: A Massive Compact Relic Galaxy in the Nearby Universe, *ApJ* **780**, L20.

Tueros, M., del Valle, M. V. and Romero, G. E. (2014), Cosmic reionization by primordial cosmic rays, *A&A* **570**, L3.

Tumlinson, J., Peeples, M. S. and Werk, J. K. (2017), The Circumgalactic Medium, *Annual Review of Astronomy and Astrophysics* **55**, 389–432.

Turner, J. L. et al. (2015), Highly efficient star formation in NGC 5253 possibly from stream-fed accretion, *Nature* **519**, 331–333.

Uhlig, M. et al. (2012), Galactic winds driven by cosmic ray streaming, *MNRAS* **423**(3), 2374.

Valdés, M., Evoli, C. and Ferrara, A. (2010), Particle energy cascade in the intergalactic medium, *MNRAS* **404**, 1569–1582.

van de Voort, F. et al. (2012), Cold accretion flows and the nature of high column density H I absorption at redshift 3, *MNRAS* **421**, 2809–2819.

van Dokkum, P. G. (2008), Evidence of Cosmic Evolution of the Stellar Initial Mass Function, *ApJ* **674**, 29.

Varenius, E. et al. (2017), The population of SNe/SNRs in the starburst galaxy Arp 220. A self-consistent analysis of 20 years of VLBI monitoring, *ArXiv e-prints* .

Vazza, F. et al. (2018), Resolved magnetic dynamo action in the simulated intracluster medium, *MNRAS* **474**, 1672.

Veilleux, S. (2008), Galactic Winds, *Astrophys. Sp. Sci. Proceedings* **4**, 245.

Veilleux, S., Bland-Hawthorn, J. and Cecil, G. (1999), A Kinematic Link Between Boxy Bulges, Stellar Bars, and Nuclear Activity in NGC 3079 and NGC 4388, *AJ* **118**, 2108–2122.

Veilleux, S., Cecil, G. and Bland-Hawthorn, J. (2005), Galactic Winds, *ARA&A* **43**(1), 769.

Veilleux, S. et al. (1994a), The nuclear superbubble of NGC 3079, *ApJ* **433**, 48–64.

Veilleux, S., Tully, R. B. and Cecil, G. (1994b), Galaxy-scale windblown superbubbles: NGC 3079., *Bulletin d'information du telescope Canada-France-Hawaii* **30**, 2–6.

Verhamme, A. et al. (2015), Using Lyman-α to detect galaxies that leak Lyman continuum, *A&A* **578**, A7.

VERITAS Collaboration et al. (2009), A connection between star formation activity and cosmic rays in the starburst galaxy M82, *Nature* **462**, 770–772.

Völk, H. J. and Atoyan, A. M. (2000), Early Starbursts and Magnetic Field Generation in Galaxy Clusters, *ApJ* **541**, 88–94.

Walsh, J. L. et al. (2017), A Black Hole Mass Determination for the Compact Galaxy Mrk 1216, *ApJ* **835**, 208.

Walter, F. et al. (2012), Evidence for Low Extinction in Actively Star-forming Galaxies at z > 6.5, *ApJ* **752**, 93.

Walter, F., Weiss, A. and Scoville, N. (2002), Molecular Gas in M82: Resolving the Outflow and Streamers, *ApJ* **580**(1), L21.

Wang, C.-H. (1991), Multiplicity distributions from $\bar{p}-p$ collisions at 1.8 TeV center of mass energy, PhD thesis, Iowa State University.

Wang, J. et al. (2011), Assembly history and structure of galactic cold dark matter haloes, *MNRAS* **413**, 1373–1382.

Wang, J.-W. et al. (2015), Probing the magnetic field structure in the filamentary cloud IC5146, *Proceedings of the International Astronomical Union* **11**(S315).

Wang, Q. D. and Liu, J. (2012), Spectroscopic evidence of charge exchange X-ray emission from galaxies, *Astronomische Nachrichten* **333**, 373.

Wang, X. and Fields, B. D. (2014), Cosmic-ray induced gamma-ray emission from the starburst galaxy NGC 253, *AIP Conference Proceedings* **1595**(1), 231.

Wang, X. and Fields, B. D. (2018), Are starburst galaxies proton calorimeters?, *MNRAS* **474**, 4073–4088.

Watson, D. et al. (2015), A dusty, normal galaxy in the epoch of reionization, *Nature* **519**, 327–330.

Watson, M. G., Stanger, V. and Griffiths, R. E. (1984), X-ray emission from M82, *ApJ* **286**, 144.

Webber, W. R. (1998), A New Estimate of the Local Interstellar Energy Density and Ionization Rate of Galactic Cosmic Cosmic Rays, *ApJ* **506**, 329–334.

Weidner, C., Kroupa, P. and Pflamm-Altenburg, J. (2011), Top-heavy integrated galactic stellar initial mass functions in starbursts, *MNRAS* **412**(2), 979.

Weinberger, L. H. et al. (2018), Lyman-α emitters gone missing: the different evolution of the bright and faint populations, *MNRAS* **479**, 2564–2587.

Weiner, B. J. et al. (2009), Ubiquitous Outflows in DEEP2 Spectra of Star-Forming Galaxies at z = 1.4, *ApJ* **692**(1), 187.

Wentzel, D. G. (1968), Hydromagnetic Waves Excited by Slowly Streaming Cosmic Rays, *ApJ* **152**, 987.

Wentzel, D. G. (1971), Acceleration and Heating of Interstellar Gas by Cosmic Rays, *ApJ* **163**, 503.

Werner, N. et al. (2018), Digging for red nuggets: discovery of hot haloes surrounding massive, compact, relic galaxies, *MNRAS* **477**, 3886–3891.

Westmoquette, M. S. et al. (2009), The Optical Structure of the Starburst Galaxy M82. II. Nebular Properties of the Disk and Inner Wind, *ApJ* **706**, 1571–1587.

Whalen, D. J. et al. (2013), The Supernova that Destroyed a Protogalaxy: Prompt Chemical Enrichment and Supermassive Black Hole Growth, *ApJ* **774**(1), 64.

Whitmore, J. (1974), Experimental results on strong interactions in the NAL hydrogen bubble chamber, *Phys. Rep.* **10**, 273–373.

Wibig, T. and Wolfendale, A. W. (2004), At what particle energy do extragalactic cosmic rays start to predominate?, *ArXiv Astrophysics e-prints* .

Wilkinson, C. L. et al. (2018), Evolution of starburst galaxies in the Illustris simulation, *MNRAS* **479**, 758–767.

Williams, C. C. et al. (2014), The Progenitors of the Compact Early-type Galaxies at High Redshift, *ApJ* **780**(1), 1.

Wolfire, M. G. et al. (1995), The neutral atomic phases of the interstellar medium, *ApJ* **443**, 152–168.

Woods, R. M. et al. (2014), The role of cold flows and reservoirs in galaxy formation with strong feedback, *MNRAS* **442**, 732–740.

Wright, E. L. (2006), A Cosmology Calculator for the World Wide Web, *PASP* **118**, 1711–1715.

Wright, W. P. et al. (2017), Neutrinos from type Ia supernovae: The gravitationally confined detonation scenario, *Phys. Rev. D* **95**(4), 043006.

Wu, K. et al. (2019), Charge exchange emission and cold clumps in multi-phase galactic outflows, *MNRAS, submitted* .

Xu, Y. et al. (2015), Rings and Radial Waves in the Disk of the Milky Way, *ApJ* **801**(2), 105.

Yamasawa, D. et al. (2011), The Role of Dust in the Early Universe. I. Protogalaxy Evolution, *ApJ* **735**, 44.

Yates, R. M., Kauffmann, G. and Guo, Q. (2012), The relation between metallicity, stellar mass and star formation in galaxies: an analysis of observational and model data, *MNRAS* **422**, 215–231.

Yoast-Hull, T. M. et al. (2017), γ-Ray emission from Arp 220: indications of an active galactic nucleus, *MNRAS* **469**, L89–L93.

Yoast-Hull, T. M., Gallagher, III, J. S. and Zweibel, E. G. (2016), Equipartition and cosmic ray energy densities in central molecular zones of starbursts, *MNRAS* **457**(1), L29.

Zatsepin, G. T. and Kuz'min, V. A. (1966), Upper Limit of the Spectrum of Cosmic Rays, *JETPL* **4**, 78.

Zhang, B. et al. (2003), High-Energy Neutrinos from Magnetars, *ApJ* **595**, 346–351.

Zhang, D. et al. (2014), Hot Galactic Winds Constrained by the X-Ray Luminosities of Galaxies, *ApJ* **784**(2), 93.

Zhang, Y. et al. (1998), Physical Properties of the Lyα Forest in a Cold Dark Matter Cosmology, *ApJ* **495**, 63–79.

Zheng, W. et al. (2012), A magnified young galaxy from about 500 million years after the Big Bang, *Nature* **489**, 406–408.

Zolotov, A. et al. (2015), Compaction and quenching of high-z galaxies in cosmological simulations: blue and red nuggets, *MNRAS* **450**(3), 2327–2353.

Zweibel, E. (2016), Maxwell Prize: The Basis for Cosmic Ray Feedback: Written on the Wind, *in APS Meeting Abstracts*, p.SR1.001.

Zweibel, E. G. (2013), The microphysics and macrophysics of cosmic rays, *Physics of Plasmas* **20**(5), 055501.